Experimental and computational studies of spectroscopic properties of 2-aminopurine and pyrrolocytosine

Experimental and Computational Studies of Spectroscopic Properties of 2-Aminopurine and Pyrrolocytosine

A thesis submitted for the degree of Doctor of Philosophy

by

Davide Ghazal

Birkbeck College, University of London

August 2014

Abstract

Pyrrolocytosine (Pc) and 2-aminopurine (2-Ap) are modified fluorescent nucleobases that can respectively replace the non-fluorescent natural nucleobases cytosine (C) and adenine (A) and therefore, can be used to probe the structure and dynamics of nucleic acids. Changes in fluorescence emission intensity of these modified bases as a function of polarity (general solvent effect) were measured. Lippert plots were generated and the difference between the excitation and emission maxima (Stokes shift) wavelengths of Pc and 2-Ap in water and acetonitrile mixtures indicate that the measured Stokes shifts are mainly due to hydrogen bonding (specific solvent effect) rather than polarity. The data of the quantum yield measurements show that the fluorescence intensity of 2-Ap decreases in organic solvents as opposed to that of Pc. The big difference in dipole moment of the bases in the excited and ground state experimentally found may be due to intramolecular charge transfer. Computational studies performed at DFT (Density Functional Theory) level by using the B3LYP functional revealed that the most stable 2-Ap tautomer is the N9H amino tautomer in both gas and liquid phase. In the case of Pc, our results show that the most stable tautomer in the gas phase is the N9H enol tautomer whereas the N1H N9H keto one is the most stable tautomer in solution. The theoretical absorption and emission maxima are in excellent agreement with the experimental data. The optimized geometry of 2-Ap A in the ground state was found to be non-planar, i.e., with an out of plane pyramidal amino group with respect to the purine ring whereas the optimized molecule appears to be planar in the first excited state. When 2-Ap A is explicitly bound to water molecules, the energy gap between the dark state n-π* and the bright state π-π* is bigger than the electronic energy gap between the two states previously predicted in implicit solvent. The quantum yield of 2-Ap in phosphate buffers is lower than the one measured in water. This decrease in fluorescence emission is almost certainly due to dynamic quenching. The fluorescence emission of both 2-Ap and Pc is drastically reduced when the bases are incorporated into single and double-stranded oligonucleotides but, the degree of fluorescence depression is more marked in water than in buffer solutions. Oligonucleotides may form secondary structures in buffers because of the presence of salts; in particular, G-quadruplexes. The spectroscopic data acquired by using UV, fluorescence, CD (circular dichroism), and anisotropy steady-state techniques seem to rule out the presence of G-quadruplex secondary structure in selected fluorescent nucleobase containing oligonucleotides.

Declaration

I declare that the practical work presented in this report is my own otherwise indicated, and that all published work has been acknowledged. Furthermore, I affirm that I neither fabricated nor falsified the results reported herein

Signed: 

PhD student: Ghazal Davide

Signed: 

Principal Supervisor: Dr Salvador Tomas

Date: 11/08/2014

Acknowledgements

I would like to thank my supervisors Dr. Salvador Tomas and Dr. Katherine Thompson for their knowledge and expertise.

Special thanks go to Tina Davitier who kindly helped me to obtain CD spectra which were included in my thesis and Charles Umesi who provided me with some computational tips.

Also, I would like to express my sincere gratitude to Abdel-ilah Sebbar for the great and interesting discussions/debates (which were not necessarily related to scientific topics) we had during our research degree.

Of course, I cannot forget the emotional support I received from my family especially, from my sister Rebecca Ghazal who played a pivotal role towards the completion of this thesis by looking after me when I was seriously sick.

Table of contents

List of Figures

List of tables

Glossary and Abbreviations

Pc	Pyrrolocytosine
Pc_{dr}	Pyrrolocytosine deoxyribose
Pc_{r}	Pyrrolocytosine ribose
2-Ap	2-Aminopurine
$2\text{-}Ap_{dr}$	2-Aminopurine deoxyribose
C	Cytosine
G	Guanine
A	Adenine
T	Thymine
DNA	Deoxyribonucleic Acid
IC	Internal Conversion
ISC	Intersystem Crossing
S_0	Ground State
S_1	First Singlet Excited Electronic State
T_1	First Triplet Excited Electronic State
k_r	Rate constant for radiative processes
k_{nr}	Rate constant for non-radiative processes
τ	Emission Lifetime
K_{SV}	Stern-Volmer quenching constant
UV	Ultra Violet
CD	Circular Dichroism
FTIR	Fourier Transform Infrared

r	Anisotropy
Φ_F	Fluorescence Quantum Yield
μ	Dipole moment
η	Refractive index
ε	Dielectric constant
a	Cavity radius
λ_{ex}	Maximum excitation wavelength
λ_{em}	Maximum emission wavelength
Δf	Orientation polarizability
DFT	Density Functional Theory
SCRF	Self-consistent Reaction Field
HOMO	Highest Occupied Molecular Orbital
LUMO	Lowest Unoccupied Molecular Orbital
f	Oscillator strength

Chapter 1 General introduction and aim of the project

The structures and dynamics of nucleic acids cannot be directly probed by using fluorescence spectroscopy because natural nucleobases exhibit very weak fluorescence. Nucleic acids can be probed by labelling them with fluorescent dyes, but the incorporation of these dyes is neither very practical nor easy. Also, the dyes can alter the properties of nucleic acids and therefore, their functions. A solution to this problem is to use fluorescent probes which are structurally similar to the natural nucleobases. These fluorescent probes are called fluorescent nucleobase analogues. Because of their similarity to natural nucleobases, fluorescent nucleobase analogues can be safely incorporated into oligoucleotides without disrupting the chemical environment in which natural nucleobases exist (Millar, 1996; Jameson and Eccleston, 1997; Rist and Marino, 2002). The fluorescent nucleobase analogues studied in this research project are: 2-aminopurine (2-Ap) an isomer of adenine and pyrrolocytosine (Pc) which resembles cytosine but unlike the natural base it has a further five-membered ring which contains one heteroatom. The Figure 1.1 shows the four natural bases (DNA bases) and the modified bases 2-Ap and Pc. These two modified nucleobases can be selectively excited in nucleic acids because their excitation wavelengths, around 303-306 nm (in water and buffer solutions) for 2-Ap and 335-337 nm (in water and buffer solutions) for Pc, are considerably longer than the excitation wavelengths of their natural counterparts which are excited at much shorter wavelengths, precisely, between 260 and 270 nm (in water and buffer solutions) (Santosh and Mishra, 1991; Berry *et al.* 2004; Seefeld *et al.* 2005). Probing the nucleic acid structures *via* fluorescent probes provides information on many biological processes for example: DNA and RNA-ligand interactions (Rist and Marino, 2000), DNA polymerase-DNA interactions (Tleugabulova and Reha-Krantz, 2007) and recognition of mismatched base pairs (Lawrence *et al.* 1986). Currently, only limited structural information can be obtained from experiments because the underlying mechanism that causes the fluorescence to change with respect to local environment is not entirely understood. The aim of this project is to gain a better understanding of how 2-Ap and Pc (as free bases and incorporated into oligonucleotides) fluorescence intensity is influenced (decreased or increased) in different solvents such as: water, phosphate buffers and organic solvents. Thus, how polarity, hydrogen bonding formation and concomitant structural changes affect the fluorescence intensity and spectroscopic properties of the probes.

Figure 1.1 Natural and modified DNA bases

This figure displays the chemical structure of the natural bases adenine (A), cytosine (C), guanine (G) and thymine (T) and the modified bases 2-aminopurine (2-Ap) and pyrrolocytosine (Pc)

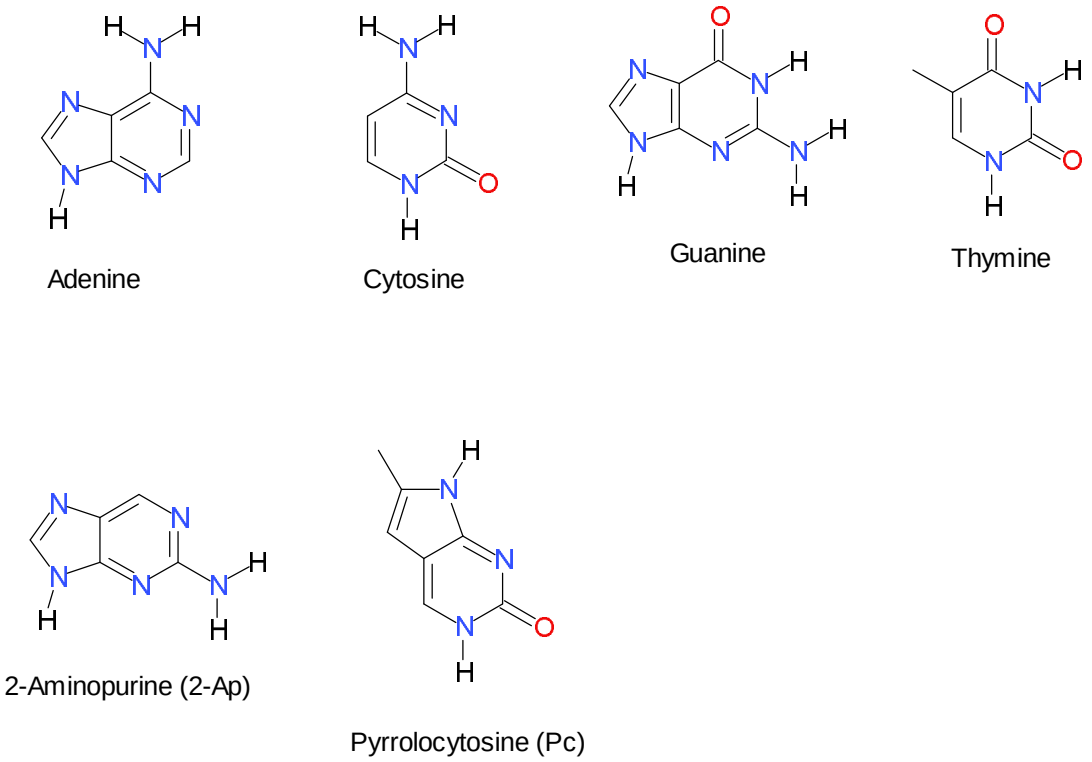

This thesis is divided into 7 chapters. **Chapter 1** is an introductory chapter on 2-Ap and Pc bases along with the aim of the project. **Chapter 2** is a chapter which is meant to introduce the reader to the basic and salient concepts in photochemistry that are relevant to this project. Furthermore, this chapter contains a literature review on the main publications on 2-Ap and Pc. In **Chapter 3** the different spectral properties of 2-Ap and Pc in organic solvents are presented herein. The emission and excitation spectra were used to measure the Stokes shifts and thus, Lippert plots were generated in order to understand how the polarity of the solvents may affect the fluorescence emission of the fluorescent probes. In **Chapter 4** DFT (Density Functional Theory) methods were used to predict the most stable 2-Ap and Pc tautomers in gas and liquid phase. The cavity radii of the optimized geometries were measured and used in the Lippert equations. The theoretical absorption and emission maxima were compared to the ones experimentally obtained. Also, the effect that explicit solvent molecules may have on the predicted molecular orbital energies and characters (for the first three vertical transitions)

of the bases was discussed by drawing energy diagrams and invoking photochemistry rules. **Chapter 5** shows a series of infrared spectra of cytosine (C) and Pc in water and organic solvents. The aim is to observe the very distinctive infrared absorption bands of the carbonyl group C=O and hydroxyl group OH of the bases in order to see whether the nature of the solvent used affects the ratio of the two tautomeric species. In **Chapter 6** an experimental study of the fluorescence emission of the bases when incorporated into oligonucleotides is reported. The impact that buffer solutions may have on the structural properties of G-rich oligonucleotides fluorescence emission is also addressed. Various steady-state techniques were used such as: UV and fluorescence as a function of temperature along with CD (Circular Dichroism) and anisotropy to discern possible secondary structures. Finally, **Chapter 7** is the general conclusions of this thesis.

Chapter 2: Basic concepts in photochemistry and literature review

2.1 Introductory concepts

Molecules possessing chromophores (a part of the molecule absorbing light) when excited by light may undergo photochemical changes. Photochemistry is the study of chemical reactions and physical changes that occur upon the interaction of matter with light due to the transfer of electrons between two quantised states. In accordance with quantum theory, light is quantised and the absorption of light by molecules occurs through photons having energy equal to the difference in energy between two electronic states. The photons are completely destroyed during the absorption process and they become part of the total energy of the absorbing molecules. Photons have both wave-like and particle-like properties and each photon possesses a particular energy abbreviated as E, see equation 2.1.

$$\mathbf{E = h}\nu \quad \mathbf{(2.1)}$$

where h is the Planck's constant and ν is the frequency of oscillator of the photon. Then, by convention the term hν is used in equations for photophysical and photochemical processes to describe the energy of photons. The equation 2.1 can also be written as the equation 2.2, where c is the speed of light and λ is the wavelength.

$$\mathbf{E = \frac{hc}{\lambda}} \quad \mathbf{(2.2)}$$

Since the speed of light is the product of the frequency times the wavelength the energy of a photon is proportional to its frequency and inversely proportional to its wavelength. Also, wavenumbers (numbers of wavelengths per centimetre) can be used being the reciprocal of wavelengths. **Erwin Schrödinger** developed a mathematical equation, see equation 2.3 that is based on the idea that the electron in the hydrogen atom displays both wavelike and particle-like behaviour.

$$E(\psi) = H(\psi) \quad (2.3)$$

The solutions of his equation describe the electronic energy states as quantised with discrete energy levels and it led to a series of mathematical functions indicated with the Greek letter psi ψ called the wavefunction. The wavefunction provides information about the probability amplitude of the position, momentum and other physical properties of the particle. The term E is the energy operator and it is the energy in eigenvalue of the operator H. The operator H (Hamiltonian operator) represents the total energy of the system, kinetic energy represented as the operator T and potential energy given as the operator V. And therefore, the relationship between the Hamiltonian operator and the energy operators T and V is shown in equation 2.4 shown.

$$H = T + V \quad (2.4)$$

The kinetic energy operator T can be written as shown in equation 2.5 where p is the momentum and m is the mass.

$$H = \frac{p^2}{2m} + V \quad (2.5)$$

Then H operator acting on the wavefunction can be given as equation 2.6 where ħ is the mathematical symbol which represents h over 2 π and the second order differential equation means differentiating the wavefunction ψ with respect to x twice holding time constant.

$$\hat{H} = -\frac{\hbar^2}{2m}\frac{\partial^2}{\partial x^2}\psi + V(x) \quad (2.6)$$

Thus, the Hamiltonian operator drives out one of the energy states which is a wavefunction. The Schrödinger equation can be solved by simplifying it, using the **Born-Oppenheimer** approximation. The approximation is based on the assumption that because nuclei are much heavier than the electrons, their motion can be neglected because they move very slowly compared to the electrons thus, separating nuclear motions from electronic motions. Then, the Schrödinger equation can be written as in the equation 2.7 shown below:

$$\mathbf{H\,\psi\,(r, R) = E\,(R)\,\psi\,(r, R)} \quad \mathbf{(2.7)}$$

Where ψ is the wavefunction for the electron with respect to the position of the nucleus, r is the distance separating the electron from the nucleus and R is the position of the nucleus and E (R) is the mathematical term representing the electronic energy depending on the nuclear coordinates. The square of the wavefunction ψ^2 describes the probability of the spatial distribution of an electron at coordinates (x,y,z) in three dimensional space. Therefore, this probability is determined by ψ^2 (x,y,z). Electrons in atomic orbitals can have different forms and they are conveniently pictured as boundary surfaces, regions of space in which there is a 90% probability of finding the electron within the enclosed volume. Atoms have quantum mechanical numbers such as:

- The principal quantum number n which has integral numbers of 1, 2, 3 etc. As the principal quantum number increases the atomic orbital is associated with higher energy.
- The orbital angular-moment quantum number *l*. A quantum number which defines the shape of the atomic orbital. These numbers are represented by letters s, p, d and f. For instance, the shape of an s orbital is spherical whereas the p orbitals are characterized by a two-lobed shaped boundary surface.
- The magnetic quantum number m_l a number which describes the orientation of the atomic orbital in space.
- The spin quantum number m_s a quantum number that can have two values + ½ and – ½ (in the case of hydrogen atom). The signs + and – indicate the two opposite

directions in which the electrons spin and conventionally represented as arrows ↑ and ↓ respectively.

The spin quantum number requires further explanation. This quantum number determines how electrons of many-electron atoms are ordered and arranged into the available atomic orbitals. The total quantum spin number of an electronic system is represented as S and it is simply the sum of the spin quantum numbers of the electrons of the system. Then, $S = \sum m_s$ and given S the spin multiplicity can be defined as 2S + 1. When the total spin number S is 0 (S = ½ – ½ = 0) the spin multiplicity is equal to 1 (2S + 1 = 1) and it is referred to as ground-state singlet, S_0. When chemical species are excited one of the electrons in the atomic orbitals (an atomic orbital can only have two electrons with different spin numbers because of **Pauli's exclusion principle**) of the ground state is promoted into a higher-energy orbital. If the excited electron has the same spin number (i.e., the excited electron and the ground-state electron are antiparallel) it is called a singlet excited state. If the spin number of the excited electron is parallel with the electron in the ground state, the excited state is called a triplet state, with spin multiplicity equal to 3 as shown in Figure 2.1. A singlet state contains one eigenstate whereas a triplet state contains three eigenstates.

Figure 2.1 Singlet and Triplet excited states

Spin multiplicity 1 (singlet state) and spin multiplicity 3 (triplet state)

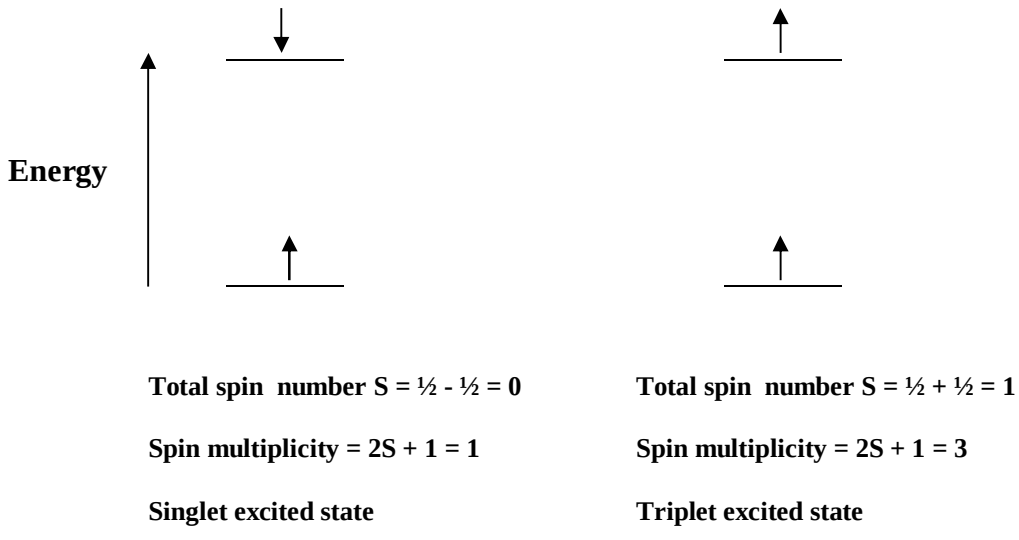

According to **Heisenberg** it is impossible to measure accurately the definite position and momentum of a particle like an electron. When the wavefunction collapses and thus, the position of an electron can be measured, the state of an electron becomes an eigenstate of position and its position has an eigenvalue. A molecular orbital (abbreviated as MO) and its associated wavefunction is formed through the interaction of the wavefunctions of two identical or similar atomic orbitals (AO). Bonding molecular orbitals are formed when the wavefunctions of the atomic orbitals enhance each other between the regions of the nuclei. The atoms are firmly held together by attraction between the nuclei and the electrons in the bonding molecular orbital. On the other hand an antibonding molecular orbital is generated when the atomic orbital wavefunctions cancel each other in the region of the nuclei. Then, antibonding molecular orbitals are formed through repelling electrons, therefore, the atoms tend to be separated from each other rather than be bound together. Energies of bonding and antibonding molecular orbitals are illustrated below in Figure 2.2.

Figure 2.2 Bonding and antibonding molecular orbitals

Bonding molecular orbitals formed from atomic orbitals A and B. The antibonding molecular orbital is recognizable by its star attached to it and has a higher energy compared to the bonding molecular orbital

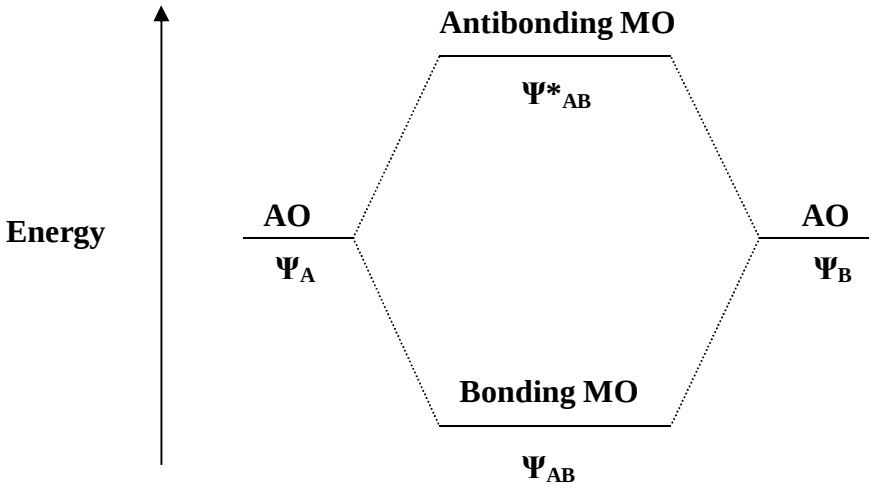

For example, two s-type atomic orbitals form a sigma bonding molecular orbital, σ MO and a sigma antibonding molecular orbital, σ* MO, whereas two p-type atomic orbitals form a pi bonding molecular orbital, π MO and a pi antibonding molecular orbital, π* MO. It should be noted that bonding and antibonding molecular orbitals are not the only molecular orbitals.

In fact, also nonbonding molecular orbitals exist. Nonbonding molecular orbitals, known as n are orbitals that contain lone pairs of electrons and they have a higher energy than bonding molecular orbitals. These n orbitals are localised on just one atom, for example, heteroatoms such as oxygen and nitrogen atoms.

2.2 Absorption of light by molecules and electronically-excited states

The total energy of a molecule can be described as electronic energy, electronic energy states, and energy due to nuclear motion, vibrational, rotational and translational energy states. Thus, the total energy of a molecule can be summarised as shown in equation 2.8.

$$\mathbf{E_t = E_e + E_v + E_r + E_t} \quad \mathbf{(2.8)}$$

The subscripts refer to the total energy, electronic energy, vibrational energy, rotational energy and translational energy respectively. Large differences in energy between the electronic, vibrational and rotational states often exist and therefore they can usually be treated separately. This fact underlies the Born-Oppenheimer approximation. According to this approximation, the energy gap between electronic states is much greater than the energy between vibrational states and in turn much greater than the energy between rotational states. When molecules absorb ultraviolet and visible light changes in both electronic and vibrational states occur between the ground state and the excited state of the molecules involved. These transitions are called vibronic transitions. As described in the **Boltzmann distribution law** N_0 represents the number of molecules in the ground state whereas N_1 represents the number of molecules in any higher states (excited states), as shown in equation 2.9 ΔE is the difference in energy between the ground and the excited states, R is the gas constant and T is the absolute temperature.

$$\frac{\mathbf{N_1}}{\mathbf{N_0}} = \mathbf{e}^{\frac{-\Delta \mathbf{E}}{\mathbf{RT}}} \quad \mathbf{(2.9)}$$

Calculations based on the Boltzmann distribution law indicate that at room temperature the majority of molecules are in the v = 0 vibrational state of the electronic ground state S_0 and therefore, absorption mainly occurs from the S_0 state. When small displacements between atoms of diatomic molecules from their equilibrium separation occur, the vibrations of these molecules can be treated as harmonic, **Hooke's law oscillators**. For an ideal harmonic the potential energy is given in equation 2.10 where r_e is the internuclear separation at equilibrium and k is the vibrational force constant.

$$\mathbf{V = \frac{1}{2}\, k\, (r - r_e)^2} \quad \mathbf{(2.10)}$$

An illustration of a harmonic oscillator is provided in Figure 2.3. The figure shows the plot of the potential energy curve equal to ½ kx^2 for ideal oscillators. Superimposed on this potential energy curve are the values of the vibrational energy for the oscillator.

Figure 2.3 Harmonic oscillator of a diatomic molecule

As shown in this illustration the energy levels of the harmonic oscillator potential are equally spaced. As the molecule moves (like a spring) about its center, the force opposing the motion is proportional to the distance away from some minimum-energy equilibrium distance

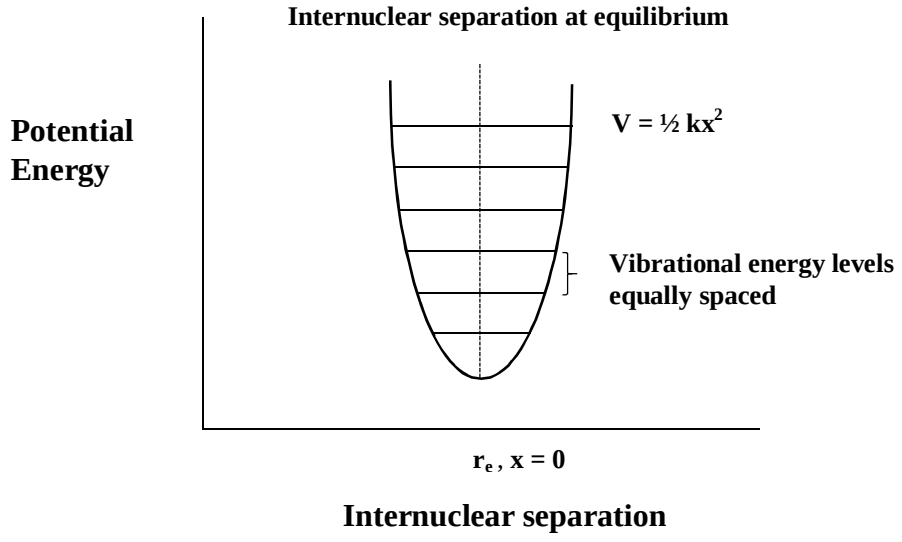

However, for large displacements equation 2.10 does not hold anymore because the vibrations are anharmonic and lead to molecule dissociation. The potential energy of a diatomic molecule for large interatomic separation is due to Morse and mathematically shown in equation 2.11.

$$V = D' [1 - e^{-\beta (r - r_e)}]^2 \quad 2.11$$

The term D' represents the dissociation energy of the molecule, the necessary energy to separate the atoms by an infinite distance. This term is measured from the minimum of the potential energy curve and equals the dissociation energy experimentally obtained D plus the zero-point of the molecule as given in equation 2.12.

$$D' = D + \frac{1}{2} h\nu_0 \quad (2.12)$$

In equation 2.11 the constant β determines how steep the potential curve can be and thus it determines its shape. This constant is related to the vibrational frequency at the zero point ν_0 and the reduced mass of the molecule m_{red} see equation 2.13.

$$\beta = v_0 \left(\frac{2\pi c m_{red}}{h D'} \right)^{\frac{1}{2}} \quad (2.13)$$

The Figure 2.4 shows a Morse curve for a diatomic molecule. The Morse curve is a representation of the variation of the potential energy of a bond with respect to interatomic distance.

Figure 2.4 Morse curve of a diatomic molecule

The horizontal lines represent the quantised vibrational energy levels of a diatomic molecule. Unlike harmonic curves which are symmetrical Morse curves are asymmetrical. Also the space separating the Morse potential energy levels decreases as the energy approaches the dissociation energy whereas this space is constant in harmonic curves

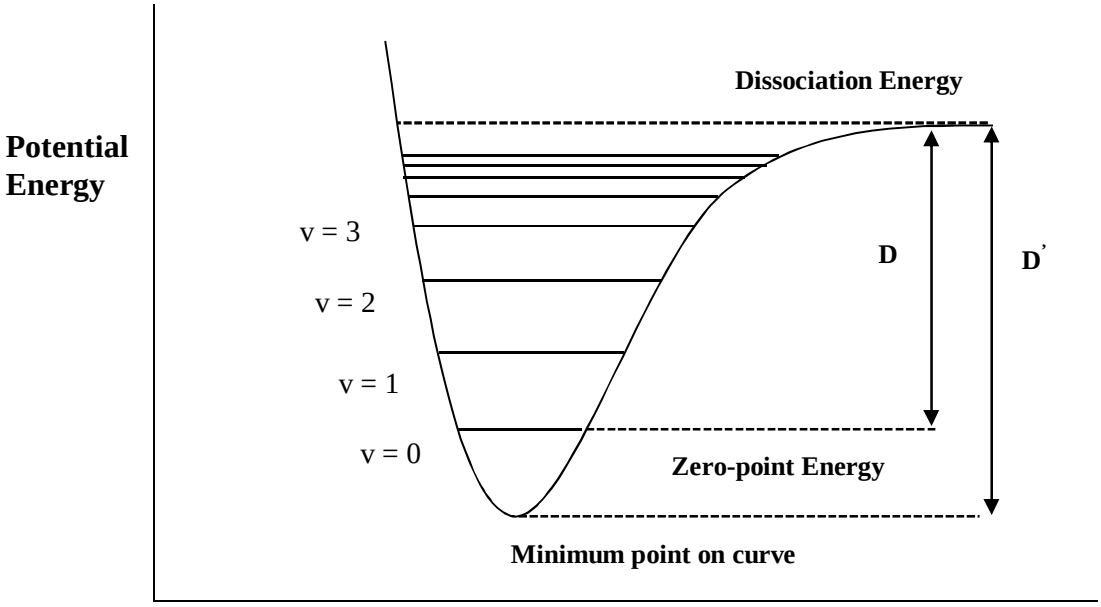

In order to understand the origin of vibrational structure in electronic spectra of molecules the **Franck Condon Principle** is used (Franck, 1926; Condon, 1926). His principle states that electronic transitions taking place from one electronic state to another occur so quickly that the nuclei can be considered stationary because of their much greater mass compared to the electrons. Electronic transitions between an electronic ground state and an electronic excited state are represented as vertical arrows within a stationary nuclear framework called vertical transitions or Franck-Condon transitions as shown in Figure 2.5. Franck-Condon transitions between two states of different energies are intense when the two involved states have similar internuclear separations. In other words, the degree of overlap of the wavefunctions between the two states determines the intensity of the vertical transition. This overlap is called Franck-Condon overlap.

Figure 2.5 A Franck Condon transition

The most intense vibronic transition is generated from the ground vibrational state to the vibrational state lying above it. Also the most probable location of the nuclei is at their equilibrium separation

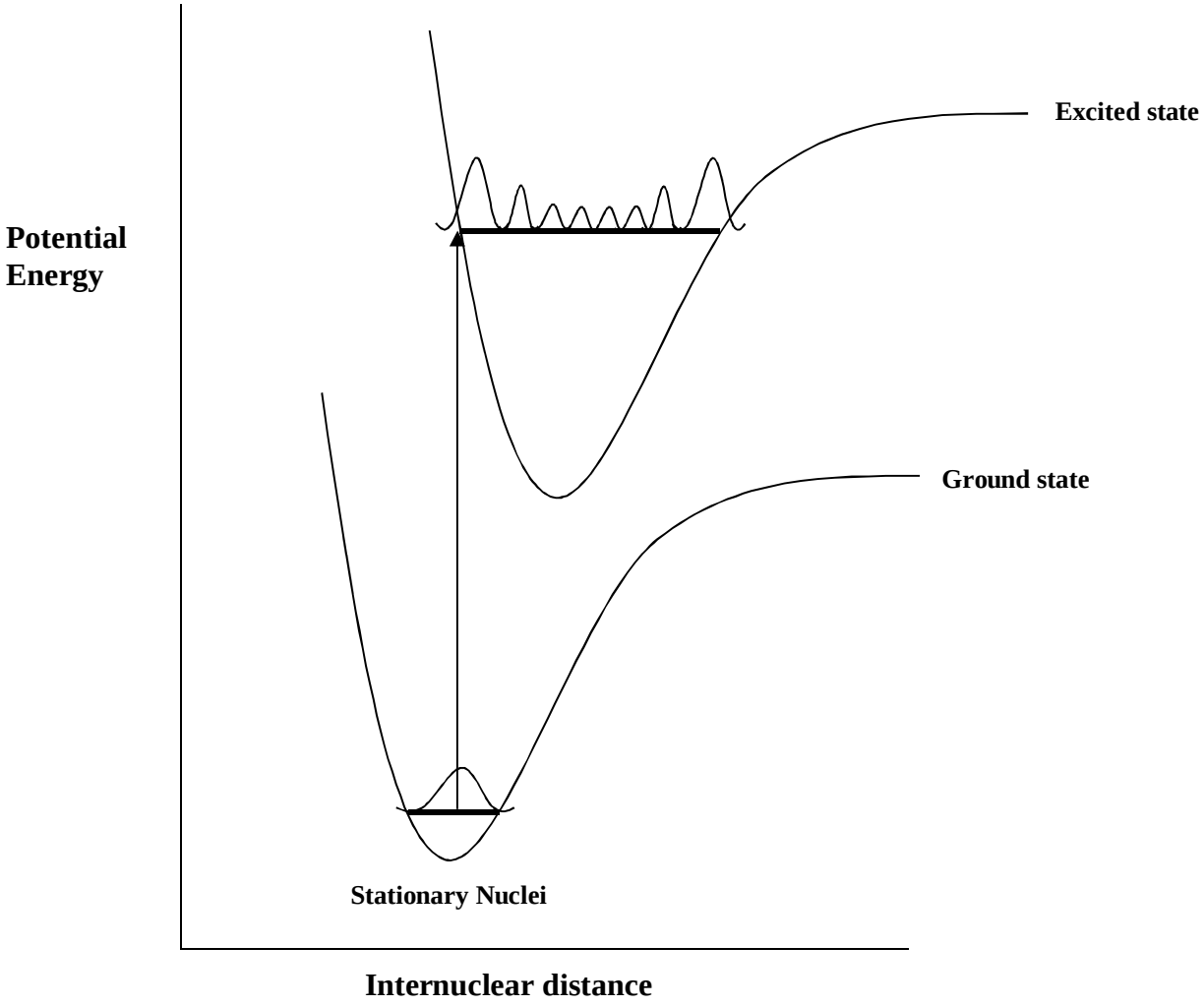

Each vibrational energy level has a specific wavefunction ψ. In the case of the vibrational level v = 0 the square of the wavefunction, ψ^2 shows that the diatomic molecule spends most of its time within the region of the equilibrium region, whereas for an excited vibrational energy level the ψ^2 function is closer to the margins of the potential curve. This means that the molecule spends most of its time in either the fully-compressed or fully-extended configuration. The overlap integral between the two vibrational wavefunctions can be calculated as shown in the mathematical formula 2.14.

$$\int \psi^{*}_{v'} \; \psi_{v''} \; d\tau_n \quad (2.14)$$

Where $d\tau_n$ is the volume element for nuclear coordinates whereas v' and v'' are the vibrational quantum numbers in the ground and excited electronic states. The intensity of an absorption is proportional to the square modulus of the overlap integral which is known as the Franck Condon Factor for the transition, see formula 2.15.

$$\left| \int \psi^{*}_{v'} \; \psi_{v''} \; d\tau_n \right|^2 \quad 2.15$$

Since the efficiency of a transition depends on the extent of overlap between the squares of the vibrational wave functions, ψ^2. In a horizontal transition (radiationless transition), the extent of overlap of the ψ^2 functions of the initial and final states is the main factor which governs the rate of internal conversion and intersystem crossing, see Section 2.3. Three principal cases of Franck-Condon factor: A, B and C are considered herein.

Figure 2.6 Case A (The Franck-Condon factor)

States that have similar geometries but large energy separation between them (the wave functions of the initial state are displayed in white whereas the wave functions of the final states are displayed in black)

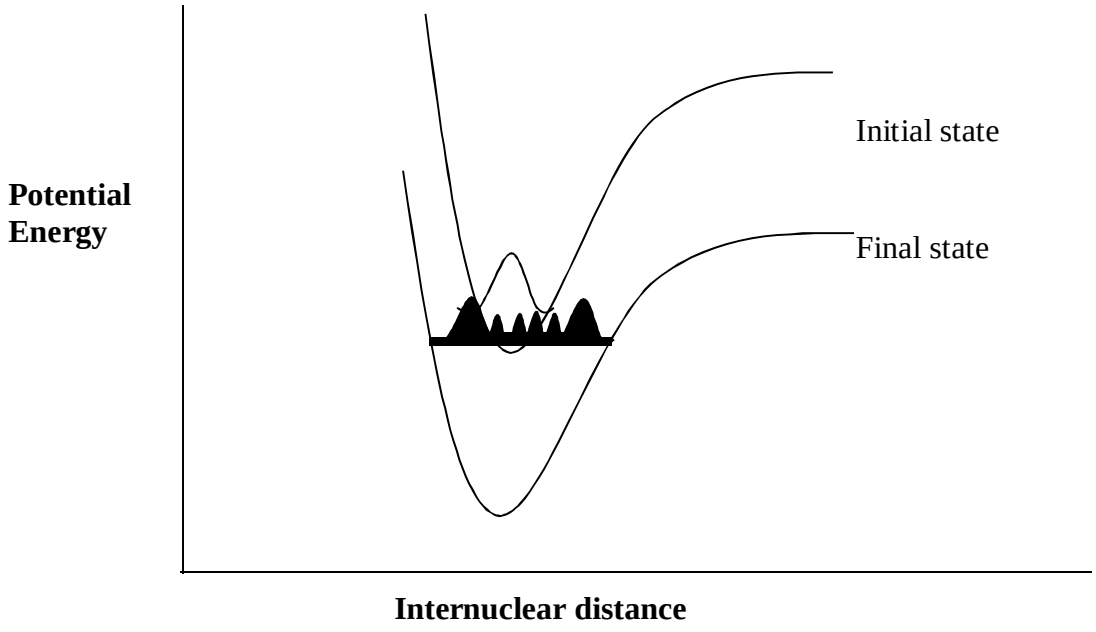

In the case A as shown in Figure 2.6 the electronic states have similar/identical geometry given the coincident minima of the Morse curve, but the separation in energy between them is reasonably large. The case A shows no change in molecular geometries between the states involved and little overlap between the isoenergetic ψ^2 functions. In such a case the rate of radiationless energy transfer between the states would be very slow and therefore, fluorescence could effectively compete with radiationless processes. The case B illustrated in Figure 2.7 is a case in which the geometries of the states are very similar along with their energies. In this case the extent of overlap between the ψ^2 functions is sufficiently large to allow rapid radiationless transfer.

Figure 2.7 Case B (The Franck-Condon factor)

Similar geometries of the electronic states separated by a small energy gap

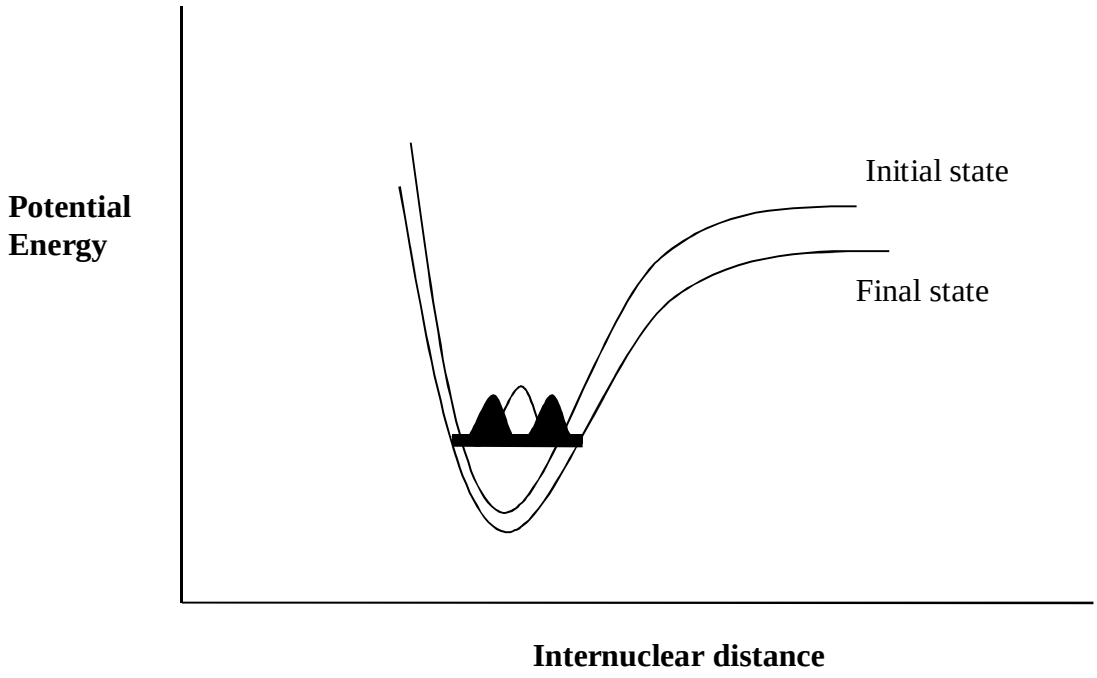

In the third case, the case C, see Figure 2.8 the geometries of the states are different shown by the minima corresponding to different internuclear distances. The separation in energy of the two states is quite large. Albeit the energy gap is reasonably large there is a significant overlap between the isoenergetic ψ^2 functions leading to a fast rate of radiationless transfer of energy.

Figure 2.8 Case C (The Franck-Condon factor)

Very different geometries of the electronic states separated by a large energy gap

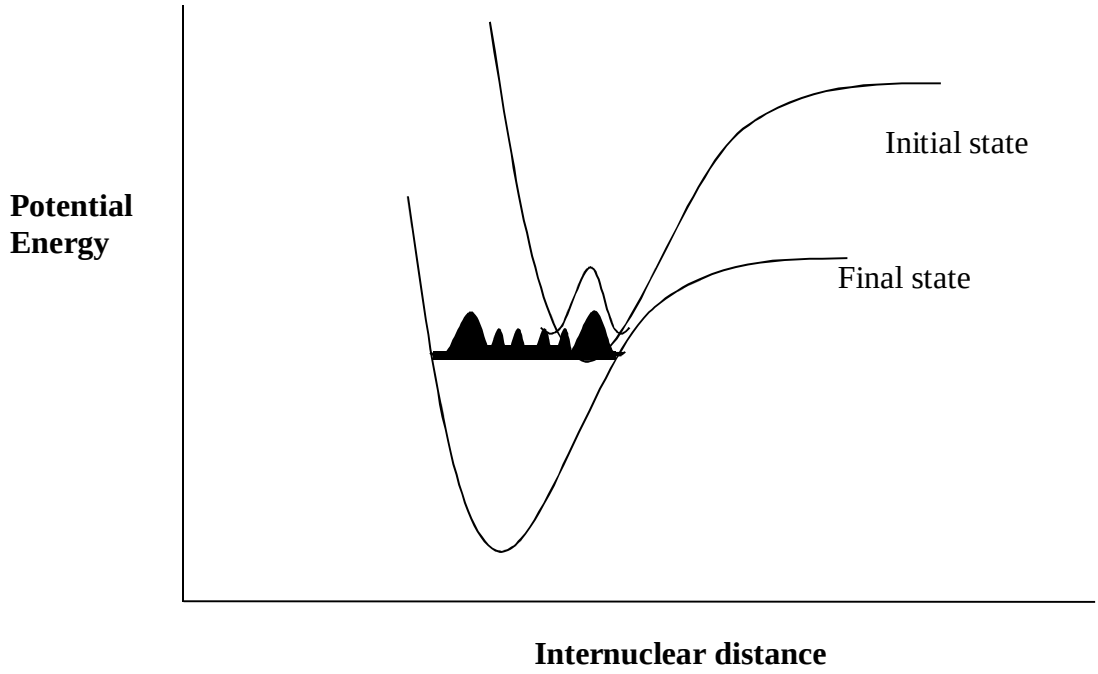

Thus, given the three cases above the efficiency rate of internal conversion and intersystem crossing is strongly dependent on both electronic and vibrational factors (electronic factors describe the probability of transitions between electronic states whereas vibrational factors describe the operation of the vibrational wave function overlap with the radiationless transitions).The absorption spectrum of a molecule is composed of different absorption bands. These bands are formed because of the characteristic electronic and vibrational energy level in which the molecule resides when excited by energy of different wavelength. Figure 2.9 shows different vibronic transitions. The intensity or probability of the transitions can differ depending on the nature of molecule (the extent of absorption of light differs from molecule to molecule, with the probability of absorption being indicated by their molar absorption coefficient ε from the Beer-Lambert law $A = \varepsilon cl$ where A is the absorbance, c the concentration of the solution and l the path length). For example, as shown in figure 2.9 the most probable and therefore, intense transition takes place between the 0 vibrational level of the ground state and the 0 vibrational level of the first excited state because of the largest Franck-Condon factor.

Figure 2.9 Absorption spectrum of a molecule

Vibronic transitions of a molecule. In this particular example, the S_0 (v = 0) – S_1 (v = 0) transition is the most intense one

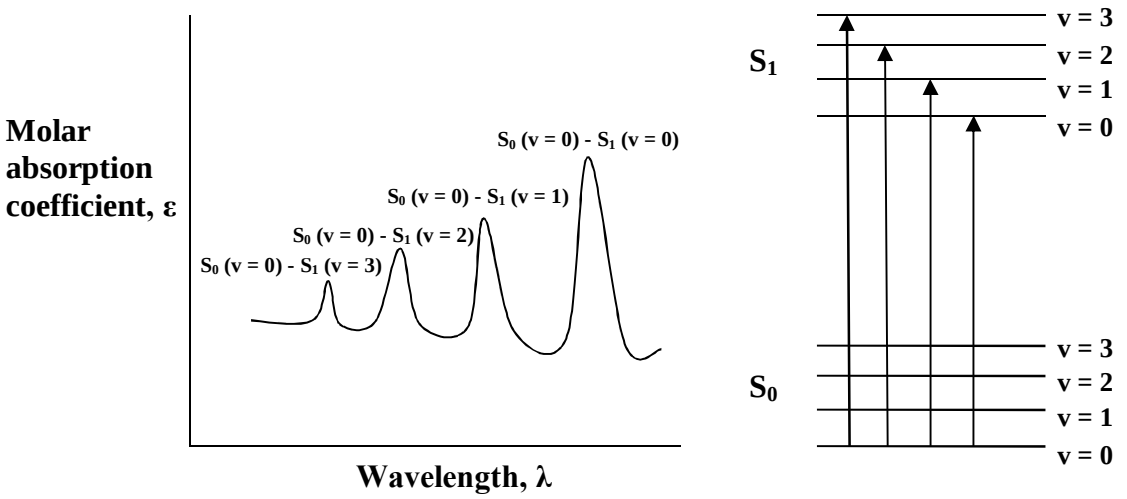

Electronic transitions can be of six types: σ-σ*, σ-π*, π-π*, π-σ*, n-σ* and n-π*. The most energetic electronic transitions are the σ-σ* transitions and they usually occur in the far-ultraviolet (below 200 nm) and they may not be accessible with standard UV-Visible spectrometer. In molecular organic photochemistry studies the main focus is on π-π* and n-π* transitions because these transitions differ in energy depending on the nature of the organic molecules and therefore, they are very indicative transitions. The HOMO (highest occupied molecular orbital) is the ground-state molecular orbital of highest energy whereas the LUMO (lowest unoccupied molecular orbital) is the excited-state molecular orbital of lowest energy. A general panel illustrating molecular orbital energies of an organic molecule is shown below in Figure 2.10. Electronic transitions can also be of Rydberg character. The Rydberg orbital can be atomic or molecular. For an atom, the Rydberg orbital has a principal quantum number greater than any occupied orbital of the ground state whereas for a molecule, it is a molecular orbital which correlates with the Rydberg atomic orbital. Typically the size of the Rydberg orbital is very large compared to the size of the atomic or molecular entity. A Rydberg transition is the promotion of an electron from a bonding orbital to a Rydberg orbital. Transitions between energy states are governed by certain constraints which are conventionally known as selection rules. Selection rules for organic molecules are divided into spin selection rules and orbital symmetry selection rules.

Figure 2.10 Molecular orbital energies of a general organic molecule

Generalised ordering of molecular orbital energies along with the possible electronic transitions of a general organic molecule

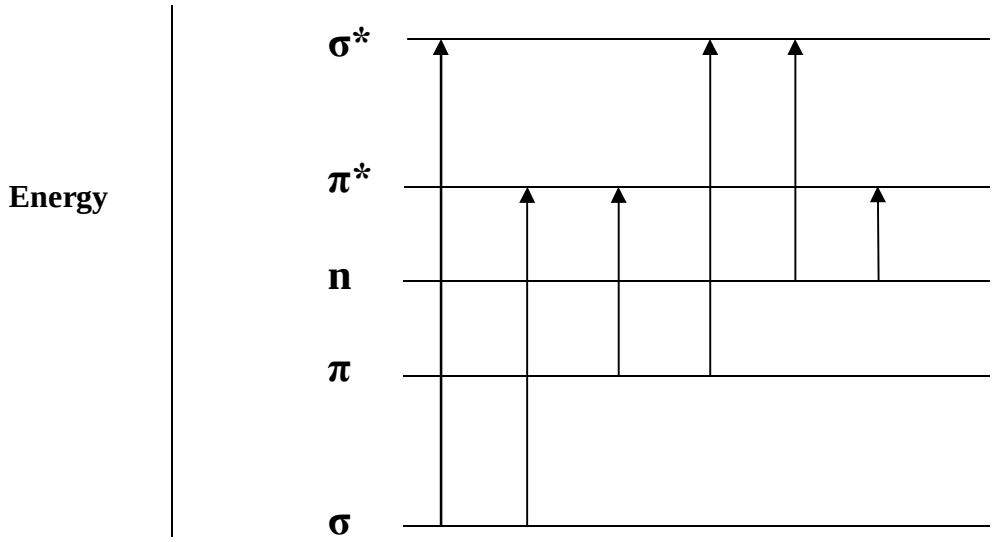

-Spin selection rules- An electronic transition should occur with no change in the total spin number of the system, thus $\Delta S = 0$ and as a consequence transitions between singlet and triplet states are forbidden or weakly permitted. The spin selection rules are derived from quantum mechanical calculations that do not consider the interactions of electrons with other electrons or nuclei in a molecule. These interactions are called spin-orbit interactions or spin-orbit coupling. As a result of these interactions a singlet state can have some triplet character and a triplet state can have some singlet character. Because of this mixing of states the spin selection rules cannot be strictly applied. Spin-orbit coupling can be understood in a crude fashion by considering the motion of an electron in a Bohr-like orbit. The electron rotating around the nucleus generates a magnetic moment. Another magnetic moment is generated from the electron spinning around itself about an axis of its own since electrons have intrinsic spin numbers. Thus, spin-orbit coupling is the result from the interaction between the two generated magnets.

-Orbital symmetry selection rules- According to quantum theory an electronic transition is very probable when the wavefunctions of the initial state ψ (ground state) and final state ψ* (excited state) resemble each other. Thus, by considering the difference in energy between the excited and the ground states it is possible to assess the intensity of the vertical transition. The bigger the molar absorption coefficient ε (obtained from the Beer-Lambert law) the greatest the degree of resemblance or similarity between the wavefunctions. A perfect example describing this is the difference in intensity between an n-π* vertical transition and π-π* vertical transition. The first transition is usually much weaker than the second one because of the orbital symmetry selection rules. The extent of overlap between the n and π orbitals is smaller than the one between two orbitals of the same character. Thus, according to the symmetry selection rules π-π* transitions are allowed whereas n-π* transitions are considered forbidden or weakly allowed. It is important to note that symmetry-forbidden transitions can be observed because of vibronic coupling. Vibronic coupling as the term implies, indicates the interaction between electronic and nuclear motions of the molecule, see Figure 2.11.

Figure 2.11 Vibronic coupling

Case A shows a pure electronic transition therefore, no vibronic coupling. In Case B the electronic transition couples with the vibrational transition therefore, vibronic coupling

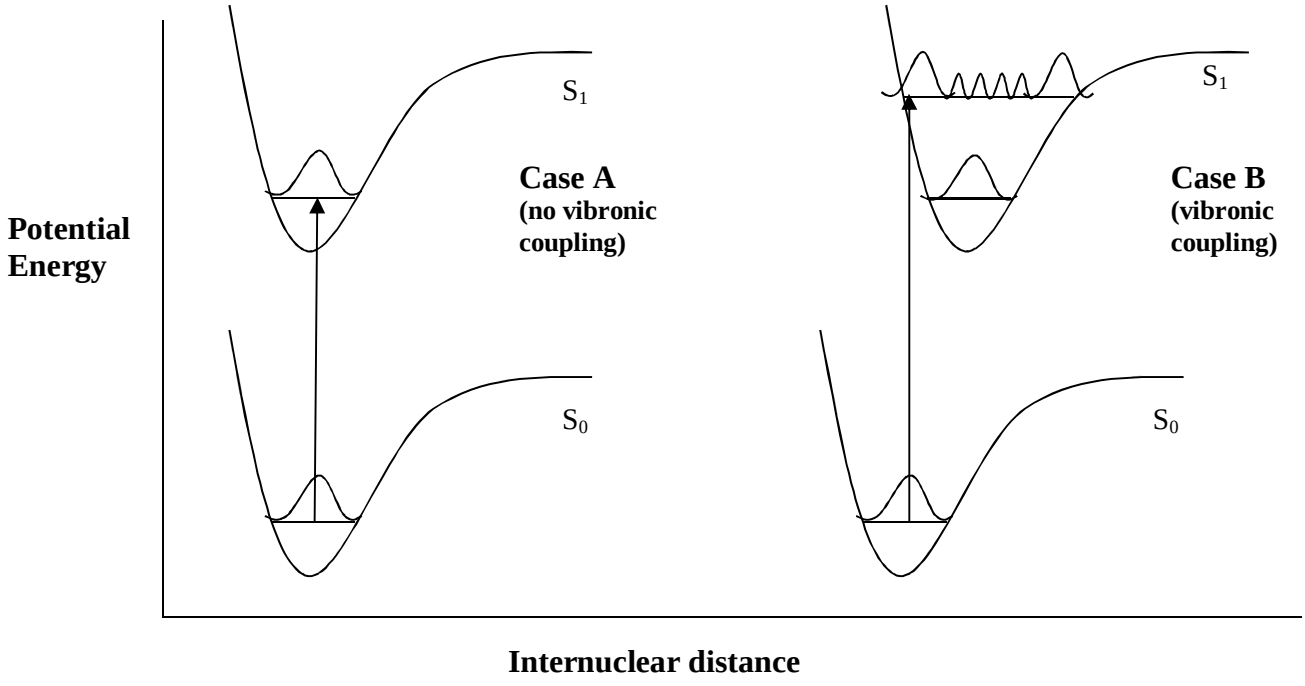

Because of vibronic coupling, vibronic bands can be observed regardless of the poor resemblance of the wavefunctions of the ground and the excited states. Vibronic coupling is a result of the breakdown of the adiabatic (invariant Born-Oppenheimer approximation) Born-Oppenheimer approximation. Vibronic couplings are essential to the understanding of non-adiabatic processes in particular near points of conical intersections. In quantum chemistry a conical intersection is defined as the intersection of two potential energy surfaces (non-adiabatic couplings between two states). Very large vibronic couplings may induce a non-radiative transition which leads the molecule back to the ground state in an ultrafast manner, thus efficiently competing with radiative processes (fluorescence and phosphorescence).

2.3 The physical deactivation of the excited states

Electronically-excited molecules possess an excess of energy due to absorption of light (photons). The loss of this energy takes place *via* various deactivation processes displayed in the diagram of Figure 2.12. The physical deactivation processes can be divided into two main branches: intermolecular processes and intramolecular processes. Intermolecular processes are classified into vibrational relaxation, energy transfer and electron transfer whereas intramolecular processes are further divided into radiative and non-radiative processes. Intermolecular processes can be described as follows:

- **Vibrational relaxation** is the loss of vibrational energy due to molecules undergoing rapid collisions with each other and with solvent molecules.
- **Energy transfer** a process in which the electronically-excited state of a molecule called the donor loses part of its energy by donating it to another molecule called the acceptor molecule which becomes an excited molecule. The acceptor molecule is also known as a quencher whereas the donor molecule is regarded as a sensitiser.
- **Electron transfer** is a process which involves a photoexcited donor molecule interacting with a ground-state acceptor molecule. As a result of this interaction an ion pair is formed which may undergo electron transfer, resulting in quenching of the excited donor molecule.

Figure 2.12 Deactivation processes of organic molecules

Diagram of physical deactivation processes of excited states of organic molecules

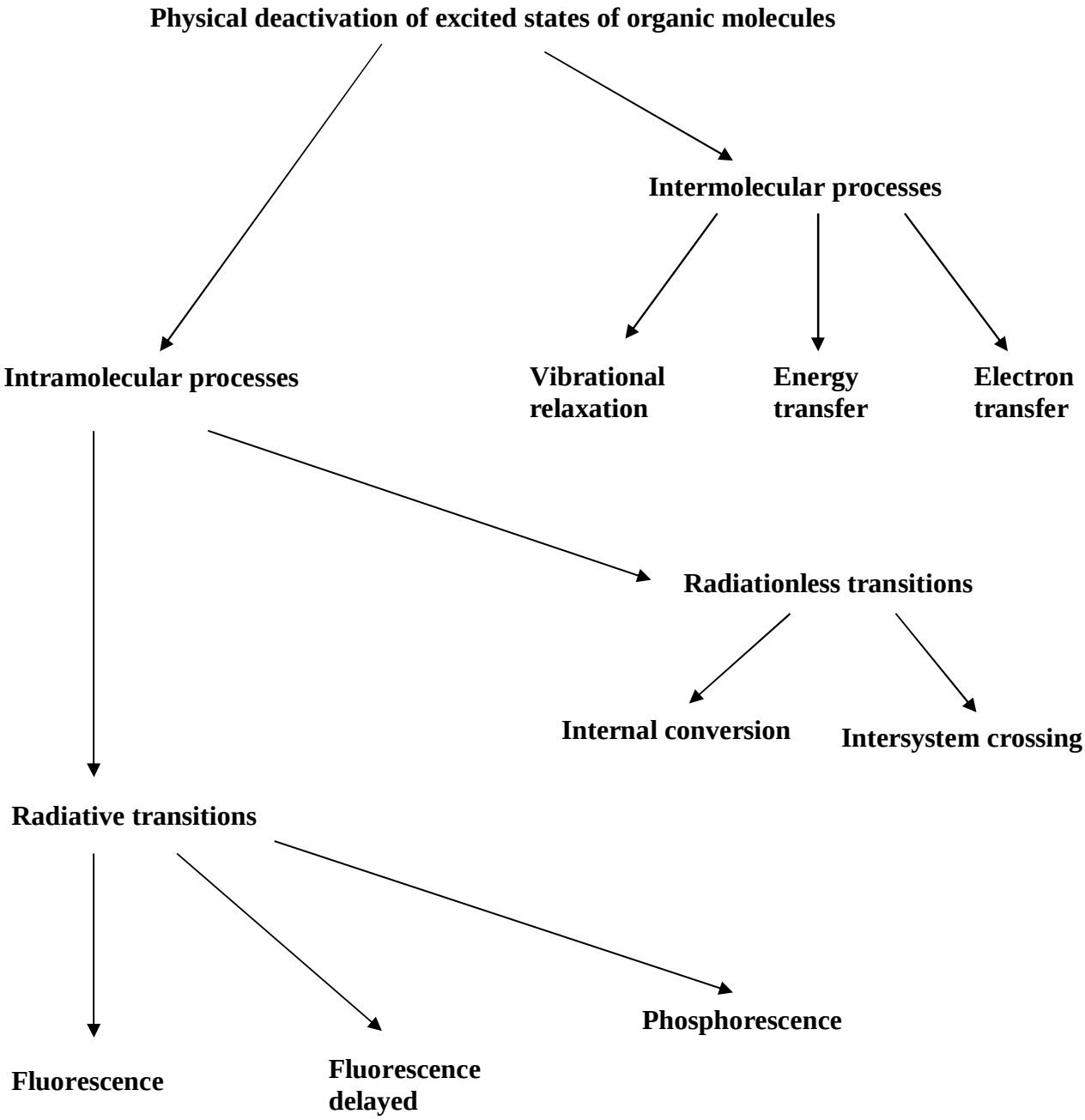

All the intramolecular and vibrational relaxation processes can be illustrated by drawing a Jablonsky diagram as the one displayed in Figure 2.13.

Figure 2.13 Jablonsky diagram

Excited-state photophysical processes of an organic molecule illustrated in a Jablonsky diagram. Vibrational relaxation processes are shown as wavy arrows

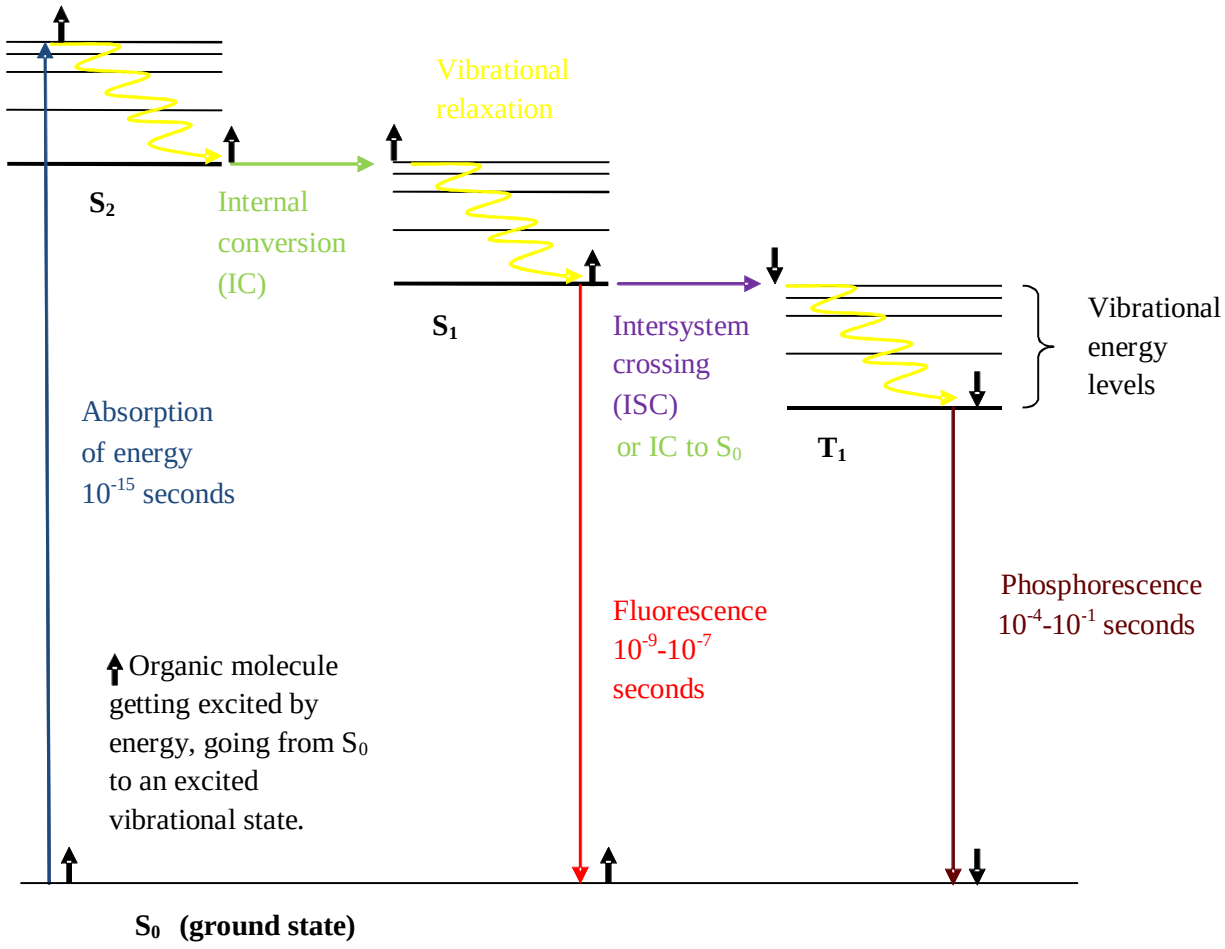

Radiationless processes are processes which do not imply changes in energy, horizontal transitions as shown in the Jablonsky diagram. Radiationless processes can be branched out into internal conversion (IC) and intersystem crossing (ISC) thus,

- **Internal conversion (IC)**, a transition between two isoenergetic states, the transition between the states is allowed (same spin multiplicity). Internal conversion between S_2 and S_1 occurs much faster than internal conversion between S_1 and S_0.
- **Intersystem crossing (ISC)** as in the case of IC it is another isoenergetic process but unlike IC it is a forbidden transition because it takes place between two states of different spin multiplicity.

Radiative processes are processes which imply changes in energy, vertical transitions and therefore, they can be explained in terms of the Franck-Condon principle. The emission of light through either fluorescence and/or phosphorescence is called luminescence.

- **Fluorescence**, a radiative transition between two states of the same spin multiplicity (permitted transition), emission that usually derives from the lowest vibrational level of the lowest excited singlet state S_1 (v = 0), as stated in the Kasha's rule. Fluorescence emissions are of the order of 10^{-9}- 10^{-6} s.
- **Phosphorescence,** is a radiative transition between two states of different spin multiplicity (forbidden transition) deriving from the lowest vibrational level of the lowest excited triplet state T_1 (v = 0). Phosphorescence is a much slower process than fluorescence which takes place within a longer timeframe, precisely 10^{-4} - 10^{-1} s.
- **Delayed fluorescence,** certain molecules can exhibit a weak fluorescence with spectral characteristics (wavelengths and relative intensities) similar to normal fluorescence, because of transitions back from triplet states to S_1. But in this case, the molecules have a lifetime resembling the one of phosphorescence and not the lifetime of fluorescence which is generally much greater than the one of phosphorescence.

Then, the total rate for the deactivation of the excited singlet-states in which excited molecules reside is given by the equation 2.16 in which k_{total} is the total rate for the deactivation of S_1, k_F is the rate constant for fluorescence, k_{ISC} is the rate constant for intersystem crossing and finally k_{IC} is the rate for internal conversion to S_0.

$$k_{total} = k_F + k_{IC} + k_{ISC} \quad (2.16)$$

2.3.1 Mirror-image symmetry

Mirror-image symmetry exists between absorption and fluorescence spectra as shown in Figure 2.14.

Figure 2.14 Mirror-image symmetry between absorption and fluorescence spectra

Energy-level diagram displaying the electronic and vibrational energy levels of the first excited state S_1 and the ground state S_0. The diagram is oversimplified because absorption bands deriving from S_0 vibrational energy levels higher than 0 are not considered

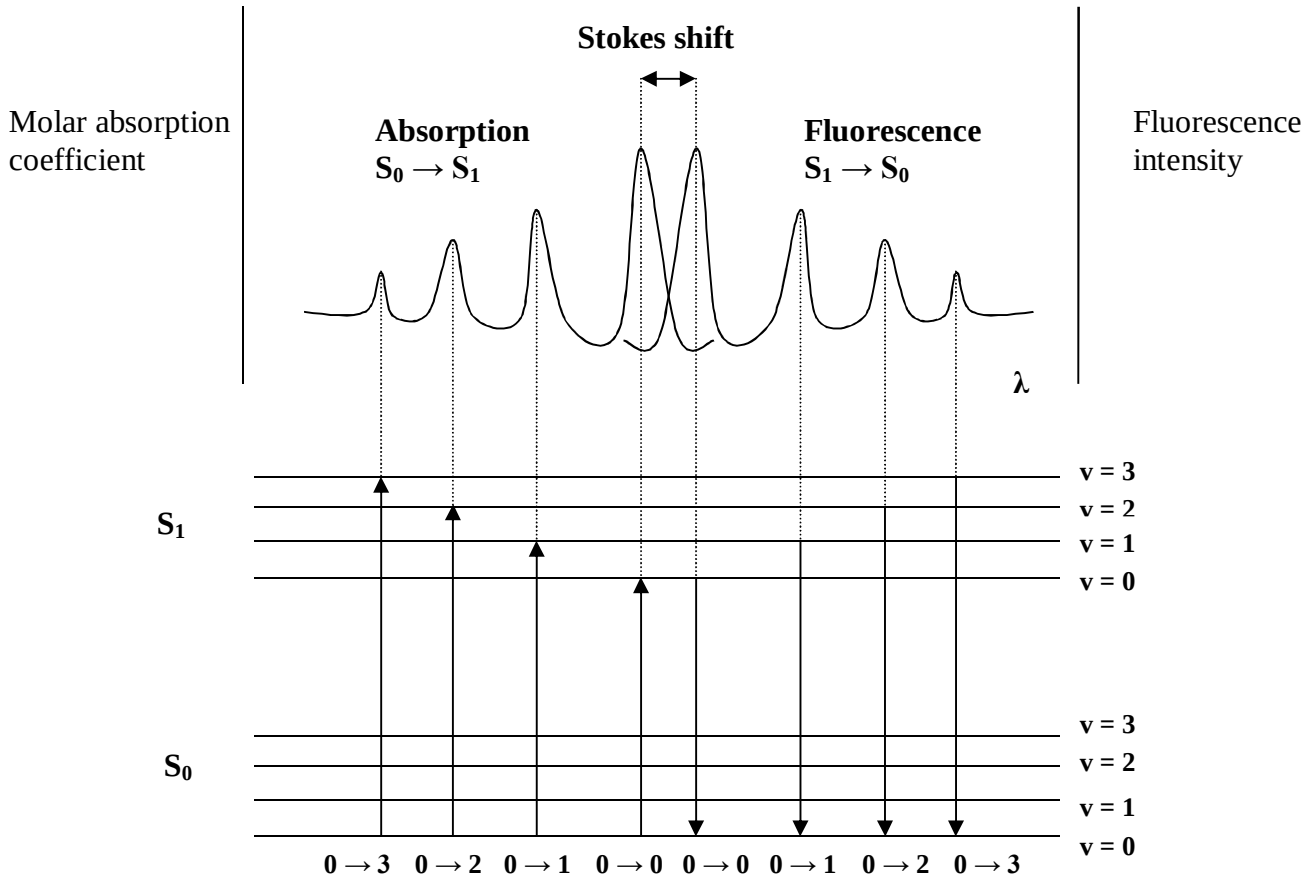

The Figure 2.14 shows a simplified mirror-image symmetry between the absorption and fluorescence spectra because the absorption bands deriving from S_0 vibrational energy levels higher than 0 were not considered but only from the vibrational level 0 (v = 0). The emission of a photon from the lowest vibrational level of the S_1 state to any vibrational level of the ground state S_0 is the fluorescence emission, **Kasha's rule** (Suppan, 1994; Klan and Wirz, 2009). The fluorescence spectrum lies at wavelengths which are longer than the absorption wavelengths because the excited molecules lose energy due to vibrational relaxation. It should also be noted that in a pure substance which does exist in a unique form in solution, the emission spectrum is invariant, being independent of the excitation wavelength. If the emission spectrum should change as the excitation wavelength varies, then it would mean that more than one emitting species may exist in solution. The independence of the excitation wavelength used to excite the molecule to collect the fluorescence emission is a consequence of the Kasha's rule. According to his rule the probability of finding an excited molecule in the lowest vibrational energy level of the first excited state S_1 is extremely high, irrespective of the excitation wavelength used to excite the molecule. Therefore, the quantum yield abbreviated as Φ_F (explained later) is independent of the wavelength of the exciting light. This was initially investigated and discovered by Vavilov (**Vavilov's rule**) (Suppan, 1994; Klan and Wirz, 2009). The emission spectrum can, to a good approximation, be treated as the mirror image of the absorption spectrum. This is true only if the mirror image of the S_0 to S_1 absorption spectrum is considered, not the total absorption spectrum, but exceptions to the Kasha's rule exist. Molecules which have a relatively large gap between S_2 and S_1, a gap which is responsible for slow IC between the states may therefore, exhibit fluorescence from the S_2 state and thus, no mirror-image symmetry due to the absorption from S_0 to S_1 is visible. Molecules fluorescing from the S_2 state are azulene and quinine, see Figure 2.15. Quinine is known to exhibit fluorescence from both S_2 and S_1 states and widely used as reference compound (Lakowicz, 1999).

Figure 2.15 The quinine molecule

The chemical structure of quinine characterized by two functional groups: quinoline, an aromatic functional group with a nitrogen atom substituting for a carbon atom, and the functional group quinicludine, which is a bicyclic amine. The functional group quinoline is believed to be responsible for fluorescence

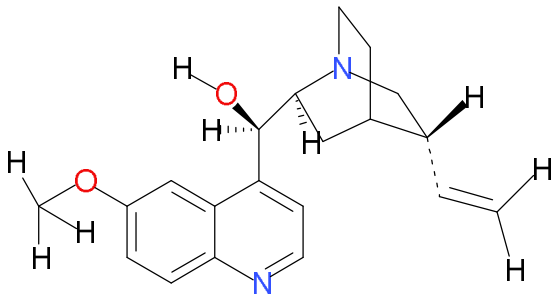

A very important feature shown in the energy-level diagram is the **Stokes shift** (Lakowicz, 1999). In Figure 2.14 the 0-0 bands do not perfectly overlap because of energy loss to the solvent environments. The influence of different solvents on the separation between the maximum absorption band and the maximum emission band is explained in Chapter 3.

2.3.2 The fluorescence quantum yield

The fluorescence quantum yield of a fluorophore (molecule emitting fluorescence) is a measure of how efficiently absorbed light is emitted, and it can be represented by the ratio of the number of photons emitted as fluorescence by molecules in the first excited state S_1 to the number of photons absorbed by molecules residing in the ground state S_0 as shown below in equation 2.17 and 2.18:

$$\Phi_F = \frac{\text{number of photons emitted } (S_1)}{\text{number of photons absorbed } (S_0)} \quad (2.17)$$

or,

$$\Phi_F = \frac{\textbf{rate of emission of photons by } (S_1)}{\textbf{rate of absorption of photons by } (S_0)} \quad (2.18)$$

When a molecule is in the lowest vibrational energy level of the first electronic excited state, S_1 (v = 0), fluorescence emission can compete with other physical processes such as IC and ISC before returning to the ground state S_0. Thus, as contained in the equation 2.19, the sum of all the quantum yields is equal to 1.

$$\Phi_F + \Phi_{IC} + \Phi_{ISC} = 1 \quad (2.19)$$

If $\Phi_F >> \Phi_{IC} + \Phi_{ISC}$ then the fluorescence quantum yield of the excited chemical species can be considered 1, because the quantum yields of internal conversion and intersystem crossing, Φ_{IC} and Φ_{ISC}, are negligible. This can be true in theory but in practice a fluorophore can have a quantum yield very close but not equal to 1, because of loss in energy due to vibrational motions. Also, it should be noted that because of the relatively large gap between the ground state and S_1, the quantum yield of internal conversion is considered to be extremely small (because of unlikely vibronic coupling) and as a consequence of that $\Phi_F + \Phi_{ISC} \approx 1$ as found in the **Ermolev's rule** (Lakowicz, 1999).

2.3.3 Fluorescence and phosphorescence lifetimes

Although in this project we only used steady-state approaches it is necessary to explain excited-state lifetimes, a very important concept which is numerously mentioned in this thesis. The fluorescence lifetime of a fluorophore is defined as the avarage time a molecule spends in an excited singlet-state before returning to the ground state. The loss of excited state energy is due to both radiative and non-radiative processes, and then, the lifetime, τ, is the inverse of the sum of the rate constant for radiative fluorescence emission and the rate constants of all the non-radiative processes. The fluorescence lifetime is very important because through it, the time necessary for the fluorophore to interact with or diffuse in its

chemical environment, and therefore, the information available from its fluorescence can be determined. As previously mentioned the competing intramolecular photophysical processes taking place from the singlet state S_1 are fluorescence, intersystem crossing and internal conversion thus, the rate of disappearance of the excited molecules A* in the first excited singlet-state is governed by the first-order chemical kinetics equation, hence:

$$\mathbf{A^* \xrightarrow{k_F} A + h\nu} \quad \mathbf{(2.20)}$$

$$\mathbf{A^* \xrightarrow{k_{IC}} A + h\nu} \quad \mathbf{(2.21)}$$

$$\mathbf{A^* \xrightarrow{k_{ISC}} A + h\nu} \quad \mathbf{(2.22)}$$

Then, the first order differential equation that describes the total deactivation of the first singlet state can be written as follows in equation 2.23:

$$\mathbf{\frac{-d[A^*]}{dt} = (k_F + k_{IC} + k_{ISC})\,[A^*] = k_{total}\,[A^*]} \quad \mathbf{(2.23)}$$

Then the integration boundaries can be applied as follows:

$$\mathbf{\int_{A_0}^{A} \frac{dA}{A} = -k_{total} \int_{t_0}^{t} dt} \quad \mathbf{(2.24)}$$

Since the integral of 1/A is the natural logarithm of A thus, equation 2.24 becomes a logarithmic equation:

$$\mathbf{\ln \frac{[A]}{[A]_0} = -k_{total}\, t} \quad \mathbf{(2.25)}$$

By manipulating equation 2.25 the exponential decay form of the transient excited singlet-state can be written as follows:

$$[A] = [A]_0 \, e^{-k_{total} \, t} \quad (2.26)$$

where $[A]_0$ is the initial concentration of the excited S_1 molecules at time equal to 0, [A] is the concentration of the excited molecules in the S_1 state after a certain time has elapsed. The lifetime is defined as the reciprocal of the rate constant for fluorescence and non-radiative processes, reported in equation 2.27.

$$\tau = \frac{1}{k_F + k_{IC} + k_{ISC}} = \frac{1}{k_{total}} \quad (2.27)$$

The excited singlet-state lifetime τ can then be substituted for the rate constant in equation 2.26

$$[A] = [A]_0 e^{\frac{-t}{\tau}} \quad (2.28)$$

Thus, when $t = {}^1\tau$ the power of the natural base e is equal to -1:

$$[A] = [A]_0 e^{-1} = [A]_0 \frac{1}{e} \quad (2.29)$$

The term F can be used in place of A to describe how fluorescence decays in an exponential fashion as a function of time.

$$F(t) = F_0\, e^{-1} = F_0 \frac{1}{e} \quad (2.30)$$

Therefore, the excited singlet-state lifetime is the time required for a fraction of excited molecules to decrease by a factor of 1/e or to circa 37% (1/2.718) of the original. The exponential decay as a function of time with F_0 as the initial fluorescence and F the final fluorescence after a certain period of time is illustrated in Figure 2.16.

Figure 2.16 Exponential decay of fluorescence emission as a function of time

An example of time-resolved fluorescence emission decay function which can be obtained by counting the number of photons within a given period of time after excitation

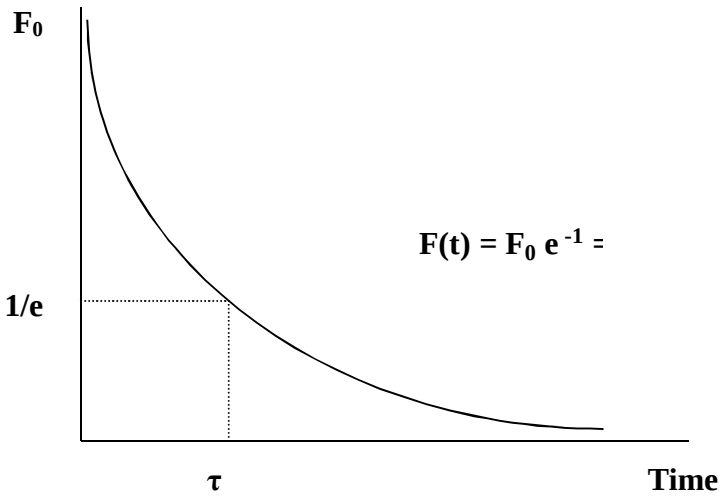

The quantum yield can be reported as a function of the rate (see equation 2.18):

$$\Phi_F = \frac{k_F}{k_F + k_{IC} + k_{ISC}} = \frac{k_F}{k_{total}} \quad (2.31)$$

The excited singlet-state radiative lifetime is the lifetime of the excited molecules in the S_1 state in the absence of riadiationless transitions (IC and ISC) which can be arbitrarily represented as ${}^1\tau_0$ is the reciprocal of the rate constant for fluorescence k_F as shown in equation 2.32.

$$ {}^1\tau_0 = \frac{1}{k_F} \quad \textbf{(2.32)} $$

Obviously, k_{total} cannot be smaller than k_F and therefore, mathematically the excited singlet-state lifetime τ or ${}^1\tau$ is smaller than the excited singlet-state radiative lifetime ${}^1\tau_0$. The difference between the two lifetimes becomes smaller as the radiationless processes IC and ISC from the S_1 state take place much slower than fluorescence. Then, by manipulating equations 2.27, 2.31 and 2.32 the fluorescence quantum yield is also equal to:

$$ \Phi_F = \frac{{}^1\tau}{{}^1\tau_0} \quad \textbf{(2.33)} $$

As in the case of S_1 the excited molecules in the T_1 state have specific lifetimes. In short, by analogy with the lifetime of the molecules in the S_1 state the equation 2.32 can be used by replacing k_F with k_P which is the rate of phosphorescence and then the lifetime of the first triplet state is:

$$ {}^3\tau_0 = \frac{1}{k_P} \quad \textbf{(2.34)} $$

And, hence the equation 2.34 can be formulated if non-radiative processes are taken into account especially, ISC as later explained:

$$^3\tau_0 = \frac{1}{k_P + k_{ISC}} \quad (2.35)$$

2.3.4 El-Sayed's selection rules for intersystem crossing

The extent of luminescence emission depends on the rate constants which regulate the competing processes occurring from S_1 and T_1 states. The Figure 2.17 below illustrates the competing photophysical and photochemical processes occurring from both S_1 and T_1. A large gap in energy between S_1 and S_0 which can efficiently preclude Internal Conversion and Intersystem Crossing followed by vibrational relaxation from S_1 and T_1 to the ground state S_0.

Figure 2.17 Competing luminescence processes occurring from S_1 and T_1

Competing photophysical and photochemical processes taking place from S_1 and T_1

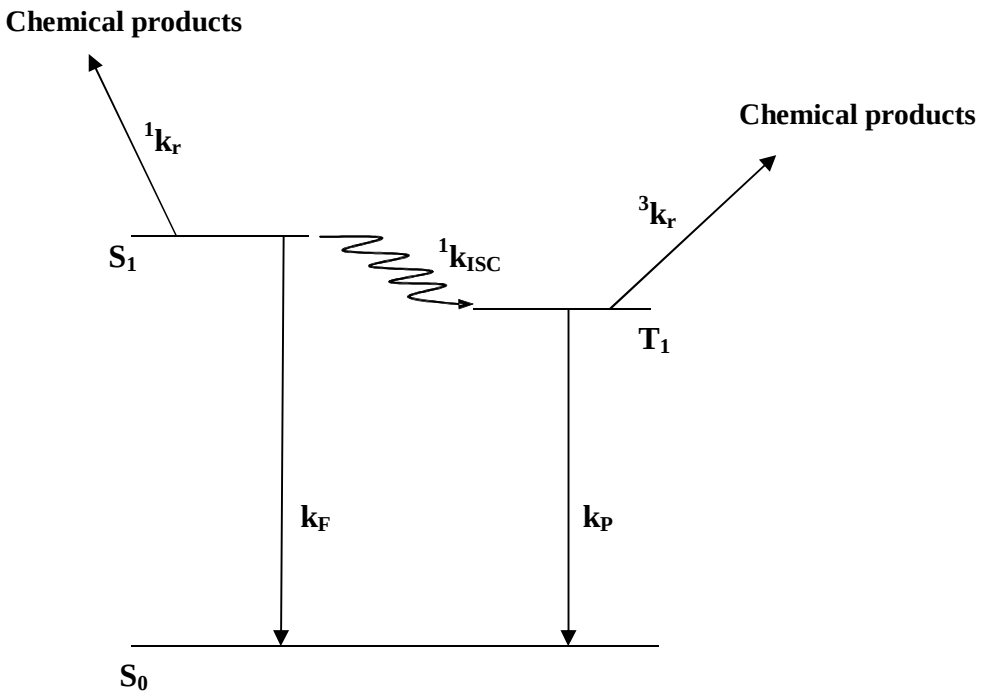

Given the large energy gap between S_1 and S_0 the excited molecule can efficiently relax to the ground state only by processes involving luminescence or chemical reaction. The fluorescence quantum yield of this photophysical system is given in the equation 2.36.

$$\Phi_F = \frac{k_F}{k_F + {}^1k_{ISC} + {}^1k_r} \quad (2.36)$$

And the quantum yield of phosphorescence is calculated as follows in equation 2.37:

$$\Phi_P = \left(\frac{k_P}{k_p + {}^3k_r}\right)\left(\frac{{}^1k_{ISC}}{{}^1k_{ISC} + k_F + {}^3k_r}\right) \quad (2.37)$$

Then, fluorescence is observed when $k_F > {}^1k_{ISC} + {}^1k_r$ whereas phosphorescence is observed when:

$$k_P > {}^3k_r \text{ and } {}^1k_{ISC} > k_F + {}^3k_r \quad (2.38)$$

Since the term k_{ISC} is present in both the fluorescence and phosphorescence quantum yield equations the magnitude of ${}^1k_{ISC}$ is important and has the following implications:

- If ${}^1k_{ISC} >> {}^1k_r$ any photochemical reactions from S_1 may occur with a very low quantum yield
- When ${}^1k_{ISC} >> {}^1k_F$ fluorescence is hardly observed
- If ${}^1k_{ISC}$ and ${}^1k_F$ are comparable then the T_1 state is formed and therefore, phosphorescence is observed unless ${}^3k_r >> k_P$.

The magnitude of $^1k_{ISC}$ depends on El-Sayed's selection rules. According to El-Sayed's the rate of intersystem crossing from the lowest singlet state to the triplet manifold is large when the transition occurs between states of different orbital type. For example:

$^1(n\text{-}\pi^*)$ ⇝ $^3(\pi\text{-}\pi^*)$ much faster than $^1(n\text{-}\pi^*)$ ⇝ $^3(n\text{-}\pi^*)$

$^1(\pi\text{-}\pi^*)$ ⇝ $^3(n\text{-}\pi^*)$ much faster than $^1(\pi\text{-}\pi^*)$ ⇝ $^3(\pi\text{-}\pi^*)$

2.3.5 The energy gap law

The transfer of energy between two electronic states depends on the separation in energy between the two states. The probability of intramolecular energy transfer is very high if the gap in energy ΔE between the states is relatively small. Therefore, the probability of energy transfer is inversely proportional to the energy gap between the states involved. The rate of IC between electronic states is determined by the magnitude of the energy gap separating the states. The rate of internal conversion is very large between states higher than S_1 because the energy gaps between these states are small whereas the rate of internal conversion is not that large between S_1 and S_0 because the gap between the states is large and fluorescence can compete with IC. Thus, the rate of IC is governed by the following equation:

$$\mathbf{k_{IC} = e^{-\alpha \Delta E}} \quad \mathbf{(2.39)}$$

where α is the proportionality constant and ΔE is the energy gap between the two considered states. Also, the efficiency of intersystem crossing (ISC) is determined by the magnitude in energy separating Singlet and Triplet states, ΔE_{ST} (singlet-triplet splitting).

Electronic transitions occur faster when a minimum quantum mechanical reorganization of the wavefunctions is attained. This reorganization energy includes the energy involved to change both electronic structure and nuclear geometry. The closer the resemblance between $\Psi(S_0)$ and $\Psi(S_1)$ the larger the rate constant for fluorescence and shorter the radiative lifetime. In Perturbation Theory, weak perturbations are applied to distort the zero-order wavefunction Ψ_0 in order to provide a better estimate of the probability amplitude (P) for the transition between the two states. For instance, as shown in the following equations:

$$\mathbf{\Psi(S_1) + P(S_1 \rightarrow S_0) \rightarrow \underbrace{\Psi(S1) \pm \lambda\Psi(S_0)}_{\lambda,\ \text{resonance mixing}} \rightarrow \Psi(S_0)} \quad \mathbf{(2.40)}$$

$$\mathbf{\lambda = \frac{strength\ of\ perturbation}{energy\ of\ separation} = \frac{\langle \Psi(S_1) |\ P(S_1 \rightarrow S_0)\ | \Psi(S_0) \rangle}{\Delta E(S_1 \rightarrow S_0)}} \quad \mathbf{(2.41)}$$

$$\mathbf{\Psi_1 = \Psi_0 + \lambda \Psi_0^{'}} \quad \mathbf{(2.42)}$$

The energy gap law describes the transition probability which is dependent upon the resonance between the energy states and the transition energy. The electronic rates of fully allowed transitions are limited only by the zero-point electronic motion which occurs at about (10^{15} - 10^{16} s^{-1}). If nuclear or spin configurations of the singlet state S_1 (or triplet state T_1) and the ground state S_0 are not equal then mixing of $\Psi(S_0)$ and $\Psi(S_1)$ (or $\Psi(T_1)$) is poor, and electron transition is rate-limited by the time necessary for vibrational (and/or spin) reorganization to take place (Anslyn and Dougherty, 2006).

2.3.6 Deactivation of the excited molecules *via* dynamic and static quenching

Fluorescence intensity can be decreased *via* various intermolecular processes as shown in Figure 2.12. The reduction in fluorescence intensity is known as fluorescence quenching. The most common processes by which a fluorophore undergoes fluorescence quenching are dynamic or static quenching. Dynamic or collisional quenching does occur when excited fluorophores (X) are deactivated or diminished upon contact with solvent or other solute molecules in solutions. These molecules are called quenchers (Q). After interacting with the solvent molecules the excited molecules eventually return to the ground state emitting less light depending on the quenching rate constant abbreviated as k_Q. In other words, the extent of quenching depends on how fast the quencher can diffuse through the solution and collide with the fluorophores. This intermolecular deactivation can be described by the following energy steps:

Absorption of light: $\mathbf{X + h\nu \longrightarrow X^*}$ **(2.43)**

Dynamic quenching: $\mathbf{X^* + Q \xrightarrow{k_Q} X + Q^*}$ **(2.44)**

Then, the rate of deactivation of the excited fluorophores depends on the nature of the quencher and therefore, the excited probes are deactivated depending on the quenching rate constant k_Q. The kinetics of this intermolecular process follows the Stern-Volmer relationship which is derived as follows:

In absence of quencher:

$$\Phi_F = \frac{k_F}{k_F + k_{IC} + k_{ISC}} = \frac{k_F}{\frac{1}{\tau}} = k_F \tau \quad (2.45)$$

In absence of any quenching agent or molecule the deactivation process of the S_1 state is a unimolecular deactivation process which follows therefore, first order reaction kinetics.

In presence of quencher:

$$^{Q}\Phi_F = \frac{k_F}{k_F + k_{IC} + k_{ISC} + k_Q[Q]} = \frac{k_F}{\frac{1}{\tau} + k_Q[Q]} \quad (2.46)$$

Then in presence of quencher, the excited molecule can get deactivated *via* another deactivation pathway. Quenching is a bimolecular process because two reacting molecules are involved, X and Q. If the fluorescence quantum yield in absence of quencher, equation 2.45 is divided by the fluorescence quantum yield in presence of quencher, equation 2.46, an expression known as the Stern-Volmer plot is generated.

$$\frac{\Phi_F}{^{Q}\Phi_F} = \frac{\frac{k_F}{\frac{1}{\tau}}}{\frac{k_F}{\frac{1}{\tau} + k_Q[Q]}} = 1 + k_Q\tau[Q] = 1 + K_{SV}[Q] \quad (2.47)$$

The term K_{SV} which is the product of the lifetime times the rate quenching constant is the Stern-Volmer quenching constant (quenching rate constant for dynamic processes). The ratio of the quantum yields can be simply substituted with the ratio of fluorescence emissions and lifetimes thus, equation 2.47 becomes:

$$\frac{\Phi_F}{^{Q}\Phi_F} = \frac{I_F}{^{Q}I_F} = \frac{\tau}{^{Q}\tau} = 1 + K_{SV}[Q] \quad (2.48)$$

The Figure 2.18 illustrates the dynamic quenching process.

Figure 2.18 Deactivation of the S_1 state *via* intermolecular collisions

Fluorescence quenching occurs at the lowest excited state S_1 where the emission of light to the ground state generates fluorescence. Interactions of excited molecules X with the quencher Q do not take place during absorption and IC because these two processes are too fast to allow interactions between X and Q.

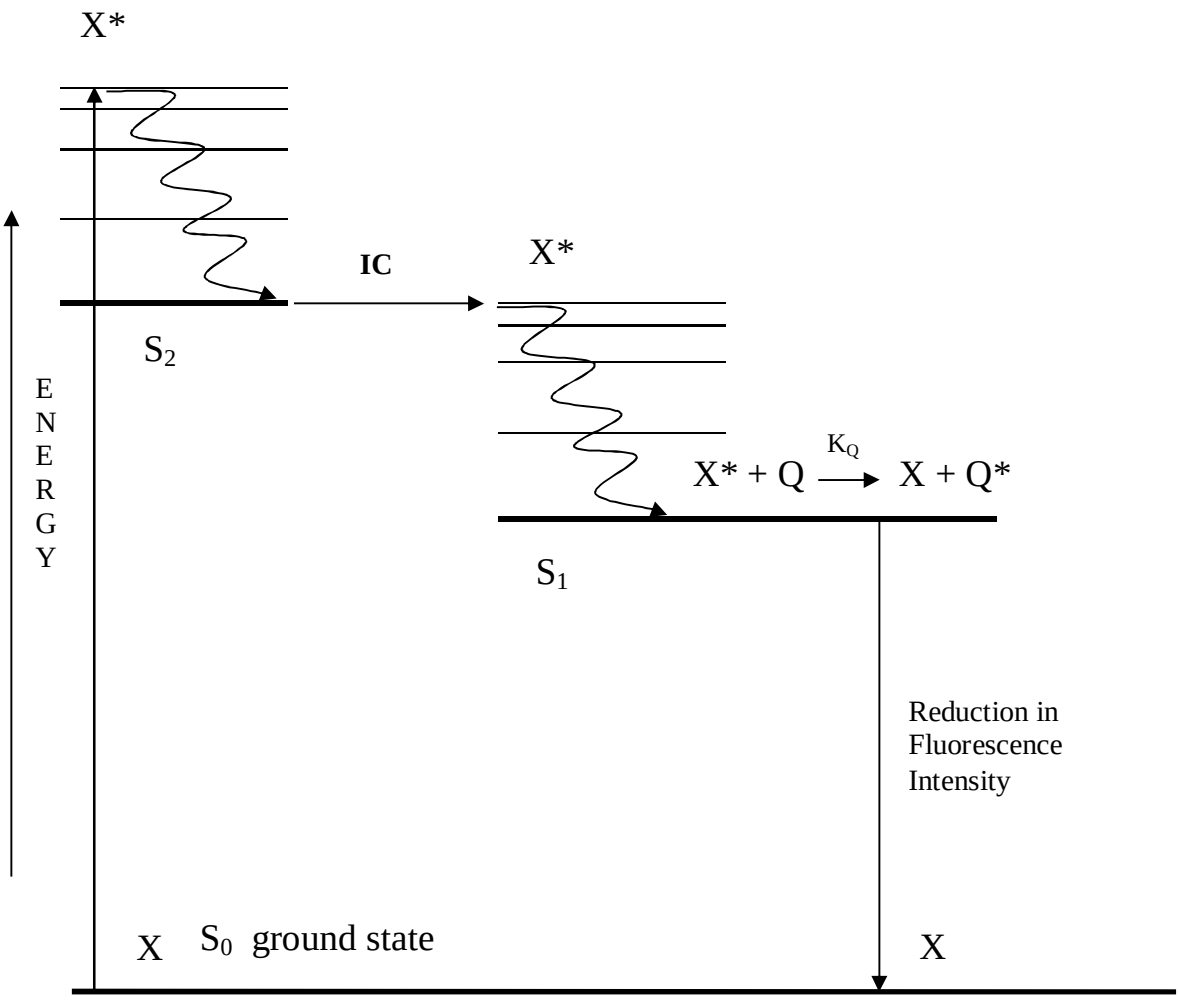

Other than collisional quenching or dynamic quenching, another process called static quenching can occur. This particular fluorescence quenching is due to the formation of non-fluorescent complex between the fluorophore molecules and the quenchers. This association between the fluorophore and quencher causes a reduction in fluorescence and the effectiveness of static quenching depends on the quenching constant rate for static processes k_S. In many cases, collisional quenching and static quenching can be recognized by looking at their differences in absorption spectra. In the case of static quenching the complex formed has normally a different absorption spectrum from the fluorophore absorption spectrum. On

the other hand, collisional quenching is a transient excited state interaction which does not change the absorption spectrum of the fluorophore. A special case of static quenching is self-quenching. Self-quenching appears when the fluorophore behaves as a quencher itself. This case of static quenching is particularly observed when working with very concentrated solutions of fluorophores. The derivation of the static quenching expression follows the following steps:

Formation of the ground state complex: $\mathbf{X + Q \xrightarrow{K_S} X\text{---}Q}$ **(2.49)**

The association constant or static quenching constant k_s is then:

$$\mathbf{K_S = \frac{[XQ]}{[X][Q]}} \quad \mathbf{(2.50)}$$

The concentration [XQ] is the complex concentration. Since the total fluorophore concentration X_0 is equal to:

$$\mathbf{[X_0] = [X] + [XQ]} \quad \mathbf{(2.51)}$$

Hence the numerator [XQ] can be rewritten as follows below:

$$\mathbf{K_S = \frac{[X_0] - [X]}{[X][Q]}} \quad \mathbf{(2.52)}$$

Thus, equation 2.52 becomes:

$$K_S = \frac{[X_0]}{[X][Q]} - \frac{1}{Q} \quad (2.53)$$

Therefore:

$$\frac{[X_0]}{[X]} = \frac{I_F}{{}^{Q}I_F} = 1 + K_S[Q] \quad (2.54)$$

The equations 2.48 and 2.54 have an identical form and both predict a linear relationship between fluorescence emission ratio and quencher concentration with an intercept equal to 1. Then the first question that immediately arises is: how one can discern or recognize dynamic quenching from static quenching? An experiment which can help understand whether the quenching is dynamic or static is measuring the change in fluorescence emission in presence of quencher as a function of temperature. An increase in temperature causes the slope of the linear function to increase if the quenching is purely dynamic because higher temperatures increase diffusion rates. On the other hand, the slope of the function due exclusively to static quenching decreases as a function of temperature because ground state complex formation is normally inversely proportional to temperature (Fraiji *et al*. 1992; Lakowicz, 1999). Figure 2.19 illustrates the effect of the temperature on the dynamic and static quenching constants.

Figure 2.19 Effect of temperature on static and dynamic quenching

As the temperature increases K_{SV} increases whereas K_S decreases

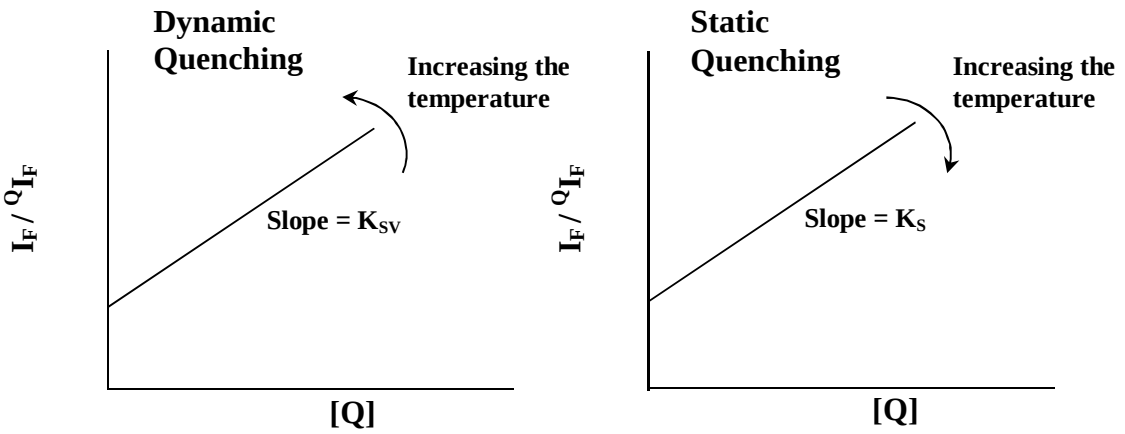

Even though the effect of temperature on the emission of the fluorophore in presence of quenchers can help understand the type of quenching mechanism, fluorescence emission measurements are better combined with the measurements of the fluorescence lifetimes. In fact, comparing the fluorescence emission in presence and absence of quenchers with the emission lifetime changes as a function of quencher concentration is the only diagnostic test to know whether the quenching is dynamic or static. This comparison is illustrated in Figure 2.20.

Figure 2.20 Diagnostic plots to distinguish between static and dynamic quenching

Plotting fluorescence emissions along with fluorescence lifetimes as a function of quencher concentration

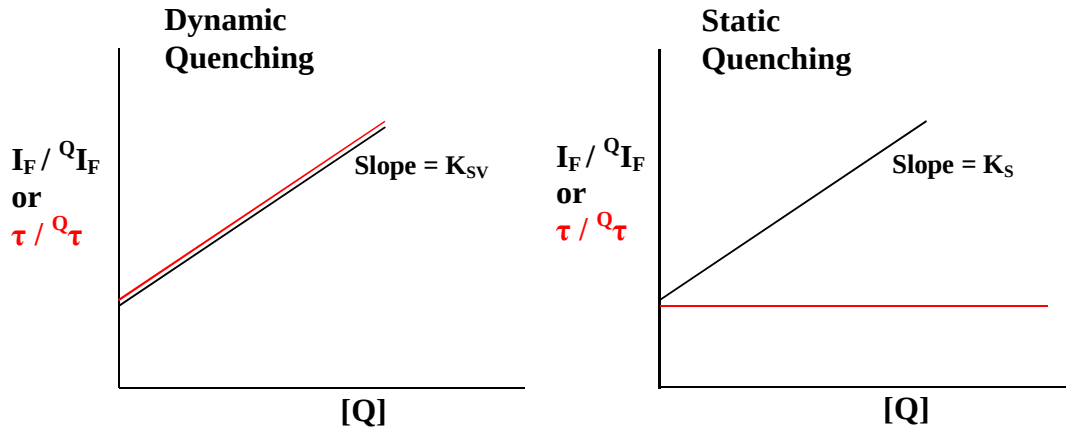

As shown in Figure 2.20 it is clear that the two types of quenching can be separated based on the emission lifetimes because the lifetime measurements are not affected by the formation of ground state complexes, XQ because the fluorophores which did not form complexes with the quenchers still have the same emission properties. Essentially, only the number of fluorescent probes is reduced (Fraiji *et al*. 1992; Lakowicz, 1999). It is important to know that the quenching process may not be dynamic or static only but a combination of both processes. This combined or mixed quenching process can be described in the following equation:

$$\frac{I_F}{{}^{Q}I_F} = (1+ k_{SV}[Q])\ (1+ k_S[Q]) = 1 + (k_{SV} + k_S)[Q] + k_{SV}\ k_S[Q^2] \quad (2.55)$$

Equation 2.55 predicts an upward curvature by plotting the fluorescence emissions against the quencher concentration and a quadratic relationship between the emission lifetimes and the quencher concentration as illustrated in Figure 2.21.

Figure 2.21 Combined quenching

Combined or mixed quenching (a combination of static and dynamic quenching). A quadratic function is predicted by plotting fluorescence emissions against the quencher concentration and a linear function when the emission lifetimes are plotted against the concentration

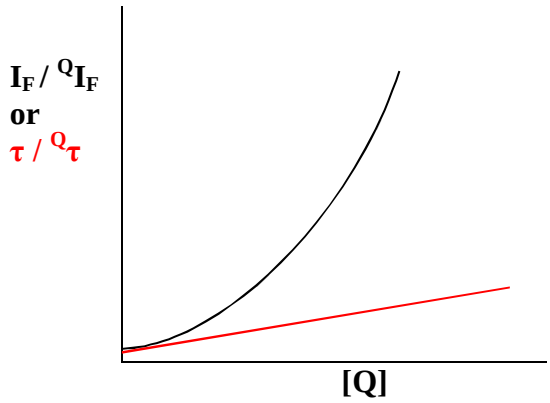

2.3.7 Deactivation of the excited molecules *via* electronic energy transfer

Other than dynamic and static quenching which are energy transfer processes, energy can be transferred through electronic energy mechanisms. Intermolecular electronic energy transfer can be further divided into radiative and non-radiative transfer which branch out into trivial mechanism, coulombic mechanism and electron exchange mechanism respectively as shown in Figure 2.22.

Figure 2.22 Electronic energy transfer processes

The branching out of electronic energy transfer mechanism

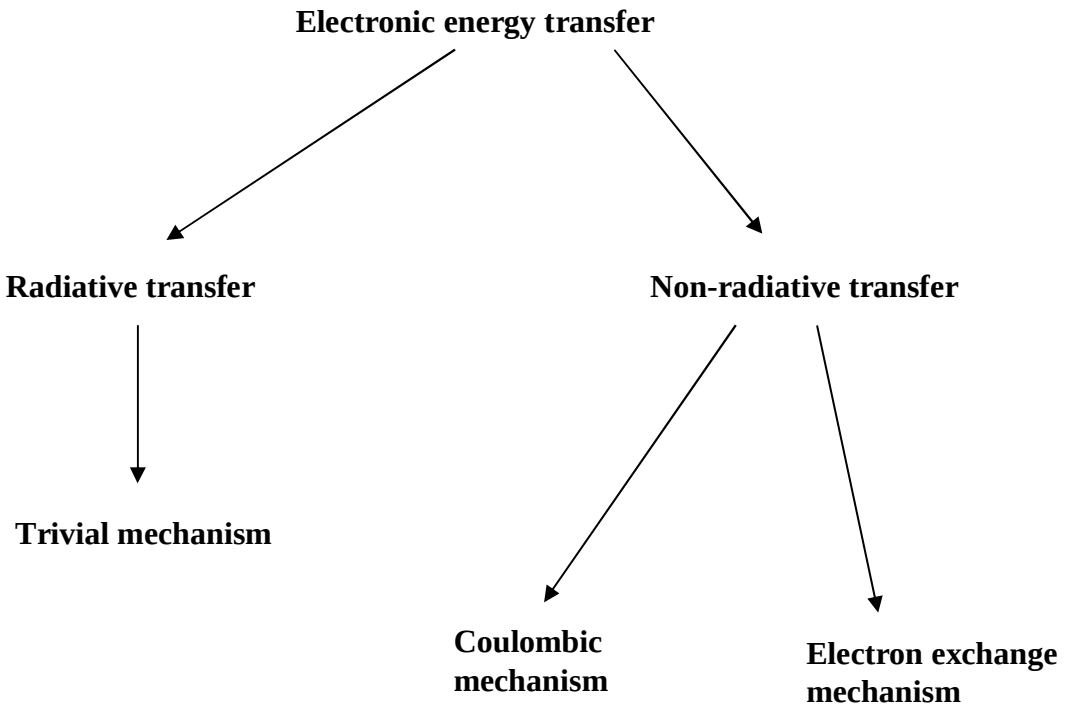

The radiative transfer (trivial mechanism) involves the emission of light by an excited molecule called the donor (D), followed by the absorption of the emitted photon by another molecule or acceptor (A). The mechanism can take place over large distances. Hence, the mechanism is the following:

$$D^* \longrightarrow D + h\nu$$

$$h\nu + A \longrightarrow A^*$$

Coulombic energy transfer is also known as FRET (Förster Resonance Energy Transfer). The **Förster energy** transfer is the exchange in energy by electronic coupling between the donor molecule and the acceptor molecule. The transfer occurs without photon emission and the exchange in energy depends on many factors such as spectral overlap between the excitation and emission spectra, the quantum yield of the donor and the relative orientation of the transition dipoles of the donor and acceptor molecules but above all the most important factor is the distance between the donor and acceptor. In fact, the exchange in energy is highly distance dependent. In particular, according to Förster theory the probability of Coulombic energy transfer falls off inversely with the sixth power of the distance between the donor and the acceptor molecules. Electron exchange which is better known as **Dexter energy** transfer is a processes that unlikely the Förster one involves close approach because the electron exchange energy transfer requires the overlap of the wavefunctions.

2.4 2-Aminopurine (2-Ap) and Pyrrolocytosine (Pc) literature

Adenine and its constitutional isomer 2-Ap have different photophysical properties. The modified natural base 2-Ap as shown in Figure 2.23 is highly fluorescent in water, $\Phi_F = 0.66$ (Holmen *et al.* 1997) with long fluorescence lifetimes, $\tau \approx 10$ ns (Ward *et al.* 1969). On the other hand, the natural base adenine has an extremely small fluorescence quantum yield in water was found to be within the following range: Φ_F 0.0005 – Φ_F 0.0030 (Callis, 1983; Peon and Zewail, 2001; Crespo-Hernandez *et al.* 2004) and much shorter lifetimes compared to 2-Ap, $\tau \approx 290$ - 720 fs (Peon and Zewail, 2001; Gustavsson *et al.* 2002).

Figure 2.23 Adenine and 2-Aminopurine (2-Ap)

The natural nucleobase adenine with the amino group on position 6 of purine, and the isomer 2-aminopurine (N9H tautomer) with the amino group on position 2 of purine

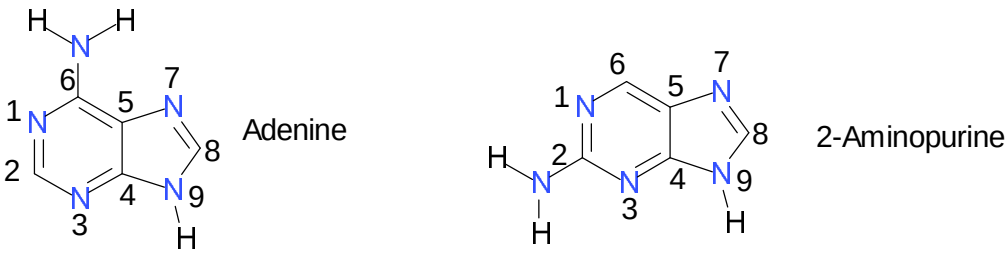

So, why is 2-aminopurine a highly fluorescent base whereas adenine is a weakly fluorescent base? One of the most likely hypotheses relies on the Lim's Proximity Effect (Lim, 1977; Lim, 1986) which explains ultrafast internal conversion (Wassam and Lim, 1978) by vibronic coupling between the two low-lying ππ* and nπ* excited states, and nearby low energy states, favouring radiationless transitions to the ground state S_0. In adenine a small gap in energy exists between the lowest nπ* and ππ* excited states, the smaller the gap, the more efficient the coupling between these states. The vibronic coupling (and resulting Frank-Condon (FC) factor) is large leading to internal conversion (IC) with subsequent radiationless transitions to the ground state S_0 and dissipation of energy *via* vibrational relaxation. In the case of 2-aminopurine, the lowest ππ* state is much lower in energy with respect to nπ*, and thus, the vibronic coupling is not large enough and hence, the FC factor associated with it is not sufficiently large to lead to non-radiative transitions to the ground state (Broo, 1998; Rachofsky *et al*. 2001). The Figure 2.24 shown below illustrates the difference in energy gap between the two low-lying states n-π* and π-π* of Adenine and 2-Ap. The efficiency of radiationless decay has been attributed to the role of conical intersections (CI) (Köppel *et al*. 1984; Klessinger and Michl, 1995; Yarkony, 1995; Robb *et al*. 1998; Chachisvlis and Zewail, 1999; Pecourt *et al*. 2000; Domke *et al*. 2004; Olivucci, 2005) which can be described as crossing of energy states (intersection space), usually S_1/S_0 states, which are responsible for ultrafast non-radiative decay by IC to S_0. In both adenine and 2-Ap conical intersections exist between the excited states and the ground state (Perun *et al*. 2005; Perun *et al*. 2006), but in the case of 2-Ap CIs are inaccessible because of high energy barriers and thus CIs are inefficient in quenching the fluorescence of 2-Ap compared to adenine (Seefeld *et al*. 2005; Serrano-Andrés *et al*. 2006). When 2-Ap is incorporated into oligonucleotides as part of a DNA fragment, its fluorescence is strongly quenched. The degree of quenching depends on the nature of the neighbouring bases (Nordlund *et al*. 1989; Guest *et al*. 1991; Hochstrasser *et al*. 1994; Kelley and Barton, 1999; Larsen *et al*. 2001; Fiebing *et al*. 2002). In the instance of 2-Ap flanked by guanine bases the observed stronger decrease in fluorescence compared to the other bases may be attributed to electron transfer (Kelley and Barton, 1999; Wan *et al*. 2000; Fiebing *et al*. 2002; O'Neill *et al*. 2003) even though no charge-separated product state was observed (Larsen *et al*. 2004; O'Neill *et al*. 2004). The quenching of 2-Ap when flanked with guanine bases may also be caused by transition to a dark state rather than by electron transfer (Somsen *et al*. 2005). Controversy about the mechanism/s responsible for 2-Ap fluorescence quenching when the base is stacked with nucleobases still exists (Reynisson and Steenken, 2004; Wan *et al*. 2005).

Figure 2.24 Lim's proximity effect between n-π* and π-π*

Small energy difference between the two low-lying states n-π* and π-π* of Adenine as opposed to 2-Ap

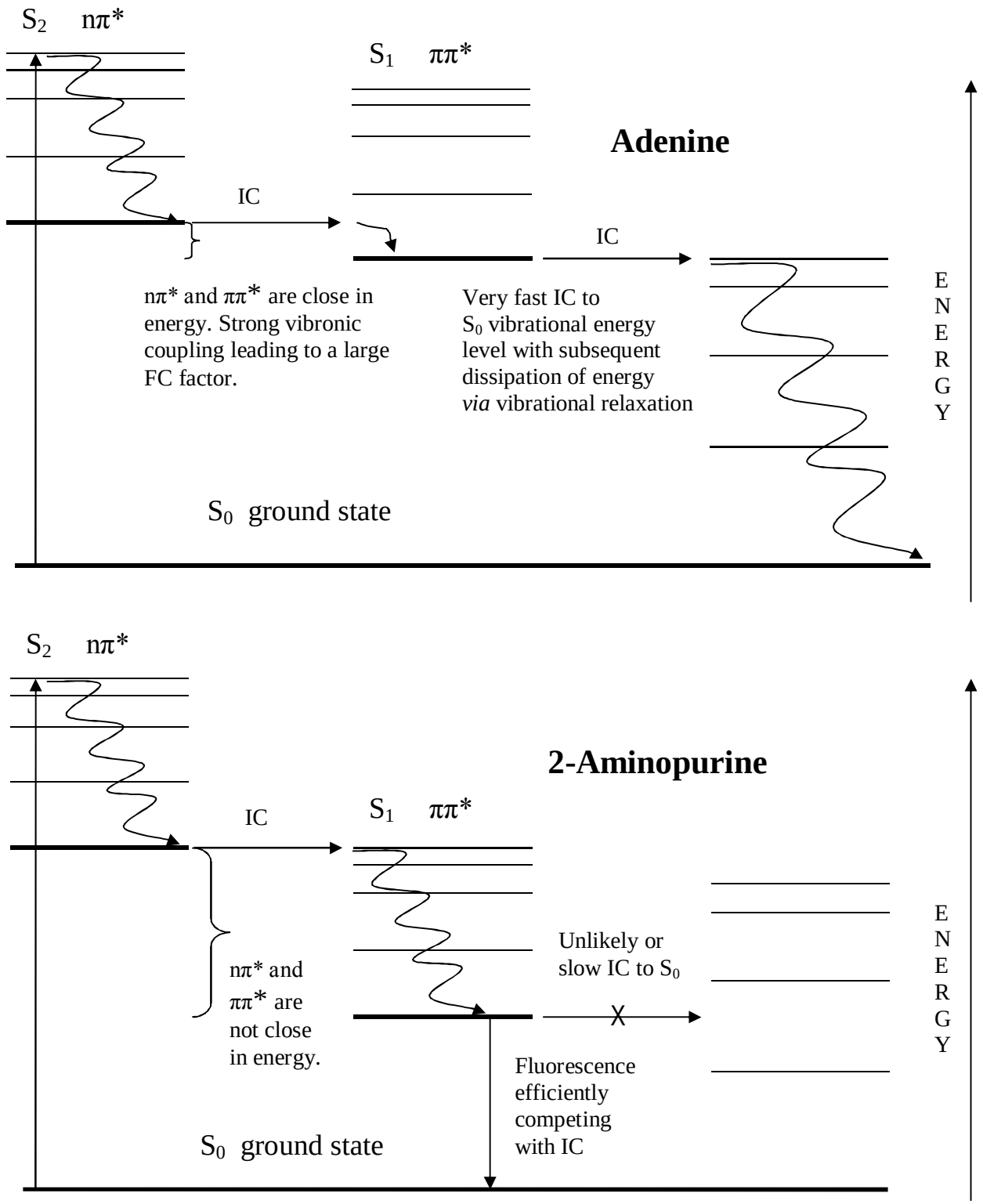

Pyrrolocytosine can replace the natural nucleobase cytosine. The two bases are shown in Figure 2.25. As is the case with the natural nucleobase adenine, cytosine has a relatively low quantum yield in water $\Phi_F = 0.0001$ and a short fluorescence lifetime $\tau \approx 1$ ps (Callis, 1983) whereas its structurally modified counterpart pyrrolocytosine has a larger quantum yield $\Phi_F = 0.038$ and longer fluorescence lifetime $\tau \approx 2.9$ ns (Hardman *et al*. 2008).

Figure 2.25 Cytosine and Pyrrolocytosine (Pc)

The natural nucleobase cytosine and the structurally similar pyrrolocytosine base (both bases are N1H tautomers)

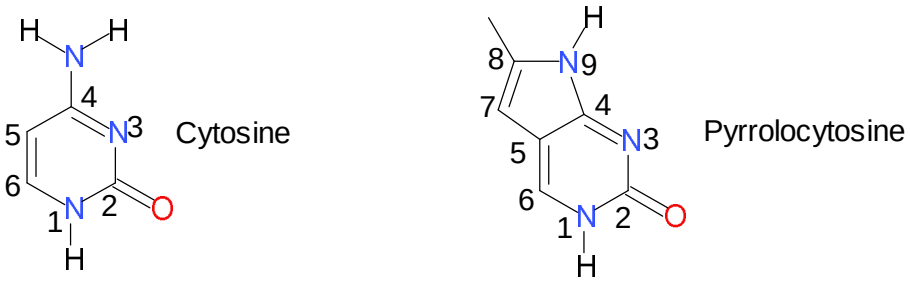

Cytosine exhibits very low fluorescence emission due to an ultrafast non-radiative pathway from its lowest excited state to the ground state; the photophysical mechanism responsible for this ultrafast deactivation of the lowest excited state of the analogue base is still under investigation (Crespo-Hernandez *et al*. 2004). Strong vibronic coupling between the lowest bright state π-π* and the dark state n-π* which then may relax to the ground state is a possible explanation for the very low quantum yield of the natural base (Canuel *et al*. 2005).

Another hypothesis is that the pyrimidine base's excited populations may decay *via* two distinct pathways in aqueous solution: ultrafast internal conversion to the ground state and decay to a dark state n-π* (Hare *et al*. 2007). The fluorescence of Pc decreases upon RNA duplex formation (Tinsley and Walter, 2006). They recorded the fluorescence emission of Pc over a wide range of ionic strength, pH and temperature, and it decreased up to 60% when Pc was incorporated into a single-stranded RNA and by 75% as a double-stranded RNA relative to the free base. The decrease in fluorescence emission of Pc when incorporated into oligonucleotides (experimentally measured) is in agreement with computational data (Thompson and Miyake, 2005). The reduction in fluorescent quantum yield when Pc is

stacked with guanine bases was observed as expected given the lower computed oscillator strength compared to that of the free base, but no specific evidence was found that the involved π states spread over more than one base (Hardman and Thompson, 2006). Electron charge transfer between the excited Pc molecule guanine bases may also occur which would be responsible for excited state depopulation of Pc resulting to shorter lifetimes and therefore, lower quantum yields (Hardman *et al*. 2008).

Chapter 3: Solvatochromic studies of 2-aminopurine and pyrrolocytosine

3.1 Introduction to solvatochromic study

Solvatochromism can be defined as the influence of the solvent molecules on the electronic absorption and fluorescence spectra of the solute molecules or probes. Therefore, a solvatochromic shift is the displacement of an electronic spectrum of solute molecules or probes that occurs when moving from one solvent to another of different nature. The solvatochromic shift is an important aspect of the influence of the solvents on the studied probes because it provides information on the absolute and relative electronic states of the molecules analysed. Also, physical properties such as dipole moments and specific interactions such as hydrogen bonding formation between solvent solute molecules can be studied. When fluorophores are excited to a Franck Condon state or FC (see Chapter 2 Section 2.2) in polar solvents the emission of the fluorophores is usually redshifted compared to non-polar solvents and the extent of redshift depends on the polarity of the solvents used. Upon excitation the excited dipole moments of the fluorophore may get larger or smaller and the degree of change depends on the nature of the solvent used. A dramatic change in the electron density of the excited probe results in a big change in the magnitude or direction of the dipole moment (the definition of dipole moment is given in Section 3.2) which is due to intramolecular charge transfer. Then, a large redistribution of charges may lead to conformational changes of the probes in the excited state, therefore, affecting the fluorescence intensity of the probes themselves. Eventually, the solvent molecules reorient around the dipole moment of short-lived excited fluorophore molecules. This solvent relaxation decreases the energy of the fluorophore which emits at longer wavelengths. As the solvent polarity is increased, the extent of redshift becomes larger. The determination of the ground state dipole moment μ_g and the excited state dipole moment μ_e of a fluorescent probe is important because their difference provides information on the extent of electron or charge distribution of the fluoroprobe when excited in a particular solvent. The Figure 3.1 is a simple illustration that shows the reorientation of solvent molecules around the short-lived excited fluorophore molecule.

Recent studies on the mechanical stability of DNA when pulled from a highly polar environment (usually water) to a non-polar environment showed that double-stranded DNA molecules tend to dissociate into single-stranded molecules (Cui *et al.* 2007; Abe *et al*. 2012). Thus, understanding how 2-Ap and Pc fluorescence emissions are affected by solvents of

different polarity may help to assess the degree of dissociation of the double-stranded DNA molecules.

Figure 3.1 Reorientation of solvent molecules around an excited fluorophore

Fluorophore molecule (big circle) surrounded by the solvent molecules (small circles). The excited state dipole moments μ_e and ground state dipole moments μ_g are depicted as arrows. Upon excitation the electronic distribution of the short-lived fluorophore changes and the solvent molecules reorient themselves accordingly in order to reach a relaxed state

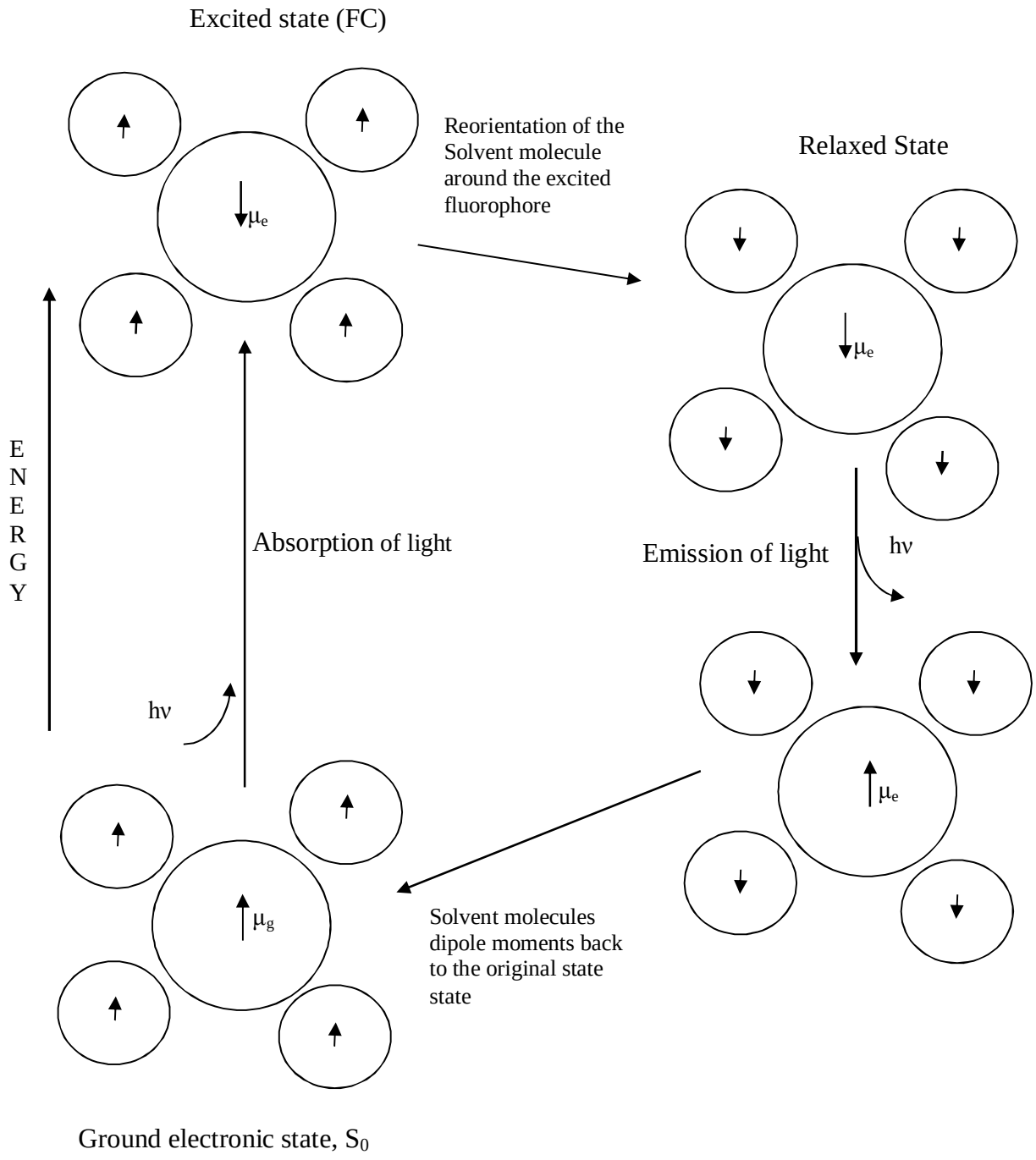

It should be noted that the solvent molecules are strictly in their ground electronic state because their lowest excited states are much higher in energy (energy of a much shorter wavelength would be necessary to excite the solvent molecules compared to the fluorophore molecules) than the ones of the fluorophore and as a consequence of that, their dipole moments do not change.

3.2 The Lippert equation

Effects that influence the fluorescence spectrum of a solute due to polarity of the solvent, also called general solvent effects, can be explained through the Lippert model. Specifically, the general solvent effects are: fluorophore dipole solvent dipole interactions, fluorophore dipole solvent polarizability interactions, fluorophore polarizability solvent dipole moment interactions and fluorophore polarizability solvent polarizability interactions (Valeur, 2002). The Lippert model does not account for specific solvent effects such as: hydrogen bonding, charge shift, fluorophore-fluorophore interactions and fluorophore conformational changes (Lippert, 1957; Matanga *et al.* 1956) and it is valid if the following conditions are satisfied:

I – The dipole moments of the ground and excited states of the fluorophore should be unaffected in magnitude and direction by the reorientation of the solvent molecules.

II – The cavity radius (see equation 3.1) is unchanged upon excitation. (Any change in molecular volume or conformation of the fluorophore molecule is regarded as a specific solvent effect).

III – The fluorophore molecules must not fluoresce prior to complete solvent relaxation (in other words, fluorescence must take place from the fully relaxed state, see figure 3.1).

The Lippert equation is shown below, (Lakowicz, 2006)

$$\upsilon_{ex} - \upsilon_{em} = \frac{2}{hc}\left(\frac{\varepsilon - 1}{2\varepsilon + 1} - \frac{\eta^2 - 1}{2\eta^2 + 1}\right)\frac{\left(\mu_e - \mu_g\right)^2}{a^3} + \text{constant} \quad (3.1)$$

Where ε is the dielectric constant or relative permittivity which is a quantity measuring the ability of a substance to store electrical energy in an electric field. The ratio of the permittivity of a substance to the permittivity of free space gives the dielectric constant value of that specific substance. The diffractive index given as η is defined as the ratio of the velocity of light in vacuum to its velocity in a specified medium. The difference υ_{ex} - υ_{em} is the Stokes shift given as wavenumbers then in cm^{-1}. The Stokes shift (see Chapter 2 Figure 2.14) can be defined as the spectral difference between the maximum in absorption or excitation band and the maximum emission or fluorescence band. Usually the absorption or excitation and emission bands are mirror images with the fluorescence band shifted towards longer wavelengths. This spectral shift may be interpreted as a function of solvent polarity. The symbols h and c represent Planck's constant and the speed of light in a vacuum respectively. The letter a stands for the radius of the cavity in which the fluorophore resides. The choice of the cavity radius deserves particular attention. If the fluorophore or solute molecules studied have a shape more similar to a sphere than an ellipsoid then, the cavity radius can be assumed to be spherical and it can be approximated as the molecular radius of the fluorophore itself. (The cavity radii of 2-Ap and Pc are assumed to be spherical). The dipole moments of the fluorophore in the excited and ground states are μ_e and μ_g.

The mathematical terms inside the parentheses are the orientation polarizability called *Δf*, (3.2)

$$\Delta f = \left(\frac{\varepsilon - 1}{2\varepsilon + 1} - \frac{\eta^2 - 1}{2\eta^2 + 1} \right) \quad \textbf{(3.2)}$$

The Franck-Condon principle (see Chapter 2 Section 2.2) states that nuclei do not move during an electronic transition on the other hand the electrons instantaneously redistribute themselves, being much lighter than nuclei, thus, generating short-lived excited state dipoles. The refractive index parameter accounts for this instantaneous electron redistribution, whereas the dielectric constant accounts for the much slower molecular redistribution (solvent molecules around the fluorophore molecule). The constant in equation 3.1 is the Lippert constant. This constant is present because even with an orientation polarizability equal to 0, $\Delta f = 0$, the excitation spectrum and the emission spectrum do not perfectly

coincide, resulting in a small Stokes shift. The solvent sensitivity of a fluorophore can be estimated with a Lippert plot by plotting the Stokes shift, υ_{ex} - υ_{em}, against the orientation polarizability, Δf. The slope of this plot represents the square of the difference of the dipole moment of the fluorophore in the excited state and in the ground state, μ_e - μ_g. Although the Lippert plot is an approximation because it ignores specific solvent effects, the linearity of the plot is considered as evidence that polarity is the main factor affecting the spectral shifts of fluorophores in solvents (Ooshika, 1954; Matanga *et al.* 1956).

The dipole moment μ is simply defined as the product of equal positive and negative charges by their separation distance:

$$\mu = q \times d \qquad \underbrace{q^{+} \ldots\ldots\ldots\ldots\ldots q^{-}}_{d} \qquad (3.3)$$

Therefore, the dipole moment is a vector and in a molecule which may contain many positive and negative charges, the total dipole moment is the sum of all the vectors of the individual dipoles. The resulting vector is given as the integral called P which is the dipole moment of the charge distribution as shown in equation 3.4.

$$\mathbf{P} \equiv \int \mathbf{r}' \ \rho(\mathbf{r}') \ d^3 \mathbf{r}' \qquad (3.4)$$

Where r' is the vector from the origin to the point with charge density ρ (r'), thus for a number of charges (n) the dipole moment can be written as:

$$\mathbf{P} = \sum_{i}^{n} q_i \ \mathbf{r}_i' \qquad (3.5)$$

The absolute value of the dipole moment is the dipole strength which is a scalar number usually expressed in Debyes (D) when the cgs system is adopted.

3.3 The determination of the quantum fluorescence yields, materials and methods

The quantum yields (Φ_F) of 2-Ap and Pc in different solvents were measured by using steady state spectroscopic techniques (UV-visible spectroscopy and fluorescence spectroscopy). The quantum yield is the ratio of the number of photons emitted as fluorescence to the number of photons absorbed as mentioned in Chapter 2 in Section 2.3.2. The quantum yields were measured using the comparative method (comparison of the known fluorescence emission of quinine in sulphuric acid with fluorophores of unknown fluorescence emission). Quinine, see Figure 2.15, is a compound with a strong fluorescence emission, relatively inexpensive and readily available (Standard sample ≥ 99.0 % Fluka). This method requires the use of two instruments: an UV/Visible spectrometer to obtain the absorption spectra of the samples and a fluorimeter to obtain the emission spectra of the samples at a fixed excitation wavelength (the maximum absorbance wavelength) (Rhys and Winfield, 1983).

Then, starting with the fluorescent probe (Pc or 2-Ap in different solvents),

$$\mathbf{\Phi_F = K \frac{Fx}{Ax}} \quad \mathbf{(3.6)}$$

Φ_F is the quantum yield of the fluorescent probe

Fx is the integrated fluorescence of the probe

Ax is the maximum absorbance of the probe

K is an unknown constant or correction factor which accounts for the different sensitivities of the detectors used

For quinine,

$$\Phi_{Fq} = K \frac{Fq}{Aq} \quad (3.7)$$

Φ_{Fq} is the known quantum yield of quinine

Fq is the integrated fluorescence of quinine

Aq is the maximum absorbance of quinine

Thus, by comparative method,

$$\frac{\Phi_{Fx}}{\Phi_{Fq}} = \frac{K}{K} \frac{\frac{Fx}{Ax}}{\frac{Fq}{Aq}} \quad (3.8)$$

Now, providing that the instruments used for the fluorophore and quinine are the same, the two constants or correction factors K can be cancelled, and therefore,

$$\Phi_{Fx} = \Phi_{Fq} \frac{Fx}{Ax} \frac{Aq}{Fq} \quad (3.9)$$

In equation 3.9 the only unknown term is Φ_{Fx} whereas the term Φ_{Fq} is the absolute quantum yield of quinine (in 0.5 M sulphuric acid) which is 0.546 measured by Melhuish (Melhuish, 1961; Vellapodi *et al.* 1980). The ratio Fx/Ax can be rewritten as 1/mx where mx is equal to Ax/Fx the gradient found by plotting the absorbance values of the probe against the integrated fluorescence areas of the probe. The term Aq/Fq can be rewritten as mq, the gradient found by plotting the absorbance values of quinine against the integrated fluorescence areas of quinine. Thus, the formula 3.9 becomes,

$$\Phi_{Fx} = \Phi_{Fq} \frac{mq}{mx} \quad (3.10)$$

Since the quantum yields of the probes were measured in different solvents the refractive indexes (the speed of light passing in vacuum divided by the speed of light in the medium) of the solvents used are to be taken into account, and therefore,

$$\Phi_{Fx} = \Phi_{Fq} \frac{mq}{mx} \frac{\eta_x^2}{\eta_q^2} \quad (3.11)$$

With the subscripts η_x and η_q representing the refractive indices of solvent x and quinine.

The errors in the quantum yield measurements were calculated by obtaining the errors in the gradients generated by plotting the absorbance measurements against the fluorescence measurements given as error bars of ± 2 standard deviations or 2σ. If we assume that the measurements obtained of each dependent variable y_i (absorbance measurements) is distributed about its true value x_i or independent variable (fluorescence measurements) then, the following equation: $y_{line} = mx_i + c$ with a width parameter σ_y can be used. Hence, the residuals $y_i - y_{line}$ are also normally distributed around the same central value and with the same width parameter σ_y. An estimate of the uncertainty associated with a straight line is obtained by using a sum of the squares as shown in equation 3.12.

$$\sigma_y = \sqrt{\frac{1}{N} \sum_{i=1}^{N} (y_i - y_{line})^2} \quad (3.12)$$

Thus, by replacing $mx_i + c$ with the best fit among the points, y_{line} the equation 3.12 is transformed into 3.13 where N is the number of readings:

$$\sigma_y = \sqrt{\frac{1}{N}\sum_{i=1}^{N}\left(y_i - mx_i - c\right)^2} \quad \textbf{(3.13)}$$

The uncertainty associated with the intercept was not calculated because the intercept c is equal to 0 as shown in all the plots of absorbance against fluorescence reported in this thesis. In fact, if no photons are absorbed then the fluorescence intensity must be 0. Having said that, the only variable left which requires error prediction is the slope m. The uncertainty in the slope can be calculated *via* a simple propagation of errors, precisely as shown in equation 3.14 and 3.15. The equation 3.14 is used to calculate the value of the slope by adopting the weighted least square method (Bevington, 1992).

$$m = \frac{\sum \frac{x_i y_i}{\sigma_{y_i}^2}}{\sum \frac{x_i^2}{\sigma_{y_i}^2}} \quad \textbf{(3.14)}$$

The variation of the uncertainty in the slope is measured by using the value of m previously calculated in equation 3.15.

$$\sigma_m^2 = \frac{\frac{1}{N-1}\sum\left(y_i - m_{x_i}\right)^2 \sum \frac{x_i^2}{\sigma_{y_i}^4}}{\left(\sum \frac{x_i^2}{\sigma_{y_i}^2}\right)^2} \quad \textbf{(3.15)}$$

Then after calculating the uncertainty in the slopes of quinine (q) and the unknown compound (x) (Pc or 2-Ap in different solvents), the error in the quantum yield measurements follows the solution of the equation 3.16.

$$\sigma_x = \sqrt{\Phi_{Fx}^2 \left(\frac{\Phi_{mx}^2}{m_x^2} + \frac{\sigma_{mq}^2}{m_q^2} \right)} \quad \textbf{(3.16)}$$

The modified free bases 2-Ap (minimum 99.0 % Sigma) and Pc (100 % purity by HPLC, Berry Associates Inc Dexter USA) were used as received and dissolved in the following organic solvents: n-propanol or 1-propanol C_3H_8O (99.5 % Sigma-Aldrich), ethanol C_2H_6O (99.7-100 % BDH Chemicals Ltd), acetonitrile C_2H_3N (99.9 % BDH Chemicals Ltd), isopropanol or 2-propanol C_3H_8O (≥ 99.5 % BDH Chemicals Ltd), methanol CH_4O (99.8 % BDH Chemicals Ltd), ethyl acetate $C_4H_8O_2$ (≥ 99.7 % Sigma-Aldrich), dimethyl sulfoxide (DMSO) C_2H_6SO (≥ 99.0 % Fisher Chemicals), tetrahydrofuran (THF) C_4H_8O (≥ 99.9 % (Aldrich), chloroform $CHCl_3$ (≥ 99.9 % Sigma-Aldrich) and diethyl ether $C_4H_{10}O$ (≥ 99.5 % Fisher Chemicals).

The absorption spectra were obtained using a Thermospectronic UV-1 double-beam spectrometer with spectrometer bandwidth of 2.0 nm. The cuvettes used for spectroscopic measurements are quartz cuvettes with an optical path length of 10 mm. When using 10 mm cuvettes the solution concentrations should not greatly exceed an absorbance value of 0.1 (concentration of the samples circa 2.0×10^{-5} M). Much above this value, non-linear effects may occur because of the reabsorption phenomenon known as inner filter effect, rendering the quantum yield measurements not accurate; also the fluoroprobes may form excimers at high concentrations and fluorophore-fluorophore interactions which are specific solvent effect (Dhami *et al*. 1995).

The emission (the emission spectrum can be described as a plot of number of photons emitted as a function of wavelength when the molecule is irradiated at a fixed excitation wavelength) and excitation (the excitation spectrum is also a plot of number of photons emitted as a function of wavelength, but unlike the emission spectrum, this time the emission wavelength is held constant and the excitation wavelength varies) spectra were obtained by using an Hitachi fluorimeter spectrometer with bandwidth of 2.5 nm. Ten measurements of excitation and emission spectra for each solution sample were collected at an interval of 2 minutes from one reading to another. The mathematical means and standard deviations were calculated and

uncertainty errors were reported. An example of a typical fluorimeter layout is displayed in Figure 3.2.

Figure 3.2 Illustration of a schematic fluorimeter

A fluorimeter composed of the following parts: source of light, excitation monochromator, sample cell, emission monochromator, PMT, amplifier and recorder

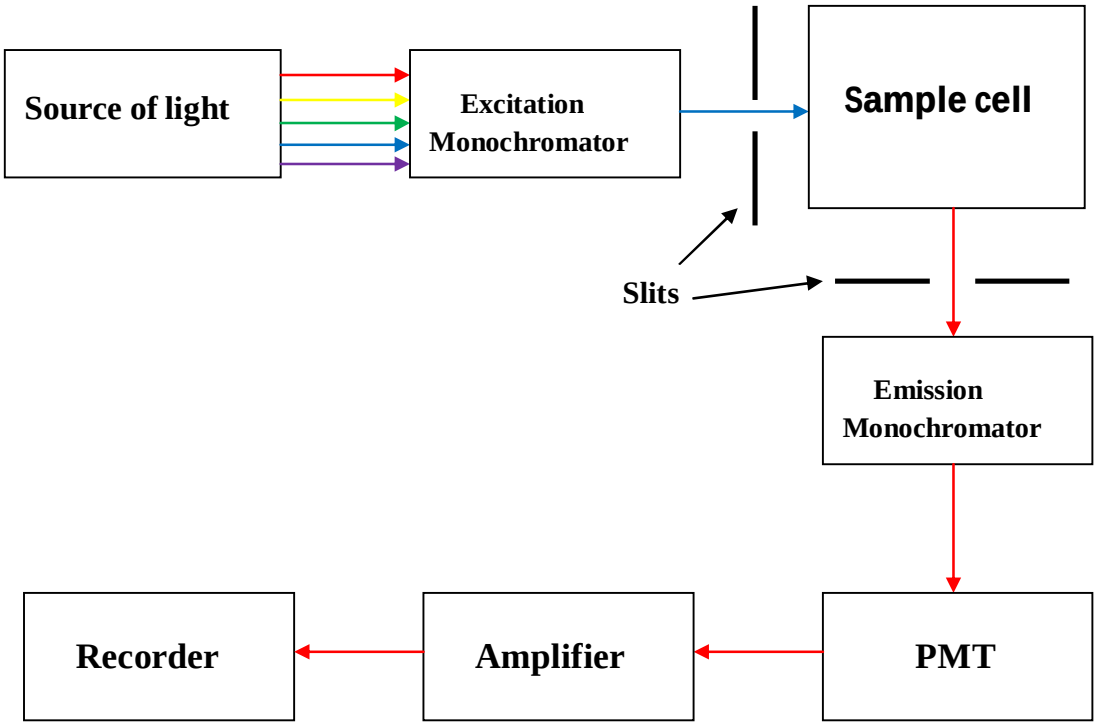

The source of light is a Xenon lamp with a light output from 250 to 800 nm. The monochromators which filter out specific radiations at different energies are characterized by the following parameters:

- **Bandpass:** The wavelength range that the monochromator transmits.
- **Dispersion:** Wavelength dispersing power given by the ratio of spectral range (nm)/ slit width (nm).
- **Resolution:** The minimum bandpass that a spectrometer produces.

The layout of a monochromator is shown in Figure 3.3

Figure 3.3 Illustration of a fluorimeter monochromator

A monochromatic system attained by rotating the diffraction grating

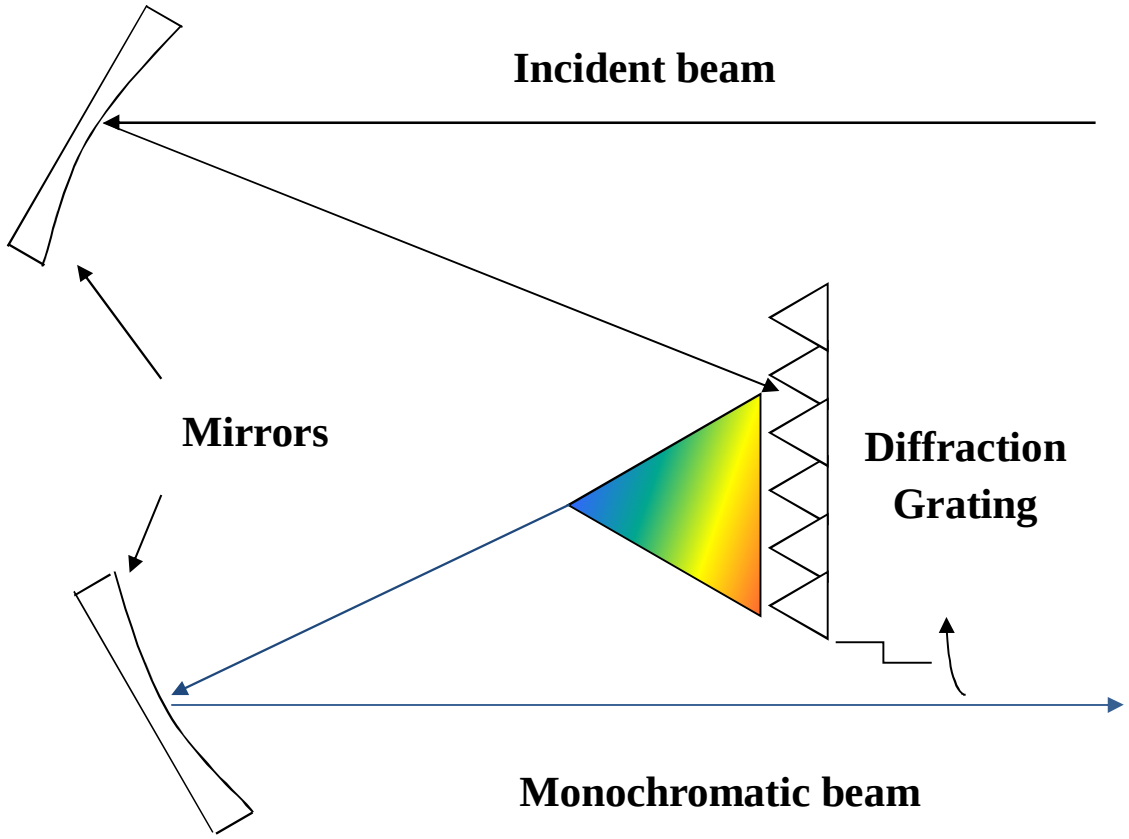

The physical width and angular spread of the selected radiation are controlled *via* the slits and the mirrors are used to focus or collimate the beams. The cuvettes containing the samples to be analysed are inserted into the sample chamber. The PMT (photomultiplier tube) is a detector and commonly used because of its high gain, low noise and wide frequency response. A PMT is made of the following main parts: a photocathode, a photoanode and dynodes. Photons strike the photocathode, from which electrons called photoelectrons are generated because of photoelectric effect. After that, the electrons are accelerated towards a series of electrodes called dynodes, bringing about a cascade of photoelectrons. Depending on the number of dynodes present and the accelerating voltage, a single photon can generate up to 10^7 photoelectrons. This amplified signal is collected *via* the photoanode where it is measured. The PMT is illustrated in Figure 3.4.

Figure 3.4 The PMT detector

A simple PMT sketch that shows how a cascade of electrons are generated from a single photon interacting with a photocathode.

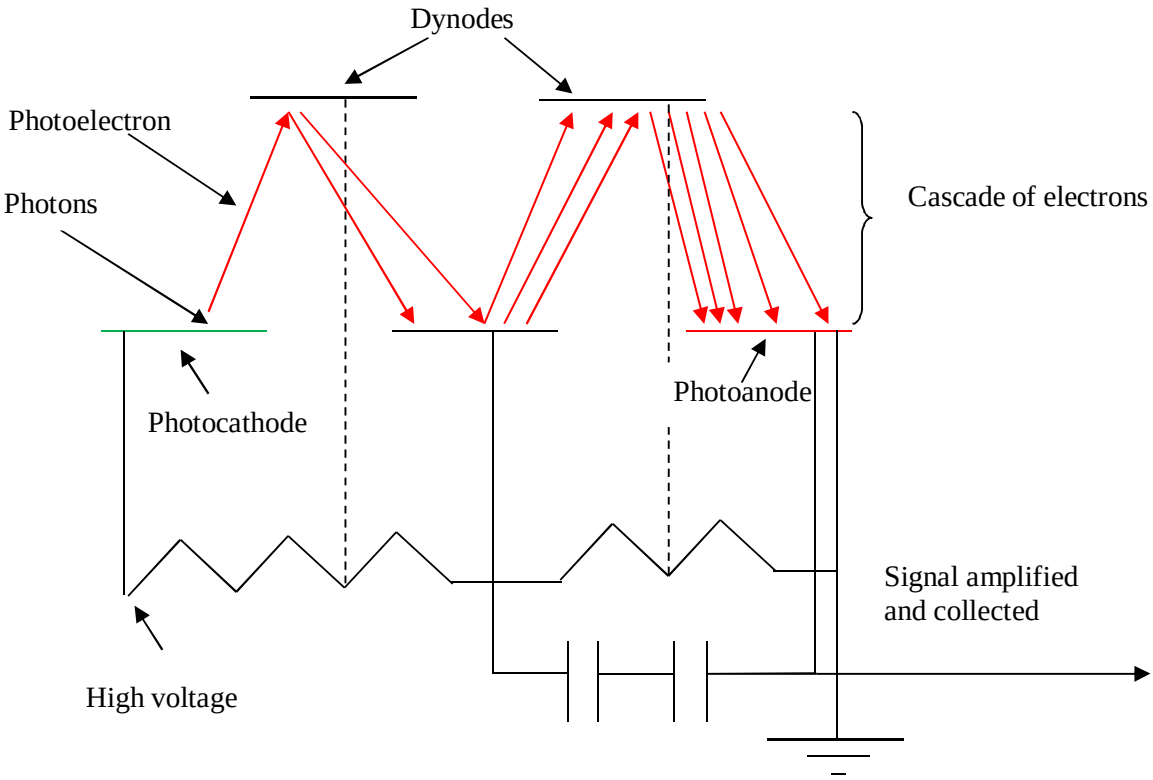

Finally, amplifiers and recorders, complete the fluorimeter by enhancing the signals obtained and processing the data acquired during the spectroscopic measurements.

The areas of the integrated fluorescence emission of the probes in different solvents (emission spectra) were measured by using Excel by subtracting the areas generated from the solvents used. Particular attention was paid for the Raman peak which is one of the major sources of errors in fluorescence measurements. Also, the first and second order peaks (due to diffraction of light when the beam interacts with the grating of the monochromators) were excluded by using appropriate limits of integration.

3.4 Results and discussion

The quantum yield measurements along with their emission and excitation spectra of 2-Ap and Pc in water and organic solvents are presented in this Chapter. Once the wavelengths of the excitation and emission spectra maxima were obtained the Stokes shifts were calculated. The Lippert plots were then generated to understand the effects of solvent polarity on 2-Ap and Pc.

3.4.1 Lippert plot of 2-Ap in organic solvents and water

The normalised excitation and emission spectra (the normalisation was calculated by considering the maximum intensity of each individual spectrum as 1) of 2-Ap in water and organic solvents and their respective Stokes shift in cm^{-1} are shown in Figure 3.5 along with the spectroscopic measurements such as the quantum yields and the maxima excitation and emission wavelengths and the measured Stokes shifts obtained from the difference between the maxima excitation and emission. The spectral parameters are also summarised in Table 3.1.

Figure 3.5 Excitation and emission spectra of 2-Ap in organic solvents and water

Normalised excitation spectra (illustrated in blue) and emission spectra (illustrated in red) of 2-Ap in water and organic solvents. The Stokes Shift (cm^{-1}) are displayed for each solvent

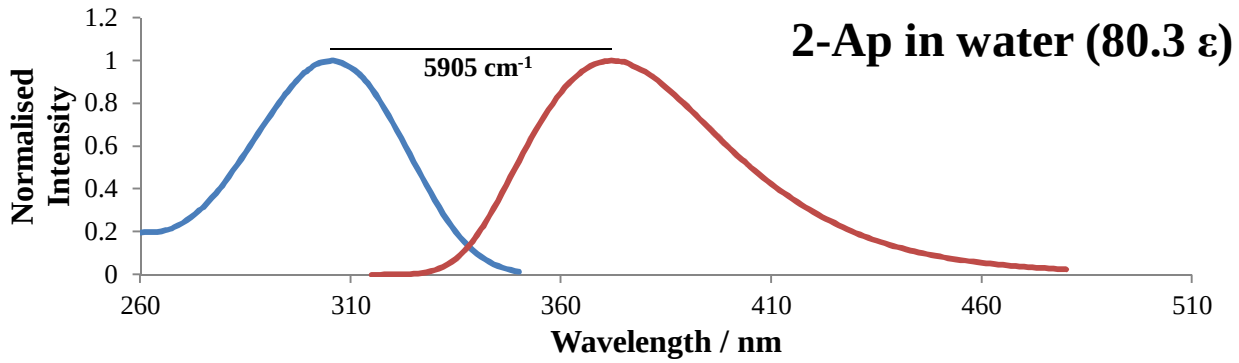

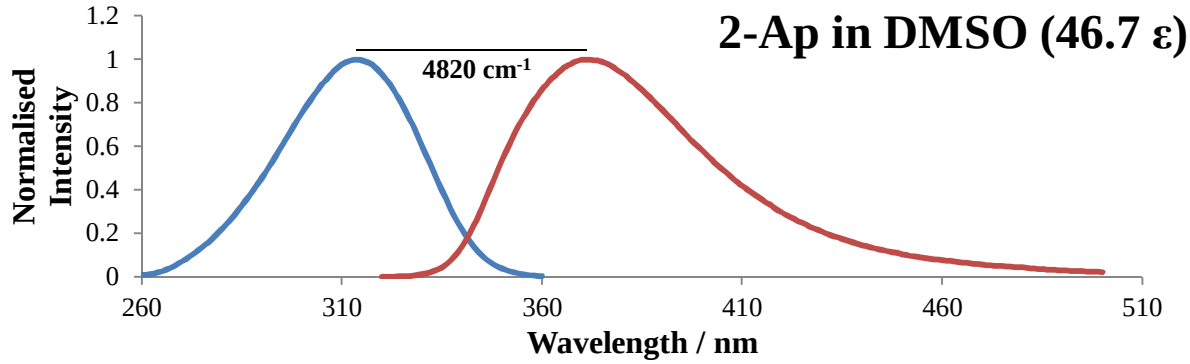
2-Ap in DMSO (46.7 ε)
4820 cm-1
Normalised Intensity
Wavelength / nm
1.2
1
0.8
0.6
0.4
0.2
0
260
310
360
410
460
510

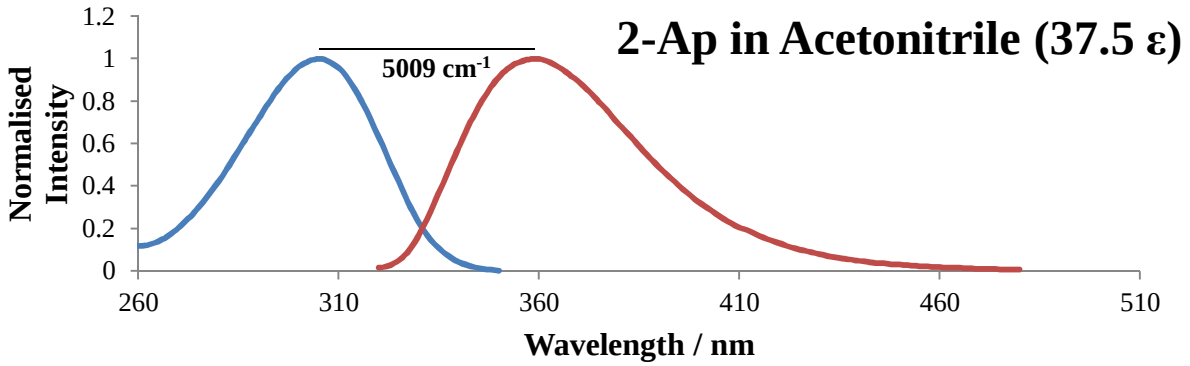
2-Ap in Acetonitrile (37.5 ε)
5009 cm-1
Normalised Intensity
Wavelength / nm
1.2
1
0.8
0.6
0.4
0.2
0
260
310
360
410
460
510

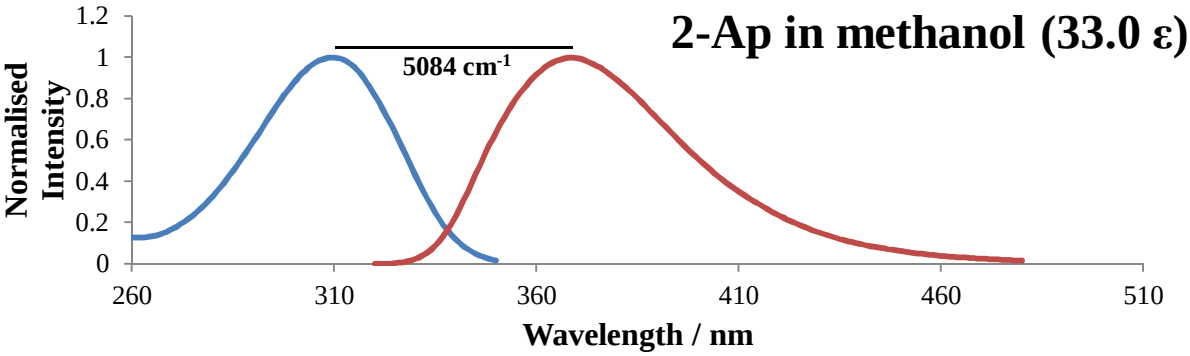
2-Ap in methanol (33.0 ε)
5084 cm-1
Normalised Intensity
Wavelength / nm
1.2
1
0.8
0.6
0.4
0.2
0
260
310
360
410
460
510

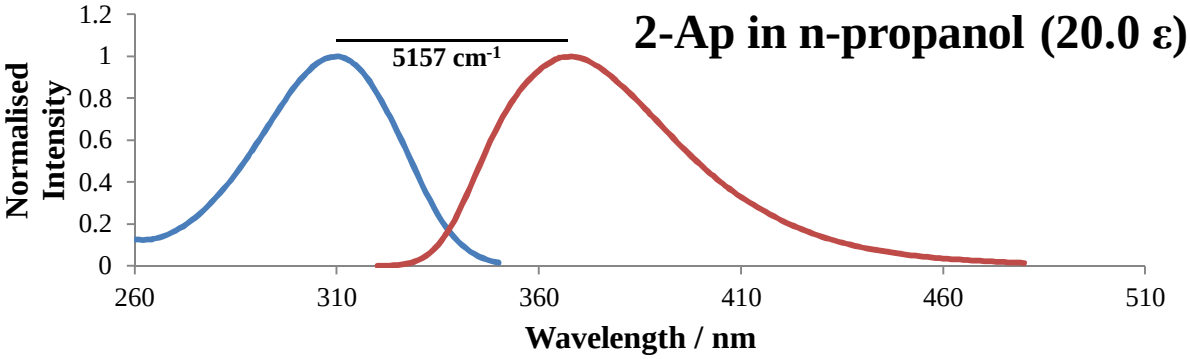
2-Ap in n-propanol (20.0 ε)
5157 cm-1
Normalised Intensity
Wavelength / nm
1.2
1
0.8
0.6
0.4
0.2
0
260
310
360
410
460
510

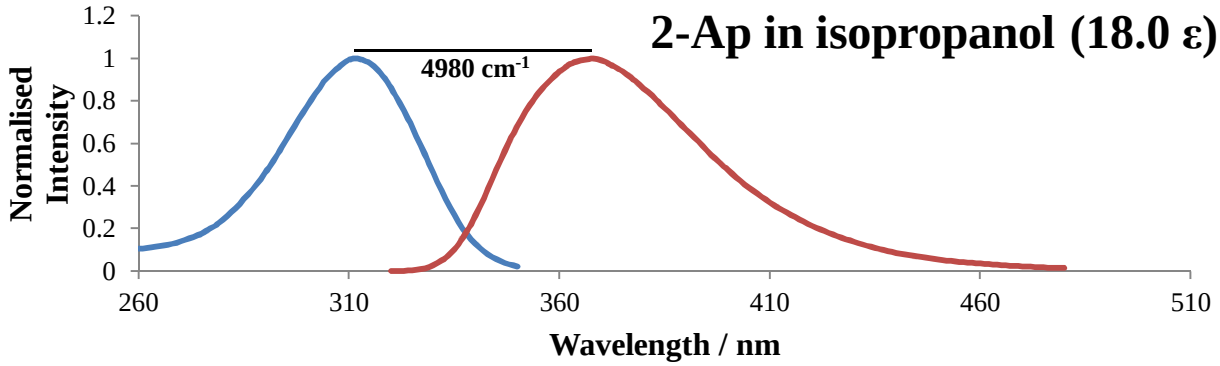
2-Ap in isopropanol (18.0 ε)
4980 cm-1
Normalised Intensity
1.2
1
0.8
0.6
0.4
0.2
0
260
310
360
410
460
510
Wavelength / nm

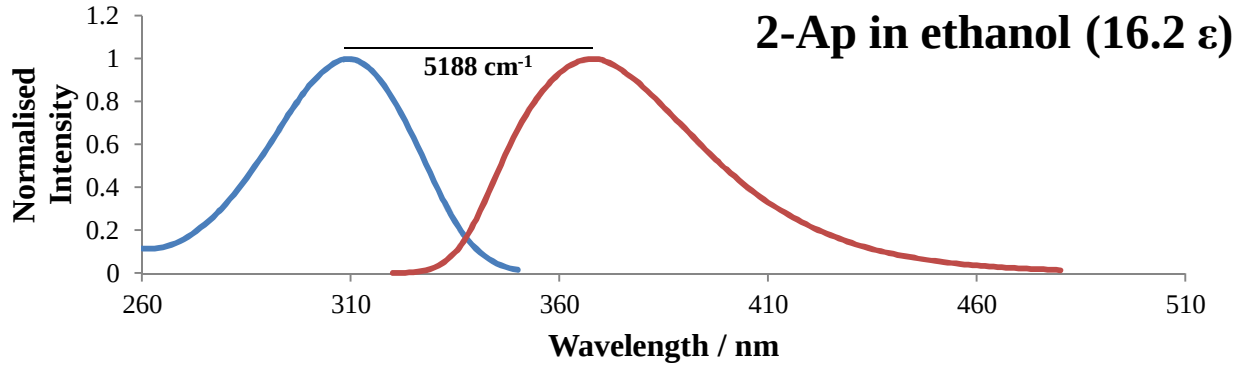
2-Ap in ethanol (16.2 ε)
5188 cm-1
Normalised Intensity
1.2
1
0.8
0.6
0.4
0.2
0
260
310
360
410
460
510
Wavelength / nm

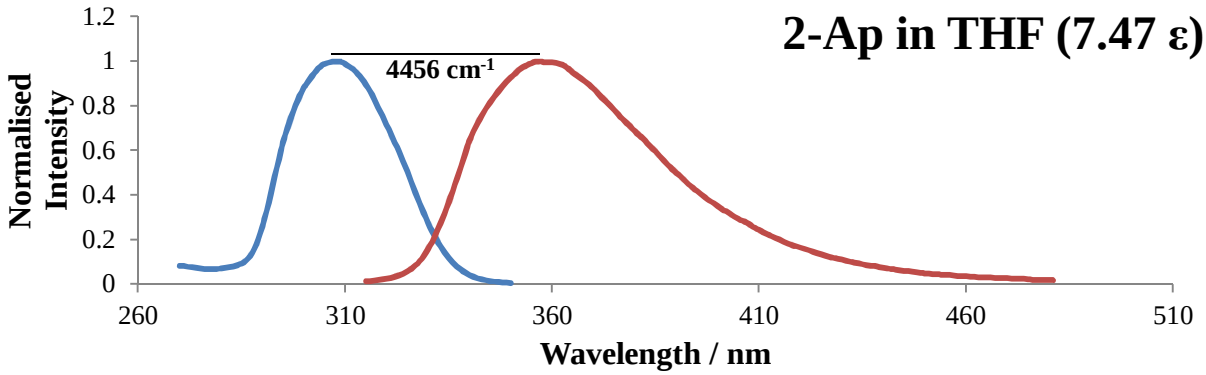
2-Ap in THF (7.47 ε)
4456 cm-1
Normalised Intensity
1.2
1
0.8
0.6
0.4
0.2
0
260
310
360
410
460
510
Wavelength / nm

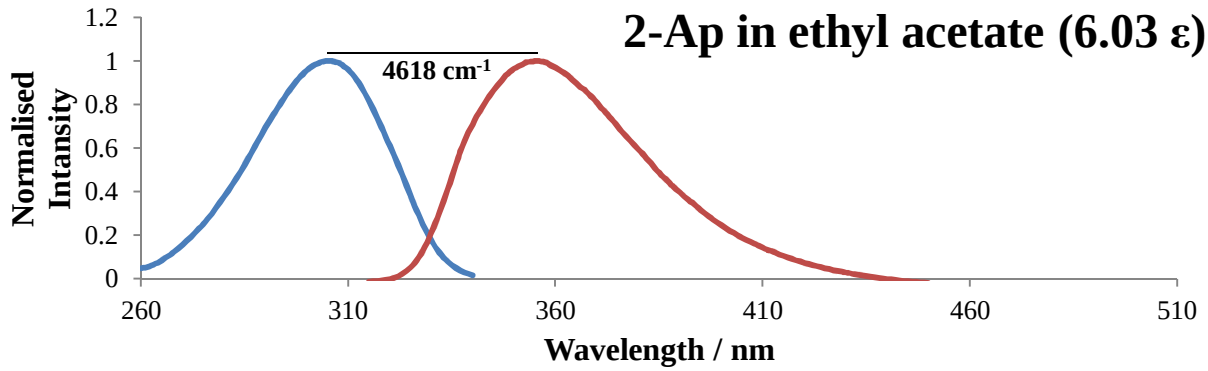
2-Ap in ethyl acetate (6.03 ε)
4618 cm-1
Normalised Intansity
1.2
1
0.8
0.6
0.4
0.2
0
260
310
360
410
460
510
Wavelength / nm

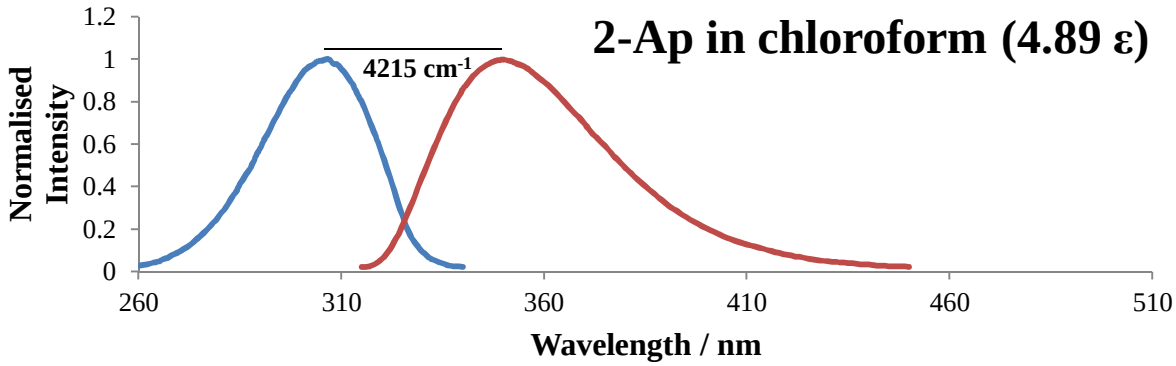

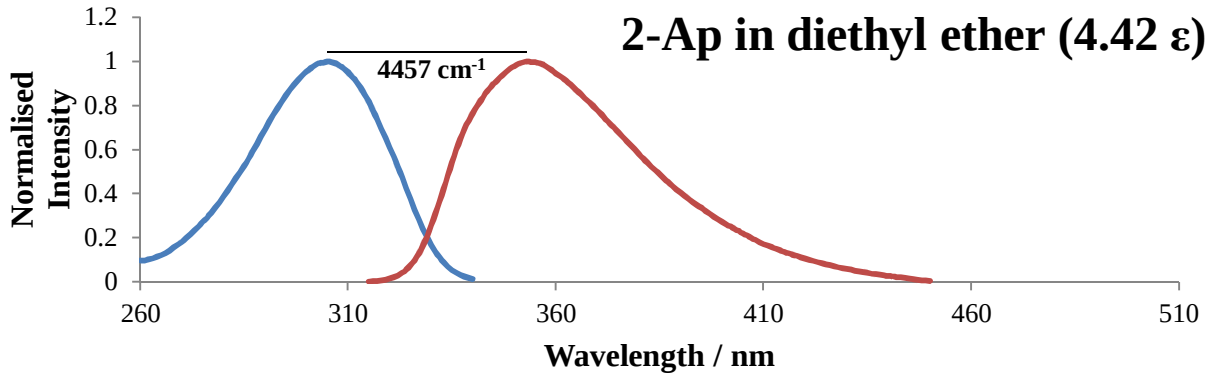

The resulting excitation spectra are reasonable mirror images (for example, see Chapter 2 Figure 2.14) of the emission spectra with exception of 2-Ap in THF where the shape of the excitation spectrum is much sharper than the shape of the emission spectrum.

Table 3.1 Spectroscopic data of 2-Ap in organic solvents and water

Φ_F, λ_{ex}, λ_{em} and the Stokes shifts of 2-Ap are shown in this table

Solvent	$\Phi_F \pm 2\sigma$	λ_{ex} ***/nm***	λ_{em} ***/nm***	$\upsilon_{ex} - \upsilon_{em}$ ***/cm^{-1} (Stokes shift)***
Methanol	0.450 ± 0.012	310.0	368.0	5084
Ethanol	0.394 ± 0.009	309.0	368.0	5188
Isopropanol	0.409 ± 0.012	311.0	368.0	4980
n-propanol	0.505 ± 0.010	310.0	369.0	5157
Acetonitrile	0.095 ± 0.008	305.0	360.0	5009
DMSO	0.292 ± 0.008	314.0	370.0	4820
Water	0.686 ± 0.016	305.0	372.0	5905
THF	0.144 ± 0.005	308.0	357.0	4456
Chloroform	0.129 ± 0.004	305.0	350.0	4215
Ethyl Acetate	0.122 ± 0.003	305.0	355.0	4618
Diethyl Ether	0.112 ± 0.006	305.0	353.0	4457

The excitation and emission maxima along with the Stokes shifts of diethyl ether, ethyl acetate, n-propanol, methanol, DMSO and water in Table 3.1 are in agreement with the literature (Evans *et al*. 1992). Also, the obtained quantum yield measurements of 2-Ap in water (0.686 ± 0.016) and methanol (0.450 ± 0.012) are in accordance with two different articles found in the literature, respectively 0.660 and 0.440 (Holmen *et al*. 1997; Hogendorf *et al*. 2009). The quantum yield measurements of 2-Ap in solvents except for water and methanol on the other hand have not been, to the best of our knowledge, previously reported. The Table 3.2, shown below contains the values of the dielectric constants (ε), refractive index (η) and dipole moments (μ) for the various solvents (Reichardt, 1990; Lide, 2000), and the orientation polarizability, Δf, calculated by using the dielectric constant and refractive index values into the equation 3.2.

Table 3.2 Parameters of organic solvents and water

The refractive index η, dielectric constant ε, dipole moment μ of the solvent and orientation polarizability, Δf, as defined in equation 3.2

Solvent	***η (at 20℃)***	***ε (at 20℃)***	***μ /D***	$\Delta f = \left(\frac{\varepsilon-1}{2\varepsilon+1} - \frac{\eta^2-1}{2\eta^2+1}\right)$
Methanol	1.3290	33.0	1.70	0.3086
Ethanol	1.3600	16.2	1.69	0.2743
Isopropanol	1.3770	18.0	1.58	0.2725
n-propanol	1.3840	20.0	1.55	0.2740
Acetonitrile	1.3440	37.5	3.93	0.3054
DMSO	1.4790	46.7	3.96	0.2206
Water	1.3330	80.3	1.86	0.3202
THF	1.4060	7.47	1.69	0.2087
Chloroform	1.4460	4.89	1.02	0.1503
Ethyl Acetate	1.3720	6.03	1.78	0.1999
Diethyl Ether	1.3520	4.42	1.11	0.1697

Plotting the Stokes shift values against the orientation polarizability values, the Lippert plot was drawn and is shown in Figure 3.6.

Figure 3.6 Lippert plot of 2-Ap

The Lippert plot of 2-Ap in water and organic solvents generated by plotting the Stokes shift values against the orientation polarizability values

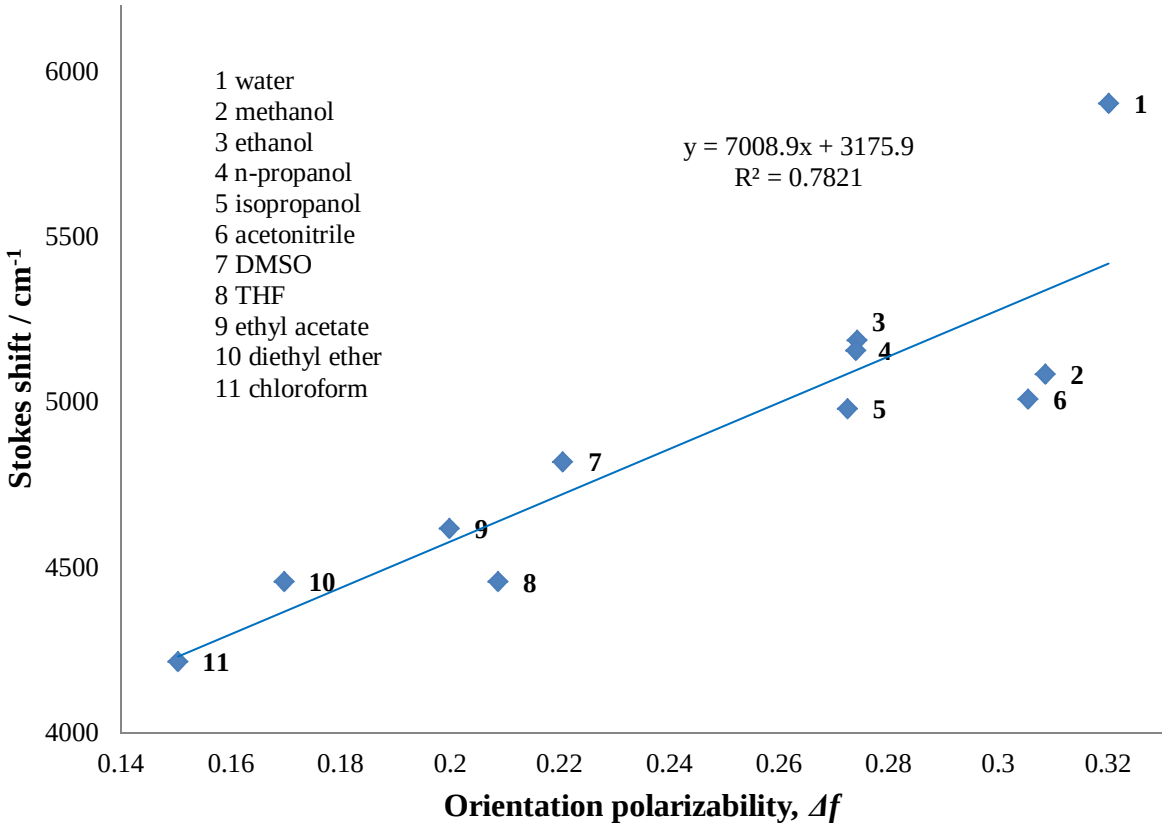

The regression coefficient (R^2) was found to be ~ 0.80 a reasonable correlation among the points. Lippert suggested a regression coefficient of ≥ 0.80 as an indicator of satisfactory linearity (Lippert, 1957; Parker, 1968). The points (3), (4) and (5) which are the protic solvents ethanol, n-propanol and isopropanol, were found to have very similar Stokes shifts as expected given their similar physical properties and Δf values. Water (1) along with acetonitrile (6) deviate somehow from the linear trend. Water possesses the largest Stokes shift (5905 cm^{-1}) among all the points whereas chloroform has the smallest Stokes shift (4215 cm^{-1}). The Figure 3.7 displays the 2-Ap Lippert plots of the protic and aprotic solvents as separate group.

Figure 3.7 2-Ap Lippert plots (protic and aprotic solvents considered)

The 2-Ap Lippert plots considering protic (green squares) and aprotic (red triangles) solvents are shown

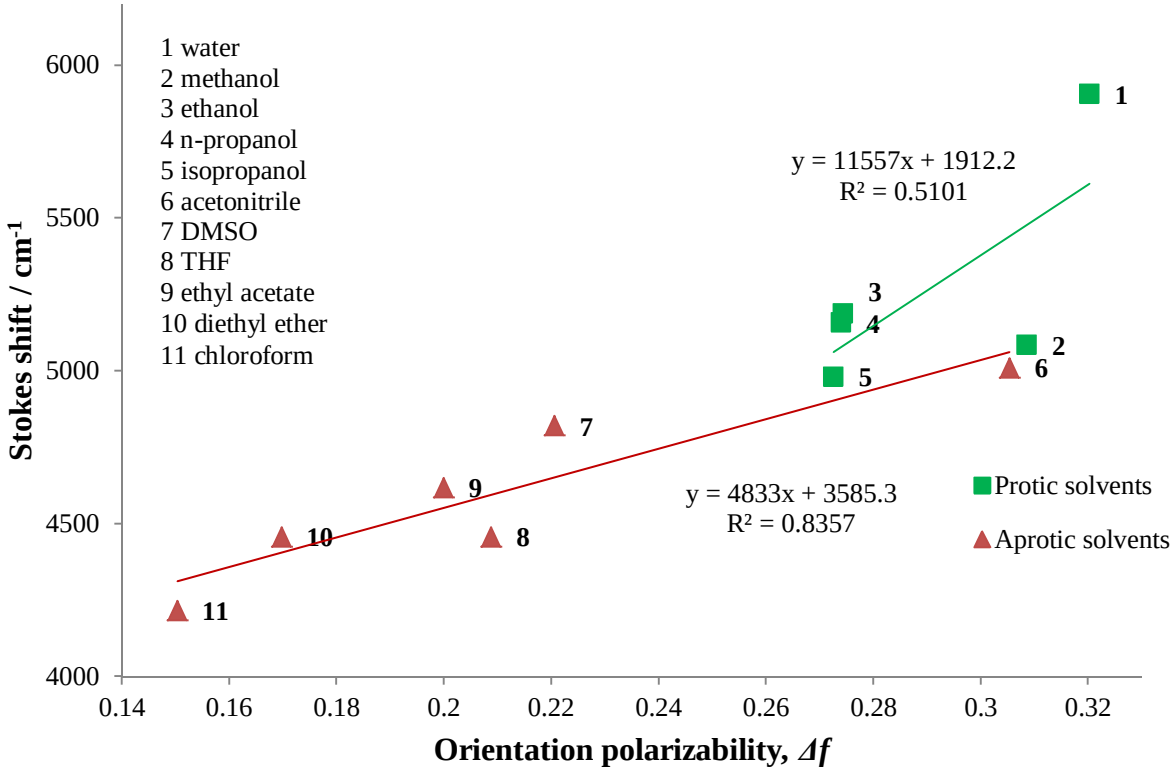

The correlation among the points of the Lippert plot of 2-Ap in protic solvents, Figure 3.7, is poor. Poor linearity between protic solvents may signify that the nature of protic solvents is more important than the value of their respective dielectric constant (general solvent effects) or that somehow water is much more efficient at forming hydrogen bonds with 2-Ap (specific solvent effects) than alcohol molecules even though alcohols themselves can also form hydrogen bonds. Smagowicz and Wierzchowski observed a large difference in spectral shifts of 2-Ap in water compared to alcohols (they used methanol, n-propanol and butanol) considering water a better proton-doning solvent (Smagowicz and Wierzchowski, 1974). A reasonable correlation among the aprotic points was found. The Figure 3.8 illustrates the relationship between quantum yields and Stokes shifts.

Figure 3.8 2-Ap quantum yields against stokes shifts

Plotting the quantum yield measurements of 2-Ap against the Stokes shifts

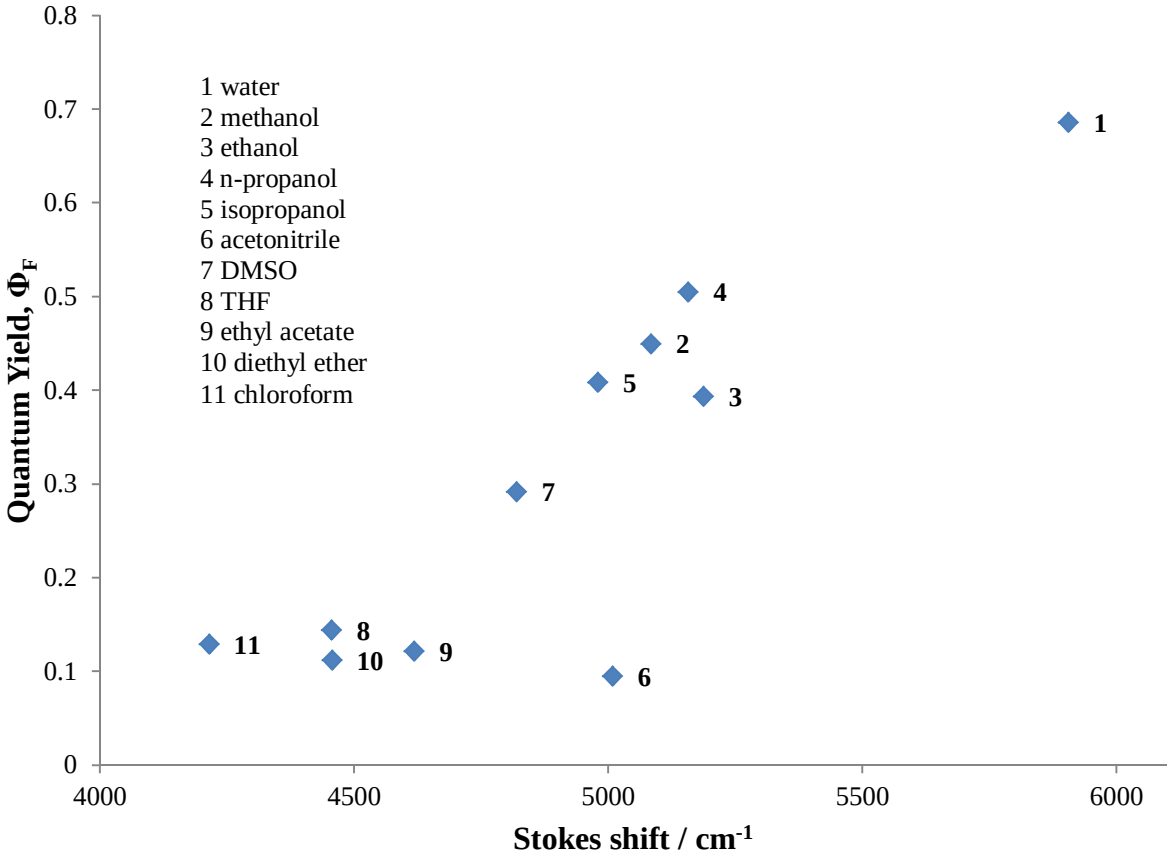

From Figure 3.8 no clear mathematical relationship between the Stokes shifts and the quantum yield measurements can be observed among the points. It can be seen that the quantum yields and Stokes shifts of 2-Ap in protic solvents are larger than the ones measured in aprotic solvents but no clear trend between protic and aprotic solvents was found. Since protic solvents, especially water, are likely to form hydrogen bonds with 2-Ap which would result in specific solvent effects, quantum yields of 2-Ap in different water-acetonitrile mixtures (volume percentage mixtures, acetonitrile is completely miscibile in water) were measured. Any drastic change in Stokes shifts of a protic-non-protic mixture should confirm specific solvent effects. The Stokes shift values obtained along with the calculated orientation polarizability values of water-acetonitrile mixtures, Table 3.3 and 3.4, were plotted to generate another Lippert plot as illustrated in Figure 3.9.

Table 3.3 Spectroscopic data of 2-Ap in water-acetonitrile mixtures

Φ_F, λ_{ex}, λ_{em} and Stokes shift of 2-Ap in water-acetonitrile mixtures (volume percentage mixtures)

Solvent acetonitrile:water	$\Phi_F \pm 2\sigma$	***λ_{ex} /nm***	***λ_{em} /nm***	***$\upsilon_{ex} - \upsilon_{em}$ /cm^{-1} (Stokes shift)***
100 : 0	0.095 ± 0.008	305.0	360.0	5009
90 : 10	0.329 ± 0.010	307.0	365.0	5176
80 : 20	0.397 ± 0.008	308.0	367.0	5219
70 : 30	0.411 ± 0.008	308.0	369.0	5367
60 : 40	0.466 ± 0.012	308.0	369.0	5367
50 : 50	0.494 ± 0.010	308.0	369.0	5367
40 : 60	0.542 ± 0.010	307.0	370.0	5546
30 : 70	0.562 ± 0.009	307.0	370.0	5546
20 : 80	0.604 ± 0.009	307.0	371.0	5619
10 : 90	0.645 ± 0.014	306.0	371.0	5725
0 : 100	0.686 ± 0.016	305.0	372.0	5905

The Table 3.4 shows the refractive indexes of the mixtures calculated with the Lorentz-Lorenz formula for binary liquid mixtures, see equation 3.17 (Mehra, 2003).

$$\frac{\eta^2 - 1}{\eta^2 + 2} = V_1 \frac{\eta_1^2 - 1}{\eta_1^2 + 2} + V_2 \frac{\eta_2^2 - 1}{\eta_2^2 + 2} \quad \textbf{(3.17)}$$

Equation 3.17 contains the refractive indexes of the two mixture components, η_1 and η_2 with the volume fractions, V_1 and V_2 and η is the reference refractive index for the mixture. The dielectric constant values of the components have been obtained from the literature (Gagliardi *et al.* 2007) and the orientation polarizability values calculated *via* the formula displayed in the Table 3.4.

Table 3.4 Parameters of water-acetonitrile mixtures

The refractive index values, the dielectric constant values and the orientation polarizability values of water-acetonitrile mixtures

Solvent acetonitrile:water	***η (at 20 ℃)***	***ε (at 20 ℃)***	$\Delta f = \left(\frac{\varepsilon - 1}{2\varepsilon + 1} - \frac{\eta^2 - 1}{2\eta^2 + 1}\right)$
100 : 0	1.3440	37.5	0.3054
90 : 10	1.3426	40.4	0.3074
80 : 20	1.3410	43.9	0.3106
70 : 30	1.3396	47.6	0.3113
60 : 40	1.3384	52.2	0.3131
50 : 50	1.3369	56.9	0.3148
40 : 60	1.3355	62.0	0.3164
30 : 70	1.3340	67.1	0.3179
20 : 80	1.3328	72.0	0.3191
10 : 90	1.3314	75.8	0.3197
0 : 100	1.3300	80.3	0.3202

The Lippert plot of 2-Ap in water-acetonitrile mixtures is illustrated in Figure 3.9. The plot was generated from the data shown in the Tables 3.3 and 3.4. The Lippert plot shows a non-linear behaviour, a behaviour which implies the presence of specific solvent effect (hydrogen bonding) along with general solvent effects (polarity effects). In fact, a large increase in Stokes shift is recorded when water is added to acetonitrile (from 5009 cm^{-1} to 5176 cm^{-1}). Also, the quantum yield measurement of 90 : 10 acetonitrile-water mixture increases much more in proportion to the other water-acetonitrile mixture, see Table 3.3.

Drastic changes in Stokes shifts of other compounds in non-polar solvents (2-Anilinonaphatalene in cyclohexane and 2-Acetylantharacene in hexane) were observed when small quantities (3-4 % volume to volume) of polar solvents (ethanol and methanol) were added and these drastic changes in emission spectra maxima were attributed to specific solvent effects, specifically hydrogen bonding formation (Cherkasov, 1960; Brand *et al*. 1971; Tamaki, 1980; Tamaki, 1982).

Figure 3.9 Lippert plot of 2-Ap in water-acetonitrile

Lippert plot of 2-Ap in water-acetonitrile mixtures (volume percentage mixtures). Polynomial function (grade 3) software used Excel

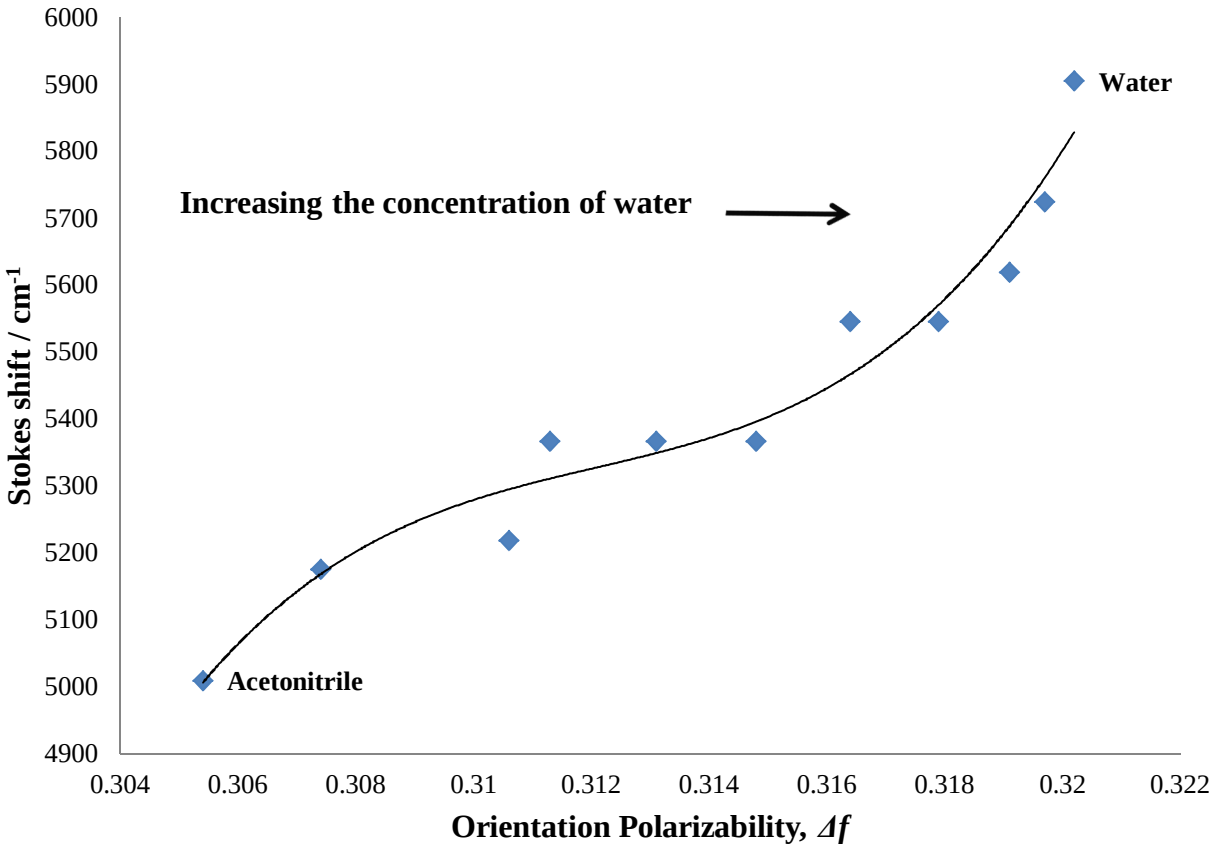

3.4.2 Calculation of 2-Ap Δμ

The difference in dipole moment Δμ between the excited state dipole moment and the ground state dipole moment can be calculated by using the slope of the 2-Ap Lippert plot in Figure 3.6. Thus, from the Lippert equation 3.1 the slope is equal to:

$$\text{slope} = \frac{2\Delta\mu^2}{hca^3} \quad (3.18)$$

Since the slopes obtained from the Lippert plots are in cm^{-1} the cgs units are to be adopted to calculate the difference in dipole moment Δμ in Debyes (D). Then, the Plack's constant h and the speed of light c are respectively 6.626 x 10^{-27} erg s, 2.9979 x 10^{10} cm s^{-1}. The cavity radius a is given in Angstroms Å (1 Å = 10^{-8} cm) and it was theoretically calculated to be 4.03 Å; the cavity radius of the optimized geometry of 2-Ap N9H amino tautomer in the gas phase, as shown in Section 4.5 Table 4.3. The Table 3.5 shows the difference in dipole moment of 2-Ap between excited and ground states using three different slopes (all solvents, protic solvents and aprotic solvents) obtained from the Lippert plots shown in the Figures 3.6 and 3.7.

Table 3.5 Difference in dipole moment of 2-Ap in different solvents

This table shows the difference in dipole moment between the excited state and the ground state of 2-Ap in different solvents. The slope and the regression coefficient obtained from three different Lippert plots are also reported

2-Ap Lippert plot in different solvents	All solvents considered	Protic solvents considered	Aprotic solvents considered
Slope of the Lippert plot (cm^{-1})	7008.9 ± 1233.3	11557.0 ± 6539.11	4833.0 ± 1071.7
R^2 (regression coefficient)	0.7821	0.5101	0.8357
Δμ (difference in dipole moment) D	**6.75 ± 0.62**	**8.67 ± 2.96**	**5.60 ± 0.66**

The experimentally calculated difference in dipole moment between the excited state and the ground state of 2-Ap in aprotic solvents (best regression coefficient among the plots reported) was found to be 5.60 D, see Table 3.5. This difference in dipole moments is reasonably in agreement with the one found by Evans and others (Evans *et al*. 1992). They stated a Δμ of about 5.00 D with a cavity radius of 3.8 Å using the following solvents: 1-4- dioxane, ethyl ether, ethyl acetate, butanol, 1-propanol, methanol, DMSO, water and glycerol-water mixtures. The plot they obtained (correlation coefficient not given) was generated by excluding water and DMSO. The experimental $\Delta\mu_e$ = 5.60 D results to be larger than the theoretical one $\Delta\mu_t$ = - 0.09 D (3.16 - 3.25), see Section 4.7.1 Table 4.10

3.4.3 Lippert plot of Pc in organic solvents and water

As in the case of 2-Ap the normalised excitation and emission spectra of Pc in water and organic solvents (the normalisation was calculated by considering the maximum intensity as 1) are shown in Figure 3.10 along with the spectroscopic measurements such as the quantum yields and the Stokes shifts obtained from the difference between the maxima excitation and emission contained in Table 3.6.

Figure 3.10 Excitation and emission spectra of Pc in organic solvents and water

Normalised excitation spectra (illustrated in blue) and emission spectra (illustrated in red) of Pc in water and organic solvents. The Stokes Shift (cm-1) are displayed for each solvent

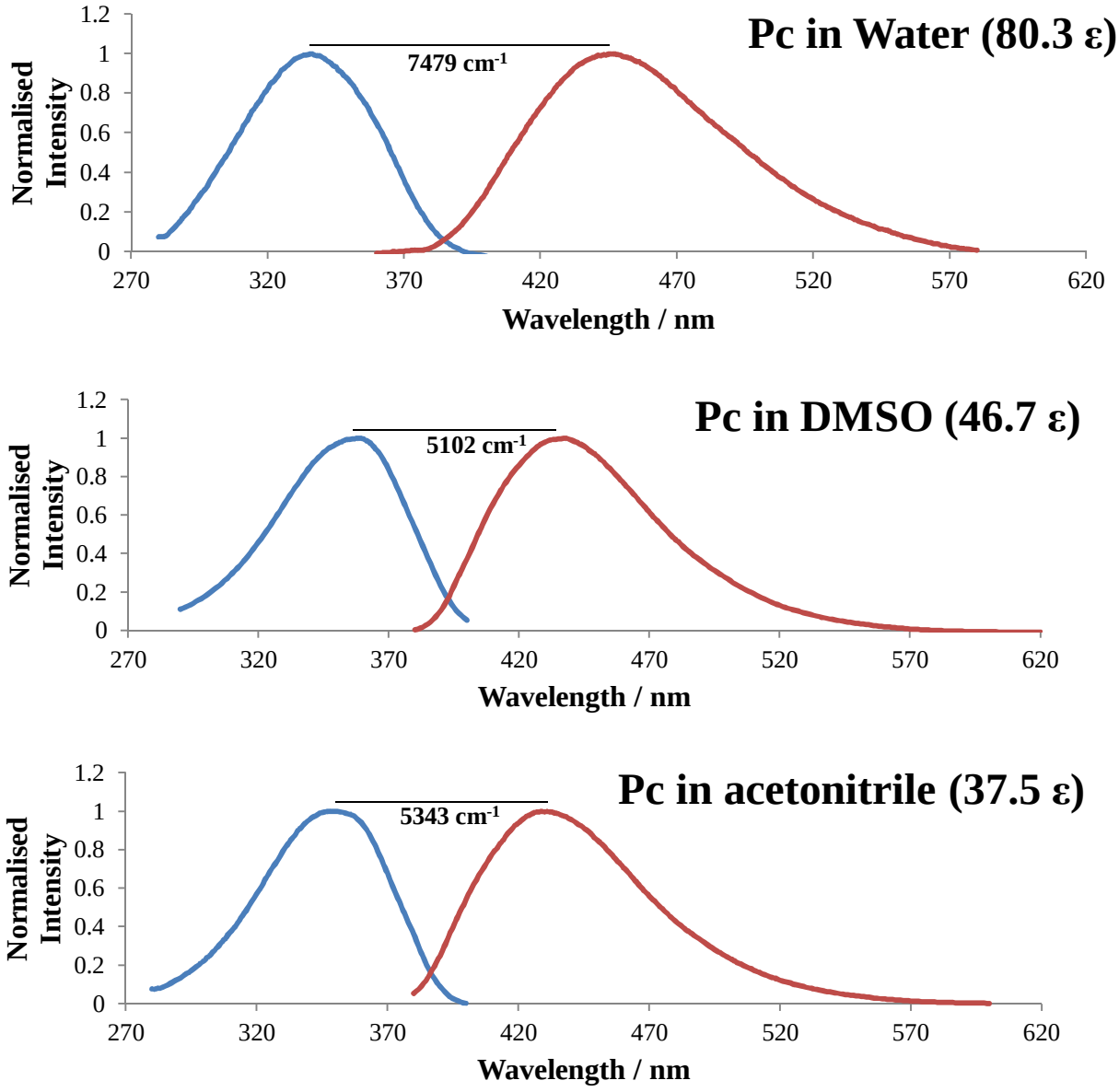

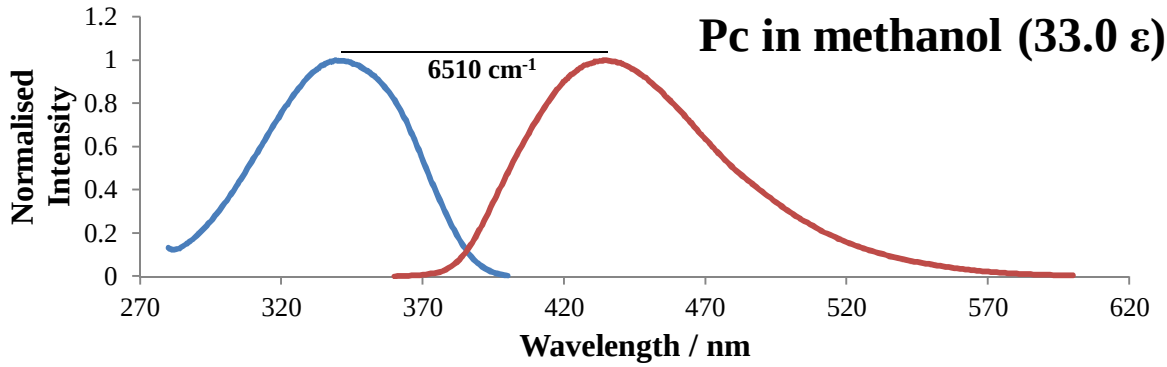
Pc in methanol (33.0 ε)
6510 cm-1
Normalised Intensity
Wavelength / nm

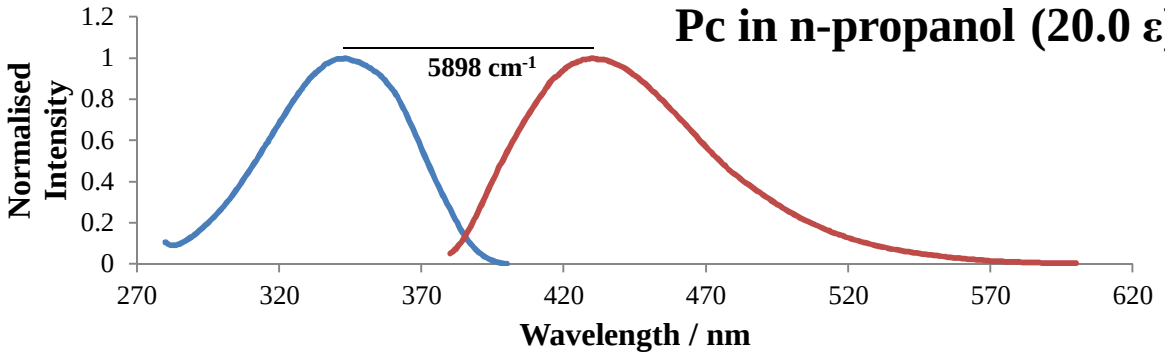
Pc in n-propanol (20.0 ε)
5898 cm-1
Normalised Intensity
Wavelength / nm

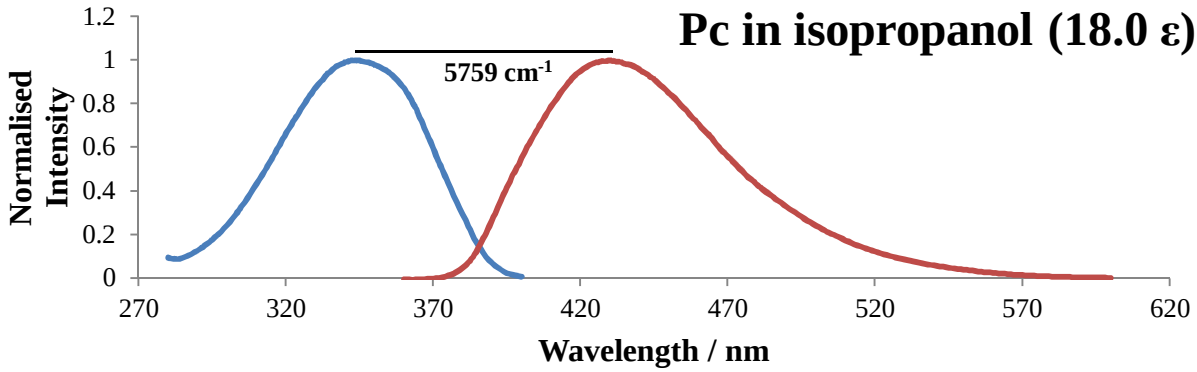
Pc in isopropanol (18.0 ε)
5759 cm-1
Normalised Intensity
Wavelength / nm

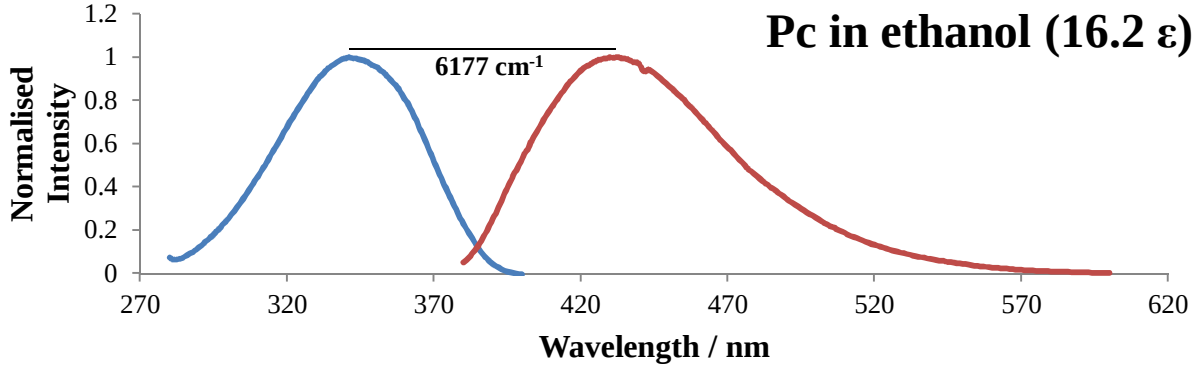
Pc in ethanol (16.2 ε)
6177 cm-1
Normalised Intensity
Wavelength / nm

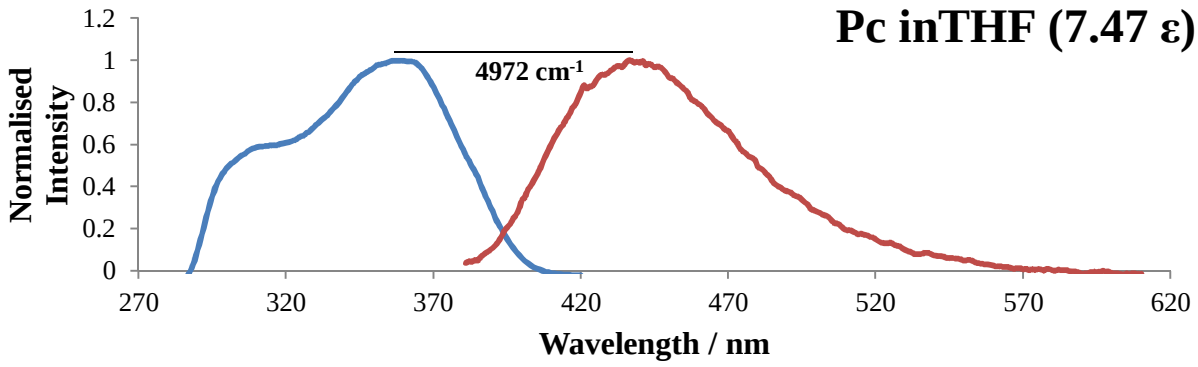
Pc inTHF (7.47 ε)
4972 cm-1
Normalised Intensity
1.2
1
0.8
0.6
0.4
0.2
0
270
320
370
420
470
520
570
620
Wavelength / nm

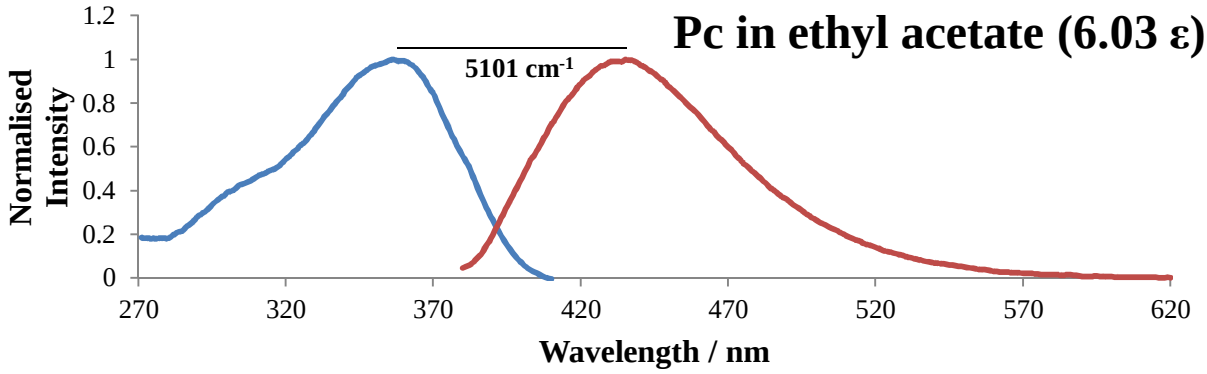
Pc in ethyl acetate (6.03 ε)
5101 cm-1
Normalised Intensity
1.2
1
0.8
0.6
0.4
0.2
0
270
320
370
420
470
520
570
620
Wavelength / nm

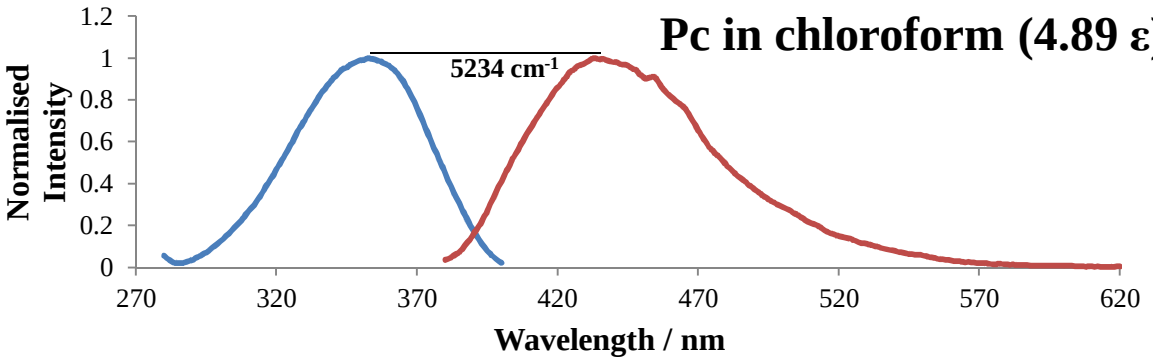
Pc in chloroform (4.89 ε)
5234 cm-1
Normalised Intensity
1.2
1
0.8
0.6
0.4
0.2
0
270
320
370
420
470
520
570
620
Wavelength / nm

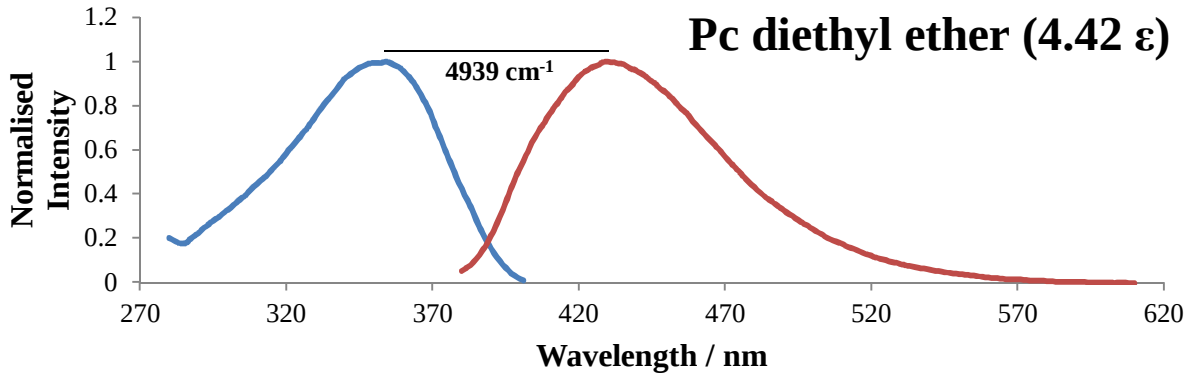
Pc diethyl ether (4.42 ε)
4939 cm-1
Normalised Intensity
1.2
1
0.8
0.6
0.4
0.2
0
270
320
370
420
470
520
570
620
Wavelength / nm

As already observed with 2-Ap in THF the excitation spectrum of Pc in THF is not the mirror image of the corresponding emission spectrum. The excitation spectrum appears not to be as structureless as the emission spectrum. Also, the excitation spectrum of Pc in ethyl acetate appears to have a little hump within the 290-320 nm region of the spectrum which was not revealed in the emission spectrum. Striking differences in the shapes of the excitation and emission spectra may be due to many factors. Normally, broader and featureless spectra may be indicative of hydrogen bonding formation in the excited states whereas sharper and more-structured spectra may suggest absence of hydrogen bonding formation (Han and Zhao, 2011).

The absorption and excitation spectra are usually superimposable when there is only a single species in the ground state. If more than one species is present or when the one single species is present in different forms such as aggregates and complexes or even tautomers the absorption and excitation spectra may no longer be superimposable (Matei *et al*. 2010). The excitation and absorption spectra (the absorption spectra are shown in Chapter 4) were compared with special attention to 2-Ap and Pc in THF but no particular displacement or change in shape was observed. Nevertheless, it should be noted that the absorption and excitation spectra can still be superimposable even in the presence of different species if these species have a very close or identical energy in the ground state.

Table 3.6 Spectroscopic data of Pc in organic solvents and water

Φ_F, λ_{ex}, λ_{em} and the Stokes shift values of Pc in water and organic solvents

Solvent	$\Phi_F \pm 2\sigma$	λ_{ex} ***/nm***	λ_{em} ***/nm***	$\upsilon_{ex} - \upsilon_{em}$ ***/cm^{-1} (Stokes shift)***
Methanol	0.207 ± 0.010	339.0	435.0	6510
Ethanol	0.302 ± 0.004	341.0	432.0	6177
Isopropanol	0.312 ± 0.010	344.0	429.0	5759
n-propanol	0.332 ± 0.004	343.0	430.0	5898
Acetonitrile	0.175 ± 0.006	349.0	429.0	5343
DMSO	0.456 ± 0.012	358.0	438.0	5102
Water	0.044 ± 0.004	335.0	447.0	7479
THF	0.076 ± 0.003	359.0	437.0	4972
Chloroform	0.105 ± 0.006	353.0	433.0	5234
Ethyl Acetate	0.125 ± 0.003	356.0	435.0	5101
Diethyl Ether	0.095 ± 0.009	354.0	429.0	4939

The Stokes shifts contained in the table 3.6 were plotted against the solvent parameters in the Table 3.2 in order to generate the Pc Lippert plot shown in Figure 3.11.

Figure 3.11 Lippert plot of Pc

The Lippert plot of Pc in water and organic solvents

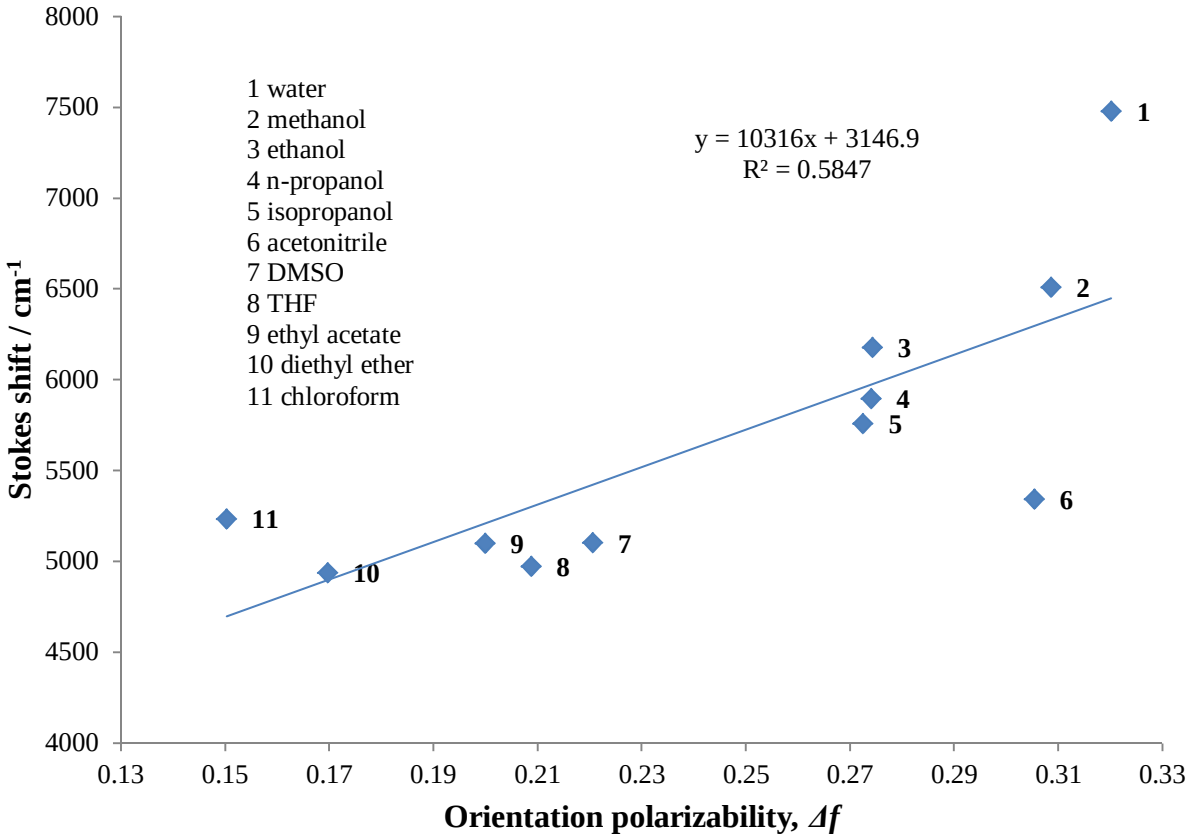

Unlike, the 2-Ap Lippert plot (see Figure 3.6) a slightly poor correlation (R^2 ~ 0.6) among the points was found for the Pc Lippert plot as displayed in Figure 3.11. The poor correlation is mainly due to the scattering of the points representing water (1) and acetonitrile (6) as they clearly diverge in opposite directions from the other points. The slope is bigger than the one of 2-Ap indicating a higher sensitivity to the solvents studied. Like 2-Ap, Pc in water has the largest Stokes shift. Figure 3.12 illustrates the Pc Lippert plots of protic and aprotic solvents.

Figure 3.12 Pc Lippert plots (protic and aprotic solvents considered)

The Pc Lippert plots considering protic (green squares) and aprotic (red triangles) solvents are shown

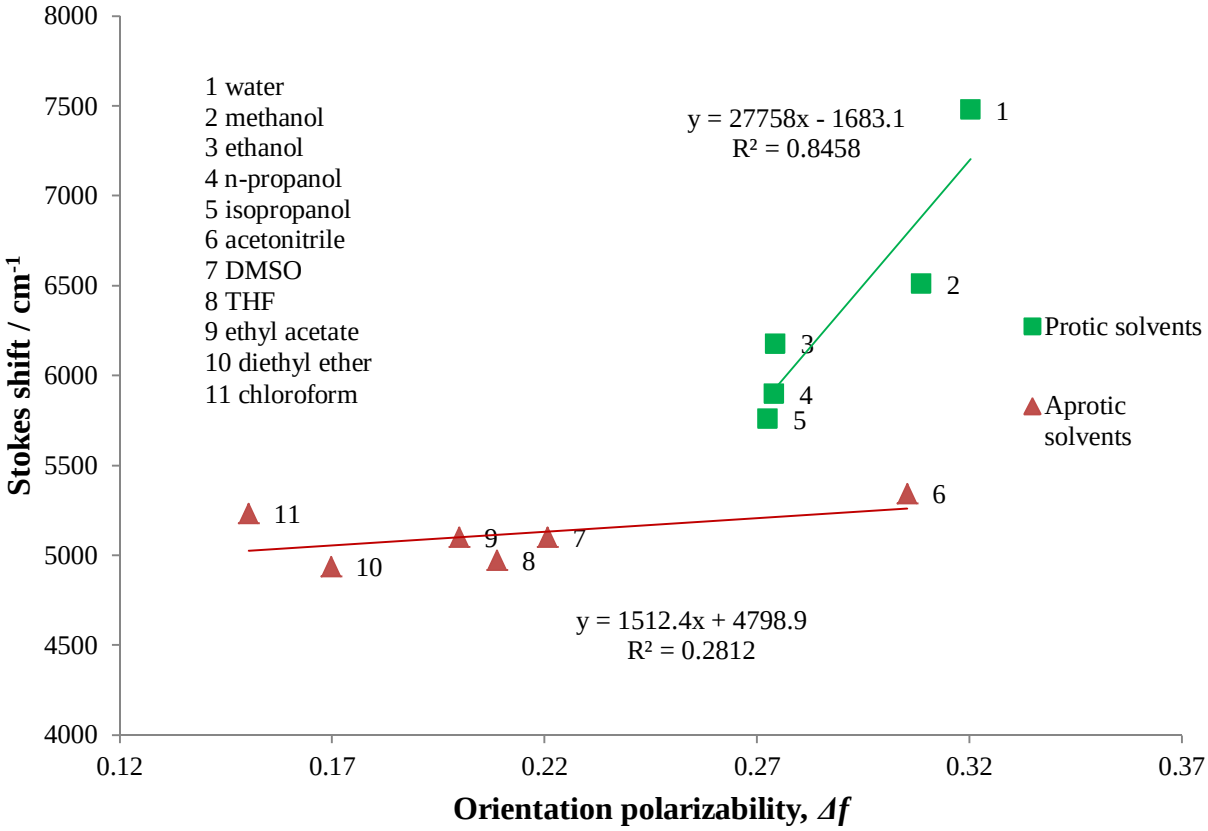

The plots obtained deserve particular attention because they are in contrast with the ones generated for 2-Ap (see Figure 3.7). A good correlation coefficient was found for Pc measured in protic solvents ($R^2 > 0.80$). This good correlation is usually unexpected when dealing with solvents capable of hydrogen bonds with the fluorophore. A possible explanation is that, unlike for 2-Ap, the protic solvents used with Pc may equally participate in hydrogen bonding formation (specific solvent effects) with the fluorophore and therefore, the good linearity and large slope value obtained would be simply caused by the difference in dielectric constant (general solvent effect) within the solvents. Even a more puzzling slope is the one obtained from Pc in aprotic solvents. Unlike, the Lippert plot of 2-Ap in aprotic solvents as shown in Figure 3.7 which has a reasonable regression coefficient $R^2 = 0.8357$, a very poor correlation was found for Pc in aprotic solvents, $R^2 = 0.2812$.

It should be noted that the slope for Pc in aprotic solvents appears to be almost flat with a very poor correlation as already mentioned and the slope is very small in spite of the inclusion of DMSO (7) and acetonitrile (6) which have high dielectric constants, but the slope appears to be flat only if compared with the one generated from the protic solvents. If the Lippert plot of Pc in aprotic solvents is reported alone as displayed in Figure 3.13, then the highlighted very poor fit to a linear function shows a slope which does not look flat anymore.

Figure 3.13 Pc Lippert plot (aprotic solvents considered only)

Highlighted Lippert plot of Pc in aprotic solvents, the slope does no longer appear as a horizontally flat slope

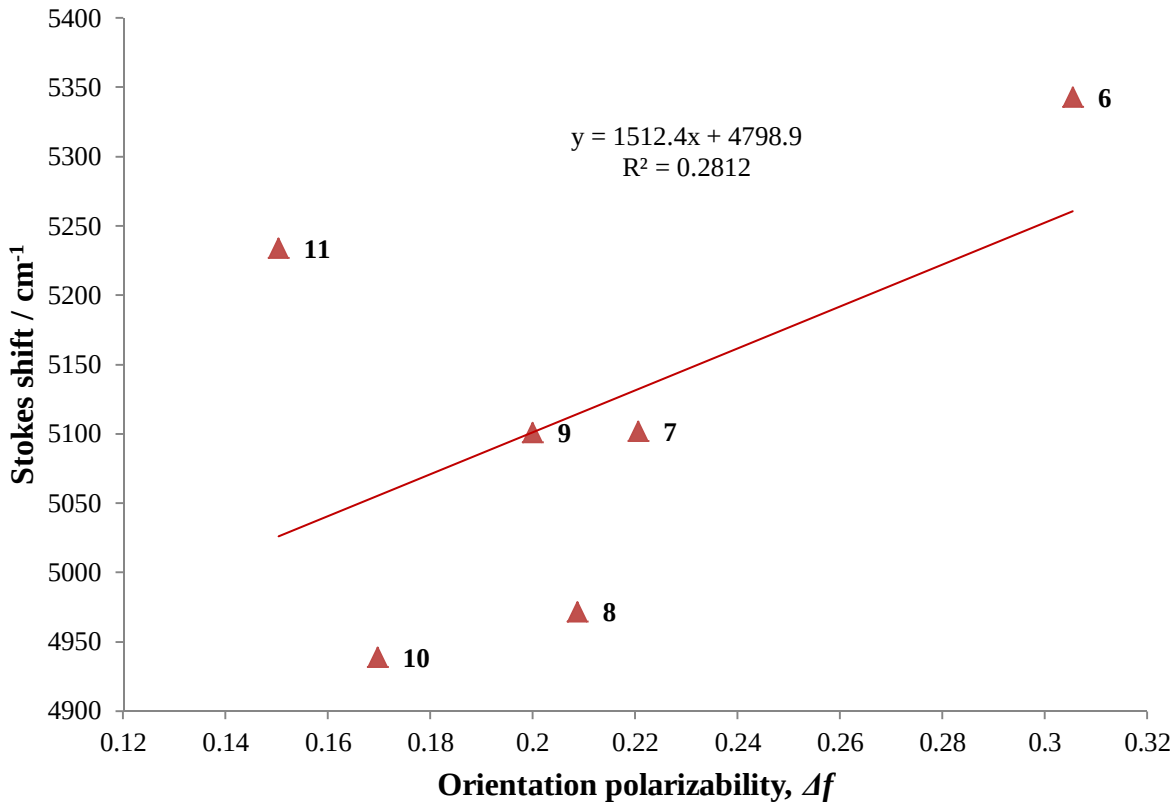

As in the case of 2-Ap, see Figure 3.8, the quantum yield measurements of Pc in different solvents were plotted against the Stokes shifts as shown in Figure 3.14.

Figure 3.14 Pc quantum yields against stokes shifts

Plotting the quantum yield measurements of Pc against the Stokes shifts

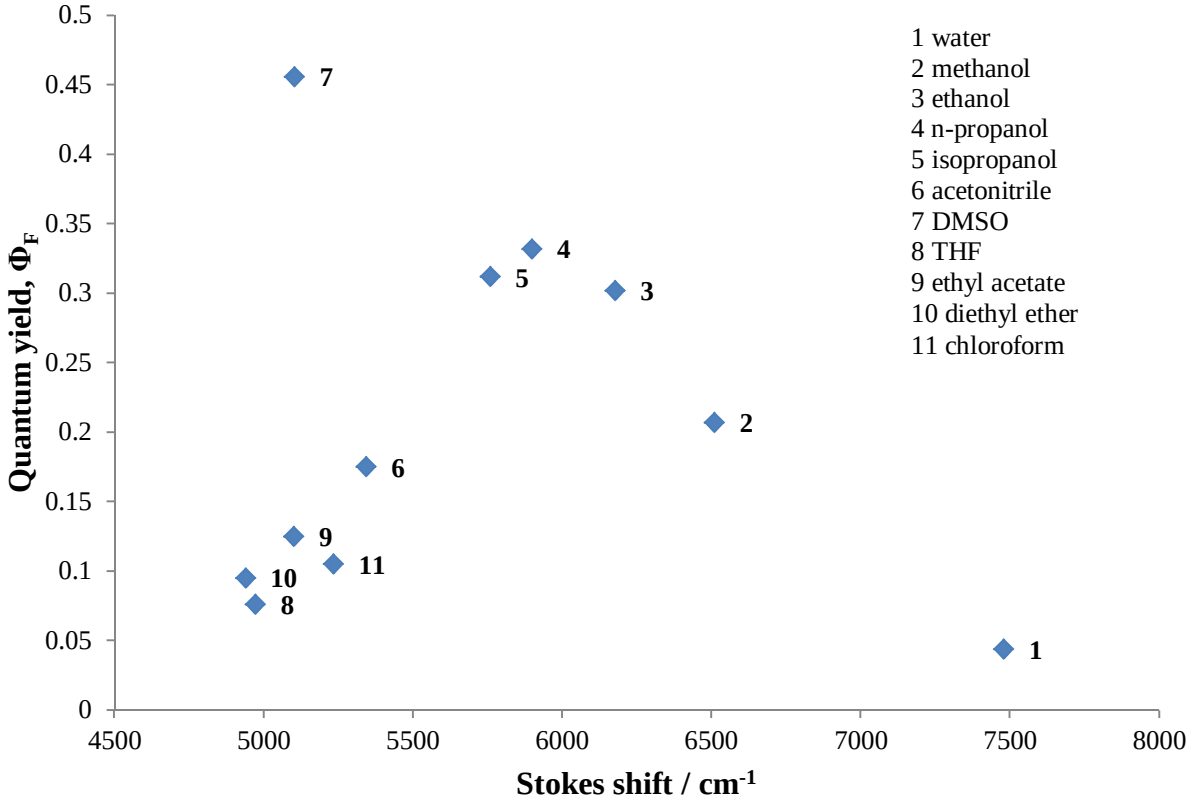

The Figure 3.14 shows no visible linear relationships among the points because of high degree of scattering within the plot. In particular, Pc in DMSO has a very large quantum yield (0.456 ± 0.012) compared to any other aprotic solvent and it is also by far the biggest even when compared to any protic solvent used. Exceptionally big quantum yield combined with a relatively small Stokes make its position within the plot anomalous with respect to the aprotic solvents. In contrast to DMSO, water diverges from all the other solvents because of its remarkably small quantum yield (0.044 ± 0.004 as opposed to 0.686 ± 0.016 of 2-Ap in water 0.686 ± 0.016) associated with the largest Stokes shift measured in all solvents. Similarly to 2-Ap the difference in quantum yield measurements between the solvents with low dielectric constant is not so striking (going from 0.076 ± 0.003 in THF (8) to 0.125 ± 0.003 in ethyl acetate (9)).

Like 2-Ap, Pc spectroscopic measurements were carried out in a water-acetonitrile mixture to discriminate general solvent effects from specific solvent effects such as hydrogen bonding. The quantum yield measurements of Pc in water-acetonitrile mixtures along with Stokes shifts are shown in Table 3.7.

Table 3.7 Spectroscopic data of Pc in water-acetonitrile mixtures

Φ_F, λ_{ex}, λ_{em} and Stokes shift of Pc in water-acetonitrile mixtures (volume percentage mixtures)

Solvent acetonitrile:water	$\Phi_F \pm 2\sigma$	λ_{ex} ***/nm***	λ_{em} ***/nm***	υ_{ex}-υ_{em} ***/cm^{-1} (Stokes shift)***
100 : 0	0.175 ± 0.006	349.0	429.0	5343
90 : 10	0.165 ± 0.003	344.0	437.0	6186
80 : 20	0.151 ± 0.003	343.0	437.0	6271
70 : 30	0.134 ± 0.004	342.0	439.0	6460
60 : 40	0.127 ± 0.003	340.0	439.0	6632
50 : 50	0.114 ± 0.004	340.0	440.0	6684
40 : 60	0.098 ± 0.004	340.0	440.0	6684
30 : 70	0.085 ± 0.004	339.0	442.0	6874
20 : 80	0.061 ± 0.004	336.0	443.0	7188
10 : 90	0.052 ± 0.004	336.0	445.0	7289
0 : 100	0.044 ± 0.004	335.0	447.0	7479

The Lippert plot shown in Figure 3.15 below is generated from the Stokes shift values taken from Table 3.7 and the orientation polarizability values in Table 3.4. The Lippert plot obtained is a non-linear plot. The non-linear beahaviour is due to a drastic change in Stokes shift (from 5343 cm^{-1} to 6186 cm^{-1}, (see Table 3.7) when water is added to acetonitrile solution. This small amount of water (10%) does not drastically change the refractive index and dielectric constant of the mixture; hence this Stokes shift is predominantly a result of a specific solvent effect, not just polarity. In this case, the specific solvent effect is almost certainly hydrogen bonding formation due to presence of water molecules.

Figure 3.15 Lippert plot of Pc in water-acetonitrile

A non-linear Lippert plot of Pc in water-acetonitrile mixtures (volume percentage mixtures). Polynomial function (grade 3) software used Excel

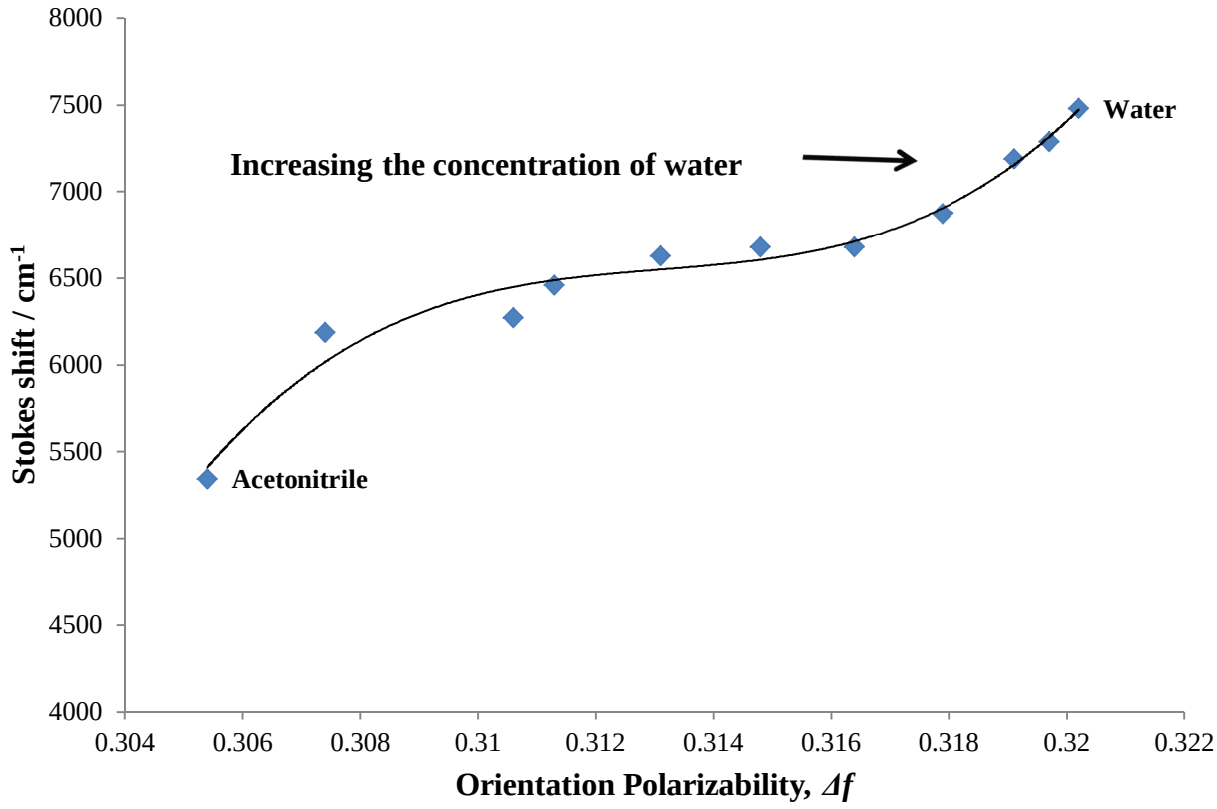

3.4.4 Calculation of Pc Δμ

The situation with Pc appears more complicated than the one with 2-Ap because of a poor correlation among the points considering all the solvents, regression coefficient $R^2 \sim 0.58$, see Figure 3.11. The slope generated which is 10316 cm^{-1} may be therefore inaccurate, leading to poor $\Delta\mu_e$ values. Thus, the slope considering protic solvents see Figures 3.12, has been instead considered for the calculation of Δμ. The differences in dipole moments are included in Table 3.8 and they were calculated by using the equation 3.18. The theoretically calculated cavity radius used in the equation was found to be 4.40 Å, see Chapter 4 Sections 4.5 Table 4.4.

Table 3.8 Difference in dipole moment of Pc in different solvents

This table shows the difference in dipole moment between the excited state and the ground state of Pc in different solvents. The slope and the regression coefficient obtained from three different Lippert plots are also reported

Pc Lippert plot in different solvents	All solvents considered	Protic solvents considered	Aprotic solvents considered
Slope of the Lippert plot (cm^{-1})	10316.0 ± 2898.0	27758.0 ± 6841.9	27758.0 ± 4798.9
R^2 (regression coefficient)	0.5847	0.8458	0.2812
Δμ (difference in dipole moment) D	**9.34 ± 1.42**	**15.32 ± 1.90**	**3.58 ± 1.98**

The theoretically calculated $\Delta\mu_t$ was found to be 0.96 D (see Table 4.12 in Section 4.7.2 of Chapter 4), a much smaller $\Delta\mu_t$ was found when compared to $\Delta\mu_e$ shown in Table 3.8. If a smaller slope is considered into the equation 3.18 then a smaller $\Delta\mu_e$ can be obtained which would be more similar to $\Delta\mu_t$. For example, if the slope of Pc in aprotic is considered the difference in dipole moment was calculated to be 3.58 D a much closer value to the theoretical one (but a very low regression coefficient was calculated).

A much smaller slope may be predicted/generated if solvents with very low-dielectric constants (non-polar solvents) are used. Thus, it would be interesting to generate a Pc Lippert plot in non-polar solvents only in order to be compared with a Pc Lippert plot generated from aprotic solvents only. Unfortunately, in our hands Pc is not sufficiently soluble in non-polar solvents with very low dielectric constants to obtain reliable fluorescence readings. In fact, past experiments with hexane $\varepsilon = 1.89$, cyclohexane $\varepsilon = 2.02$, toluene $\varepsilon = 2.36$ and other low-dielectric constant solvents proved to be unsuccessful in dissolving the fluorophore. As a rule of a thumb Pc can be considered non soluble in a solvent with a dielectric constant lower than 4. The same rule can be safely applied to 2-Ap.

The fluorescent base Pc may appear to have a larger difference in Δμ than 2-Ap because of poorer correlation between the points or most likely because it possesses an electron-donating group or substituent (CH_3) and an electron-acceptor group or substituent (C=O). The electron

transfer taking place between these two groups via the π system of the organic molecule would act as the main cause for a larger intramolecular charge transfer and therefore, a larger difference in dipole moment, Δμ. Strong electron-acceptor and donor groups within a fluorescence probe may cause TICT (twisted intramolecular charge transfer) (Rotkiewicz *et al*. 1973; Grabowski *et al*. 1979). TICT triggers a change in the geometry of the probe when irradiated by light. This conformational change can be treated as a specific solvent effect and therefore, almost certainly the cavity radius of the probe in the ground state is different from the one in the excited state.

3.5 Summary, concluding remarks

The solvation study of Pc and 2-Ap in water and organic solvents has revealed similarities and differences between the bases and some of these similarities and differences are briefly described below:

- The largest Stokes shift was recorded in water for both Pc (7479 cm^{-1}) and 2-Ap (5905 cm^{-1}).
- The largest quantum yield measurement of 2-Ap is in water (0.686 ± 0.016) whereas the one of Pc is in DMSO (0.456 ± 0.012).
- The Lipper plots of Pc and 2-Ap in water-acetonitrile mixtures appear to be non-linear and this behaviour is attributed to specific solvent effects; almost certainly the specific effect is hydrogen bonding.
- In both bases a shift to longer wavelengths (red or bathochromic shift) is observed going from aprotic solvents to protic solvents.
- The two bases undergo intramolecular charge transfer upon excitation, $\mu_e > \mu_g$ because of the calculated Δμ which for both the bases is large and positive. The values are 9.34 D for Pc and 6.75 D for 2-Ap if all solvents are considered.
- The two fluoroprobes cannot be dissolved in solvents which are considered to be non-polar (dielectric constants, $\varepsilon < 4$).

Albeit the Lippert plots are simple to generate they seem to be very dependent on the choice of the solvents used and a good linear correlation between the points is not an absolute indicator of general solvent effects or polarity effects. Using solvents having the same nature

or functional group, for example alcohols can greatly affect the Lippert plot because of having almost the same orientation polarizability and thus, the calculation of Δμ because of inaccurate slopes. It would be interesting to generate Lippert plots from the bases in protic solvents, aprotic solvents and non-polar solvents considering solvents which do not share the same functional group only; compare the plots and calculate the differences in dipole moments. But unfortunately, as already stated the bases cannot dissolve in solvents with very low dielectric constants.

The Lippert model is not the only model to investigate the effect of polarity on the absorption and fluorescence spectra of fluoroprobes. Single and multiparameter approaches can also be adopted besides the Lippert model. There are different single parameter approaches but the most widely known is the one based on the polarity scale of Reichardt (Reichardt, 1990). The Stokes shifts are plotted against the solvent values of interest contained in the E_T 30 scales, polarity scales obtained by using betaine dyes in various solvents (the transition energy for the longest wavelength absorption band of the dissolved betaine dyes measured in kcal/mol). Often two distinct lines are generated from aprotic solvents and protic solvents. The reliability of the linear relationships between the Stokes shifts in cm^{-1} and the values of the polarity scales in kcal/mol depend on the degree of resemblance between the dye and the fluoroprobe. A much more complex and laborious approach is a multiparameter one. The most successful multiparameter approach for solvation study is the one of Kamlet and Taft (Kamlet *et al*. 1977). The scales of Kamlet and Taft are also known as π* scales. The maxima of the absorption bands are related through mathematical equations to three main parameters: the π* parameter which is a measure of solvent polarity, the parameter α is an index of HBD (hydrogen bond donor) and the parameter β is an index of solvent HBA (hydrogen bond acceptor). The advantage of multiparameter scales over single parameter scales is that the specific solvent effects, specifically hydrogen bonding (hydrogen-bond acceptor and donor) are also taken into account and not only polarity effects, by calculating which parameter is the most effective for the base studied in different solvents. Generally, the quantum yield measurements of the bases in solvents with low dielectric constants were found to be much smaller than the quantum yield measurements obtained in alcohols. It would be worthwhile to measure the lifetimes, τ of the bases in organic solvents. The lifetime measurements would permit the calculation of k_{total} ($k_F + k_{ISC} + k_{IC}$) which is the total rate of deactivation of S_1, see equation 2.27 of Chapter 2. After obtaining k_{total} the rate constant for fluorescence emission k_F can be calculated, by using the experimentally measured quantum yields, from equation

2.31, and therefore, speculating on the extent of the rate of deactivation due to the rate of internal conversion k_{IC} and intersystem crossing k_{ISC}.

Chapter 4: Computational study on 2-aminopurine and pyrrolocytosine

4.1 Computational Chemistry. Introduction to Density Functional Theory (DFT)

The term computational chemistry is used when mathematical and theoretical chemistry principles, laws and approximations are incorporated into computer programs to solve problems and perform calculations. The *ab initio* (it is Latin and it stands for "from the beginning") methods are computational chemistry methods which compute solutions to the Schrödinger equation by using a series of rigorous approximations. For example, many *ab initio* methods take into account the Born-Oppenheimer approximation (see Chapter 2 Sections 2.1 and 2.2). Even though Density Functional Theory methods are considered *ab initio* methods, the electronic structure of the molecules investigated is obtained by using functionals (functions of functions), parameters derived from empirical data. By using DFT methods the total electron energy is expressed in terms of the total electron energy density instead of the wavefunction of the electron energy that would be obtained by using different *ab initio* such as the conventional Hartree-Fock (HF) methods. DFT methods are used in physics and chemistry to investigate molecular structures, specifically: changes in molecular geometries, potential energies and stabilities of molecules, bond strengths, thermochemical properties and spectroscopic properties such as IR, Raman, UV-visible and NMR spectra. DFT methods were used to investigate Pc and 2-Ap using Gaussian 03 (G03) and 09 (G09) (Frisch *et al*. 2003). The electronic structures of the fluorophores in vacuum and different solvents were calculated with a particular emphasis on the change in dipole moments between the ground state (S_0) and the first excited state (S_1) in order to compare computational data with experimental data obtained in the previous chapter. Also, the first three singlet and triplet electronic transitions of the bases were obtained to correlate them to photochemical deactivation processes of the excited states by invoking photochemistry laws and rules. The maxima of the theoretical absorption and emission bands were also compared with the experimental ones. In the past, computational study on the four natural bases (adenine, guanine, thymine and cytosine) at the Time-Dependent Density Functional Theory (TDDFT) using the B3LYP functional in combination with the basis set 6-31G was found to be in a satisfactory agreement with the corresponding experimental data (Crespo-Hernandez *et al*. 2004; Shulka and Leszczknsi, 2004; He *et al*. 2005). In fact, the B3LYP functional has been credited to provide very good geometries and vibrational frequencies at a reduced computational cost with respect to other theoretical methods or less reliable methods such as

the semiempirical methods (Sahu *et al*. 2005). Another relatively inexpensive approach for modelling excited states of natural bases is configuration interaction with single excitations (CIS) which is an *ab initio* method (Foresman *et al*. 1992). Even though CIS is an inexpensive computational method, it significantly overestimates transition energies because dynamic electron correlation is neglected (Andersson *et al*. 1992). Thus, a common approach to this overestimation is to scale CIS transitions by an empirical factor in order to compare theoretical transitions with experimental transition (Andersson *et al*. 1992). The advantage of B3LYP over CIS is that no scaling is necessary, a factor which makes the DFT functional a simpler and faster computational approach to be adopted (Crespo-Hernandez. 2004).

4.2 Computational details

The Gaussian 03 and 09 suites of connected programs (Frish *et al*. 2003) developed for performing a variety of *ab initio* calculations were used for all the calculations in this project. The software Molekel (Flükiger *et al*. 2000) and Chemcraft (Zhurko, 2006) were adopted for visualization of the molecular geometries, vibrational frequencies and isosurfaces rendering for pictorially represented molecular orbitals. In the case of G03, the computational calculations were performed on a Linux workstation which has 4 dual-core AMD Opteron 8214 processors and 8 GB of memory as hardware. Gaussian 09 was accessed by registration with NSCCS (National Service for Computational Chemistry Software). The NSCCS hardware is based and managed at the Rutherford Appleton Laboratory (RAL) of the Science and Technology Facilities Council (STFC). The NSCCS Cluster, called Columbus. Columbus, is a Silicon Graphics Altix UV 1000 with 64 x Intel E7-8837, 2.66 GHz, 24 MB cache, 8 cores per node (512 cores), 2 TB of memory and 10 GB of network.

A conventional Gaussian Input file is composed of four sections. 1) The Link 0 section for check points and memory specifications. 2) The route section which contains the specification of the method, the basis set and the keyword used for specific calculations. 3) The title section and 4) the coordinate section. The coordinate section contains the molecule specification which can be expressed either in Cartesian coordinates or in Z-matrices. This section contains also the charge and the spin multiplicity. Additional sections containing variables can also be used. An example of a Gaussian input file section is shown in Figure 4.1.

The route section contains the functional B3LYP with the basis set G-31G. The functional stands for Becke Three Parameter Lee-Yang-Parr which is a class of approximations to the exchange-correlation energy functional in density functional theory. The Becke 3-Parameter is the exchange functional whereas the Lee Yang Parr parameter is the correlation functional (Becke, 1988; Lee *et al*. 1988; Becke, 1993).

The capital letter G indicates Gaussian type orbitals (GTOs) which are used to describe atomic orbitals (AOs). The numbers 6-31 stand for: 6 GTOs for core orbital, 3 GTOs for inner valence and 1 GTO for outer valence. The letters d and p are polarization functions added to heavy and hydrogen atoms. These functions are used to obtain more realistic approximation of the atomic system by letting the atomic orbitals distort from an initial/original shape to a slightly different shape under the influence of the surroundings. In other words, the electron density for the treated orbitals gets distorted.

The key words opt and freq were used to perform optimization followed by frequency calculations of the input geometry. Geometry optimization is a mathematical process that attempts to find the configuration of minimum energy of the studied molecule. The first step is to calculate the wave function and energy at a starting geometry. This process continues until a new geometry of a lower energy with respect to the previous found was found, thus the calculation stops when the geometry of the lowest energy was obtained (the force on each atom is equal to 0). It is important to understand that this process does not always find the global minimum (the geometry with the lowest energy). In fact, the process stops when a stationary point was found but this point might be a saddle point. In order to find the true stationary point frequency calculations are required. The keyword frequency instructs Gaussian to calculate the vibrations of the optimized molecule. The frequencies of the molecule depend on the second derivative of the energy with respect to the nuclear positions. In order to know whether the point found is the global minimum or a saddle point the stability of the molecule must be tested. Stability test confirms the presence of computed imaginary frequencies. Imaginary frequencies are negative frequencies which indicate instability within the molecule in other words they confirm the presence of a saddle point. The absence of negative frequencies indicates that either the local or global minimum was reached.

The numbers 0 and 1 in the coordinate section were chosen which indicate that the molecule has no charge on it, charge = 0 and its spin multiplicity = 1, thus singlet multiplicity which means that the molecule has no unpaired electrons.

Figure 4.1 Gaussian input file

A Gaussian input file showing the content of the four sections all divided by a blank line. The molecule specifications of a Pc base are given as Cartesian coordinates corresponding to the atoms of the base

```
%mem=500MB

#B3LYP/6-31G(d,p) opt freq

Pc in gas phase opt geom

0 1
 H                    29.7609  -13.8791   0.0226
 C                    32.5909  -13.287    0.0491
 C                    32.3519  -15.7987   0.0258
 C                    31.8085  -14.5679   0.0331
 N                    30.3915  -14.6475   0.0236
 N                    28.9008  -16.5097   0.0084
 C                    30.0467  -15.9742   0.0151
 C                    31.2109  -16.7105   0.0151
 C                    31.1945  -18.0322   0.0064
 N                    29.9153  -18.6425  -0.0011
 C                    28.8412  -17.9443   0.0013
 H                    26.884   -17.8859   0.0041
 O                    27.6032  -18.5671  -0.0006
 H                    31.9604  -12.5109   0.0509
 H                    33.1729  -13.2413  -0.7629
 H                    33.1613  -13.2544   0.8699
 H                    33.3231  -16.037    0.0275
 H                    32.0368  -18.5712   0.0051
```

4.3 Tautomerism of 2-Ap and Pc

2-Ap may exist in different tautomers, the 2-Ap amino and imino tautomers: N9H amino tautomer (2-Ap A), N7H amino tautomer (2-Ap B), N1H amino tautomer (2-Ap C), N3H amino tautomer (2-Ap D), N9H N1H imino tautomer (2-Ap E), N7H N1H imino tautomer (2-Ap F), N9H N3H imino tautomer (2-Ap G) and N7H N3H imino tautomer. The amino and imino tautomers are shown in Figure 4.2.

Figure 4.2 2-Ap tautomers

The 2-Ap amino and imino tautomers are displayed below

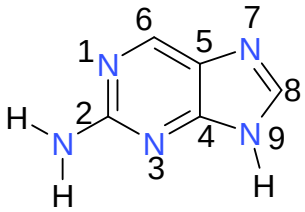

2-Ap N9H amino tautomer (2-Ap A)

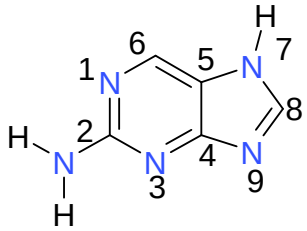

2-Ap N7H amino tautomer (2-Ap B)

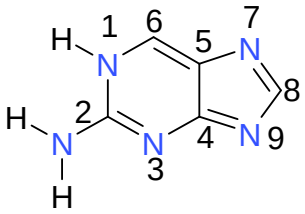

2-Ap N1H amino tautomer (2-Ap C)

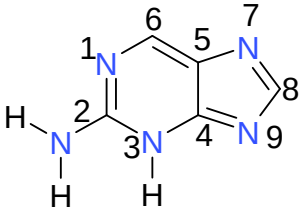

2-Ap N3H amino tautomer (2-Ap D)

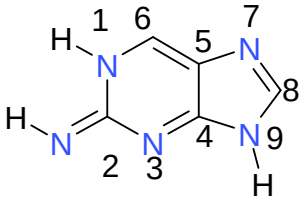

2-Ap N9H N1H imino tautomer (2-Ap E)

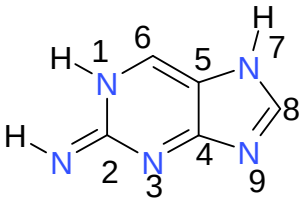

2-Ap N7H N1H imino tautomer (2-Ap F)

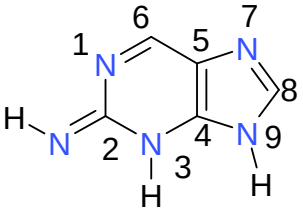

2-Ap N9H N3H imino tautomer (2-Ap G)

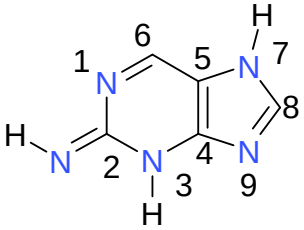

2-Ap N7H N3H imino tautomer (2-Ap H)

According to Neely *et al.* 2-Ap in water exists as N9H and N7H amino tautomers having different lifetimes and their proportions are: 60 % and 40 % respectively (Neely *et al.* 2004). In the gas phase and solid state (crystal state) the dominance of the N9H tautomer is much bigger (Seefeld *et al.* 2005; Neely *et al.* 2007). Both the tautomers are known to be fluorescent emitting species (Mishra *et al.* 2000; He *et al.* 2005). Pc may also be found in different tautomers: Pc N1H NH9 keto tautomer (Pc A), Pc N3H N9H tautomer (Pc B), Pc N3H N9H keto tautomer (Pc C), Pc N9H enol tautomer (Pc D), Pc N1H enol tautomer (Pc E) and Pc N3H enol tautomer (Pc F). The Pc tautomers are displayed below in Figure 4.3.

Figure 4.3 Pc tautomers

This figure shows the keto and enol tautomers of Pc

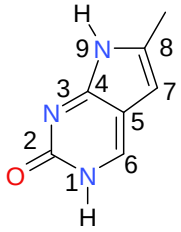

Pc N1H N9H keto tautomer (Pc A)

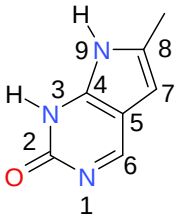

Pc N3H N9H keto tautomer (Pc B)

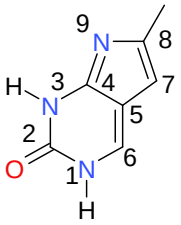

Pc N3H N9H keto tautomer (Pc C)

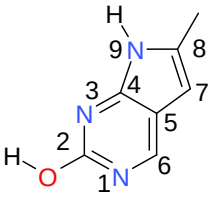

Pc N9H enol tautomer (Pc D)

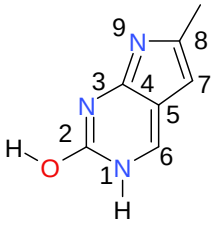

Pc N1H enol tautomer (Pc E)

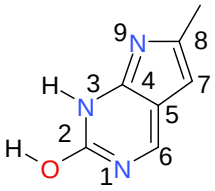

Pc N3H enol tautomer (Pc F)

4.4 Optimization of tautomers and SCRF (self-consistent reaction field)

The ground state geometries of 2-Ap and Pc tautomers were optimized at B3LYP/6-31G (d,p) level of theory. G03 generates an optimized geometry by adjusting the initial input geometry until a stationary point on the potential surface is found (a point on the potential energy surface where the forces are considered to be zero). In order to request geometry optimization the keyword "opt" is used in the route section. Once the optimized geometry is obtained a frequency calculation can be performed by using the keyword "freq" in the route section. A frequency calculation on the optimized configuration is required because this calculation provides force constants and vibrational frequencies and therefore, reveals whether the optimized geometries used are at the true minima or not. The effects of different solvents on the tautomers are modelled by self-consistent reaction field (SCRF). SCRF methods model the solvent as a perpetuity or continuum of uniform dielectric constant ε, the reaction field. The solute or probe studied is placed into a cavity within the effect of the solvent. SCRF models differs in how the cavity and the reaction field are defined. The Tomasi's Polarized Continuum Model, abbreviated as the keyword (PCM), defines the cavity not as simple and fixed spherical cavity as in the case of the Onsager model, but it treats the cavity as a series of interlocking atomic spheres (Frish *et al.* 2003; Foresman and Frisch, 1996). Hence, the route section used for the optimization of the bases in different solvents is the following:

#B3LYP/6-31G (d,p) opt freq SCRF=(pcm,solvent=name of the solvent)

The Table 4.1 includes the dipole moments in debye (D) of the optimized geometries of 2-Ap tautomers along with their calculated single point energies given in atomic units (a.u). The Gaussian simulations showed that 2-Ap N9H amino tautomer (2-Ap A) is the most energetically stable 2-Ap tautomer in vacuum, water and organic solvents. The table 4.2 shows the same calculations for Pc. In the case of Pc tautomers, the calculations revealed that Pc N1H N9H enol tautomer (Pc D) is the most energetically stable tautomer in vacuum whereas Pc N1H N9H keto tautomer (Pc A) is the most energetically stable tautomer in water and organic solvents.

Table 4.1 Dipole moments and single point energy calculations of 2-Ap tautomers

This table displays the dipole moments expressed in debyes (D) of the optimized geometries of 2-Ap tautomers in vacuum and different solvents along with their single point energy calculations in atomic units (a.u). The energies of the most stable tautomers are given in red

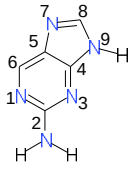 2-Ap A	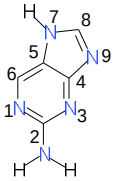 2-Ap B	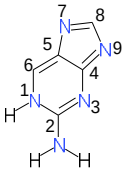 2-Ap C	 2-Ap D	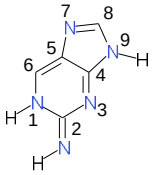 2-Ap E	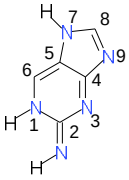 2-Ap F	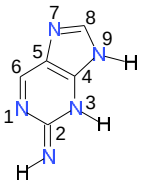 2-Ap G	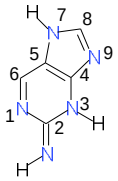 2-Ap H
2-Ap in vacuum							
3.2514 D **-467.2161 au**	4.0731 D -467.2094 au	7.7146 D -467.1877 au	6.1017 D -467.1948 au	3.3473 D -467.1758 au	9.6430 D -467.1617 au	5.4632 D -467.1790 au	6.5049 D -467.1836 au
2-Ap in water							
4.6774 D **-467.2444 au**	6.1816 D -467.2425 au	13.0673 D -467.2331 au	9.7301 D -467.2330 au	5.0803 D -467.2057 au	14.3539 D -467.2136 au	8.3171 D -467.2178 au	9.4596 D -467.2201 au
2-Ap in methanol							
4.6220 D **-467.2434 au**	6.1625 D -467.2412 au	12.8992 D -467.2313 au	9.6715 D -467.2317 au	4.9913 D -467.2044 au	14.1567 D -467.2114 au	8.2084 D -467.2163 au	9.3475 D -467.2187 au
2-Ap in ethanol							
4.5891 D **-467.2429 au**	6.0256 D -467.2406 au	12.3807 D -467.2298 au	9.8150 D -467.2312 au	4.9529 D -467.2035 au	14.0511 D -467.2103 au	8.1444 D -467.2154 au	9.2884 D -467.2180 au
2-Ap in chloroform							
4.1959 D **-467.2356 au**	5.4334 D -467.2317 au	11.0963 D -467.2177 au	8.5933 D -467.2207 au	4.5061 D -467.1961 au	12.7566 D -467.1957 au	7.3705 D -467.2052 au	8.5263 D -467.2084 au
2-Ap in acetonitrile							
4.6280 D **-467.2436 au**	6.0855 D -467.2414 au	12.5047 D -467.2310 au	9.8939 D -467.2322 au	4.9959 D -467.2042 au	14.1764 D -467.2117 au	8.2207 D -467.2164 au	9.3616 D -467.2189 au
2-Ap in DMSO							
4.6440 D **-467.2438 au**	6.1111D -467.2418 au	12.5573 D -467.2315 au	9.6401 D -467.2320 au	5.0109 D -467.2044 au	14.2249 D -467.2123 au	8.2537 D -467.2169 au	9.3983 D -467.2192 au
2-Ap in THF							
4.3620 D **-467.2384 au**	5.6632 D -467.2353 au	11.6011 D -467.2226 au	8.9643 D -467.2248 au	4.6845 D -467.1991 au	13.2731 D -467.2015 au	7.6695 D -467.2092 au	8.8372 D -467.2123 au
2-Ap in diethyl ether							
4.1437 D **-467.2345 au**	5.3501 D -467.2305 au	10.8859 D -467.2160 au	8.4612 D -467.2193 au	4.4424 D -467.1950 au	12.5809 D -467.1937 au	7.2576 D -467.2036 au	8.4190 D -467.2071 au
2-Ap in 1-propanol							
4.3681 D **-467.2335 au**	5.9412D -467.2312 au	12.2979 D -467.2188 au	9.0541 D -467.2194 au	5.0109 D -467.2038 au	13.7664 D -467.1980 au	7.9199 D -467.2031 au	9.3412 D -467.2064 au
2-Ap in 2-propanol							
4.3610 D **-467.2334 au**	5.9282 D -467.2310 au	12.2755 D -467.2186 au	9.0325 D -467.2193 au	4.9511 D -467.2036 au	13.7392 D -467.1977 au	7.9043 D -467.2029 au	9.3245 D -467.2062 au
2-Ap in ethyl acetate							
4.1247 D **-467.2302 au**	5.5147 D -467.2268 au	11.5413 D -467.2125 au	8.4664 D -467.2147 au	4.6189 D -467.1982 au	12.8643 D -467.1901 au	7.3972 D -467.1983 au	8.7548 D -467.2019 au

Table 4.2 Dipole moments and single point energy calculations of Pc tautomers

This table displays the dipole moments expressed in debyes (D) of the optimized geometries of Pc tautomers in vacuum and different solvents along with their single point energy calculations in atomic units (a.u). The energies of the most stable tautomers are given in red

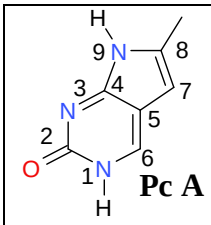 Pc A	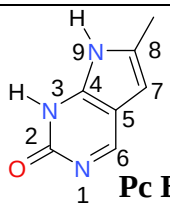 Pc B	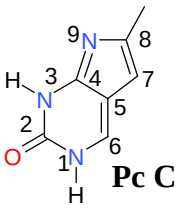 Pc C	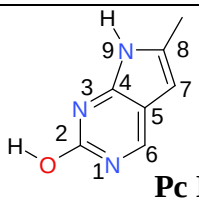 Pc D	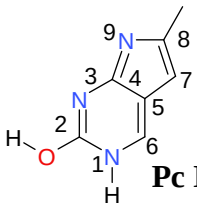 Pc E	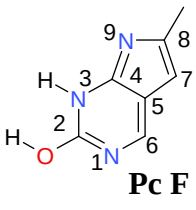 Pc F
Pc in vacuum					
6.4799 D	8.1564 D	3.4642 D	5.0840 D	5.0903 D	2.5243 D
-510.3279 au	-510.3172 au	-510.3247 au	**-510.3300 au**	-510.3027 au	-510.2975 au
Pc in water					
9.0892 D	11.7809 D	5.0915 D	6.8725 D	8.3410 D	4.2490 D
-510.3628 au	-510.3552 au	-510.3546 au	-510.3556 au	-510.3387 au	-510.3348 au
Pc in chloroform					
8.3091 D	10.6130 D	4.5276 D	6.3324 D	7.2352 D	3.6451 D
-510.3516 au	-510.3429 au	-510.3451 au	-510.3465 au	-510.3264 au	-510.3219 au
Pc in DMSO					
9.0401 D	11.6903 D	5.0465 D	6.8270 D	8.2563 D	4.1912 D
-510.3620 au	-510.3540 au	-510.3539 au	-510.3548 au	-510.3375 au	-510.3335 au
Pc in methanol					
9.0017 D	11.6450 D	5.0212 D	6.8030 D	8.2130 D	4.1727 D
-510.3615 au	-510.3537 au	-510.3536 au	-510.3545 au	-510.3371 au	-510.3332 au
Pc in ethanol					
8.9548 D	11.5611 D	4.9830 D	6.6766 D	8.1425 D	4.1281 D
-510.3608 au	-510.3527 au	-510.3529 au	-510.3554 au	-510.3362 au	-510.3322 au
Pc in THF					
8.5735 D	10.9948 D	4.7081 D	6.5069 D	7.5913 D	3.8363 D
-510.3553 au	-510.3465 au	-510.3483 au	-510.3494 au	-510.3303 au	-510.3259 au
Pc in 1-propanol					
8.9984 D	11.4104 D	4.8955 D	6.9095 D	7.7108 D	3.5364 D
-510.3516 au	-510.3424 au	-510.3426 au	-510.3438 au	-510.3239 au	-510.3185 au
Pc in ethyl acetate					
8.5062 D	10.7521 D	4.5780 D	6.5493 D	7.1330 D	3.3297 D
-510.3468 au	-510.3374 au	-510.3392 au	-510.3410 au	-510.3196 au	-510.3143 au
Pc in acetonitrile					
9.0155 D	11.6531 D	5.0286 D	6.7177 D	8.2322 D	4.1763 D
-510.3616 au	-510.3537 au	-510.3536 au	-510.3561 au	-510.3372 au	-510.3332 au
Pc in 2-propanol					
8.9837 D	11.3909 D	4.8858 D	6.8099 D	7.6933 D	3.5300 D
-510.3512 au	-510.3422 au	-510.3425 au	-510.3454 au	-510.3238 au	-510.3183 au
Pc in diethyl ether					
8.2162 D	10.4807 D	4.4688 D	6.1819 D	7.1104 D	3.5818 D
-510.3503 au	-510.3410 au	-510.3439 au	-510.3471 au	-510.3251 au	-510.3542 au

4.5 Computational calculation of the cavity radius of the fluorophores

The cavity radii *a* of the optimized geometries of 2-Ap and Pc in vacuum were calculated by using B3LYP/6-31G (d,p) level of theory with the key word "Volume" (Frish *et al.* 2003; Foresman and Frisch, 1996). Thus, the route section used is the following:

#B3LYP/6-31G (d,p) Volume

Gaussian 03 (G03) computes the molecular volume of the molecules studied, defined as the volume inside a contour of 0.001 electrons bohr^{-3} density (1 Å = 1.8897 bohr). The computed volume is only accurate to circa two significant figures (Frish *et al.* 2003; Foresman and Frisch, 1996), a sufficient accuracy to be used in the Lippert equation. The calculated cavity radii were reported in Angstroms (Å) and bohr. It should be noted that the keyword "Volume" was necessary because the Onsager self-consistent reaction field model was not adopted (the PCM model was used as previously explained), a model which automatically calculates the cavity radius after the optimization without the use of any additional keyword. The Tables 4.3 and 4.4 contain the cavity radii of 2-Ap and Pc tautomers.

Table 4.3 Cavity radii of 2-Ap tautomers calculated in vacuum

The cavity radii of the optimized geometries of 2-Ap tautomers in vacuum

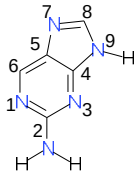	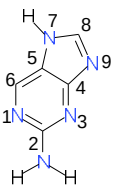	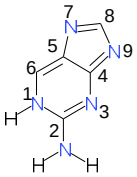	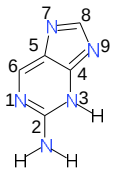	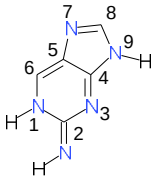	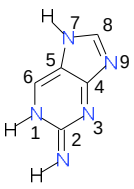	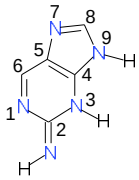	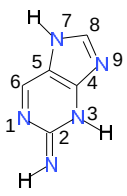
2-Ap A	**2-Ap B**	**2-Ap C**	**2-Ap D**	**2-Ap E**	**2-Ap F**	**2-Ap G**	**2-Ap H**
Cavity radii of 2-Ap tautomers (Å = Angstrom and Bohr)							
4.03 Å 7.61 Bohr	4.18Å 7.90 Bohr	4.11Å 7.76 Bohr	4.28 Å 8.09 Bohr	4.13 Å 7.81 Bohr	4.16 Å 7.86 Bohr	4.49 Å 8.48 Bohr	4.05 Å 7.66 Bohr

Table 4.4 Cavity radii of Pc tautomers calculated in vacuum

The cavity radii of the optimized geometries of Pc in vacuum

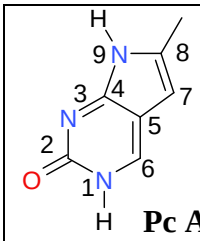 **Pc A**	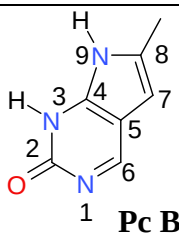 **Pc B**	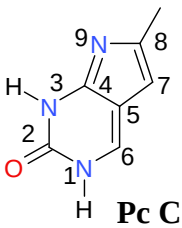 **Pc C**	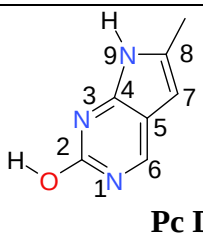 **Pc D**	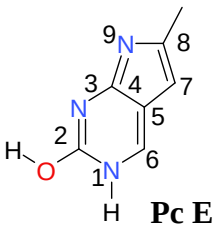 **Pc E**	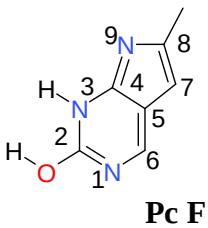 **Pc F**
Cavity radii of Pc tautomers (Å = Angstrom and Bohr)					
4.40 Å 8.31 Bohr	4.36 Å 8.23 Bohr	4.32 Å 8.16 Bohr	4.44 Å 8.38 Bohr	4.51 Å 8.52 Bohr	4.27 Å 8.08 Bohr

The Van der Walls volume, V_w which is also known the atomic or molecular volume that an individual molecule or atom occupies. If an atom is assumed to be spherical, its volume is then calculated from the following equation:

$$\mathbf{V_w = \frac{4}{3}\,\pi\, r_w^3} \quad \mathbf{(4.1)}$$

Where r_w is the Van der Walls radius (the radii of many different atomic species were experimentally calculated) (Bondi, 1964). In the case of a molecule, its volume is the volume enclosed within the Van der Walls surface. Gaussian 09 calculates the molecular volume of a molecule as the volume of the region within a defined electron density contour or surface and then, this volume is equated to that of a sphere. The adopted radius is an overestimate of that of the radius corresponding to the computed volume, precisely 0.5 Angstroms larger (Frisch *et al*. 2003).

4.6 Vertical transitions of the 2-Ap and Pc tautomers

The optimized geometries of 2-Ap N9H (A) and Pc N1H (A), the energetically most stable tautomers were used to calculate the energy of the vertical singlet and triplet electronic transitions at the Time-Dependent Density Functional Theory (TDDFT). The diffuse function notation + was used in the route section. The diffuse functions make orbitals bigger therefore, allowing them to occupy larger regions of space. This modification is very useful when working with excited states. One single plus sign adds diffuse functions on all atoms except for hydrogen atoms. The keywords "TD" (which requests an excited state energy calculation) along with "50-50" (solves for half triplet and half singlet states. The number of excited states one wants to compute can be selected by inserting the keyword TD=NStates=to the number desired. However by default three states are computed both singlet and triplet states) were entered as part of the route section for vertical transitions. TD calculates the wave functions of molecular orbitals that oscillate between the ground state and the first excited states. One the excited states are computed the vertical excitation are calculated by taking the difference between the excited and ground state potential energy (the optimized geometry of the ground state) (Frish *et al.* 2003; Foresman and Frisch, 1996). In order to visualise (*via* Molekel and Chemcraft) the electronic distribution within the excited molecules, the keywords "pop=full" "gfoldprint" and "gfinput" were added in the route section. For example the route section used for the gas phase was the following:

#B3LYP/6-31+G (d,p) TD=50-50 pop=full gfoldprint gfinput

For the solvents, the SCRF=(pcm,solvent) keywords were added to the route section.

The assignment of the molecular orbital characters shown in this Chapter were visually made and this visual assessment matches the computed characters of the molecular orbitals given the symmetry values provided in the Gaussian file.

4.6.1 Vertical transitions of 2-Ap N9H amino tautomer (2-Ap A)

The nature of the occupied and unoccupied molecular orbitals (MO) was assigned by using Chemcraft. The isosurfaces shown are both-signed and the contour value chosen was 0.036000 a.u for the majority of the MO displayed but it was increased or decreased when Rydberg MO were encountered. Also, the Gaussview style was adopted for all the structures reported. The single point geometry of the 2-Ap A tautomer displayed prior to surface rendering of molecular orbitals is shown below in Figure 4.4.

Figure 4.4 2-Ap A displayed on Chemcraft (Gaussview style)

2-Ap A tautomer displayed on Gaussview style prior to rendering of molecular orbitals. Nitrogen atoms in blue, carbon atoms in grey and hydrogen atoms in white

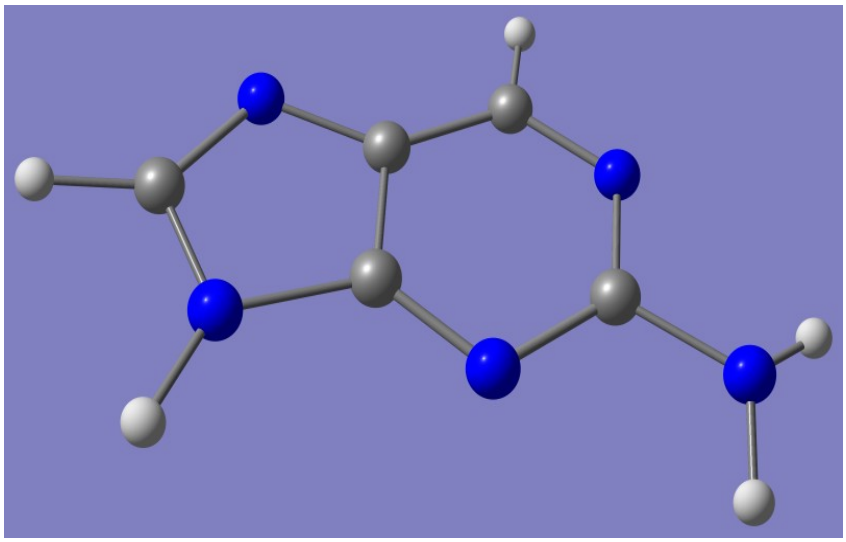

The first vertical transition is clearly a π-π*, see Figure 4.5. The second vertical transition is an n-π* as shown in Figure 4.6. In vacuum the third vertical transition were found to be of Rydberg character because of the promotion of one or more electrons from a bonding MO into a Rydberg MO. Typically, a Rydberg MO is very large compared to atoms or molecular moiety involved in the transition and it appears entirely or partially outside of the molecular framework, see Figure 4.7. In water and organic solvents (except for ethanol) the third vertical transition is π-π*, see Figure 4.8. In the case of ethanol the transition is a π-Rydberg (not shown). The Tables 4.5 and 4.6 include the assignments of the singlet and triplet electronic transitions along with ΔE of the transitions (expressed in eV and nm) and its oscillator strength *f*.

Figure 4.5 First vertical transition of 2-Ap A tautomer

A π-π* first vertical transition of 2-Ap A tautomer

Unoccupied MO
(energy level 36),
π* antibonding MO

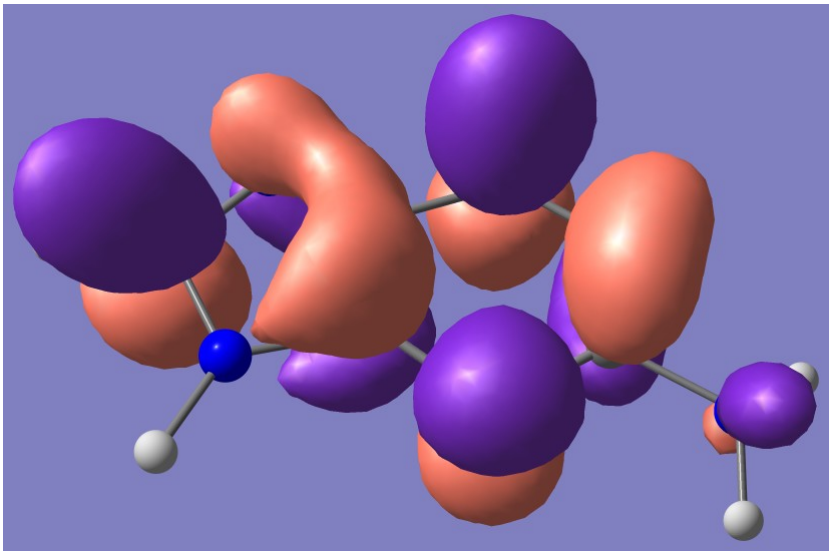

First vertical transition
of 2-Ap A tautomer in
vacuum and solution
(water and organic solvents)

π-π*

Occupied MO
(energy level 35),
π bonding MO

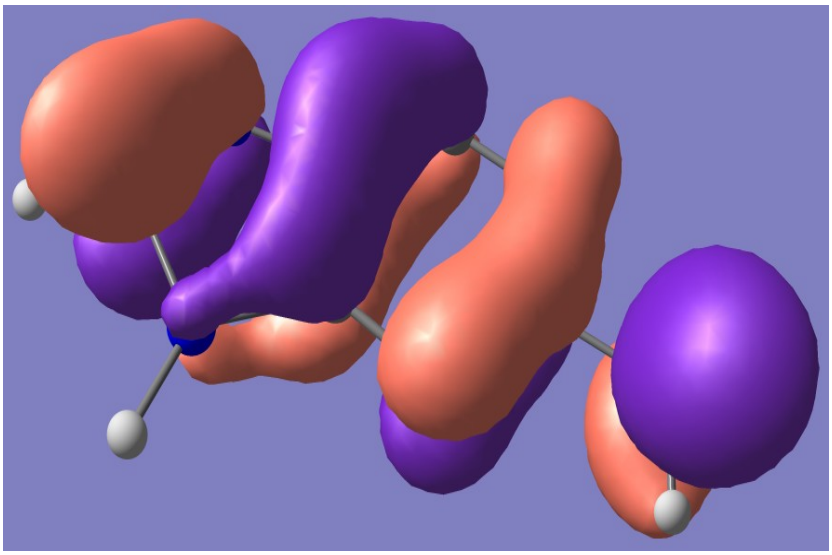

Figure 4.6 Second vertical transition of 2-Ap A tautomer

An n-π* second vertical transition of 2-Ap A tautomer

Unoccupied MO
(energy level 36),
π* antibonding MO

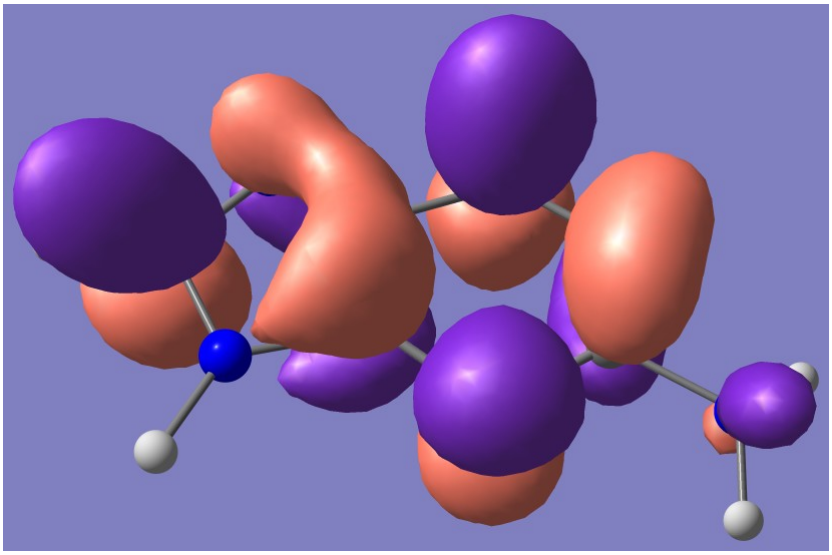

Second vertical transition
of 2-Ap A tautomer in
vacuum and solution
(water and organic solvents)

n-π*

Occupied MO
(energy level 34),
n non-bonding MO

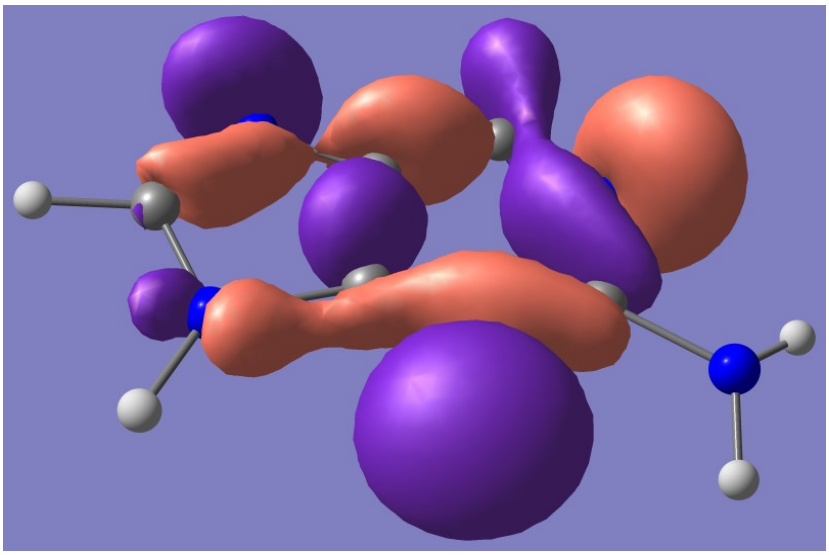

Figure 4.7 Third vertical transition of 2-Ap A tautomer in vacuum

A π-Rydberg third vertical transition type of 2-Ap N9H amino tautomer in vacuum

Unoccupied MO (energy level 37), Rydberg MO

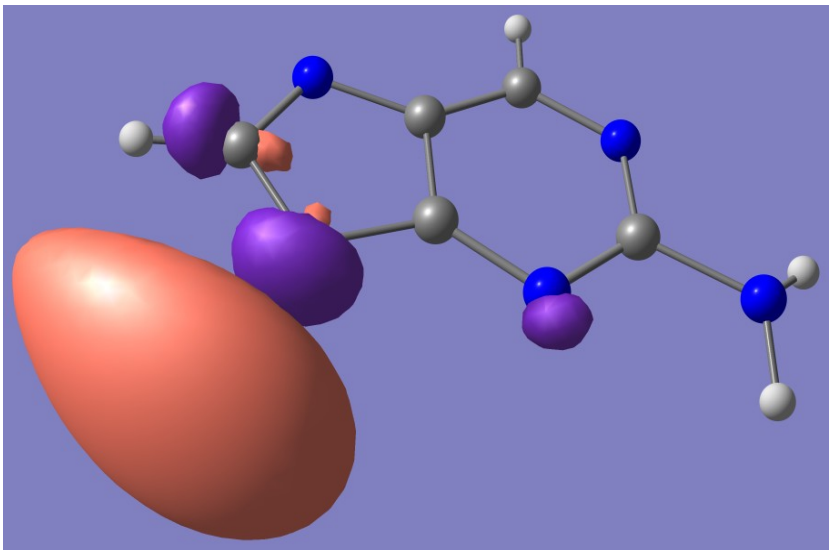

Third vertical transition of 2-Ap A tautomer in vacuum

π-Rydberg MO

Occupied MO (energy level 35), π bonding MO

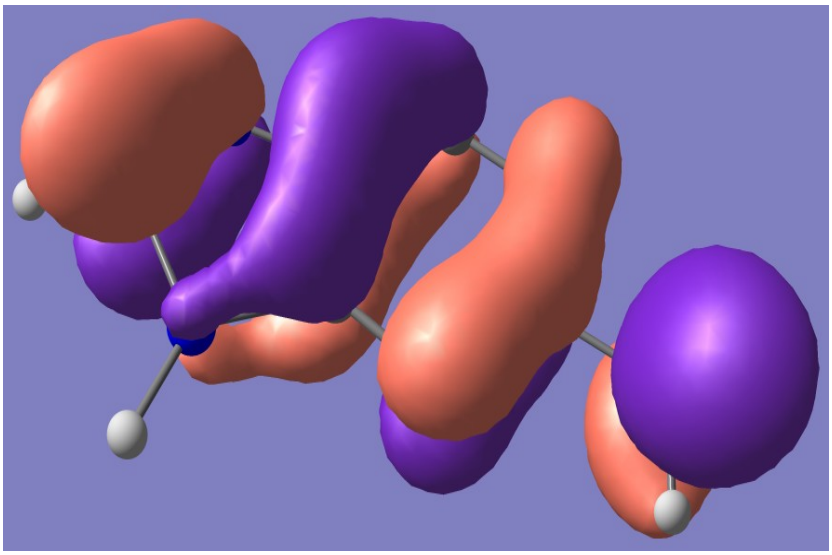

Figure 4.8 Third vertical transition of 2-Ap A tautomer in water and organic solvents

A π-π* third vertical transition of 2-Ap A tautomer in water and organic solvents (except for ethanol)

Unoccupied MO (energy level 37), π* antibonding MO

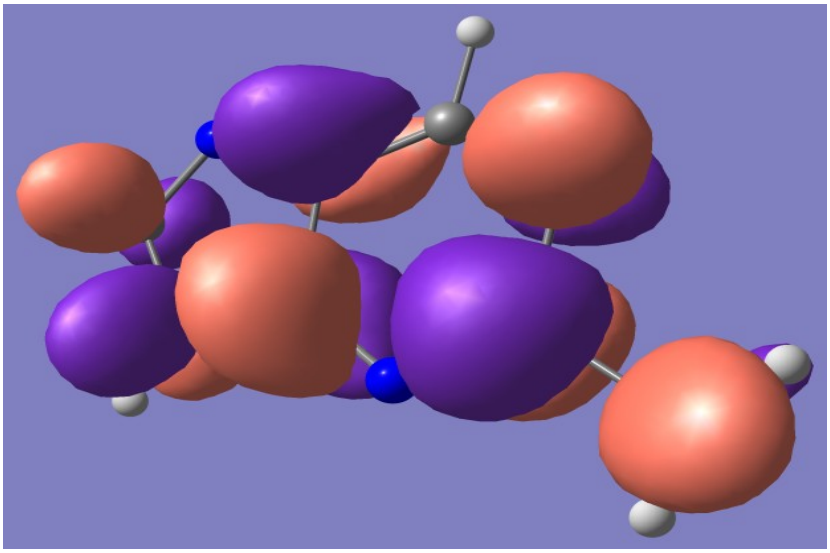

Third vertical transition of 2-Ap A tautomer in water and organic solvents (ethanol excluded)

π-π*

Occupied MO (energy level 35), π bonding MO

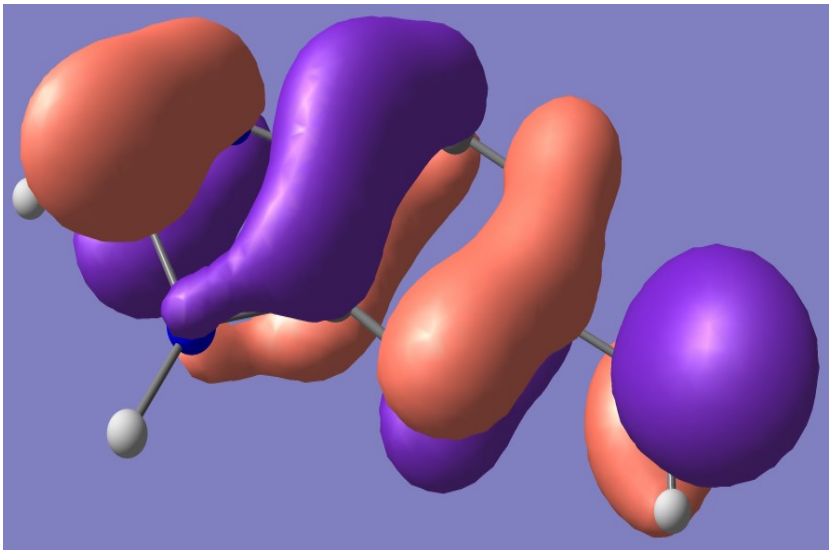

Table 4.5 2-Ap A tautomer excited singlet states

The table contains the energies in eV and nm of the first three singlet vertical transitions of 2-Ap A in vacuum and solutions. The oscillator strength *f* and the assignments of the transitions are also displayed

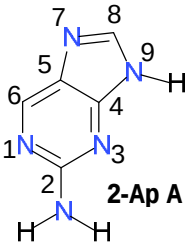 **2-Ap A**	First singlet state S_1 ΔE eV nm *f* Assignment	Second singlet state S_2 ΔE eV nm *f* Assignment	Third singlet state S_3 ΔE eV nm *f* Assignment
Vacuum	4.3570 eV 284.00 nm 0.1344 π-π*	4.4703 eV 277.35 nm 0.0023 n-π*	4.7435 eV 261.38 nm 0.0008 π-R
Water	4.2374 eV 292.60 nm 0.1594 π-π*	4.5799 eV 270.71 nm 0.0030 n-π*	4.7261 eV 262.34 nm 0.0358 π-π*
Chloroform	4.2504 eV 290.70 nm 0.1770 π-π*	4.5461 eV 272.72 nm 0.0030 n-π*	4.7343 eV 261.89 nm 0.0490 π-π*
1-propanol	4.2949 eV 288.68 nm 0.1653 π-π*	4.5837 eV 270.49 nm 0.0029 n-π*	4.7489 eV 261.08 nm 0.0387 π-π*
Acetonitrile	4.2394 eV 292.46 nm 0.1609 π-π*	4.5767 eV 270.90 nm 0.0030 n-π*	4.7271 eV 262.28 nm 0.0376 π-π*
Diethyl ether	4.2851 eV 289.34 nm 0.1696 π-π*	4.5475 eV 272.65 nm 0.0028 n-π*	4.7433 eV 261.39 nm 0.0498 π-π*
Ethyl Acetate	4.2934 eV 288.78 nm 0.1682 π-π*	4.5596 eV 271.92 nm 0.0028 n-π*	4.7462 eV 261.23 nm 0.0466 π-π*
DMSO	4.2265 eV 293.35 nm 0.1735 π-π*	4.5758 eV 270.96 nm 0.0032 n-π*	4.7269 eV 262.30 nm 0.0423 π-π*
Ethanol	4.2394 eV 292.46 nm 0.1630 π-π*	4.5742 eV 271.05 nm 0.0030 n-π*	4.7289 eV 262.18 nm 0.0031 π-R
Methanol	4.2413 eV 292.33 nm 0.1593 π-π*	4.5768 eV 270.90 nm 0.0030 n-π*	4.7299 eV 262.13 nm 0.0387 π-π*
THF	4.2626 eV 290.87 nm 0.1714 π-π*	4.5545 eV 272.22 nm 0.0030 n-π*	4.7354 eV 261.83 nm 0.0436 π-π*
2-propanol	4.2951 eV 288.67 nm 0.1654 π-π*	4.5830 eV 270.53 nm 0.0029 n-π*	4.7490 eV 261.07 nm 0.0389 π-π*

The electronic singlet-state manifolds of 2-Ap N9H amino tautomer are illustrated in Figure 4.9.

Figure 4.9 Singlet-state manifolds of 2-Ap A

Electronic energies of S_1, S_2 and S_3 states along with their characters of 2-Ap N9H amino tautomer in gas phase, water and organic solvents

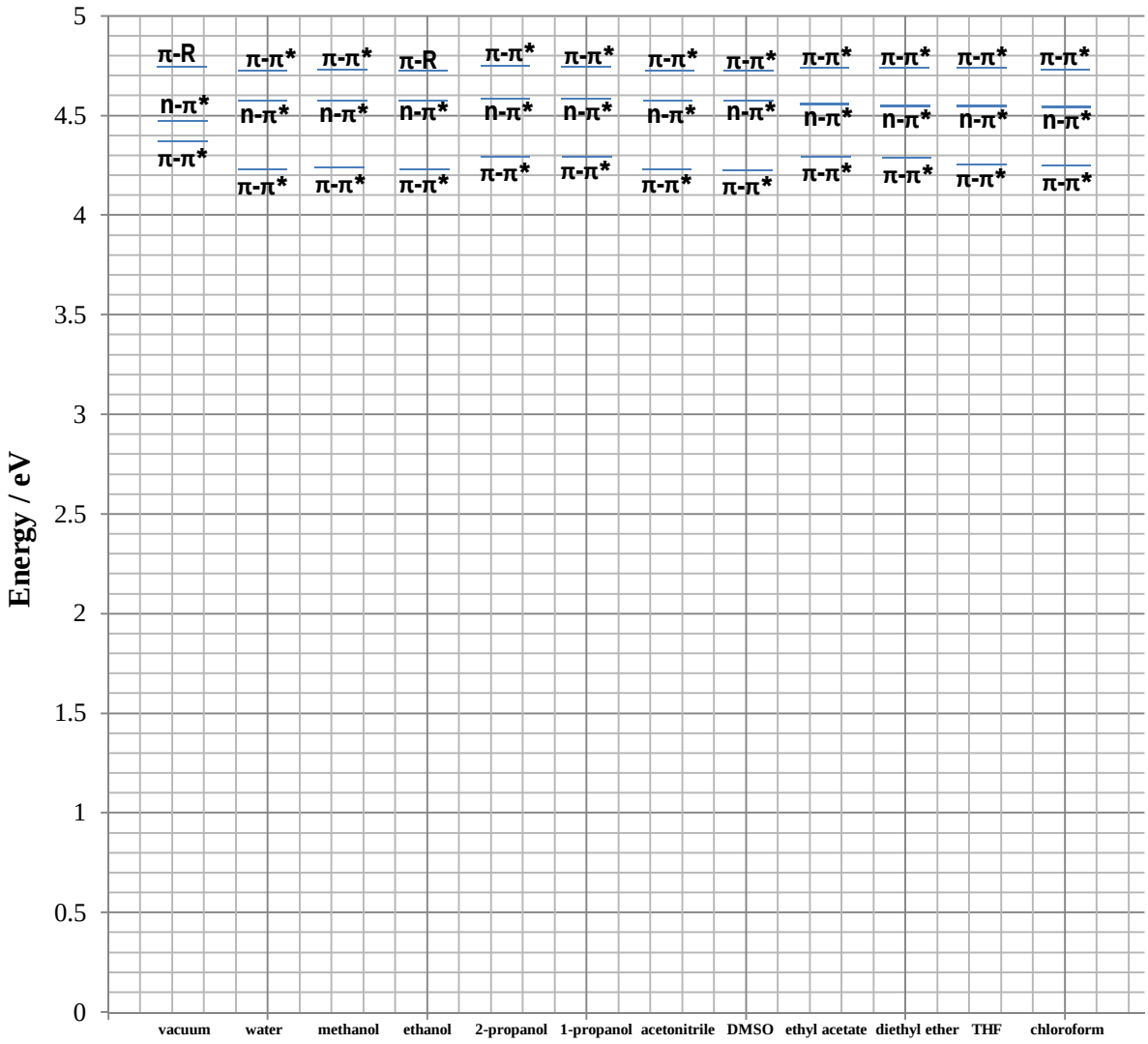

The energy gap between S_2 (n-π*) and S_1 (π-π*) appears to be smaller as the solvent polarity decreases. This decrease in energy between these two states in solvents of low dielectric constants was previously observed and studied by Rachofsky and others (Rachofsky *et al.* 2001) by using the computational method CASSCF (complete active space self-consistent field). They suggested that a solvent-mediated vibronic coupling between n-π* and π-π* states could be responsible for the reduction of 2-Ap lifetime in non-polar solvents. The proximity effect of n-π* and π-π* states on fluorescence emission and lifetimes of N-

heterocyclic compounds (Lim, 1977; Wassam and Lim, 1978; Lim, 1986) deserves further explanation. For example, azarenes containing one or more heterocyclic nitrogen atom possess low-lying n-π* states (dark states) in non-polar solvents and they have small fluorescence quantum yields. In protic solvents, azarenes have low-lying π-π*(bright states) when the lowest-lying transition is of π-π* character the fluorescence quantum yields is much bigger, as π-π* states are more efficient emitting states (Valeur, 2002). It should be noted that the oscillator strength *f* of the predicted n-π* states were found to be small because of symmetry selection rules. Transitions of n-π* character are weakly allowed due to coupling of vibrational and electronic motions in the molecule (vibronic coupling). Vibronic coupling is a result of the breakdown of the Born-Oppenheimer approximation. It should also be pointed out that the theoretically predicted Rydberg orbitals were revealed by using the diffuse function +. The calculated electronic transitions of the first three states of the probe in absence of diffuse functions did not reveal any Rydberg orbital (data not shown). Low-lying Rydberg states play an important role in many photophysical and photochemical reactions and therefore they should not be omitted (Sandorfy, 1999). The inclusion of diffuse functions generated π-π* states of lower energy and n-π* states of higher energy compared to the ones obtained without using the diffusion functions. Figure 4.10 shows the predicted transitions from two occupied molecular orbitals into two unoccupied molecular orbitals.

Figure 4.10 2-Ap A tautomer panel of the first three vertical transitions

S_1, S_2 and S_3 vertical transitions of the 2-Ap N9H amino tautomer with its respective HOMO and LUMO

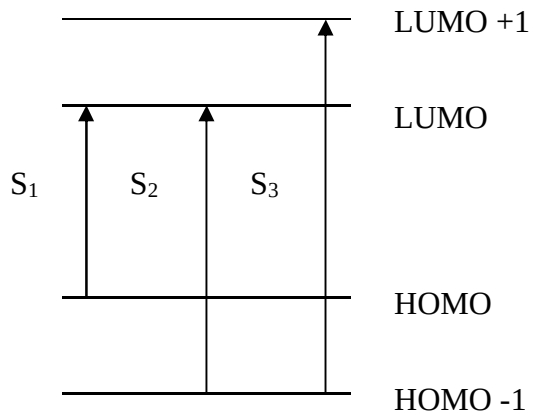

The diagram of the energy of the HOMOs (E_{HOMO}) of 2-Ap A with their respective energies in eV is shown in Figure 4.11.

Figure 4.11 E_{HOMO} of 2-Ap A

Energies of the highest occupied molecular orbitals of 2-Ap A for the first three vertical transitions

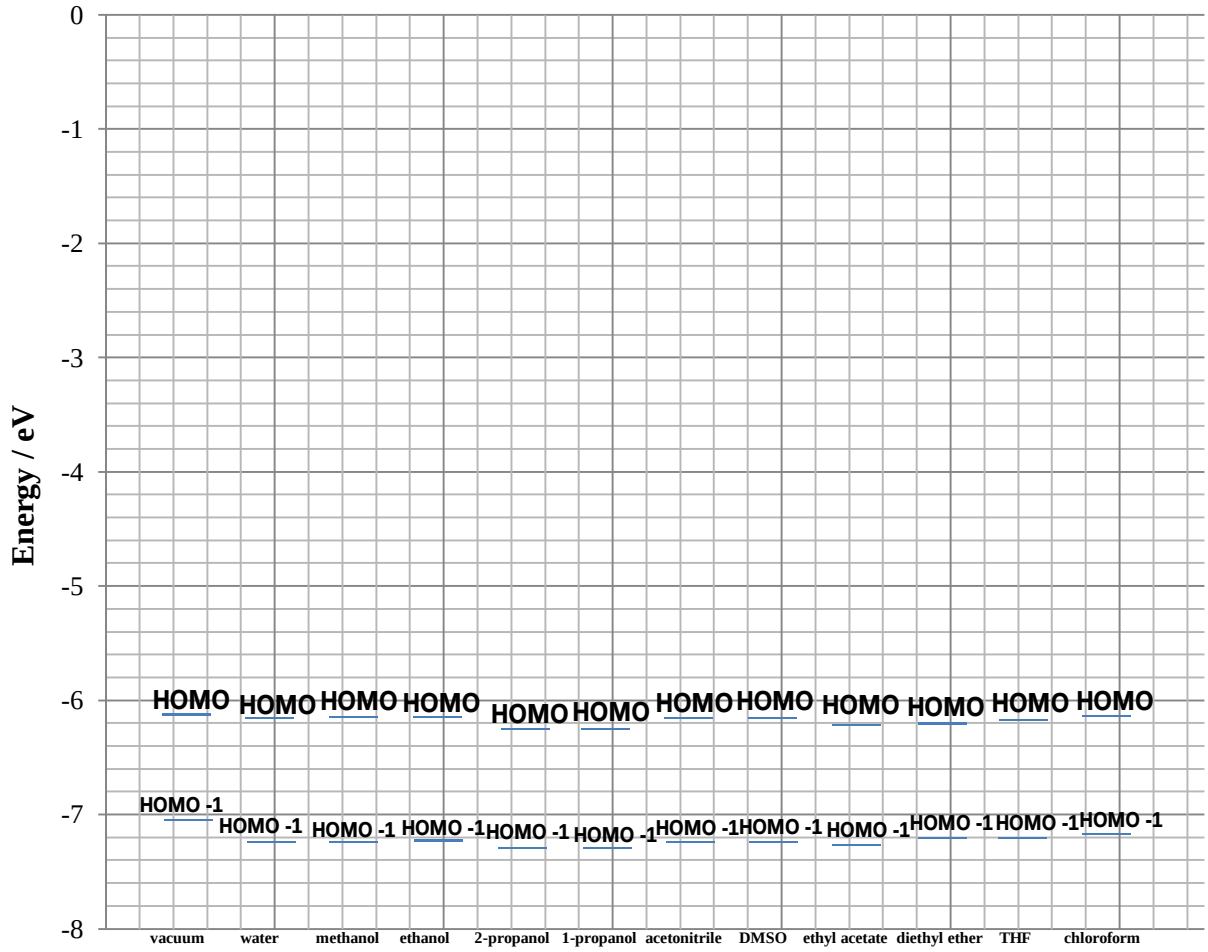

The smallest difference in energies between HOMO and HOMO -1 was the one in vacuum. A slightly smaller gap was found in non-polar solvents when compared to protic and aprotic solvents.

The energies of the LUMOs (E_{LUMO}) are displayed in Figure 4.12.

Figure 4.12 E_{LUMO} of 2-Ap A

Energies of the lowest unoccupied molecular orbitals of 2-Ap A for the first three vertical transitions

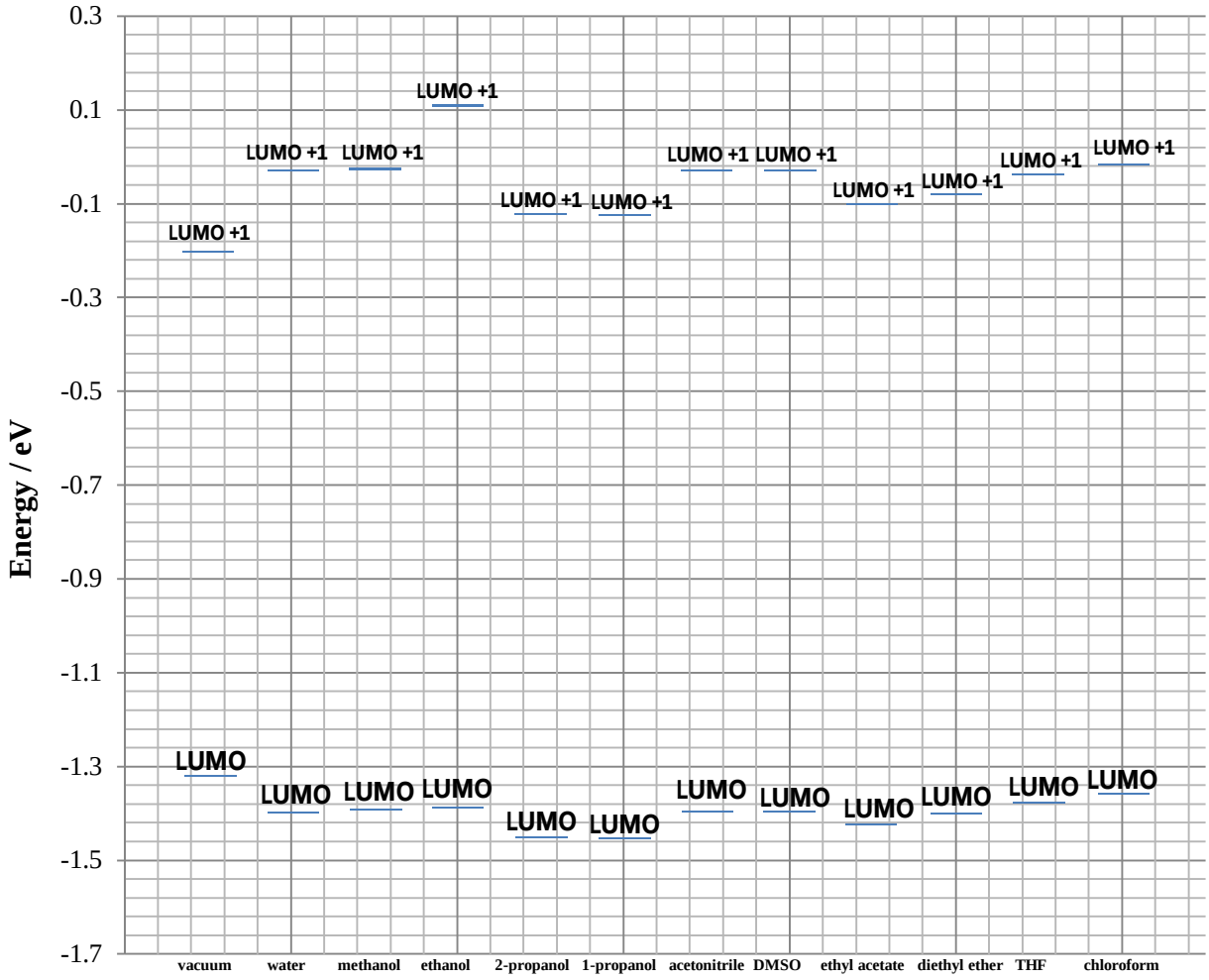

The smallest gap in energy between the LUMO and LUMO +1 was found in vacuum whereas the largest gap was found in ethanol. The LUMOs in 2-propanol and 1-propanol are the lowest in energy.

Table 4.6 2-Ap A tautomer excited triplet states

The table contains the energies expressed in eV and nm of the first three triplet vertical transitions of 2-Ap A in vacuum and solutions. The oscillator strength *f* and the assignments of the transitions are also displayed

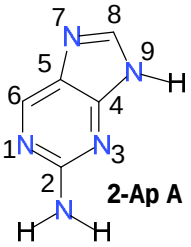 2-Ap A	First triplet state T_1 ΔE		Second triplet state T_2 ΔE		Third triplet state T_3 ΔE	
	eV	nm	eV	nm	eV	nm
	f	Assignment	*f*	Assignment	*f*	Assignment
Vacuum	3.1346 eV	395.53 nm	4.0916 eV	303.02 nm	4.2169 eV	294.02 nm
	0.0000	π-π*	0.0000	n-π*	0.0000	π-π*
Water	3.0761 eV	403.06 nm	4.2110 eV	294.43 nm	4.2148 eV	294.17 nm
	0.0000	π-π*	0.0000	n-π*	0.0000	π-π*
Chloroform	3.0942 eV	400.69 nm	4.1779 eV	296.77 nm	4.2156 eV	294.11 nm
	0.0000	π-π*	0.0000	n-π*	0.0000	π-π*
1-propanol	3.1162 eV	397.87 nm	4.2159 eV	294.09 nm	4.2246 eV	293.48 nm
	0.0000	π-π*	0.0000	n-π*	0.0000	π-π*
Acetonitrile	3.0785 eV	402.74 nm	4.2084 eV	294.61 nm	4.2141 eV	294.21 nm
	0.0000	π-π*	0.0000	n-π*	0.0000	π-π*
Diethyl ether	3.1089 eV	398.81 nm	4.1776 eV	296.78 nm	4.2169 eV	294.02 nm
	0.0000	π-π*	0.0000	n-π*	0.0000	π-π*
Ethyl Acetate	3.1158 eV	397.92 nm	4.1906 eV	295.87 nm	4.2225 eV	293.63 nm
	0.0000	π-π*	0.0000	n-π*	0.0000	π-π*
DMSO	3.0789 eV	402.69 nm	4.2092 eV	294.55 nm	4.2142 eV	294.21 nm
	0.0000	π-π*	0.0000	n-π*	0.0000	π-π*
Ethanol	3.0796 eV	402.60 nm	4.2060 eV	294.78 nm	4.2143 eV	294.20 nm
	0.0000	π-π*	0.0000	n-π*	0.0000	π-π*
Methanol	3.0786 eV	402.72 nm	4.2081 eV	294.63 nm	4.2145 eV	294.18 nm
	0.0000	π-π*	0.0000	n-π*	0.0000	π-π*
THF	3.1017 eV	399.73 nm	4.1865 eV	296.15 nm	4.2170 eV	294.01 nm
	0.0000	π-π*	0.0000	n-π*	0.0000	π-π*
2-propanol	3.1164 eV	397.84 nm	4.2152 eV	294.14 nm	4.2246 eV	293.48 nm
	0.0000	π-π*	0.0000	n-π*	0.0000	π-π*

The Figure 4.13 shows the electronic triplet-state manifolds of 2-Ap A. The energies of the states in eV were taken from the Table 4.6. (The table includes the oscillator strength *f* which is 0.0000 because electronic transitions involving singlet and triplet states are considered forbidden). No Rydberg orbitals were predicted and a considerable gap in energy was calculated between T_3 and T_2 in vacuum compared to the ones in solutions.

Figure 4.13 Triplet-state manifolds of 2-Ap A

Electronic energies of T_1, T_2 and T_3 states along with their characters of 2-Ap N9H amino tautomer in gas phase, water and organic solvents

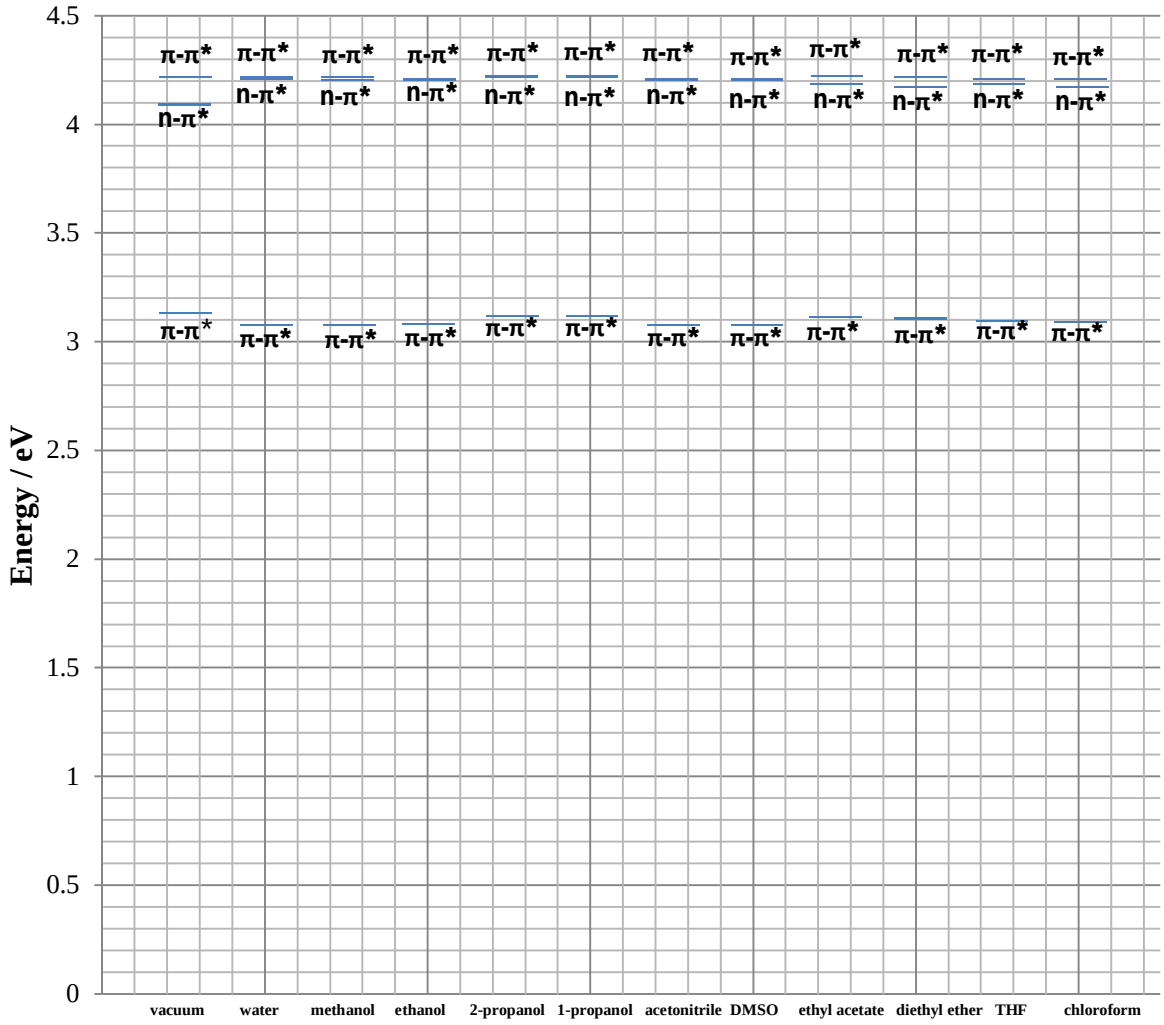

4.6.2 Comparing theoretical absorption with experimental absorption of 2-Ap

TDDFT calculations for electronic state ordering and excitation energies of 2-Ap N9H amino tautomer in water are in good agreement with the literature (He *et al*. 2005). He and colleagues found that the first vertical transition a π-π* transition, has an absorption energy of 4.16 eV (298 nm) with an oscillator strength 0.1540 and the second vertical transition n-π* has a predicted energy of 4.50 eV (275 nm) along with a much smaller oscillator strength, 0.0030, compared to the first vertical transition calculated, f = 0.1584 and 4.2374 eV (292.60 nm), see table 4.5 for comparison. An attempt was made to compare the wavelength of the theoretically predicted vertical transitions with the experimental maxima absorption bands in water and organic solvents, see Figure 4.14 and 4.15. The theoretically predicted energies of the first vertical transitions appear to be blue-shifted with respect to the experimental absorption bands representing the maxima of the first excitation transition. Whereas, the theoretically predicted energies of the second and third vertical transitions result to be red-shifted with respect to the experimental absorption bands. Also, as shown in Figure 4.14 the probability of these transitions is much smaller than the first vertical transitions as indicated by the low oscillator strengths reported in the figure. Also, very small oscillator strengths were predicted for second vertical transitions of n-π* character because it is a transition between two different types of orbitals, and therefore, symmetrically forbidden.

Figure 4.14 2-Ap absorption spectra and theoretically predicted vertical transitions

Experimental absorption spectra and predicted vertical transition represented as red lines of fixed magnitude. The oscillator strengths indicating the probability of the transitions are also reported

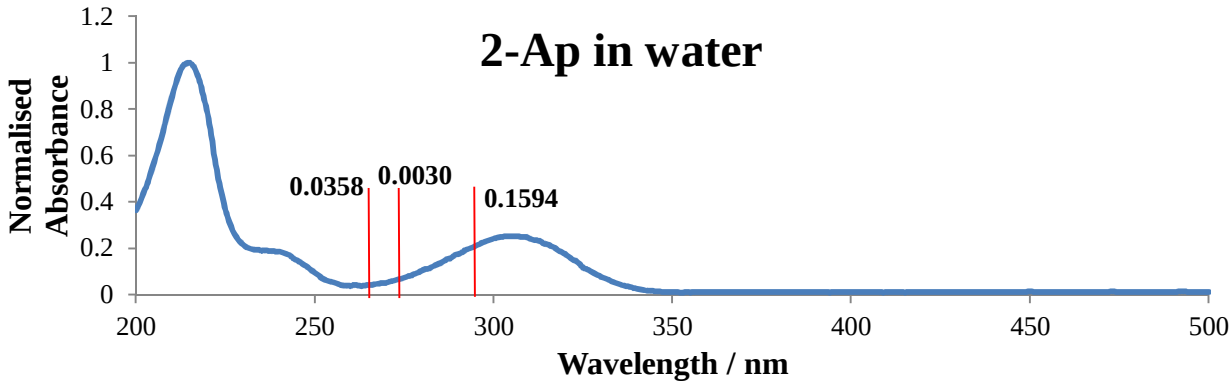

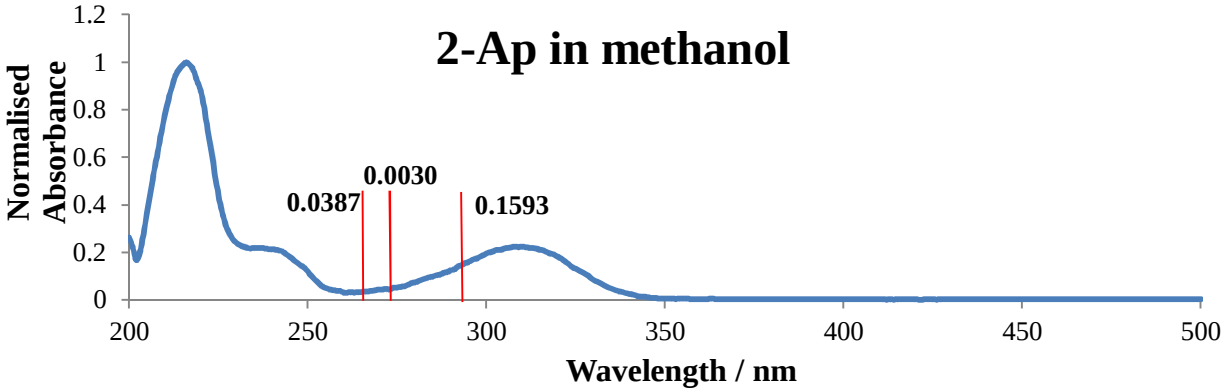
2-Ap in methanol
Normalised Absorbance
Wavelength / nm
0.0387
0.0030
0.1593

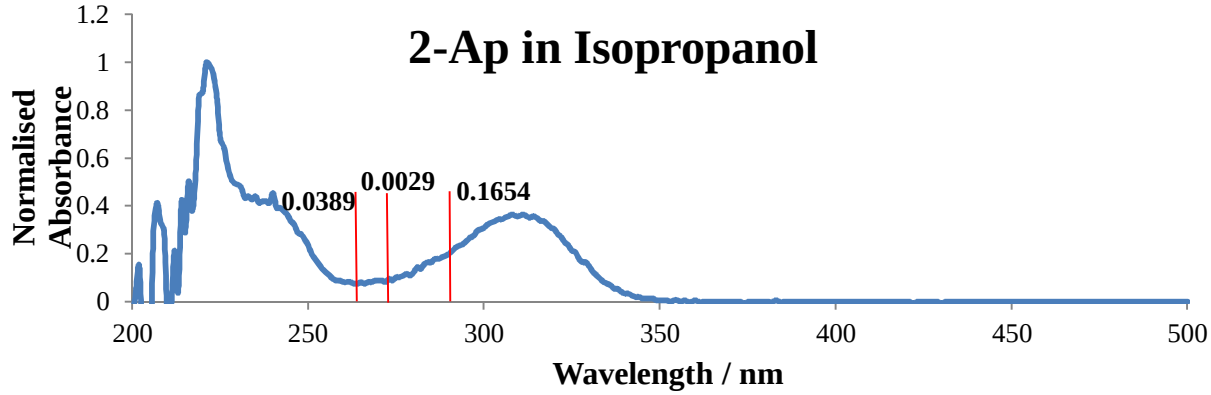
2-Ap in Isopropanol
Normalised Absorbance
Wavelength / nm
0.0389
0.0029
0.1654

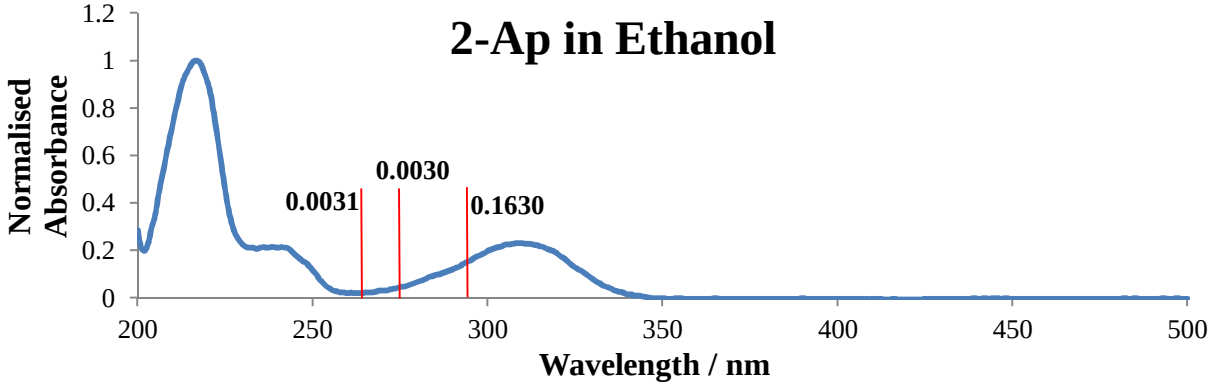
2-Ap in Ethanol
Normalised Absorbance
Wavelength / nm
0.0031
0.0030
0.1630

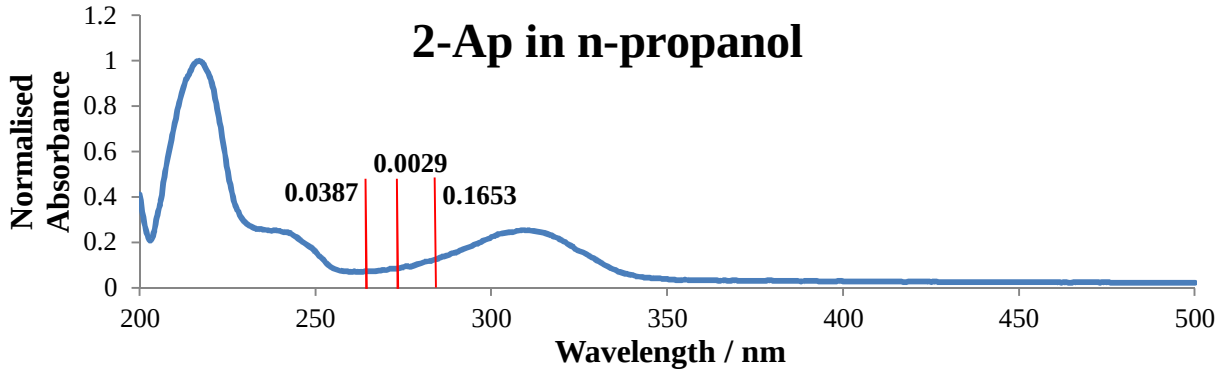
2-Ap in n-propanol
Normalised Absorbance
Wavelength / nm
0.0387
0.0029
0.1653

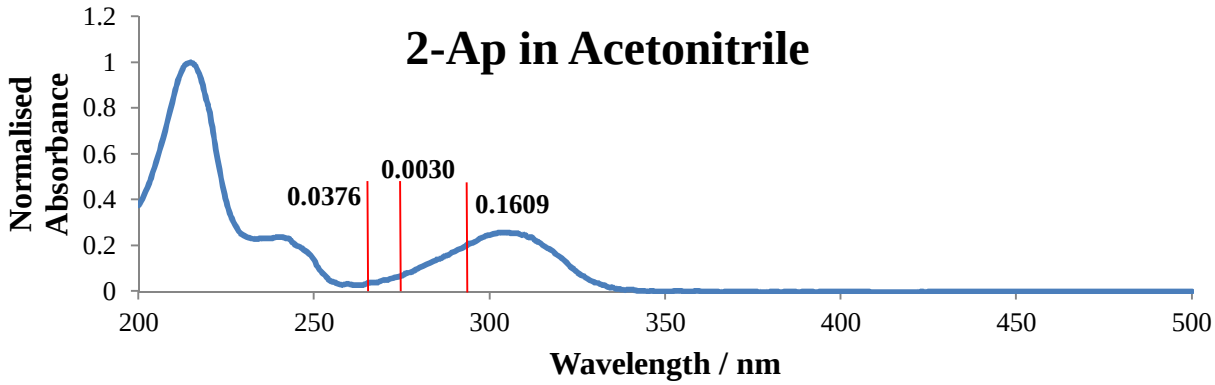
2-Ap in Acetonitrile
Normalised Absorbance
Wavelength / nm
0.0376
0.0030
0.1609

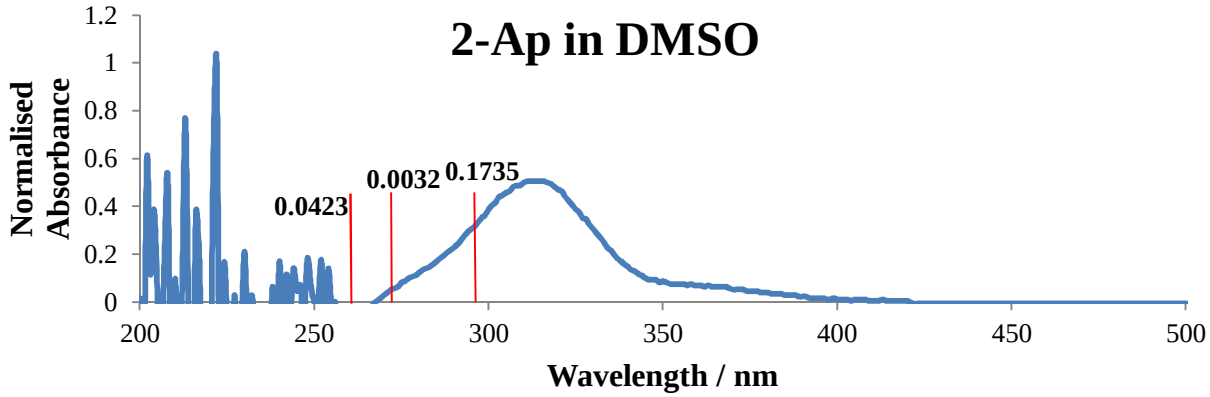
2-Ap in DMSO
Normalised Absorbance
Wavelength / nm
0.0423
0.0032
0.1735

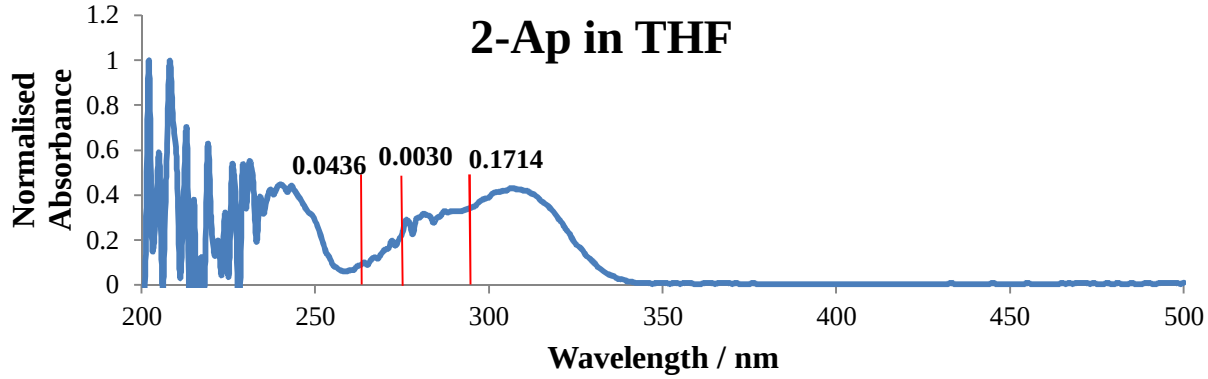
2-Ap in THF
Normalised Absorbance
Wavelength / nm
0.0436
0.0030
0.1714

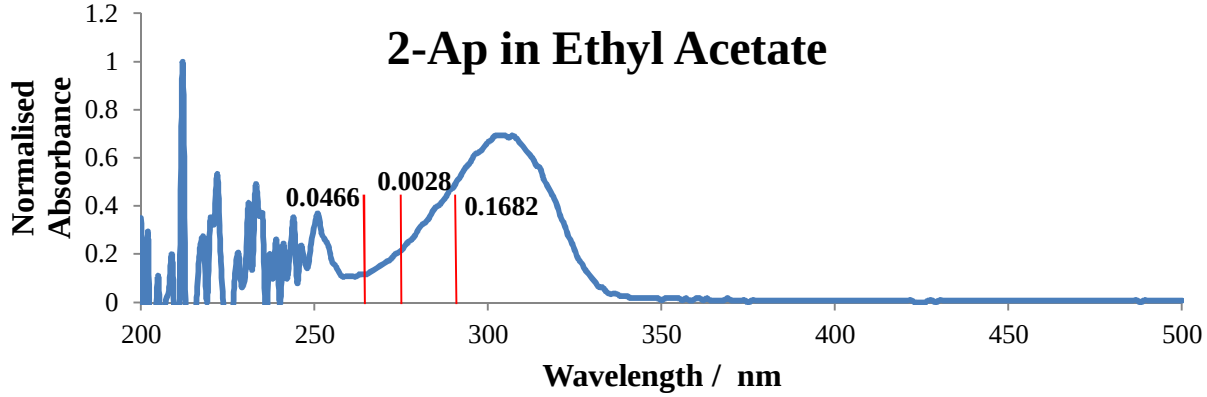
2-Ap in Ethyl Acetate
Normalised Absorbance
Wavelength / nm
0.0466
0.0028
0.1682

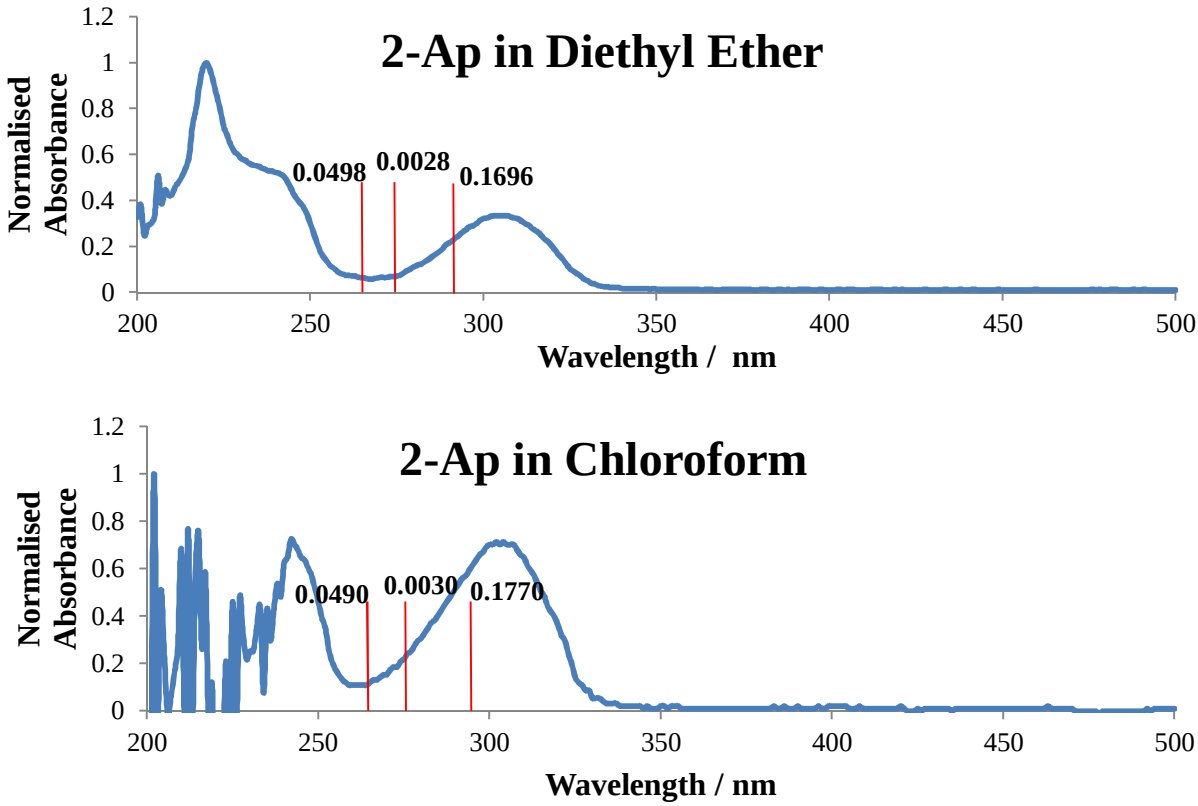

Figure 4.15 Theoretical and experimental absorption of 2-Ap in different solvents

A comparative summary of theoretical and experimental absorption of 2-Ap in different solvents

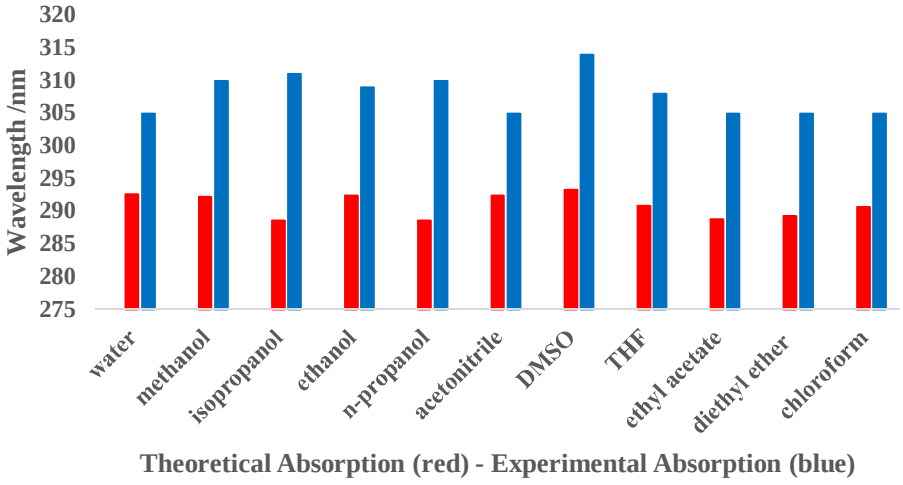

4.6.3 Vertical transitions of Pc A tautomer

As in the case of 2-Ap A the energies of the first three vertical transitions of Pc A which are an estimation of absorption maxima were calculated, and their character was assigned. The single point geometry of Pc A tautomer displayed prior to rendering of molecular orbitals is shown below in Figure 4.16.

Figure 4.16 Pc A displayed on Chemcraft (Gaussview style)

Pc A tautomer displayed on Gaussview style prior to rendering of molecular orbitals. Nitrogen atoms in blue, carbon atoms in grey, oxygen atom in red and hydrogen atoms in white

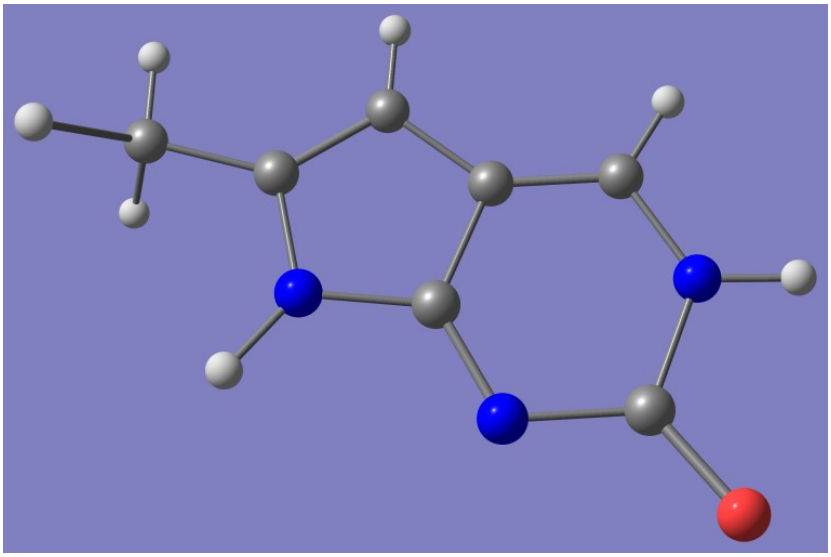

The first vertical transition of Pc A in vacuum, water and organic solvents is a π-π* electronic transition, see Figure 4.17. The second vertical transition of the probe is an electronic transition of π-π* character in water, 1-propanol, acetonitrile, DMSO, ethanol and methanol (see Figure 4.19, a π-π* electronic transition in water) whereas it is of n-π* character in vacuum, chloroform, diethyl ether, ethyl acetate, THF and 2-propanol. Figure 4.18 shows an n-π* electronic transition in vacuum. The third vertical transition results to be of π-R character in vacuum, chloroform, diethyl ether and THF, the Figure 4.20 shows an electronic transition of π-R character in chloroform. In water, 1-propanol, acetonitrile, DMSO, ethanol and methanol the third vertical transition is an n-π* transition. In the case of ethyl acetate and 2-propanol the transition was found to be of π-π* character. The table 4.7 and 4.8 include the assignments of the singlet and triplet electronic transitions along with ΔE of the transitions, expressed in eV and nm and its oscillator strength *f*.

Figure 4.17 First vertical transition of Pc A tautomer

A π-π* first vertical transition of Pc A tautomer

Unoccupied MO
(energy level 40),
π* antibonding MO

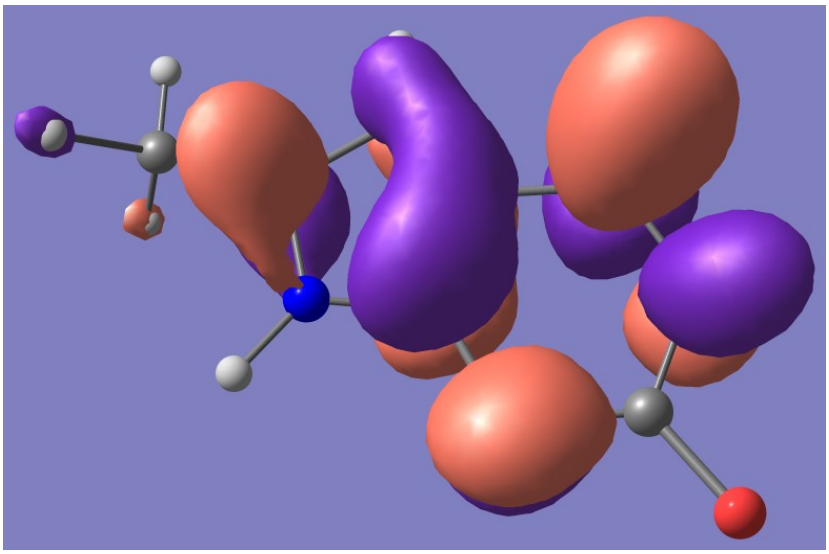

First vertical transition
of Pc N1H (A) tautomer
in vacuum and solution
(water and organic solvents)

π-π*

Occupied MO
(energy level 39),
π bonding MO

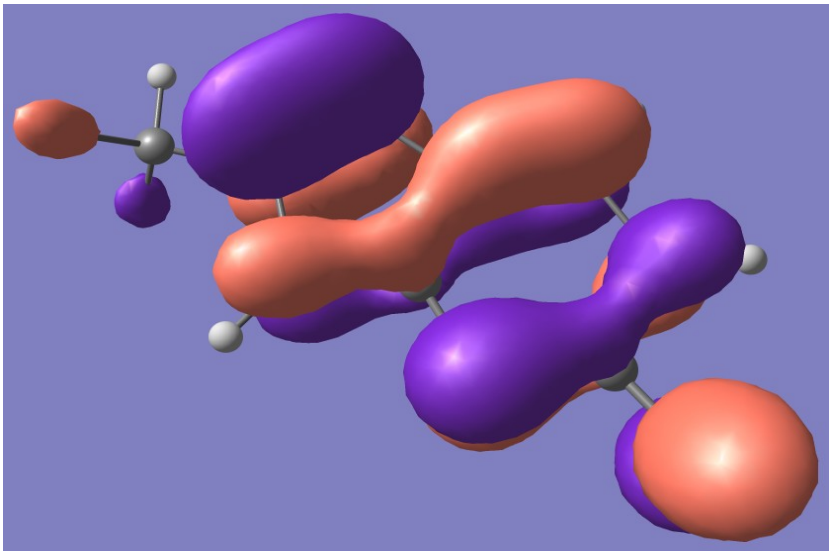

Figure 4.18 Second vertical transition of Pc A tautomer in vacuum

A n-π* second vertical transition of Pc A tautomer in vacuum

Unoccupied MO
(energy level 40),
π* antibonding MO

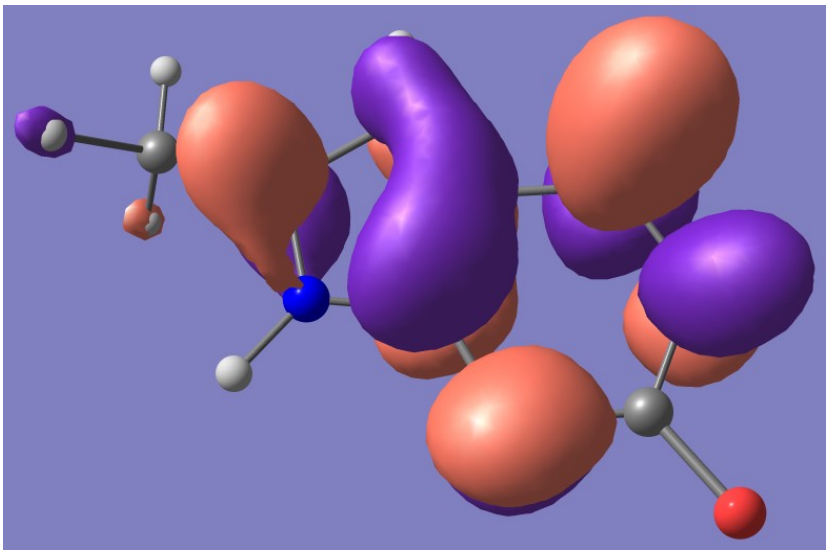

Second vertical transition
of Pc A tautomer in
vacuum

n-π*

Occupied MO
(energy level 38),
n non- bonding MO

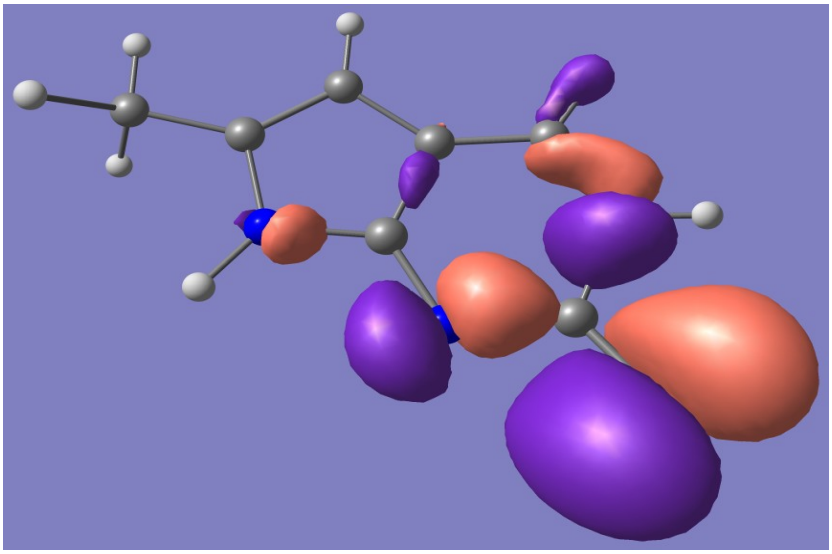

Figure 4.19 Second vertical transition of Pc A tautomer in water

A π-π* second vertical transition of Pc A tautomer in water

Unoccupied MO
(energy level 40),
π* antibonding MO

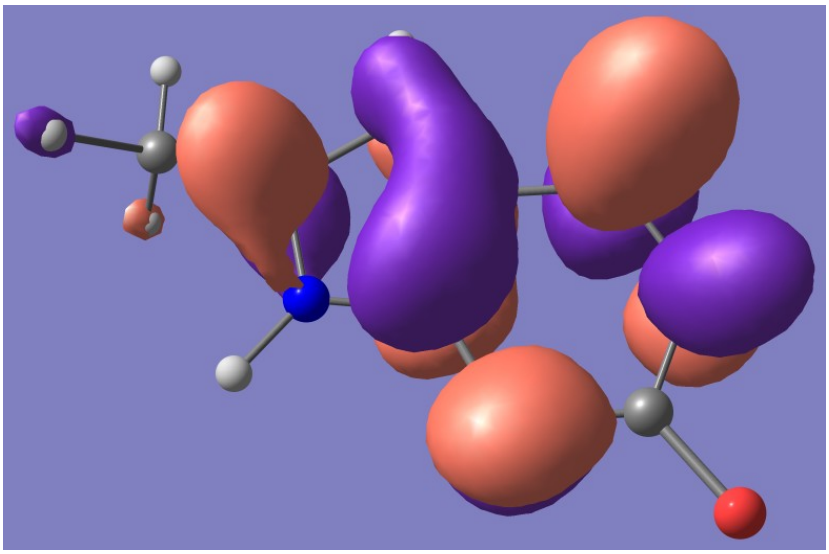

Second vertical transition
of Pc N1H (A) tautomer
in water

π-π*

Occupied MO
(energy level 38),
π bonding MO

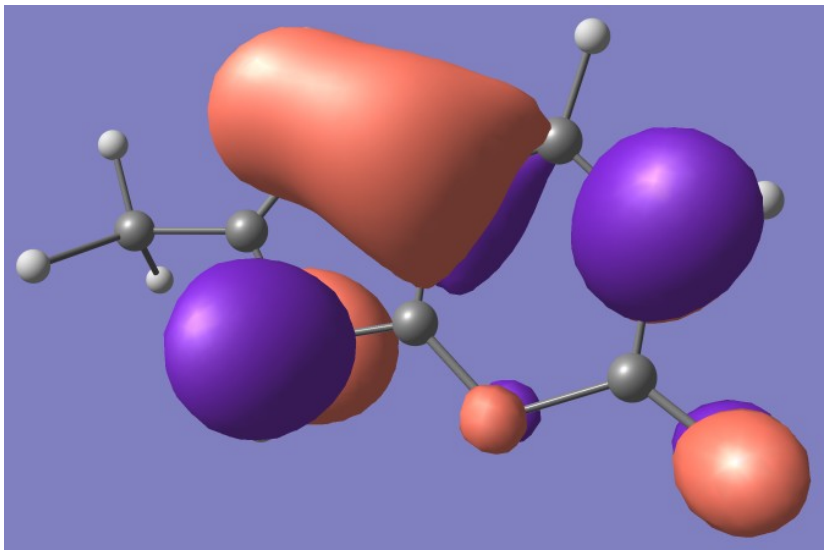

Figure 4.20 Third vertical transition of Pc A in chloroform

A π-Rydberg third vertical transition of Pc A tautomer in chloroform

Unoccupied MO (energy level 41), Rydberg MO

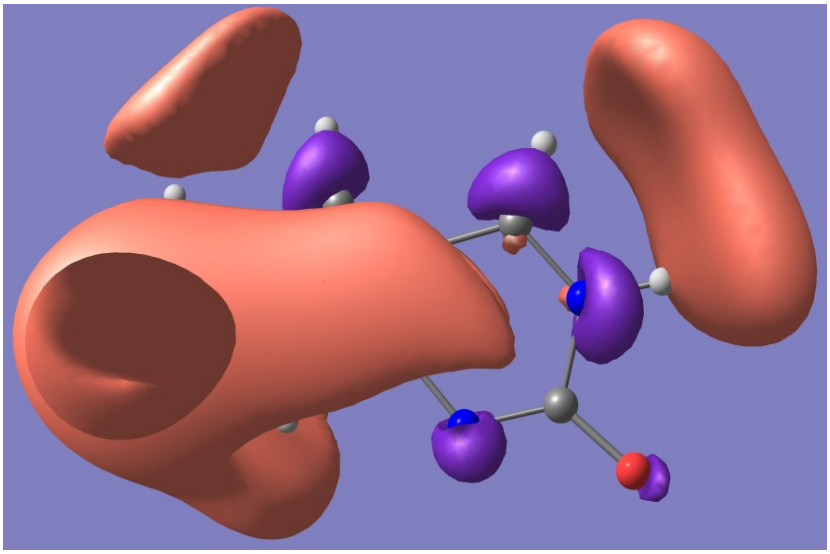

Third vertical transition of Pc A tautomer in chloroform

π-Rydberg MO

Occupied MO (energy level 39), π bonding MO

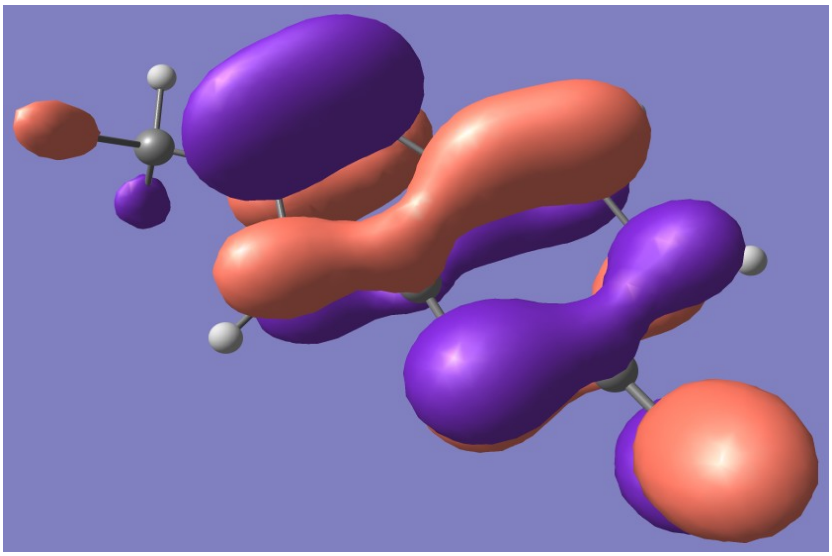

Table 4.7 Pc A tautomer excited singlet states

The table contains the energies expressed in eV and nm of the first three singlet vertical transitions of Pc A in vacuum and solutions. The oscillator strength *f* and the assignments of the transitions are also displayed

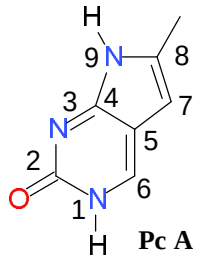 **Pc A**	First singlet state S_1 ΔE eV *f*	 nm Assignment	Second singlet state S_2 ΔE eV *f*	 nm Assignment	Third singlet state S_3 ΔE eV *f*	 nm Assignment
Vacuum	3.5850 eV 0.0737	345.84 nm π-π*	4.4219 eV 0.0004	280.39 nm n-π*	4.4708 eV 0.0000	277.32 nm π-R
Water	3.6719 eV 0.0837	337.66 nm π-π*	4.6335 eV 0.0079	267.58 nm π-π*	4.8308 eV 0.0013	256.65 nm n-π*
Chloroform	3.6264 eV 0.0924	341.89 nm π-π*	4.6028 eV 0.0010	269.37 nm n-π*	4.7098 eV 0.0000	263.25 nm π-R
1-propanol	3.6603 eV 0.0857	338.73 nm π-π*	4.6272 eV 0.0079	267.95 nm π-π*	4.8502 eV 0.0012	255.63 nm n-π*
Acetonitrile	3.6675 eV 0.0845	338.06 nm π-π*	4.6296 eV 0.0079	267.81 nm π-π*	4.8709 eV 0.0013	254.54 nm n-π*
Diethyl ether	3.6260 eV 0.0890	341.93 nm π-π*	4.5883 eV 0.0008	270.22 nm n-π*	4.6895 eV 0.0000	264.39 nm π-R
Ethyl Acetate	3.6380 eV 0.0878	340.80 nm π-π*	4.6033 eV 0.0009	269.34 nm n-π*	4.7386 eV 0.0066	261.64 nm π-π*
DMSO	3.6588 eV 0.0903	338.87 nm π-π*	4.6308 eV 0.0085	267.74 nm π-π*	4.8767 eV 0.0014	254.24 nm n-π*
Ethanol	3.6634 eV 0.0855	338.44 nm π-π*	4.6266 eV 0.0077	267.98 nm π-π*	4.8569 eV 0.0013	255.27 nm n-π*
Methanol	3.6679 eV 0.0837	338.02 nm π-π*	4.6286 eV 0.0077	267.86 nm π-π*	4.8674 eV 0.0013	254.73 nm n-π*
THF	3.6419 eV 0.0892	340.43 nm π-π*	4.6124 eV 0.0010	268.81 nm n-π*	4.7692 eV 0.0000	259.97 nm π-R
2-propanol	3.6597 eV 0.0858	338.78 nm π-π*	4.6264 eV 0.0013	267.99 nm n-π*	4.8470 eV 0.0084	255.80 nm π-π*

The electronic-state manifolds of Pc N1H N9H keto tautomer are displayed in Figure 4.21.

Figure 4.21 Singlet-state manifolds of Pc A

Electronic energies of S_1, S_2 and S_3 states along with their characters of Pc N1H in vacuum, water and organic solvents

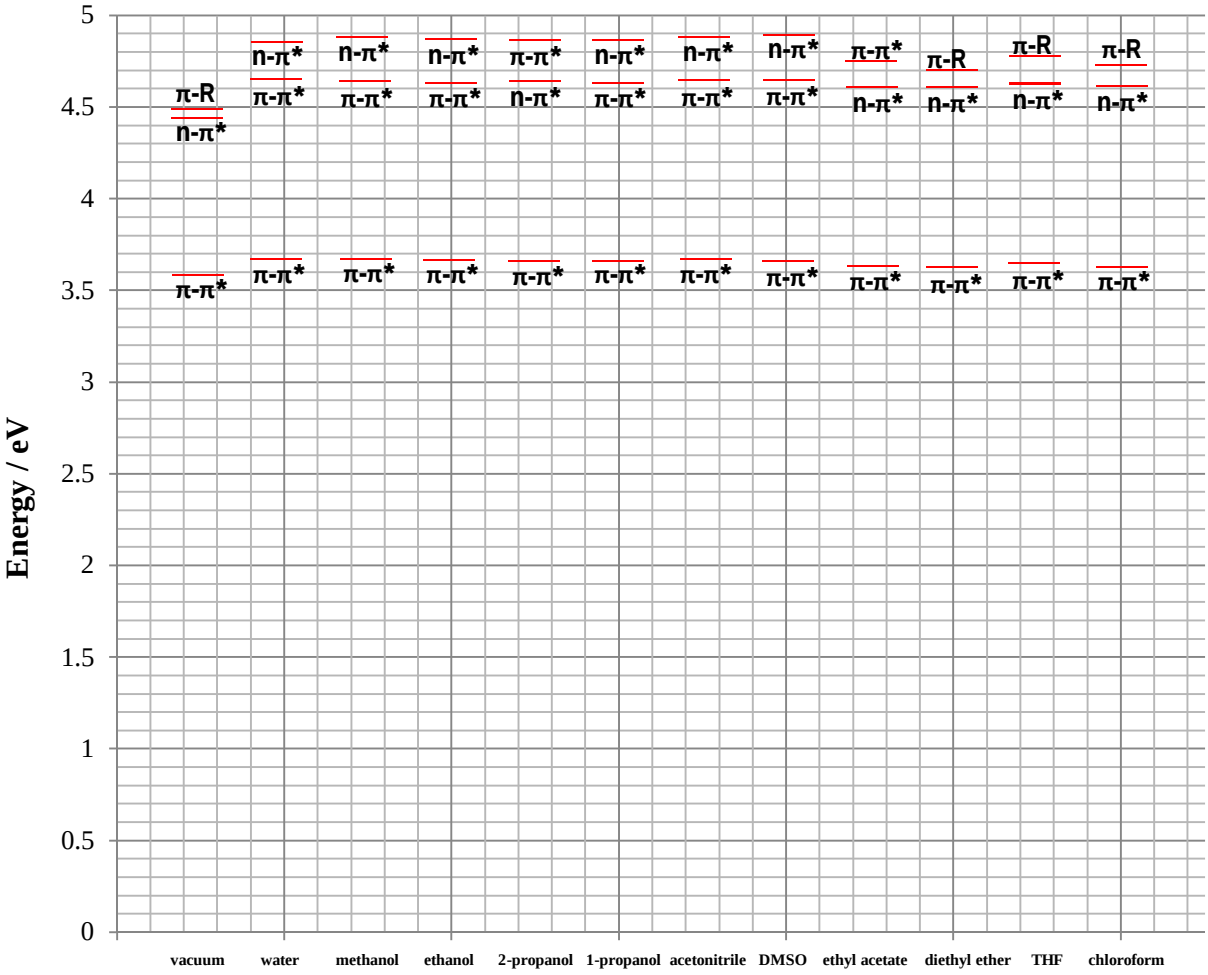

From Figure 4.21 the S_2 and S_3 states of Pc A in vacuum are within close energetic distance with respect to the states in solutions. In protic solvents and solvents having high-dielectric constants such as DMSO and acetonitrile the character of the S_2 state is of π-π* character except for 2-propanol. In the case of solvents with low-dielectric constants (ethyl acetate, diethyl ether, THF and chloroform) the S_2 state is a state of n-π* character. The gap in energy between S_3 and S_2 is slightly smaller in solvents with low-dielectric constants compared to all other solvents apart from water. Also, alike 2-Ap the observed theoretically predicted

Rydberg orbitals were revealed by using the diffuse function notation + (the data obtained without including the diffuse function has not been shown). Then, the inclusion of diffuse functions is essential when studying Rydberg states (Cramer, 2002). It was found that the predicted transitions of the molecule in protic solvents, DMSO, acetonitrile and ethyl acetate involve three occupied molecular orbitals and one unoccupied molecular orbital. In vacuum, THF, diethyl ether and chloroform the transitions occur from two occupied molecular orbitals to two occupied molecular orbitals, see Figure 4.22.

Figure 4.22 Pc A tautomer panel of the first three vertical transitions

S_1, S_2 and S_3 vertical transitions of Pc N1H between their respective occupied and unoccupied orbitals

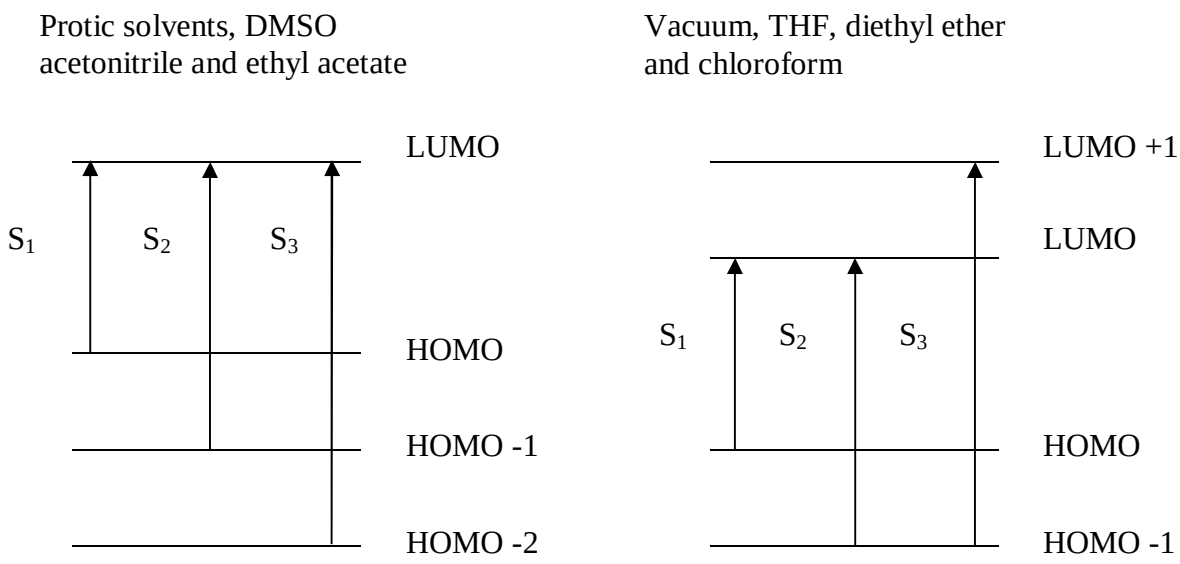

The diagram of the HOMOs (E_{HOMO}) of Pc A with their respective energies in eV is shown below in Figure 4.23. The energy transitions of this molecule involves HOMO -2 when the computed transitions between molecular orbitals were obtained in protic and aprotic solvents. In the case of non-polar solvents, it was found that HOMO -1 was involved in higher energy transitions as the first excitable state in which the molecule is excited in order to generate the first three electronic vertical transitions energies.

Figure 4.23 E_{HOMO} of Pc A

Energies of the occupied molecular orbitals of Pc A involved in the first three vertical transitions

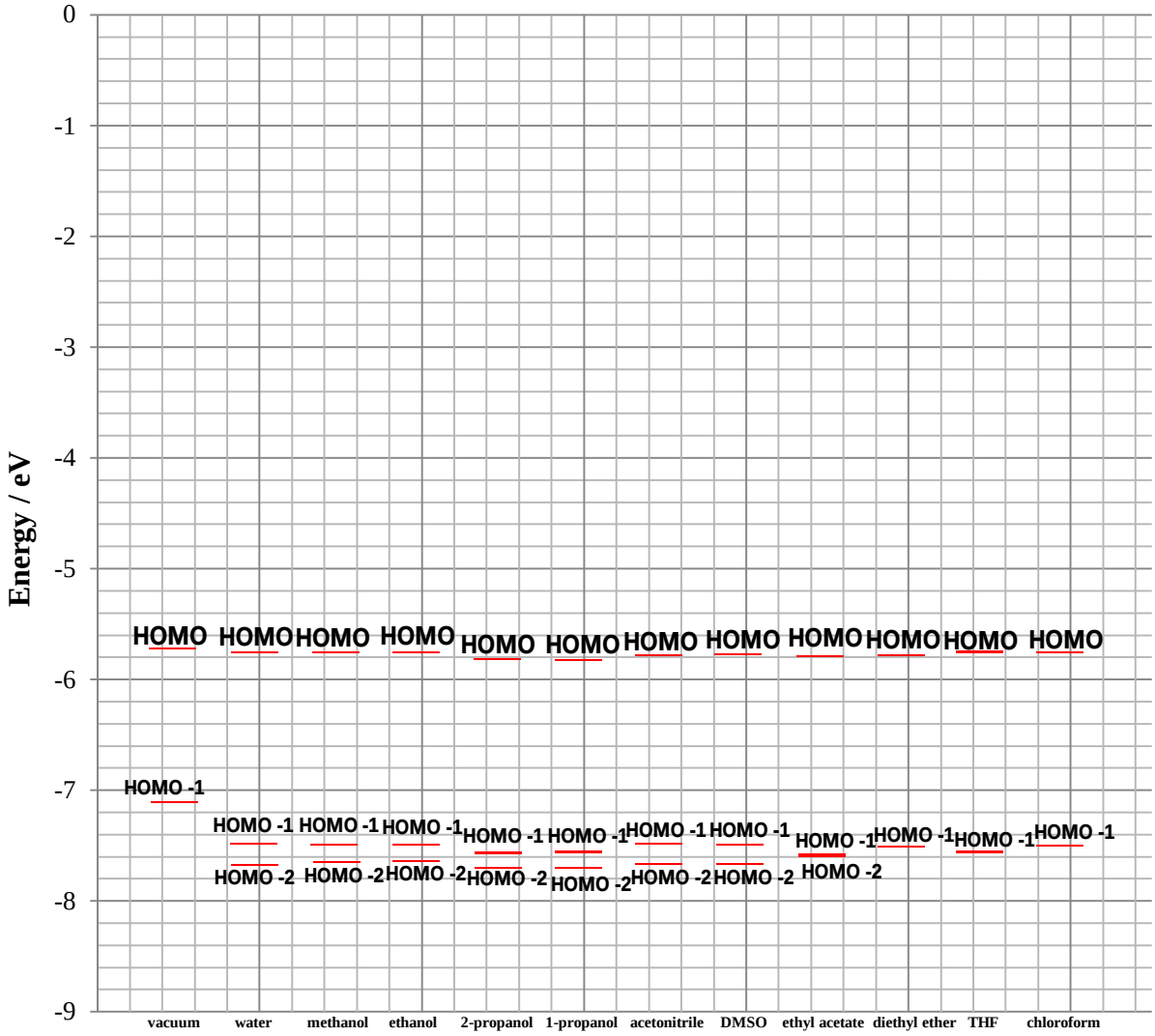

The LUMOs are displayed in Figure 4.24. The lowest LUMO in terms of energy is the one of Pc N1H in vacuum. When compared to the LUMOs of 2-Ap A in different solvents, see Figure 4.12, the LUMOs of Pc A are lower in energy. There is only one unoccupied molecular orbital involved in any of the first three vertical transitions for the molecule in protic solvents, acetonitrile, DMSO and ethyl acetate.

Figure 4.24 E_{LUMO} of Pc A

Energies of the unoccupied molecular orbitals of Pc A for the first three vertical transitions

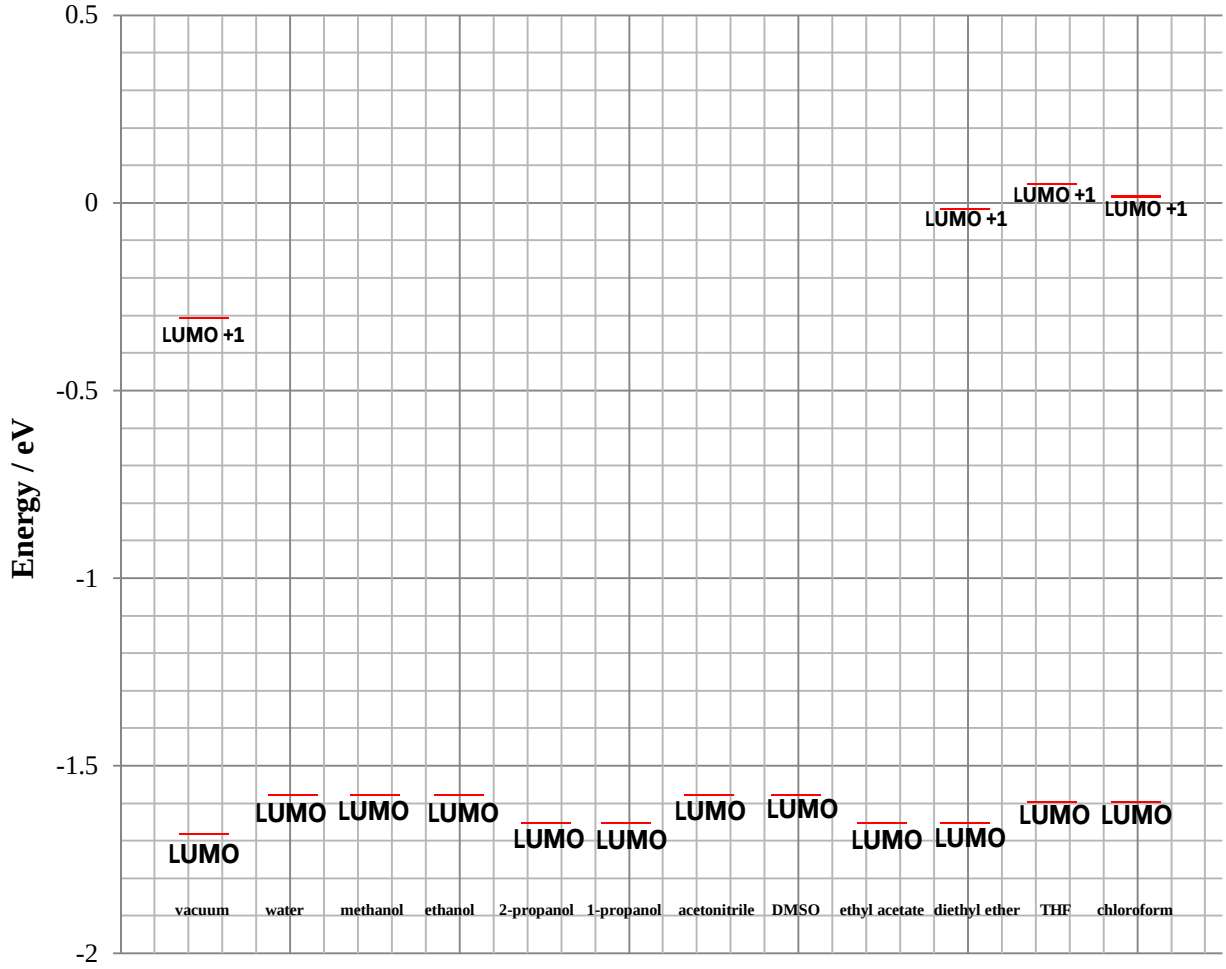

The electronic triplet-state manifolds of Pc N1H N9H keto tautomer are illustrated in Figure 4.25. The energies of the states were taken from the Table 4.8. All the electronic triplet states were found to be of π-π* character in exception for the T_3 state of the probe in vacuum which was assigned as an n-π* transition. The theoretically predicted states in vacuum appear to be lower in energy compared to the states predicted in solutions.

Table 4.8 Pc A tautomer excited triplet states

The table contains the energies expressed in eV and nm of the first three triplet vertical transitions of Pc A in vacuum and solutions. The oscillator strength *f* and the assignments of the transitions are also displayed

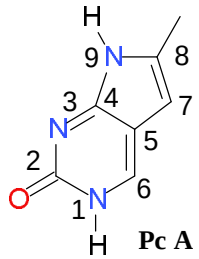 **Pc A**	First triplet state T_1		Second triplet state T_2		Third triplet state T_3	
	ΔE		ΔE		ΔE	
	eV	nm	eV	nm	eV	nm
	f	Assignment	*f*	Assignment	*f*	Assignment
Vacuum	2.2789 eV	544.04 nm	4.0470 eV	306.36 nm	4.2213 eV	293.71 nm
	0.0000	π-π*	0.0000	π-π*	0.0000	n-π*
Water	2.4595 eV	504.10 nm	4.0976 eV	302.58 nm	4.3374 eV	285.85 nm
	0.0000	π-π*	0.0000	π-π*	0.0000	π-π*
Chloroform	2.4052 eV	515.48 nm	4.0950 eV	302.77 nm	4.3552 eV	284.68 nm
	0.0000	π-π*	0.0000	π-π*	0.0000	π-π*
1-propanol	2.4374 eV	508.67 nm	4.1004 eV	302.37 nm	4.3558 eV	284.64 nm
	0.0000	π-π*	0.0000	π-π*	0.0012	π-π*
Acetonitrile	2.4545 eV	505.14 nm	4.0974 eV	302.59 nm	4.3396 eV	285.70 nm
	0.0000	π-π*	0.0000	π-π*	0.0000	π-π*
Diethyl ether	2.3906 eV	518.63 nm	4.0973 eV	302.60 nm	4.3686 eV	283.81 nm
	0.0000	π-π*	0.0000	π-π*	0.0000	π-π*
Ethyl Acetate	2.4067 eV	515.17 nm	4.0994 eV	302.45 nm	4.3634 eV	284.15 nm
	0.0000	π-π*	0.0000	π-π*	0.0000	π-π*
DMSO	2.4564 eV	504.74 nm	4.0968 eV	302.63 nm	4.3391 eV	285.74 nm
	0.0000	π-π*	0.0000	π-π*	0.0000	π-π*
Ethanol	2.4502 eV	506.02 nm	4.0976 eV	302.58 nm	4.3410 eV	285.61 nm
	0.0000	π-π*	0.0000	π-π*	0.0000	π-π*
Methanol	2.4534 eV	505.37 nm	4.0976 eV	302.58 nm	4.3394 eV	285.72 nm
	0.0000	π-π*	0.0000	π-π*	0.0000	π-π*
THF	2.4237 eV	511.54 nm	4.0969 eV	302.63 nm	4.3497 eV	285.04 nm
	0.0000	π-π*	0.0000	π-π*	0.0000	π-π*
2-propanol	2.4364 eV	508.87 nm	4.1004 eV	302.37 nm	4.3561 eV	284.62 nm
	0.0000	π-π*	0.0000	π-π*	0.0000	π-π*

Figure 4.25 Triplet-state manifolds of Pc A

Electronic energies of T_1, T_2 and T_3 states along with their characters of Pc N1H N9H keto tautomer in gas phase, water and organic solvents

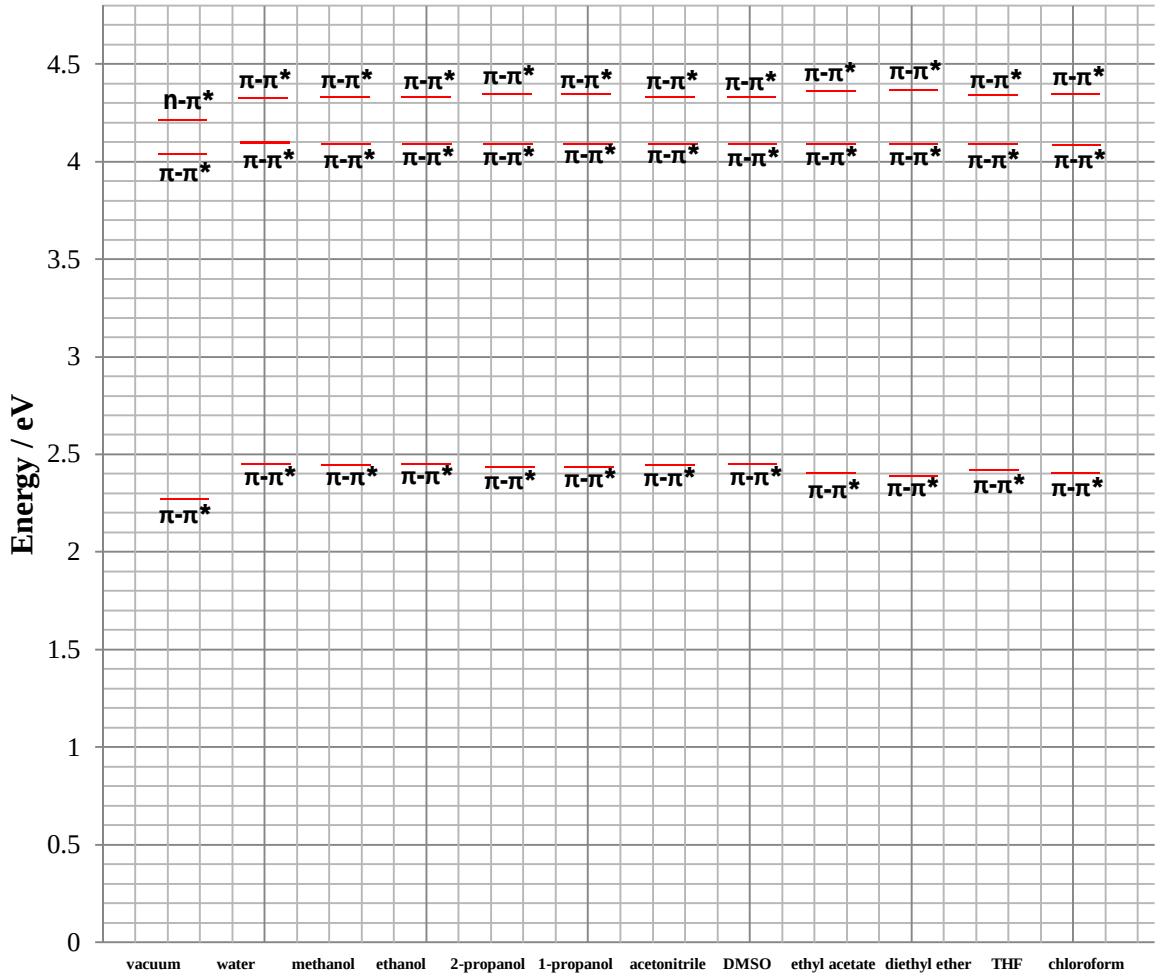

4.6.4 Comparing theoretical absorption with experimental absorption of Pc

The theoretical and experimental maxima excitation wavelengths were compared as displayed in Figure 4.26 and 4.27, and they are in an excellent agreement for the protic solvents and aprotic with high dielectric constant such as acetonitrile where the positions of the experimental bands coincide with the computed ones in the case of the first excited state S_1. When solvents with low-dielectric constants are considered, the theoretical absorption spectra were found to be red-shifted with respect to experimental spectra. The energies of the theoretically predicted maxima of the S_2 and S_3 states are very close in energy and they are both within the experimental absorption bands representing S_2 when protic and high-

dielectric constant solvents are considered. If solvents with low-dielectric constants are taken into consideration (except for diethyl ether) the calculated bands appear to be blue-shifted compared to the experimental bands. Theoretical and experimental bands are difficult to compare in chloroform because no clear distinction between the experimental bands was observed.

Figure 4.26 Pc absorption spectra and theoretically predicted vertical transitions

Experimental absorption spectra and predicted vertical transition represented as red lines of fixed magnitude. The oscillator strengths indicating the probability of the transitions are also reported

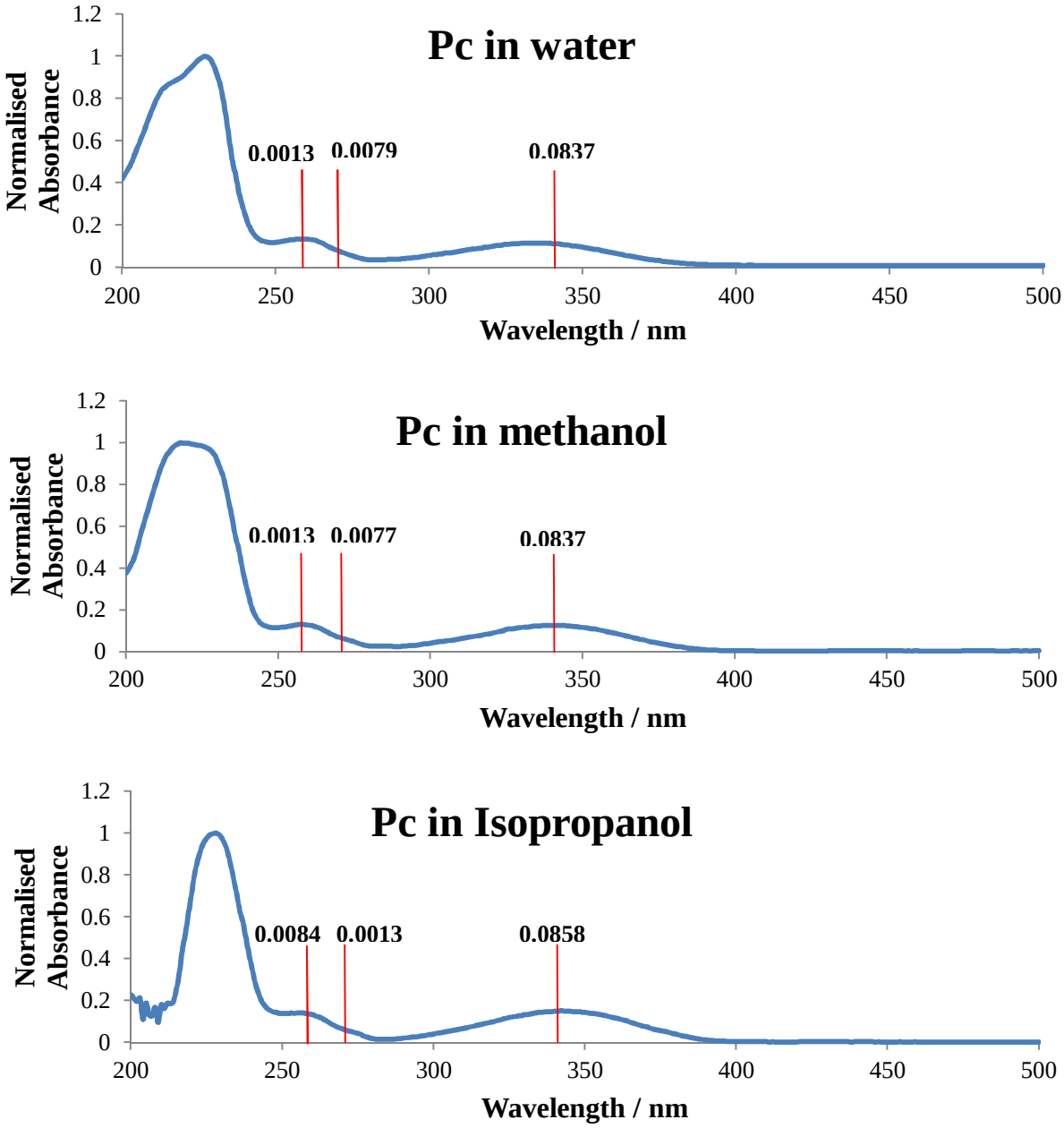

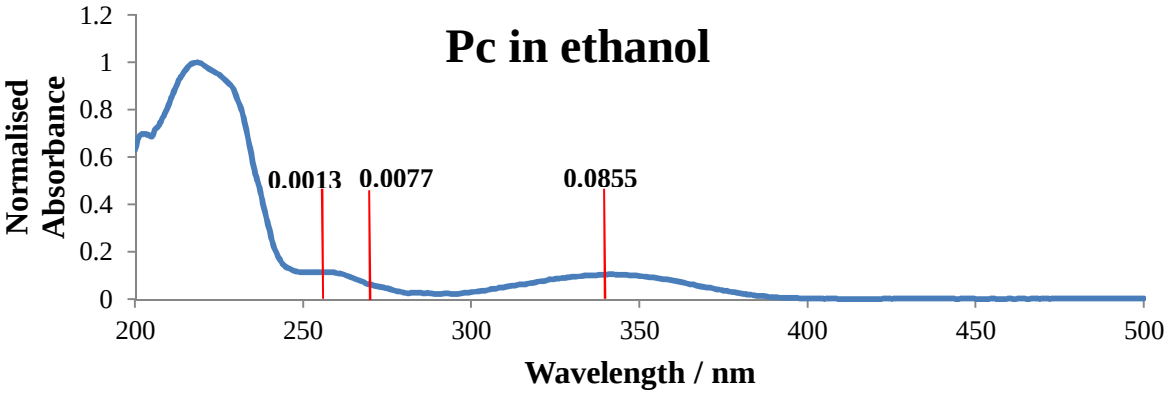
Pc in ethanol
Normalised Absorbance
1.2
1
0.8
0.6
0.4
0.2
0
0.0013
0.0077
0.0855
200
250
300
350
400
450
500
Wavelength / nm

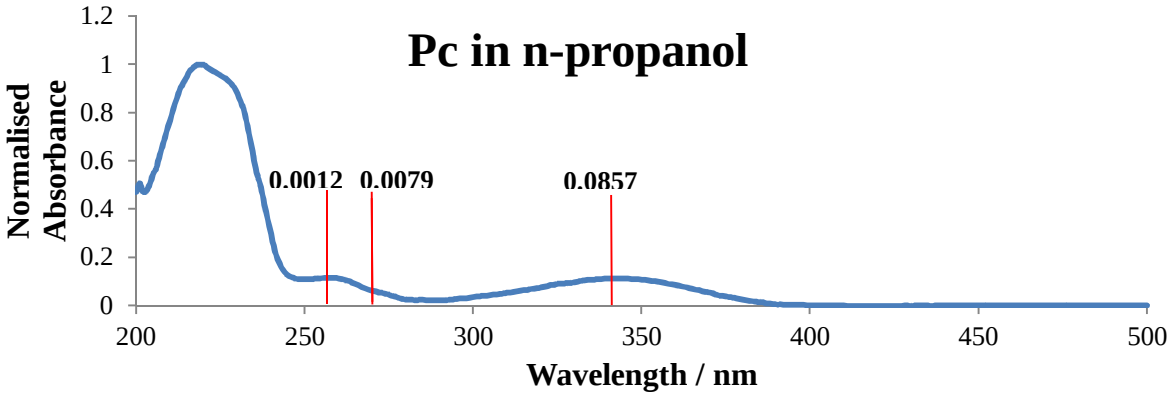
Pc in n-propanol
Normalised Absorbance
1.2
1
0.8
0.6
0.4
0.2
0
0.0012
0.0079
0.0857
200
250
300
350
400
450
500
Wavelength / nm

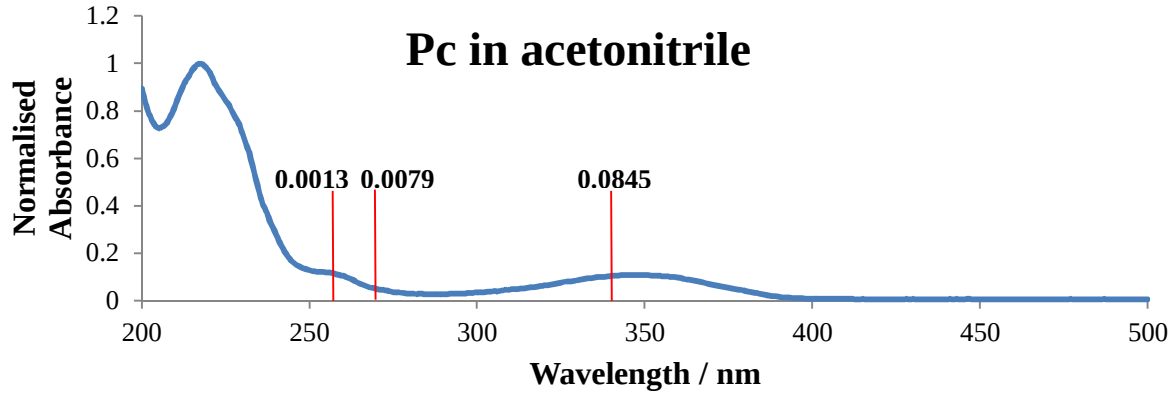
Pc in acetonitrile
Normalised Absorbance
1.2
1
0.8
0.6
0.4
0.2
0
0.0013
0.0079
0.0845
200
250
300
350
400
450
500
Wavelength / nm

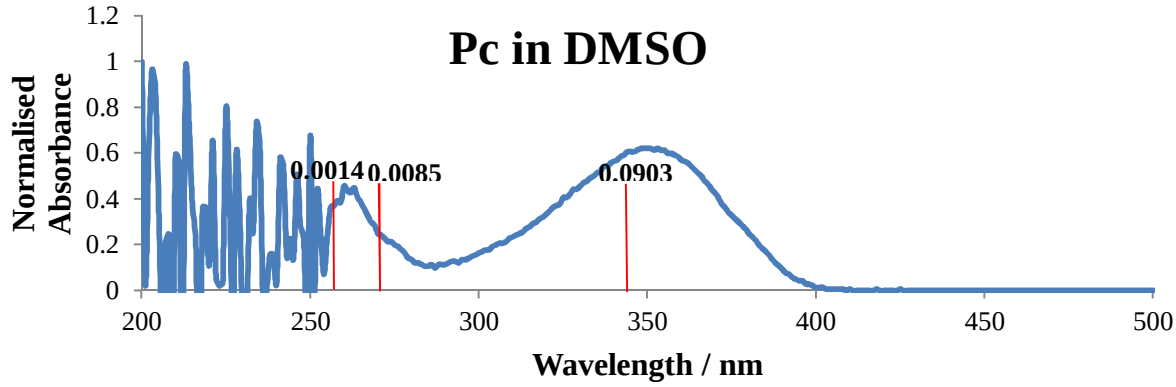
Pc in DMSO
Normalised Absorbance
1.2
1
0.8
0.6
0.4
0.2
0
0.0014
0.0085
0.0903
200
250
300
350
400
450
500
Wavelength / nm

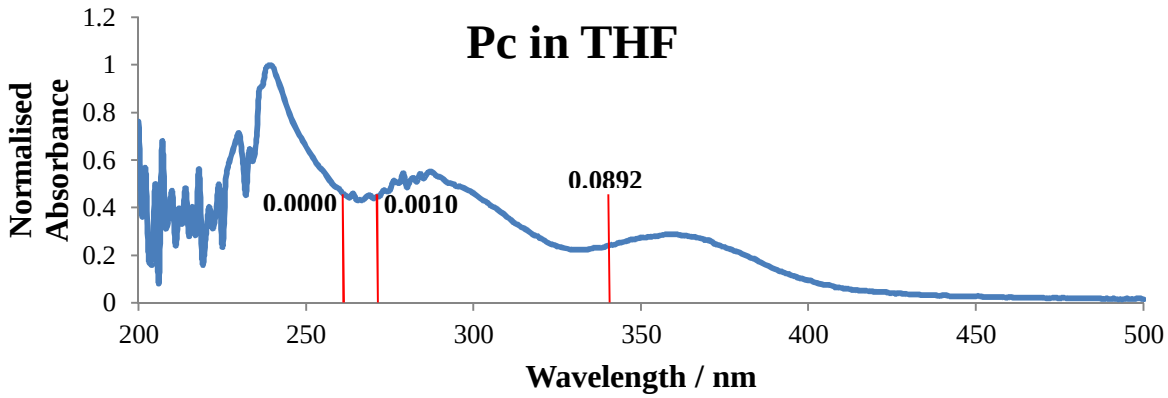
Pc in THF
Normalised Absorbance
Wavelength / nm
0.0000
0.0010
0.0892

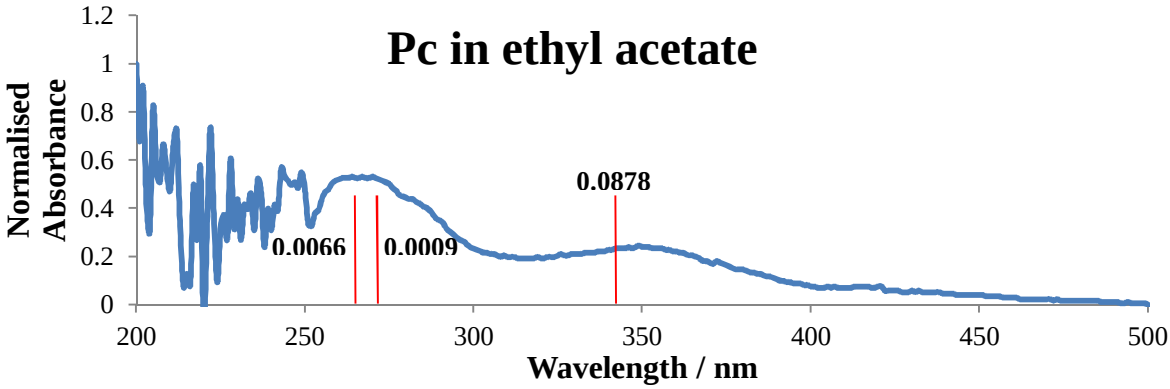
Pc in ethyl acetate
Normalised Absorbance
Wavelength / nm
0.0066
0.0009
0.0878

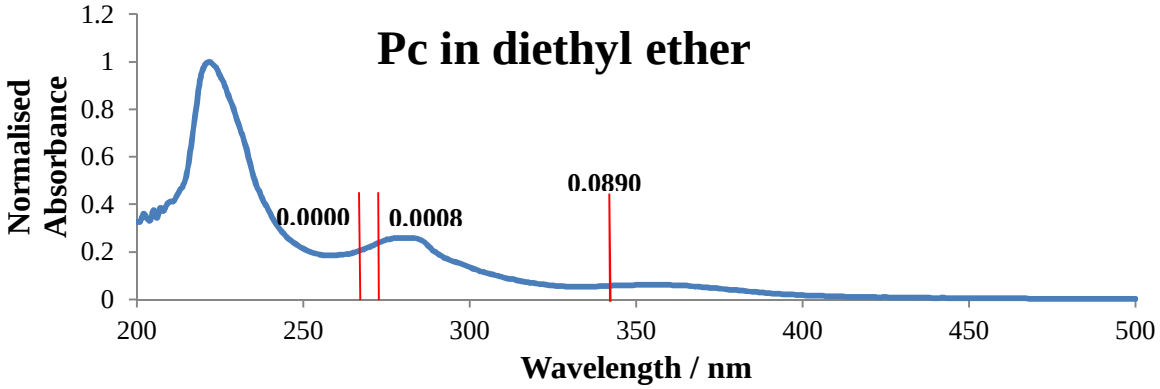
Pc in diethyl ether
Normalised Absorbance
Wavelength / nm
0.0000
0.0008
0.0890

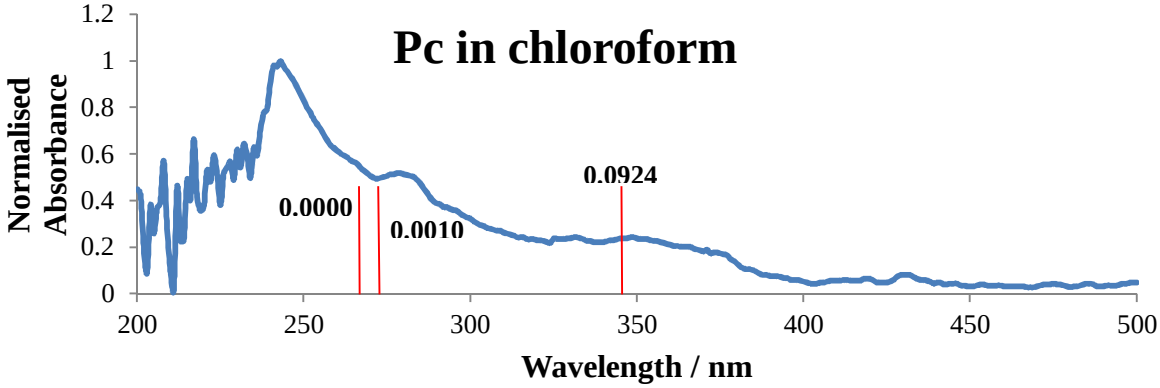
Pc in chloroform
Normalised Absorbance
Wavelength / nm
0.0000
0.0010
0.0924

Figure 4.27 Theoretical and experimental absorption of Pc in different solvents

Comparative summary of theoretical and experimental absorption of Pc in different solvents

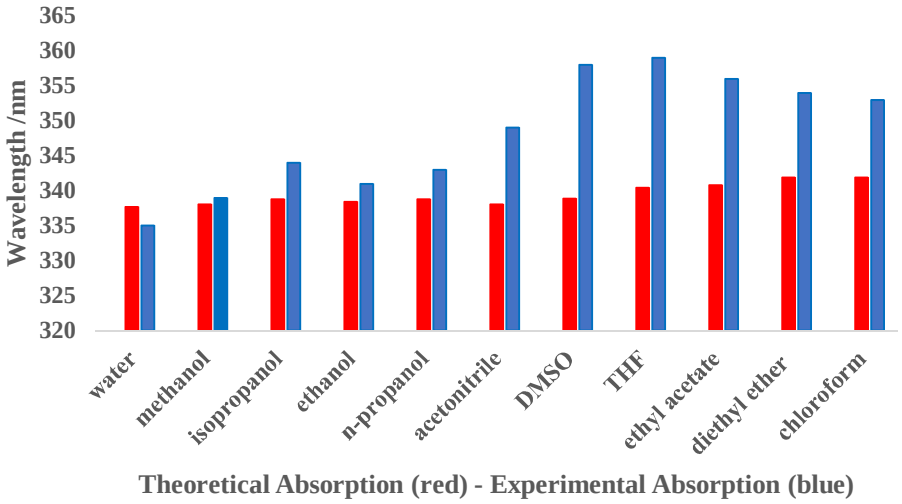

4.7 Theoretical emission (fluorescence). Optimization of the S_1 state

The theoretical emissions deriving from the S_1 state of Pc and 2-Ap were predicted by running TD calculations of the optimized ground state S_0 by using in the route section, as previously discussed, the opt and freq keywords. The figure 4.28 shows a simple potential energy diagram illustrating the S_0 and S_1 Franck Condon states with excitation and emission deriving from the minima of the potential energy curves computationally calculated by performing optimization geometries. The predicted theoretical fluorescence of the bases in vacuum and implicit solvents were compared with the experimental fluorescence reported in Chapter 3, see Figures 3.5 and 3.10 and Tables 3.1 and 3.6.

Figure 4.28 Absorption and fluorescence states

Absorption and emission (fluorescence) occurring from the equilibrium positions, the minima of the potential curves are found by performing optimization of the geometries in both ground and first excited states

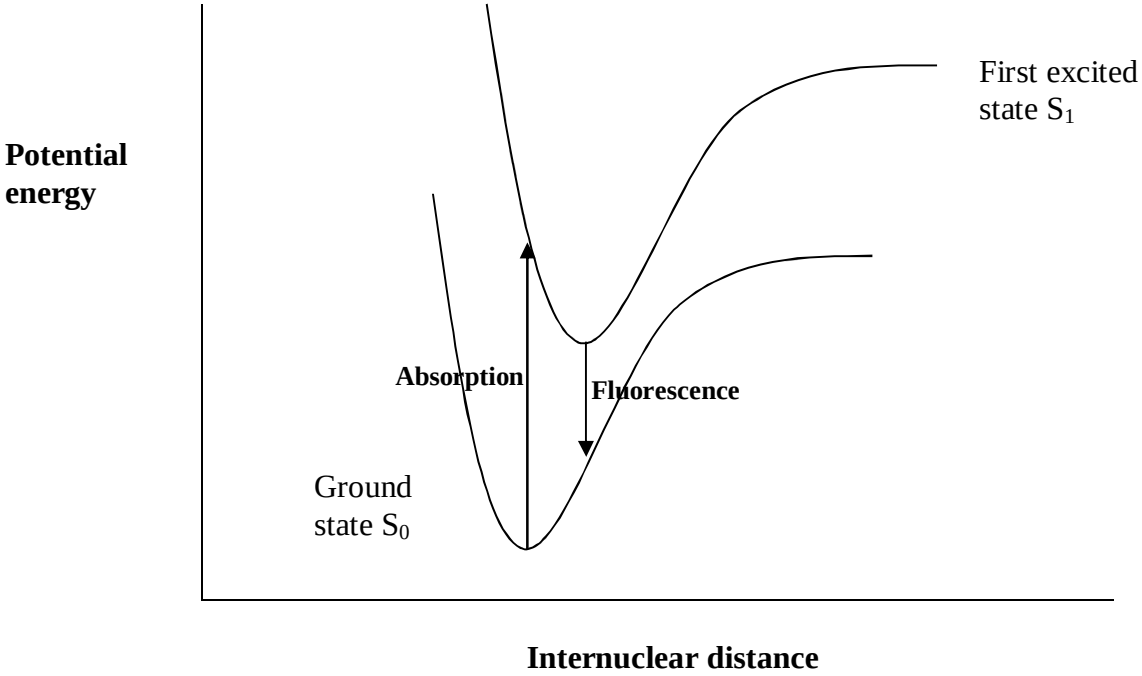

4.7.1 Comparing theoretical fluorescence with experimental fluorescence of 2-Ap

The theoretical emissions of 2-Ap (A) in vacuum and in solvents of different dielectric constant were compared with the experimental fluorescence emissions as shown in Figure 4.29 and 4.30. The computational details obtained from the calculations such as: predicted emission energies expressed in eV and nm, probability of the emissions and the dipole moments of the optimized S_1 states are contained in Table 4.9. Figure 4.29 and 4.30 show how the predicted maxima emissions compare with the experimental emissions.

Table 4.9 2-Ap (A) theoretical emissions and dipole moments of S_1

The table contains the emission energies in eV and nm of the optimized S_1 state of 2-Ap A in vacuum and solutions. The oscillator strengths *f* and dipole moments are also displayed

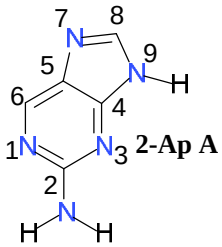 **2-Ap A**	Optimized S_1 state (π-π^*)			
	Fluorescence energy		*f*	Dipole moment (D)
	eV	nm		
Vacuum	3.8445 eV	322.50 nm	0.1200	3.1611 D
Water	3.6494 eV	339.74 nm	0.2500	4.3483 D
Chloroform	3.1754 eV	333.71 nm	0.2061	3.9575 D
1-propanol	3.6637 eV	338.41 nm	0.2411	4.2680 D
Acetonitrile	3.6559 eV	339.14 nm	0.2462	4.3141 D
Diethyl ether	3.7210 eV	333.20 nm	0.2029	3.9288 D
Ethyl Acetate	4.7024 eV	334.87 nm	0.2148	4.0345 D
DMSO	3.6533 eV	339.38 nm	0.2479	4.3294 D
Ethanol	3.6605 eV	338.71 nm	0.2431	4.2867 D
Methanol	3.6568 eV	339.05 nm	0.2455	4.3082 D
THF	3.6930 eV	335.73 nm	0.2215	4.0945 D
2-propanol	3.6649 eV	338.30 nm	0.2403	4.2611 D

Figure 4.29 2-Ap fluorescence spectra and theoretically predicted emissions

Experimental fluorescence spectra and theoretically predicted emissions of 2-Ap represented as black lines of fixed magnitude. The oscillator strength indicating the probability of the transitions are also reported

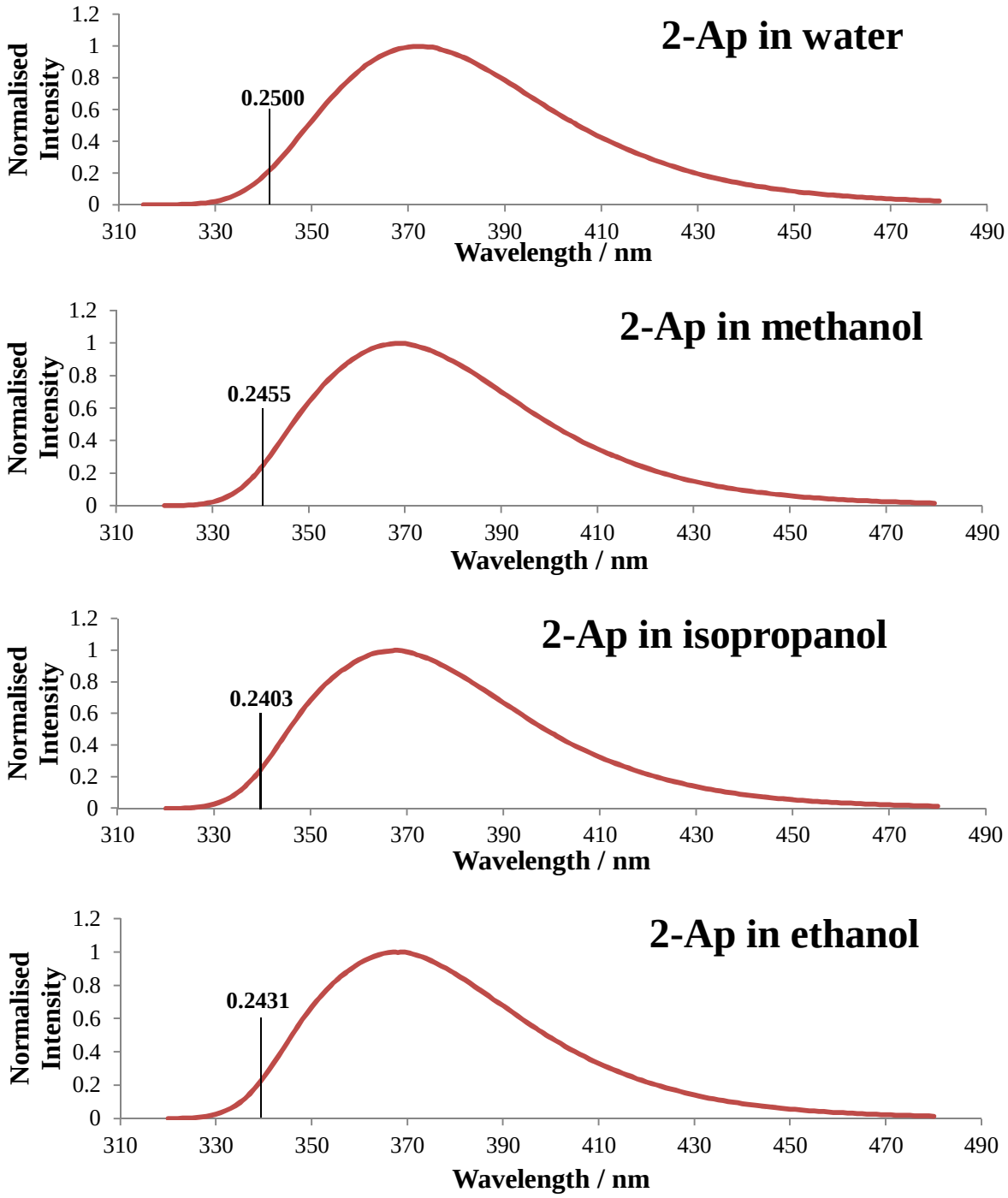

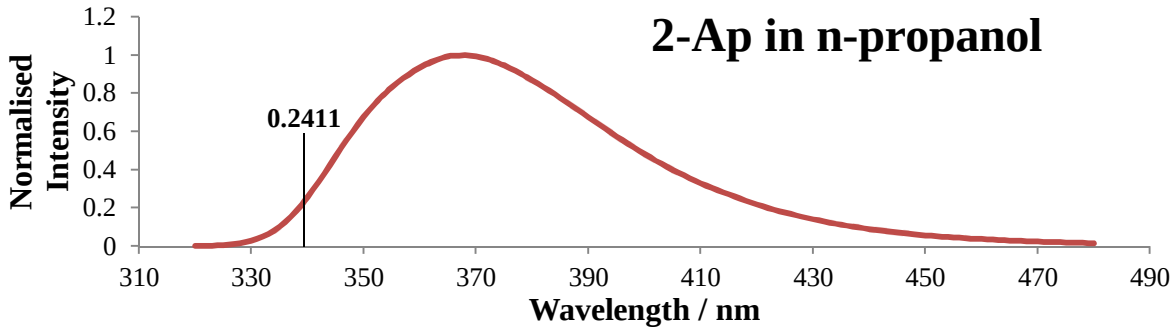
2-Ap in n-propanol
Normalised Intensity
0.2411
Wavelength / nm

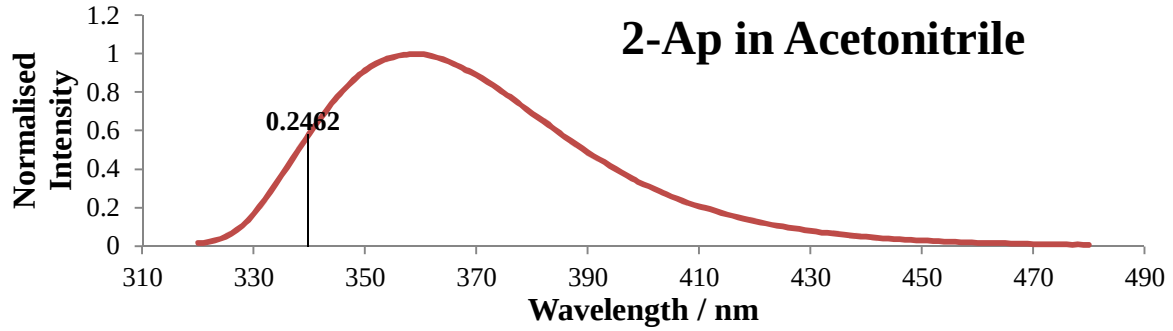
2-Ap in Acetonitrile
Normalised Intensity
0.2462
Wavelength / nm

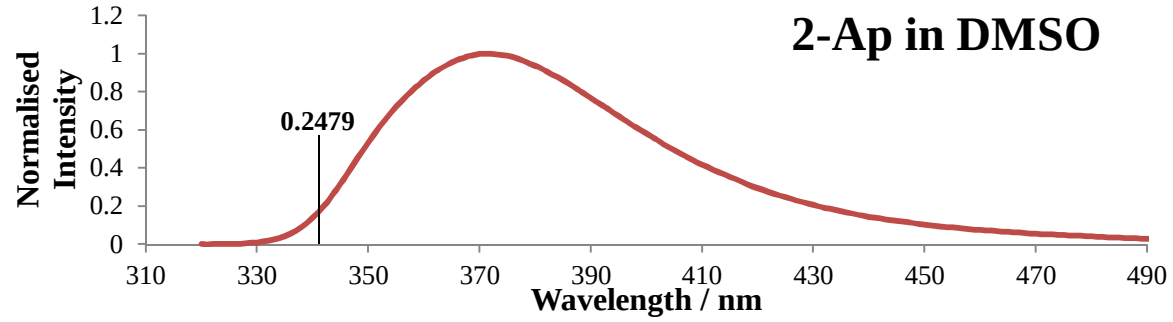
2-Ap in DMSO
Normalised Intensity
0.2479
Wavelength / nm

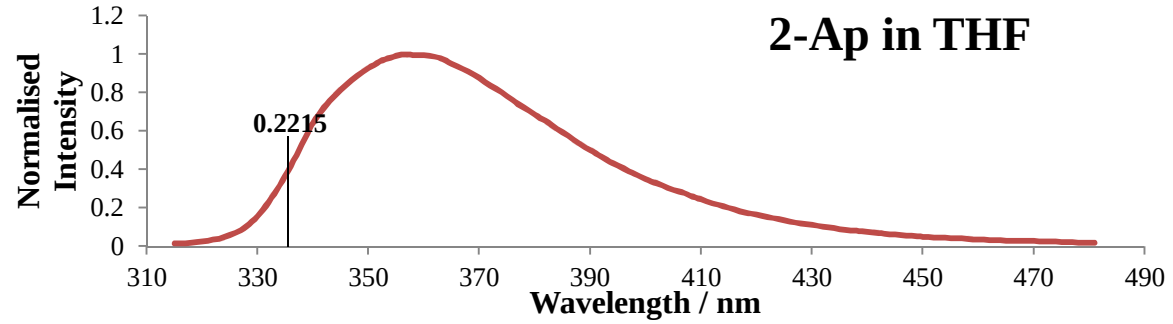
2-Ap in THF
Normalised Intensity
0.2215
Wavelength / nm

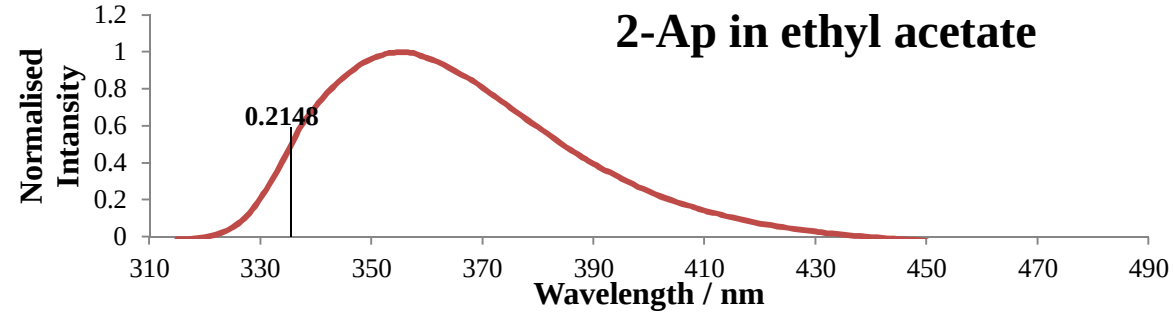
2-Ap in ethyl acetate
Normalised Intansity
0.2148
Wavelength / nm

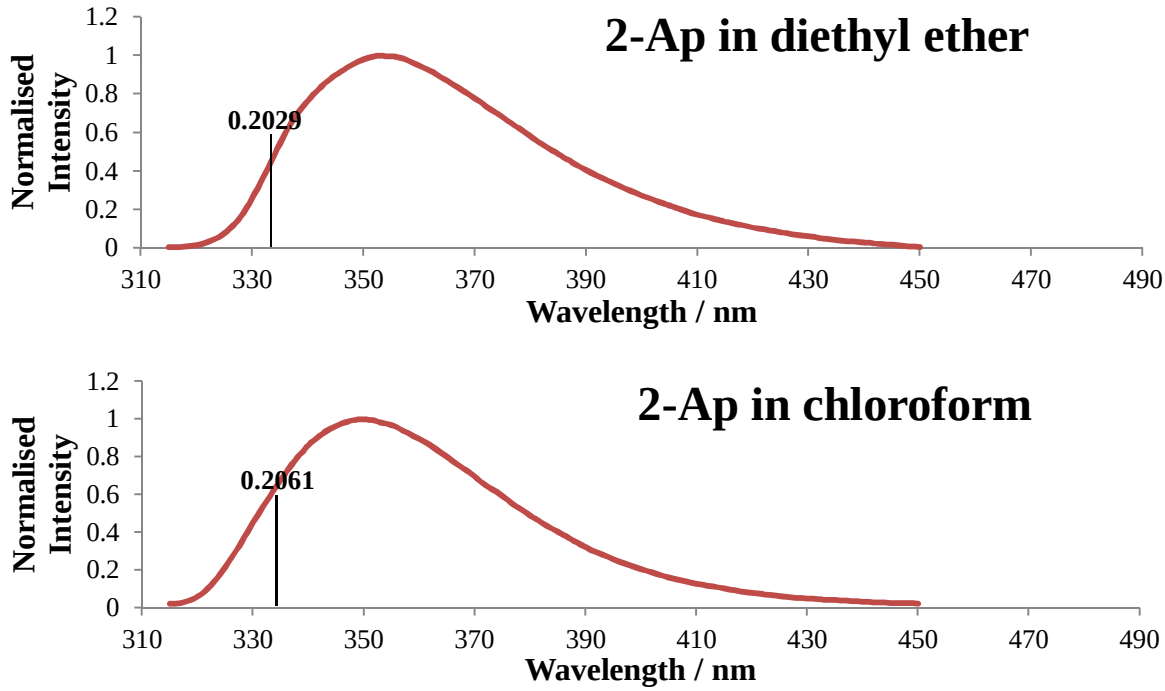

Figure 4.30 Theoretical and experimental emission of 2-Ap in different solvents

Summary of theoretical and experimental emission of 2-Ap in different solvents

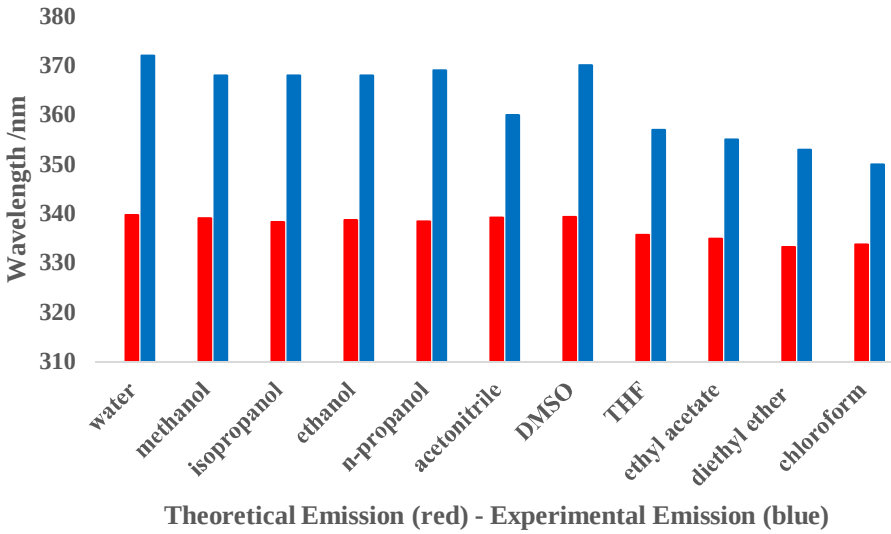

As clearly shown in Figure 4.29 the theoretically predicted emission energies are blue-shifted with respect to the experimental emissions. Also, the Figure 4.30 shows a clear distinction in theoretical and experimental fluorescence emission. The calculated dipole moments of the optimized first singlet excited states of 2-Ap A contained in Table 4.10 are slightly smaller than the ones calculated in the ground states contained in Table 4.1. The smallest difference in dipole moments was predicted in vacuum. The data in Table 4.10 reflects the difference in dipole moment between the two states.

Table 4.10 Dipole moments of 2-Ap A

Ground and excited state dipole moments of 2-Ap N9H amino tautomer in vacuum and different solvents. The table enlightens the difference between the excited and ground state dipole moment, μ_e-μ_g

2-Ap A	**Dipole moment, μ_g**	**Dipole moment, μ_e**	**$\Delta\mu = \mu_e - \mu_g$**
Vacuum	3.2514 D	3.1611 D	**- 0.0903 D**
Water	4.6774 D	4.3483 D	**- 0.3291 D**
Chloroform	4.1959 D	3.9575 D	**- 0.2384 D**
1-propanol	4.3681 D	4.2680 D	**- 0.1001 D**
Acetonitrile	4.6280 D	4.3141 D	**- 0.3139 D**
Diethyl ether	4.1437 D	3.9288 D	**- 0.2149 D**
Ethyl acetate	4.1247 D	4.0345 D	**- 0.0902 D**
DMSO	4.6440 D	4.3294 D	**- 0.3146 D**
Ethanol	4.5891 D	4.2867 D	**- 0.3024 D**
Methanol	4.6220 D	4.3082 D	**- 0.3138 D**
THF	4.3620 D	4.0945 D	**- 0.2675 D**
2-propanol	4.3610 D	4.2611 D	**- 0.0999 D**

4.7.2 Comparing theoretical fluorescence with experimental fluorescence of Pc

Like 2-Ap the theoretical emissions of Pc (A) in vacuum and solvents having different dielectric constant were compared with the experimental fluorescence as indicated in Figure 4.31 and 4.32 along with the computational data obtained from the calculations such as: predicted emission energies, dipole moments of the optimized S_1 states are contained in Table 4.11.

Table 4.11 Pc (A) theoretical emissions and dipole moments of S_1

The table contains the emission energies in eV and nm of the optimized S_1 state of Pc A in vacuum and solutions. The oscillator strengths *f* and dipole moments are also displayed

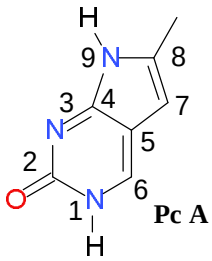 **Pc A**	Optimized S_1 state (π-π^*)			
	Fluorescence energy		*f*	Dipole moment (D)
	eV	nm		
Vacuum	2.8910 eV	428.86 nm	0.0566	7.4446 D
Water	2.8366 eV	437.08 nm	0.1031	10.0459 D
Chloroform	2.8612 eV	433.34 nm	0.0878	9.2006 D
1-propanol	2.8417 eV	436.30 nm	0.0999	9.8725 D
Acetonitrile	2.8387 eV	436.77 nm	0.1017	9.9716 D
Diethyl ether	2.8631 eV	433.05 nm	0.0866	9.1348 D
Ethyl Acetate	2.8564 eV	434.05 nm	0.0908	9.3688 D
DMSO	2.8361 eV	437.16 nm	0.1021	10.0092 D
Ethanol	2.8406 eV	436.47 nm	0.1006	9.9119 D
Methanol	2.8392 eV	436.69 nm	0.1014	9.9581 D
THF	2.8526 eV	434.64 nm	0.0931	9.4983 D
2-propanol	2.8422 eV	436.22 nm	0.0996	9.8571 D

Figure 4.31 Pc fluorescence spectra and theoretically predicted emissions

Experimental fluorescence spectra and theoretically predicted emissions of Pc represented as black lines of fixed magnitude. The oscillator strength indicating the probability of the transitions are also reported

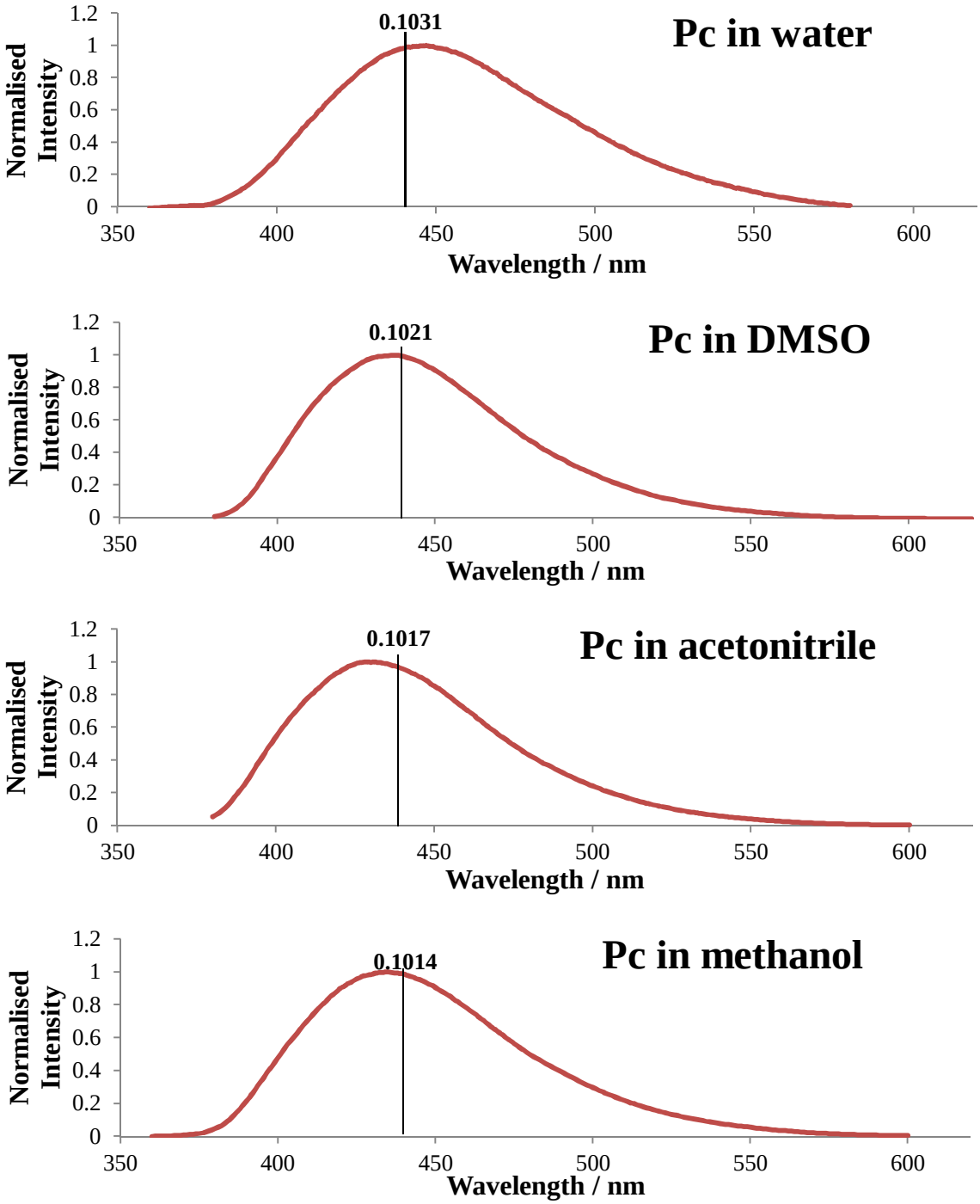

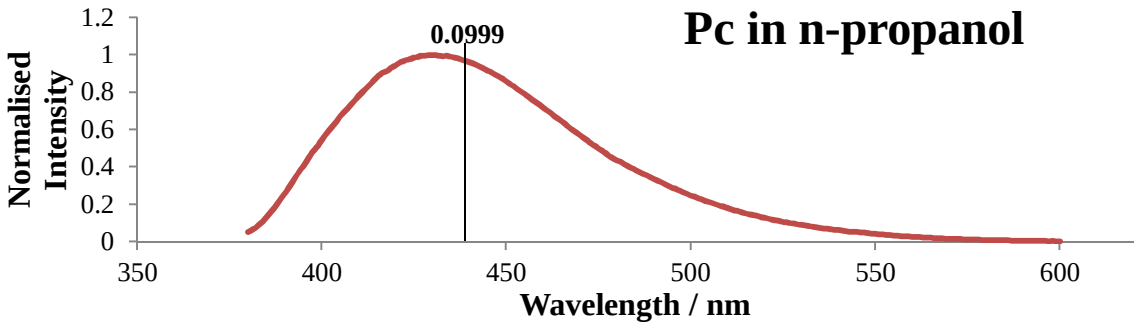
Pc in n-propanol
0.0999
Normalised Intensity
1.2
1
0.8
0.6
0.4
0.2
0
350
400
450
500
550
600
Wavelength / nm

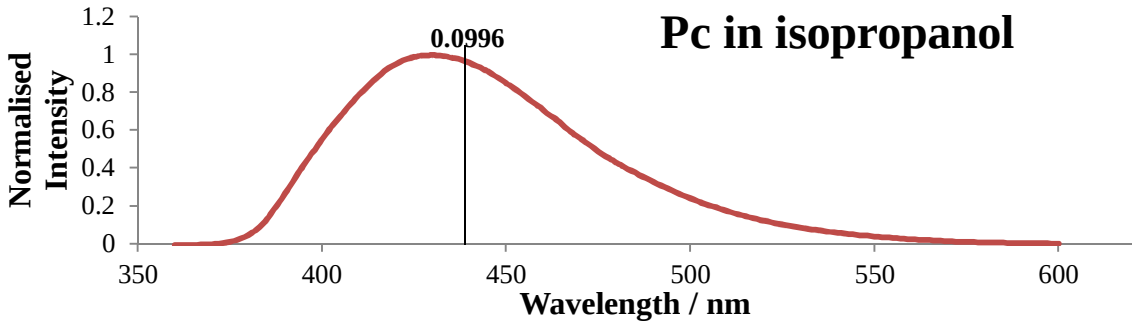
Pc in isopropanol
0.0996
Normalised Intensity
1.2
1
0.8
0.6
0.4
0.2
0
350
400
450
500
550
600
Wavelength / nm

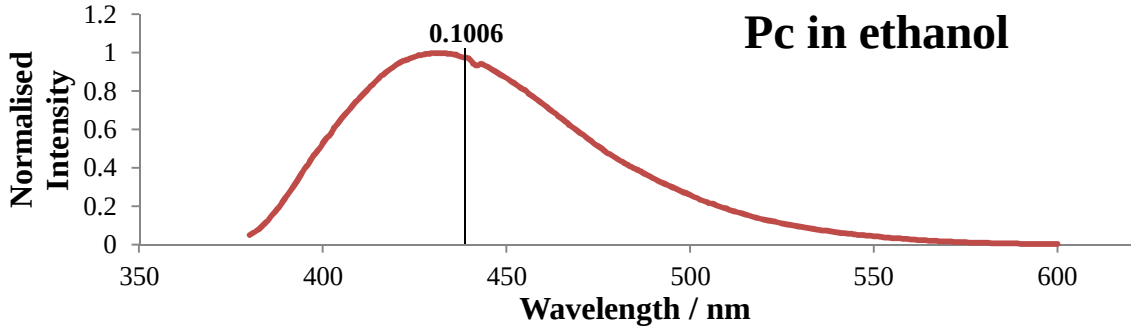
Pc in ethanol
0.1006
Normalised Intensity
1.2
1
0.8
0.6
0.4
0.2
0
350
400
450
500
550
600
Wavelength / nm

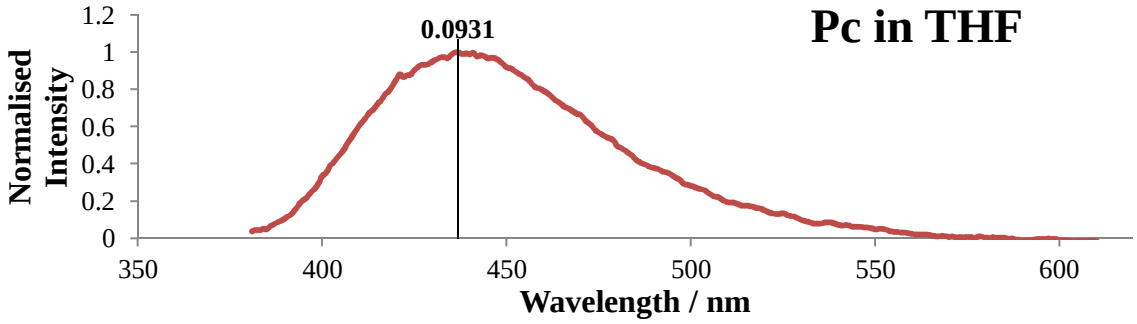
Pc in THF
0.0931
Normalised Intensity
1.2
1
0.8
0.6
0.4
0.2
0
350
400
450
500
550
600
Wavelength / nm

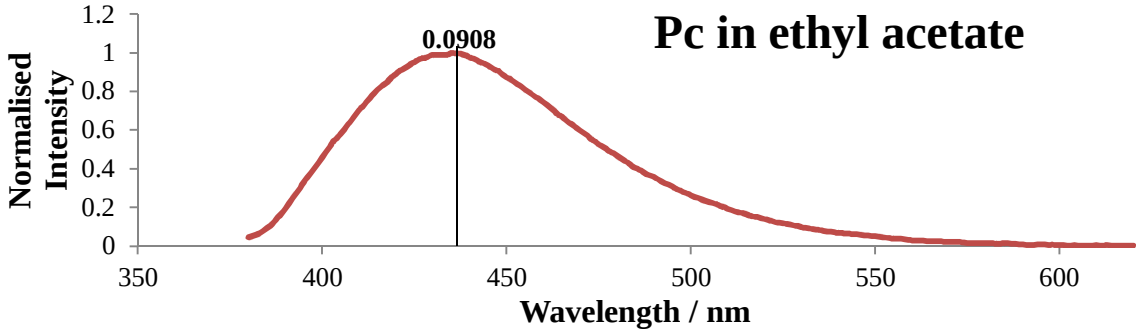
Pc in ethyl acetate
0.0908
Normalised Intensity
1.2
1
0.8
0.6
0.4
0.2
0
350
400
450
500
550
600
Wavelength / nm

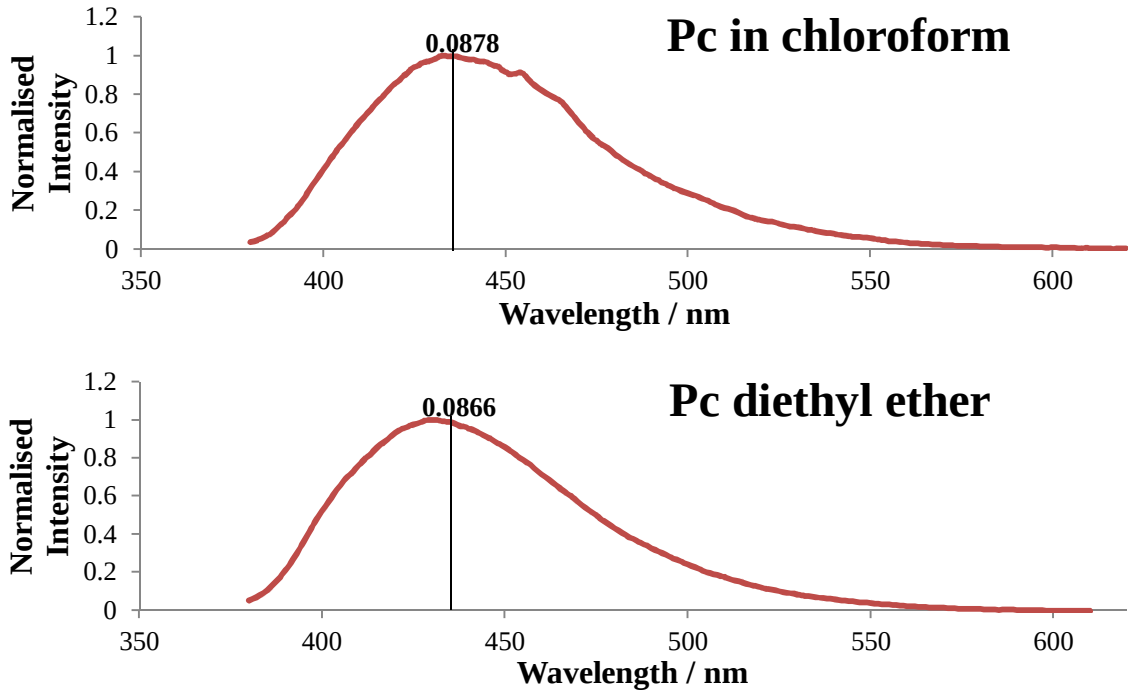

Figure 4.32 Theoretical and experimental emission of Pc in different solvents

Summary of theoretical and experimental emission of Pc in different solvents

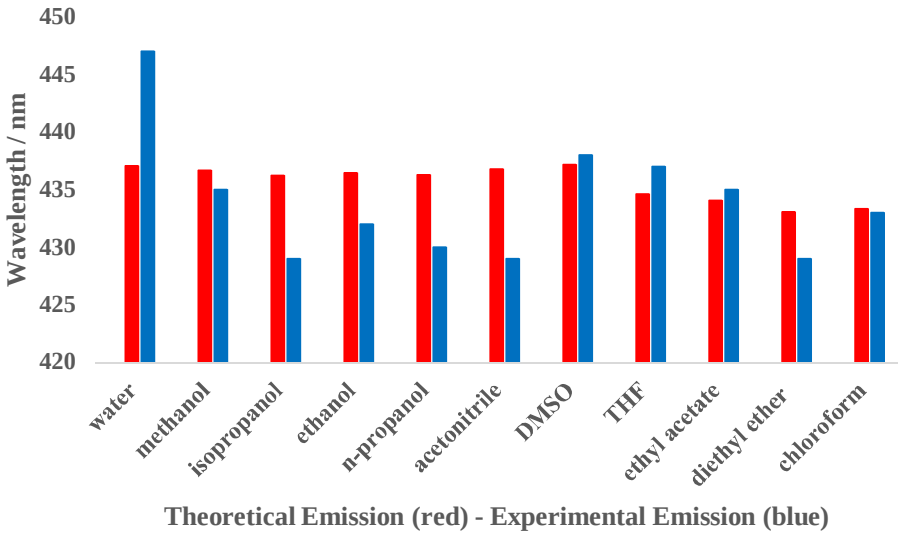

As opposed to 2-Ap, the theoretically predicted emission energies of Pc in different solvents are in better agreement with the experimental emissions as shown in Figure 4.32. In the case of Pc a larger difference between the ground and excited state dipole moment was found

compared to 2-Ap, as shown in Table 4.12. This may imply a larger redistribution of electronic charges within the molecule possibly due to a conformational change.

Table 4.12 Dipole moments of Pc

Ground and excited state dipole moments of Pc N1H tautomer in vacuum and different solvents. The table enlightens the difference between the excited and ground state dipole moment, μ_e-μ_g

Pc A	**Dipole moment, μ_g**	**Dipole moment, μ_e**	**$\Delta\mu = \mu_e - \mu_g$**
Vacuum	6.4799 D	7.4446 D	**0.9647 D**
Water	9.0892 D	10.0459 D	**0.9567 D**
Chloroform	8.3091 D	9.2006 D	**0.8915 D**
1-propanol	9.9984 D	9.8725 D	**- 0.1259 D**
Acetonitrile	9.0155 D	9.9716 D	**0.9561 D**
Diethyl ether	8.2162 D	9.1348 D	**0.9186 D**
Ethyl acetate	8.5062 D	9.3688 D	**0.8626 D**
DMSO	9.0401 D	10.0092 D	**0.9691 D**
Ethanol	8.9548 D	9.9119 D	**0.9571 D**
Methanol	9.0017 D	9.9581 D	**0.9564 D**
THF	8.5735 D	9.4983 D	**0.9248 D**
2-propanol	8.9837 D	9.8571 D	**0.8734 D**

4.8 Relationship between the oscillator strength and rate constant for fluorescence

The oscillator strength is a dimensionless quantity that indicates the probability of absorption and emission of electromagnetic energy between energy levels of atoms or molecules and it is defined as:

$$f_{ij} = \frac{8\pi^2 \, m \, \nu_{ij}}{3\hbar} \left|r_{ij}\right| \quad (4.2)$$

Where f_{ij} and vij are the oscillator strength and frequency of the involved states arbitrarily called i and j and r is the electric dipole matrix element connecting the states. The rate constant for fluorescence k_F (see Chapter 2 Section 2.3) is directly proportional to the oscillator strength, *f*. The following formula reflects this relationship.

$$k_F = \frac{1}{4\pi\varepsilon_0} \frac{64\pi^4 n \langle \nu^{-3} \rangle^{-1}}{3hc^3} D \quad (4.3)$$

From equation 4.3 k_F can be calculated by knowing: ε_0 which is the permittivity of the free space, n the refractive index of the medium, ν is the frequency and the term $\langle \nu^{-3} \rangle$ is the expectation value of ν^{-3}, h is the Plack's constant, c is the speed of light in vacuum and finally, D is the square of the transition dipole moment. The transition dipole moment or transition moment is the moment associated with the transition between two states. It is a complex vector and it is useful to determine whether transitions are allowed under the electric dipole interaction. The transition dipole moment can be written as follows:

$$D = \frac{3he^2}{8\pi^2 m_e} \frac{f}{\nu} \quad (4.4)$$

As shown in equation 4.4 the transition dipole moment is related to the oscillator strength *f*. The terms e and m are the charge on the electron and the mass of an electron respectively. Then, an increase in *f* would lead to an increase in k_F which would eventually result in a bigger quantum yield as described in equation 4.5, where k_{nr} is the rate constant for the non-radiative processes:

$$\Phi_F = \frac{k_F}{k_F + k_{nr}} \quad (4.5)$$

Also, the lifetime which is the reciprocal of all deactivation processes as shown in equation 4.6, is affected by the oscillator strength.

$$\tau = \frac{1}{k_F + k_{nr}} \quad (4.6)$$

In both Pc A and 2-Ap A DFT predicted a decrease in oscillator strength going from solvents having high dielectric constant to solvents having low dielectric constant as shown in Tables 4.9 and 4.11. This theoretical estimation is mostly in agreement with the experimental data with the exception of Pc which was found to have the smallest quantum yield in water, see Chapter 3 Tables 3.1 and 3.6.

4.9 Ground and excited state geometries

In the light of computational studies found in the literature, the ground state geometries of nucleic acid bases are reported to be planar with the exception of the amino group which is pyramidal (Leszczynski, 1992; Hobza and Sponer, 1999; Leszczynski, 2000; Sponer *et al*. 2002). Specifically, the amino group of adenine is out of plane (xy plane) by circa 20º a value found by using a technique called vibrational transition moment angles (VMTA) as shown in the work of Dong and Miller (Dong and Miller, 2002) and lately confirmed by Downton and Wang (Downtong and Wang, 2005). While the ground state geometries of natural bases were predicted to be planar their corresponding excited state energies were predicted to be non-planar by using different computational methods such as: HF, MP2 (MØller-Plesset Perturbation Theory), CIS (Configuration Interaction Singles), CASSCF and DFT (Mishra and Mishra, 2001; Salter and Chaban, 2002; Shukla and Leszczynski, 2005; Chen and Lin, 2006; Shukla and Leszczynski, 2006). According to the literature the excited state structural non-planarity may be responsible for ultrafast non-radiative deactivation of the excited bases *via* internal conversion processes to the ground state (Broo, 1998; Blancafort, 2006; Noguera *et al*. 2006; Perun *et al*. 2006; Serrano-Andres *et al*. 2006; Shukla *et al*. 2006). The optimized ground state geometry of 2-Ap A in both gas and liquid phase shows that the amino group of the modified base is pyramidal and therefore, out of plane with respect to the rest of the molecule by circa 2.5 degrees as measured by ECCE (Black *et al*. 2009). The non-planarity of the amino group almost disappears when the molecule is optimized in its first excited state S_1, regardless of being in gas or solution. The two geometries are compared in figure 4.33. Then, the planar 2-Ap A structure in the excited state may facilitate fluorescence over non-radiative processes. The geometry of Pc A results is unchanged when excited, remaining apparently planar in both S_0 and S_1 once again regardless of the phase adopted.

Figure 4.33 S_0 and S_1 optimized geometries of 2-Ap A

Optimized geometries of S_0 and S_1 geometries of 2Ap A on Gaussview and ECCE. It is clearly visible that the NH_2 group in the ground state is non-planar with respect to the purine ring by circa 2.5 degrees

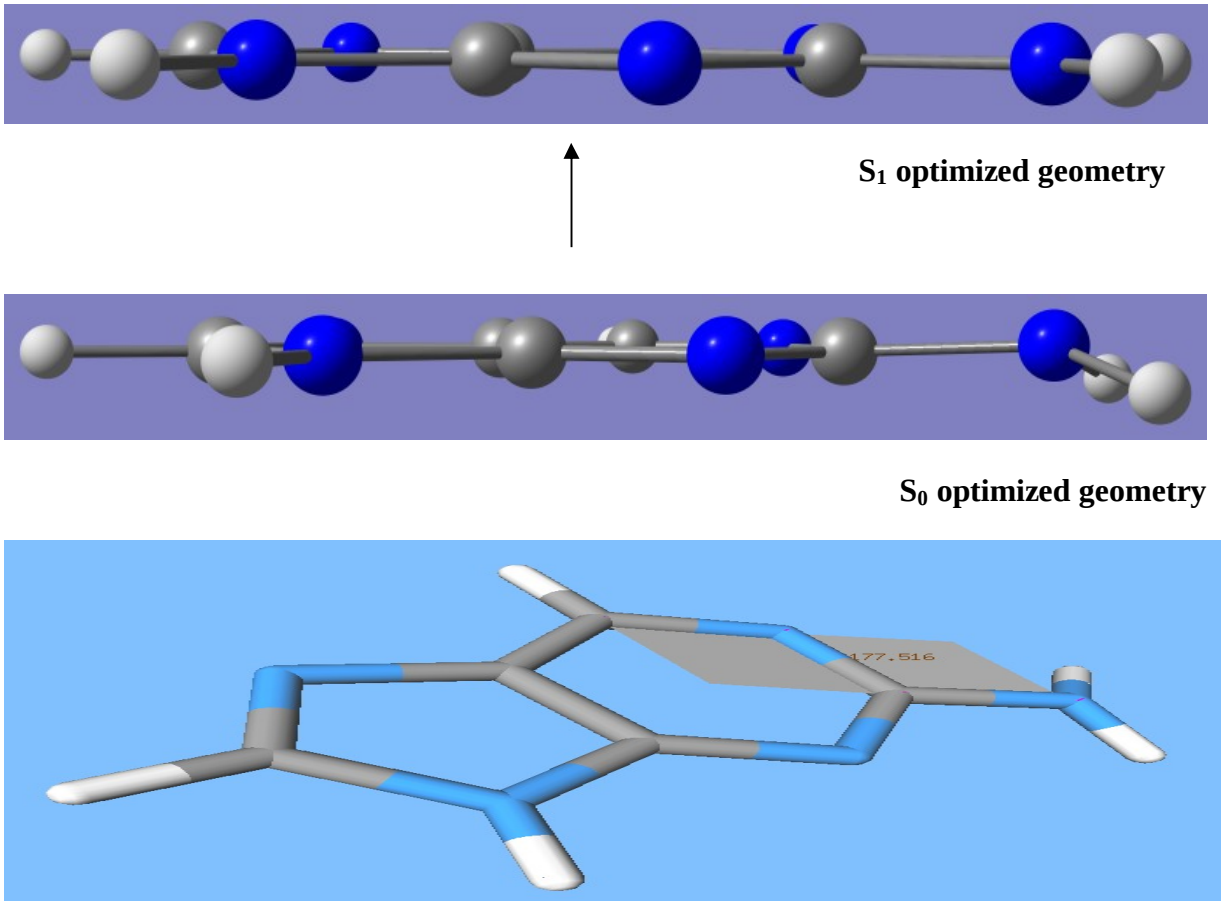

4.10 Computational study of hydrogen bonding formation on 2-Ap and Pc

2-Ap and Pc are heterocyclic compounds and because their heteroatoms are highly electronegative, can form hydrogen bonds with solvent molecules. This specific solvent effect on 2-Ap and Pc molecules was studied by manually constructing (Z-matrices) explicit water molecules to study the interaction *via* hydrogen bonds with the fluorophores. The optimized geometries of the probes bonded with explicit water molecules were computationally obtained and they were eventually used to compute vertical transitions. The first three vertical transitions, oscillator strengths, changes in dipole moments and calculated fluorescence emissions are reported.

4.10.1 2-Ap A tautomer hydrogen bonded to water molecules

The energies of the optimized geometries of 2-Ap A with one of its N atoms interacting with a water molecule are shown in Table 4.13.

Table 4.13 Single point energies of 2-Ap A interacting with one water molecule

This table displays the dipole moments (D) and single point energy calculations (a.u) of the optimized geometries of 2-Ap A tautomer interacting with one water molecule given as $E_{complex}$. The difference between $E_{complexes}$ and (2-Ap A + water molecule single point energies) are also reported, no CP corrections were used

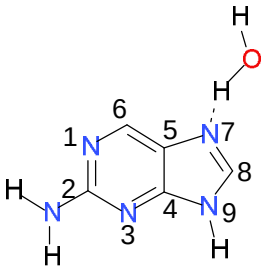	μ_g = 6.6499 D $E_{complex}$ = -543.6487 a.u $E_{complex}$ - (2-Ap + $1H_2O$) = 0.0069 a.u	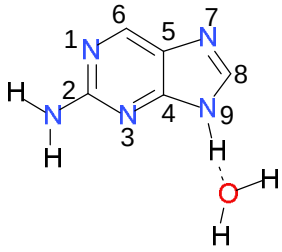	μ_g = 7.4470 D $E_{complex}$ = -543.6613 a.u $E_{complex}$ - (2-Ap + $1H_2O$) = - 0.0057 a.u
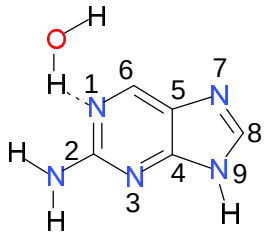	μ_g = 5.5324 D $E_{complex}$ = -543.6518 a.u $E_{complex}$ - (2-Ap + $1H_2O$) = 0.0038 a.u	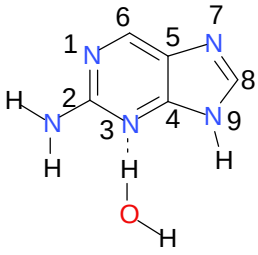	μ_g = 4.6743 D $E_{complex}$ = -543.6512 a.u $E_{complex}$ - (2-Ap + $1H_2O$) = 0.0044 a.u
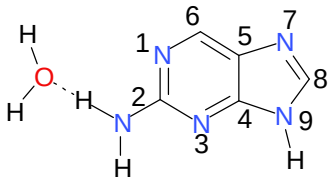	μ_g = 2.3427 D $E_{complex}$ = -543.6604 a.u $E_{complex}$ - (2-Ap + $1H_2O$) = - 0.0048 a.u	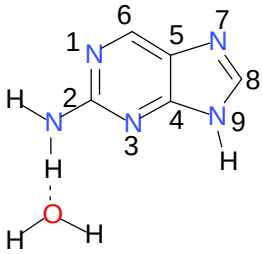	μ_g = 6.8600 D $E_{complex}$ = -543.6605 a.u $E_{complex}$ - (2-Ap + $1H_2O$) = - 0.0049 a.u

Interaction energies between two atoms or two molecules (in this particular case water molecules with fluorescent bases) are usually calculated as the energy difference between the product complex (bases interacting with one or two water molecules) and its components or monomers (base and individual water molecules). Thus, the binding energy of the complex is calculated as follows in equation 4.7.

$$\Delta E = (E_{complex}) - (\text{Sum of the Energy of each individual component}) \quad (4.7)$$

However, most common basis sets are centered or fixed on the nuclei and may not be complete leading to errors (geometry-related errors which result in overestimated energies) especially for weak interactions between the components, specifically Van der Waals interactions. The binding energy of a complex calculated as previously explained may not always be accurate because the complex is treated better than the individual components to compensate errors in energy. In fact, small basis sets stabilize the complex more than the separate components due to the basis set superposition error (BSSE). This is due to the fact that the wavefunction of the monomer/component is expanded in fewer basis functions than the wavefunction of the complex. Solutions to this problems exist. For instance the use of larger and larger basis sets until the difference in energy becomes constant, but this approach can be unfeasible for many systems and computationally expensive. Another approach is the use of Counterpoise Correction (CP). The adoption of this approach BSSE is estimated as the difference between monomer/component energies with the regular basis set and the full set of basis functions for the complex (Jansen and Ros, 1969; Feyereisen *et al*. 1996; Dunning, 2000; Valdes *et al*. 2008). This approach is very laborious because it requires many calculations, approximations and the inclusion of the ghost orbitals and consequently it was not adopted for the calculations of the binding energies of the complexes formed between 2-Ap and Pc with water molecules reported herein.

The Table 4.13 contains the dipole moments and single point energies given as 2-Ap $A_{complexes}1H_2O$. The difference in energy reported was calculated by considering the energy of 2-Ap A as free base, -467.2444 a.u taken from Table 4.1 and the theoretically predicted single point energy of one water molecule which resulted to be - 76.4112 a.u, energy obtained by using the same basis set used for the free base. Then, 2-Ap A energy + 1 water molecule

energy = - 543.6556 a.u. Alike for the free base 2-Ap A the first three vertical transitions of the complexes were calculated at TDDFT by using the functional B3LYP. The assignments and the molecular orbitals involved in the first three singlet vertical transitions are the following:

For the hydrogen bond acceptor at N7 atom the first vertical transition was found to be a π-π* (HOMO of energy level 40 – LUMO of energy level 41). The second vertical electronic transition is an n-π* transition (occupied molecular orbital of energy level 39 – LUMO of energy level 41). The third electronic transition is of π-π* character (HOMO of energy level 40 – unoccupied molecular orbital of energy level 42). The second most predominant transition was found to be another π-π* transition (occupied of energy level 38 – LUMO of energy level 41).

For the case of a hydrogen bond donor at N9 (group N9H) interacting with water, the first vertical transition resulted to be a π-π* transition (HOMO of energy level 40 – LUMO of energy level 41). The second vertical transition is an n-π* transition (occupied molecular orbital of energy level 39 – LUMO of energy level 41). The third vertical transition is of π-π* character (occupied molecular orbital of energy level 38 – LUMO of energy level 41). The second most predominant transition was computed from a HOMO of energy level 40 to an energy level 42.

In the case of the hydrogen acceptor N1 and N3 atoms, the first vertical transition is a π-π* transition (HOMO of energy level 40 – LUMO of energy level 41). The second vertical transition was found to be an n-π* transition (occupied molecular orbital of energy level 39 – LUMO of energy level 41). The third vertical transition results to be of π-π* character (HOMO of energy level 40 – unoccupied molecular orbital of energy level 42).

When the amino group of 2-Ap A participates in hydrogen bonding formation with water molecules, the predicted vertical transitions were found to be the following: a first vertical transition of π-π* character (HOMO of energy level 40 – LUMO of energy level 41). The second vertical transition was found to be an n-π* (occupied molecular orbital of energy level 39 – LUMO of energy level 41). The calculated third vertical transition is of Rydberg character, precisely a π-Rydberg (HOMO of energy level 40 – unoccupied molecular orbital of energy level 42).

The Table 4.14 contains the theoretically predicted energies, assignments and oscillator strengths of the first three singlet and triplet states.

Table 4.14 Vertical transitions of 2-Ap A hydrogen bonded to one water molecule

First three singlet and triplet state energies and oscillator strengths of 2-Ap A hydrogen bonded to one water molecule. The water molecule interacts with the heteroatoms and amino group of the probe

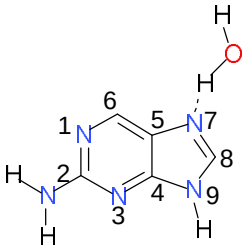	**S_1 (π-π^*)** **ΔE** 4.2753 eV 290.00 nm ***f*** 0.1616	**S_2 (n-π^*)** **ΔE** 4.5937 eV 269.90 nm ***f*** 0.0032	**S_3 (π-π^*)** **ΔE** 4.7564 eV 260.67 nm ***f*** 0.0473	**T_1 (π-π^*)** **ΔE** 3.1061 eV 399.17 nm ***f*** 0.0000	**T_2 (n-π^*)** **ΔE** 4.2200 eV 293.80 nm ***f*** 0.0000	**T_3 (π-π^*)** **ΔE** 4.2242 eV 293.51 nm ***f*** 0.0000
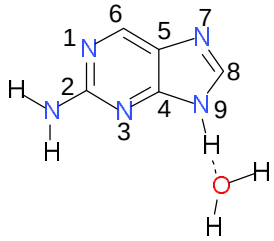	**S_1 (π-π^*)** **ΔE** 4.2375 eV 292.59 nm ***f*** 0.1598	**S_2 (n-π^*)** **ΔE** 4.5777 eV 270.84 nm ***f*** 0.0029	**S_3 (π-π^*)** **ΔE** 4.7089 eV 263.30 nm ***f*** 0.0230	**T_1 (π-π^*)** **ΔE** 3.0744 eV 403.28 nm ***f*** 0.0000	**T_2 (n-π^*)** **ΔE** 4.2087 eV 294.59 nm ***f*** 0.0000	**T_3 (n-π^*)** **ΔE** 4.2128 eV 294.30 nm ***f*** 0.0000
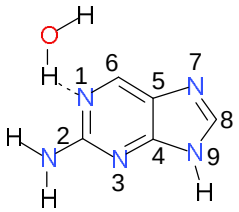	**S_1 (π-π^*)** **ΔE** 4.2122 eV 294.35 nm ***f*** 0.1564	**S_2 (n-π^*)** **ΔE** 4.6801 eV 264.92 nm ***f*** 0.0026	**S_3 (π-π^*)** **ΔE** 4.7430 eV 261.40 nm ***f*** 0.0484	**T_1 (π-π^*)** **ΔE** 3.0512 eV 406.35 nm ***f*** 0.0000	**T_2 (π-π^*)** **ΔE** 4.1954 eV 295.52 nm ***f*** 0.0000	**T_3 (n-π^*)** **ΔE** 4.3230 eV 286.80 nm ***f*** 0.0000
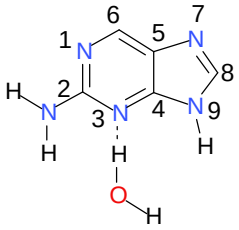	**S_1 (π-π^*)** **ΔE** 4.2789 eV 289.76 nm ***f*** 0.1719	**S_2 (n-π^*)** **ΔE** 4.6324 eV 267.65 nm ***f*** 0.0025	**S_3 (π-π^*)** **ΔE** 4.7243 eV 262.44 nm ***f*** 0.0145	**T_1 (π-π^*)** **ΔE** 3.0945 eV 400.66 nm ***f*** 0.0000	**T_2 (π-π^*)** **ΔE** 4.2396 eV 292.44 nm ***f*** 0.0000	**T_3 (n-π^*)** **ΔE** 4.2780 eV 289.82 nm ***f*** 0.0000
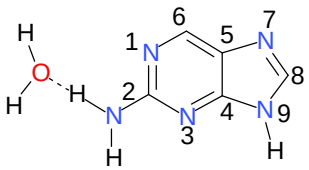	**S_1 (π-π^*)** **ΔE** 4.1563 eV 298.31 nm ***f*** 0.1608	**S_2 (n-π^*)** **ΔE** 4.5619 eV 271.78 nm ***f*** 0.0030	**S_3 (π-R)** **ΔE** 4.7176 eV 262.81 nm ***f*** 0.0069	**T_1 (π-π^*)** **ΔE** 3.0212 eV 410.38 nm ***f*** 0.0000	**T_2 (n-π^*)** **ΔE** 4.1902 eV 295.89 nm ***f*** 0.0000	**T_3 (π-π^*)** **ΔE** 4.1922 eV 295.75 nm ***f*** 0.0000
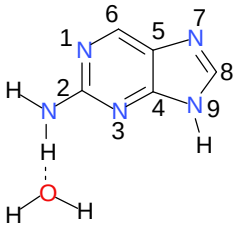	**S_1 (π-π^*)** **ΔE** 4.1554 eV 298.37 nm ***f*** 0.1514	**S_2 (n-π^*)** **ΔE** 4.5666 eV 271.50 nm ***f*** 0.0029	**S_3 (π-R)** **ΔE** 4.7187 eV 262.75 nm ***f*** 0.0057	**T_1 (π-π^*)** **ΔE** 3.0190 eV 410.69 nm ***f*** 0.0000	**T_2 (π-π^*)** **ΔE** 4.1926 eV 295.72 nm ***f*** 0.0000	**T_3 (n-π^*)** **ΔE** 4.1965 eV 295.45 nm ***f*** 0.0000

The assignments of the singlet states S_1 and S_2 of 2-Ap A when hydrogen bonded to one water molecule at different positions are same. When the amino group of the probe participates in hydrogen bonding formation the S_3 states were predicted to be of Rydberg character whereas when the acceptor hydrogen bonds atoms N1, N3 and N7 and the donor hydrogen bond group H9 are involved in hydrogen bonding formation the S_3 states were assigned as π-π*. The Figure 4.34 shows the comparison between the experimental absorption bands of 2-Ap in water with the theoretically predicted maxima of 2-Ap A non-hydrogen and hydrogen bonded to one water molecule.

Figure 4.34 2-Ap absorption spectrum and calculated 2-Ap$_{complex}$1H2O transitions

Experimental absorption spectrum of 2-Ap in water and predicted vertical transition represented as red lines for 2-Ap A in water without considering hydrogen bonding formation and as blue lines for 2-Ap A in water including hydrogen bonding formation (1 water molecule). The oscillator strengths indicating the probability of the transitions are also reported

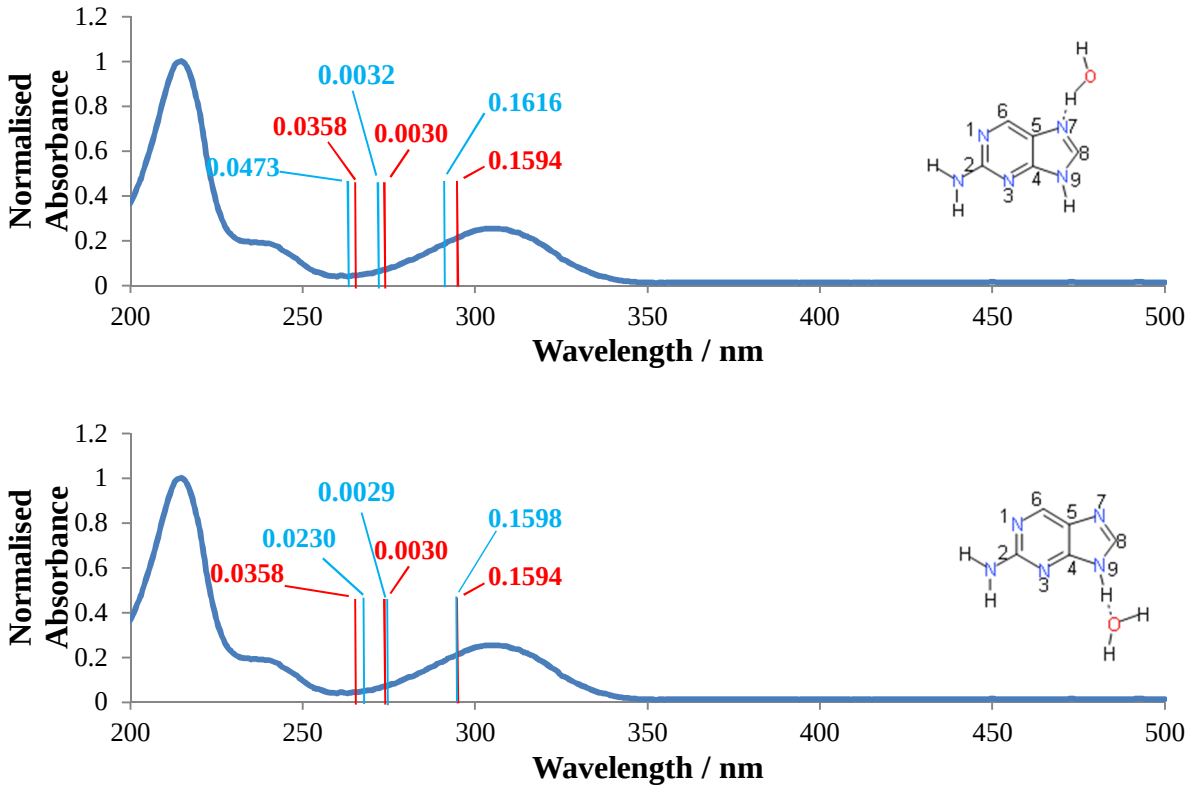

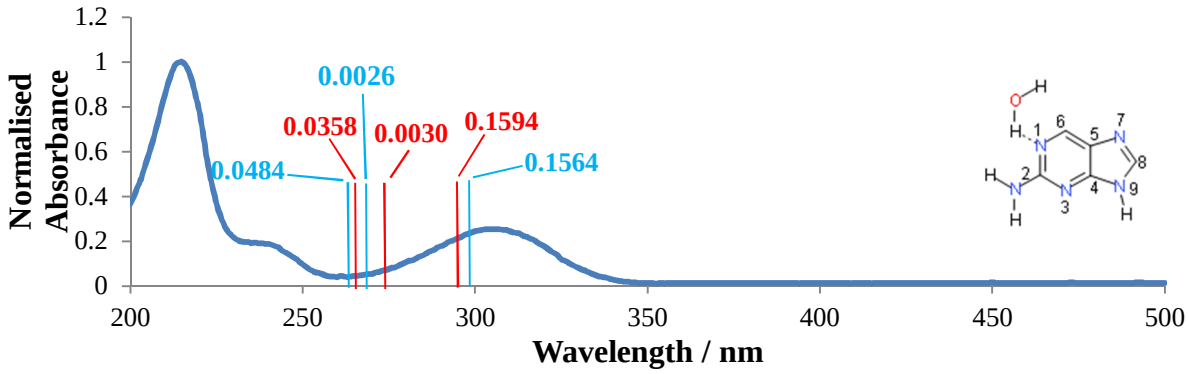
Normalised Absorbance
1.2
1
0.8
0.6
0.4
0.2
0
0.0026
0.0358
0.0030
0.1594
0.0484
0.1564
200
250
300
350
400
450
500
Wavelength / nm

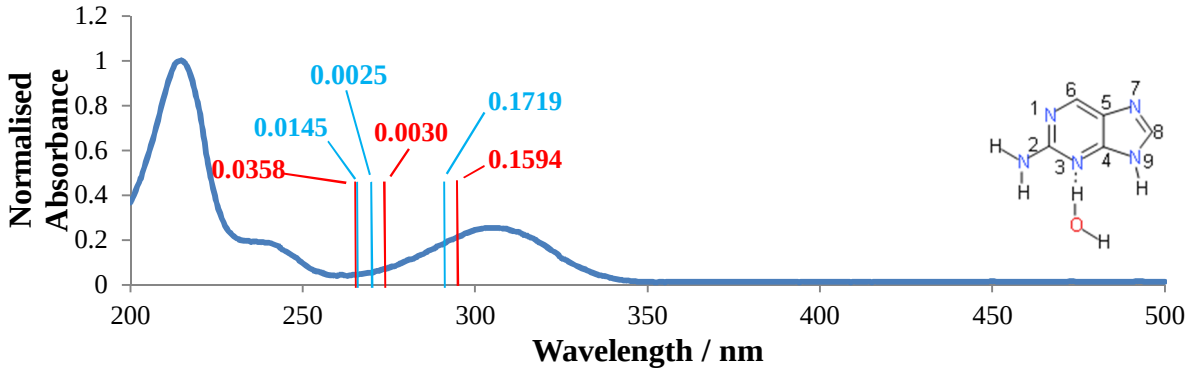
Normalised Absorbance
1.2
1
0.8
0.6
0.4
0.2
0
0.0025
0.0145
0.0030
0.1719
0.0358
0.1594
200
250
300
350
400
450
500
Wavelength / nm

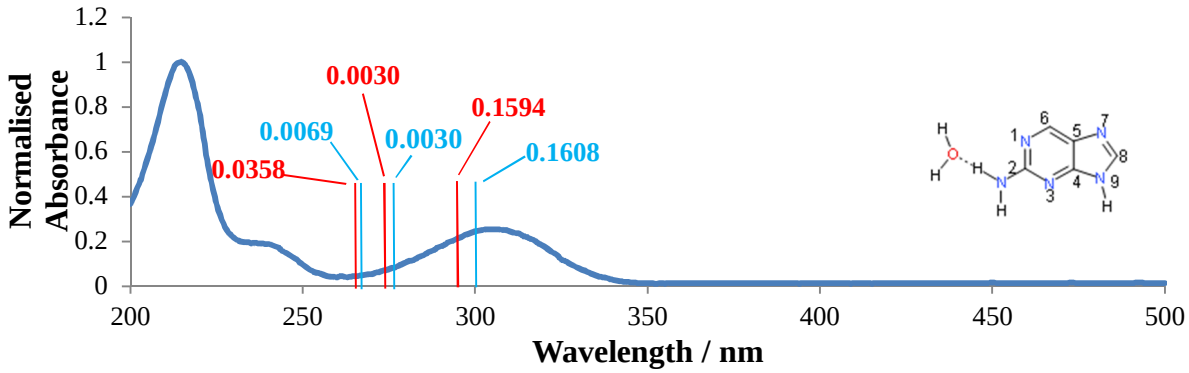
Normalised Absorbance
1.2
1
0.8
0.6
0.4
0.2
0
0.0030
0.0069
0.0030
0.1594
0.0358
0.1608
200
250
300
350
400
450
500
Wavelength / nm

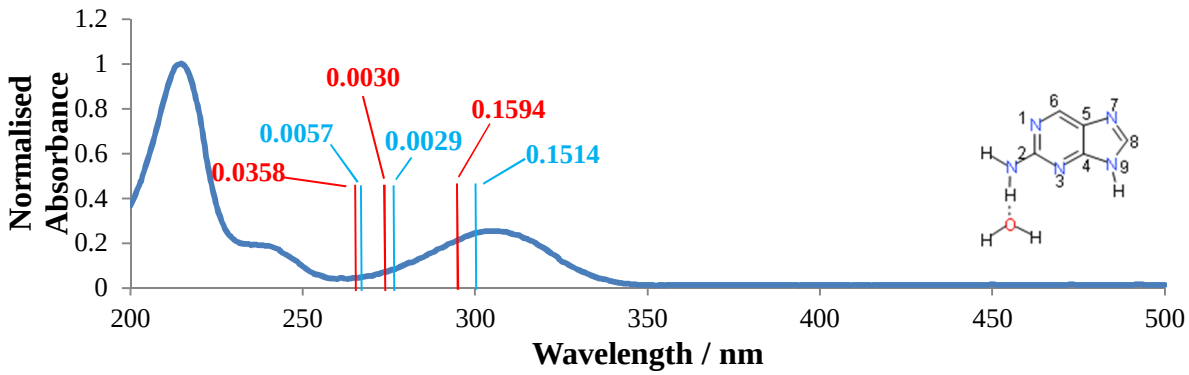
Normalised Absorbance
1.2
1
0.8
0.6
0.4
0.2
0
0.0030
0.0057
0.0029
0.1594
0.0358
0.1514
200
250
300
350
400
450
500
Wavelength / nm

The maxima of the calculated S_1 S_2 and S_3 states of 2-Ap A amino group when interacting with one water molecule are red-shifted compared to the predicted maxima of the solvated base without including hydrogen bonds. The energy of the S_1 state is in an excellent agreement with the experimental absorption band. From the results obtained, the stability of 2-Ap A hydrogen bonded to water molecule geometries increase with respect to the energy of the optimized geometry of 2-Ap A in water without hydrogen bonds, -467.244456 a.u see Table 4.1. Computational data were also obtained when more than one water molecule were considered, precisely three water molecules, hydrogen bonded to the hydrogen bond acceptor N7 and N1 atoms and the hydrogen bond donor H atom of chemically bonded to N9 (N9H group) as shown in Figure 4.35.

Figure 4.35 2-Ap A tautomer interacting with three water molecules

Optimized 2-Ap A tautomer interacting with three water molecules (N7, N1 and HN9 moieties of the probe) visualised on Chemcraft

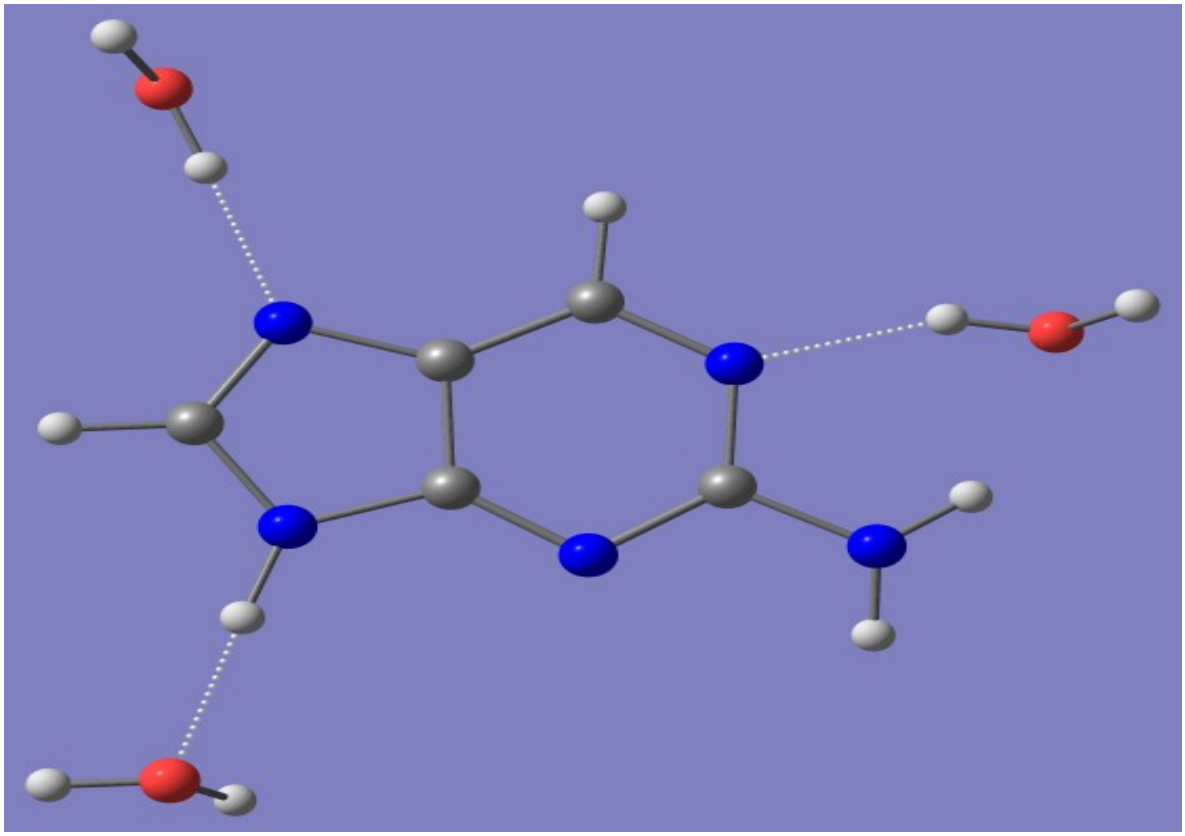

The Table 4.15 contains the single point energy of the optimized geometries of 2-Ap A hydrogen bonded to three water molecules, the dipole moment and the difference in energy between the 2-Ap $A_{complex}3H_2O$ and the energy of the base plus the energy of three water molecules, 2-Ap A + $3H_2O$ = -696.4780 a.u.

Table 4.15 Single point energies of 2-Ap A interacting with three water molecules

This table displays the dipole moments (D) and single point energy calculations (a.u) of the optimized geometries of 2-Ap A tautomer interacting with three water molecules given as $E_{complex}$. The difference between $E_{complex}$ and (2-Ap A + three water molecules single point energies) are also reported

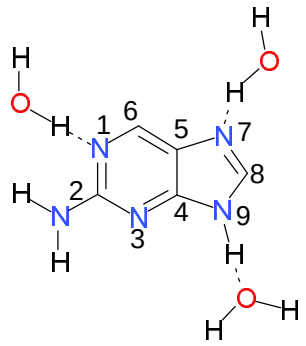

μ_g = 9.0923 D

$E_{complex}$ = - 696.4820 a.u

$E_{complex}$ - (2-Ap + $3H_2O$) = - 0.0040 a.u

The energy of 2-Ap A linked with three water molecules was found to be less than the combined energy of the solvated 2-Ap A and three water molecules, thus the 2-Ap $A_{complex}3H_2O$ results to be more stable than the free base under the influence of water molecules at the positions reported in the figure of Table 4.15. An increase in stability was also reported when one water molecule interacted with the amino group of the probe and the hydrogen atom bonded to N9, see Table 4.13. The Table 4.16 contains the computational data of the first three vertical transitions of 2-Ap A bonded to three water molecules.

Table 4.16 Vertical transitions of 2-Ap A hydrogen bonded to three water molecules

First three singlet and triplet state energies and oscillator strengths of 2-Ap A hydrogen bonded to three water molecules. The water molecules interact with the heteroatoms of the probe

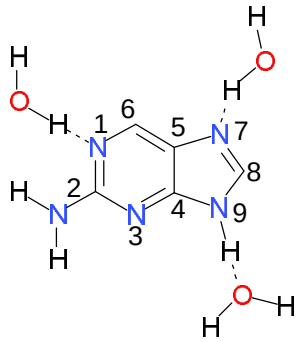

S_1 (π-π^*)	S_2 (n-π^*)	S_3 (π-π^*)	T_1 (π-π^*)	T_2 (π-π^*)	T_3 (n-π^*)
ΔE	**ΔE**	**ΔE**	**ΔE**	**ΔE**	**ΔE**
4.1863 eV	4.6553 eV	4.7219 eV	3.0372 eV	4.1982 eV	4.2943 eV
296.17 nm	266.33 nm	262.57 nm	408.21 nm	295.33 nm	288.72 nm
f	***f***	***f***	***f***	***f***	***f***
0.1510	0.0026	0.0315	0.0000	0.0000	0.0000

The first vertical transition results to be a π-π^* transition (HOMO of energy level 50 – LUMO of energy level 51). The second vertical transition is an n-π^* transition (occupied molecular orbital of energy level 49 – LUMO of energy level 51), the last vertical transition obtained is a π-π^* transition (HOMO of energy level 50 – unoccupied molecular orbital of energy level 52). The HOMO of energy level 50 is located on both the pyridine ring and imidazole ring as the unoccupied molecular orbital of energy level 52. The occupied molecular orbital of energy level 49 is delocalized on both rings with significant contribution of the nitrogen atoms of the rings. The nitrogen atom of the amino group of the pyridine ring was not affected. Intermolecular charge transfer between the solute and the water molecules was also predicted. The LUMO of energy level 51 did not show any intermolecular charge transfer, as shown in Figure 4.36. It should be noted that intermolecular charge transfer between the nitrogen lone pairs and water molecules was predicted when 2-Ap A interacted with one water molecule only. The diagram shown in Figure 4.37 illustrates the HOMOs and LUMOs of the molecule with and without the influence of hydrogen bonds. The HOMOs and LUMOs of the hydrogen bonded molecule (three water molecules) result to be slightly lower in energy when compared to the HOMOs and LUMOs of the non-hydrogen bonded molecule. The decrease in energy appears to be uniform among all the HOMOs and LUMOs and therefore, the separation in energy between them remains almost invariant. In other words, the energy gap between the HOMO and LUMO of the molecule with or without the effect of hydrogen bond formation can be considered the same.

Figure 4.36 Second vertical transition of 2-Ap A bonded to three water molecules

An n-π* transition. Manifestation of Intermolecular charge transfer from water molecules to solute molecule

Unoccupied MO
(energy level 51),
π* antibonding MO

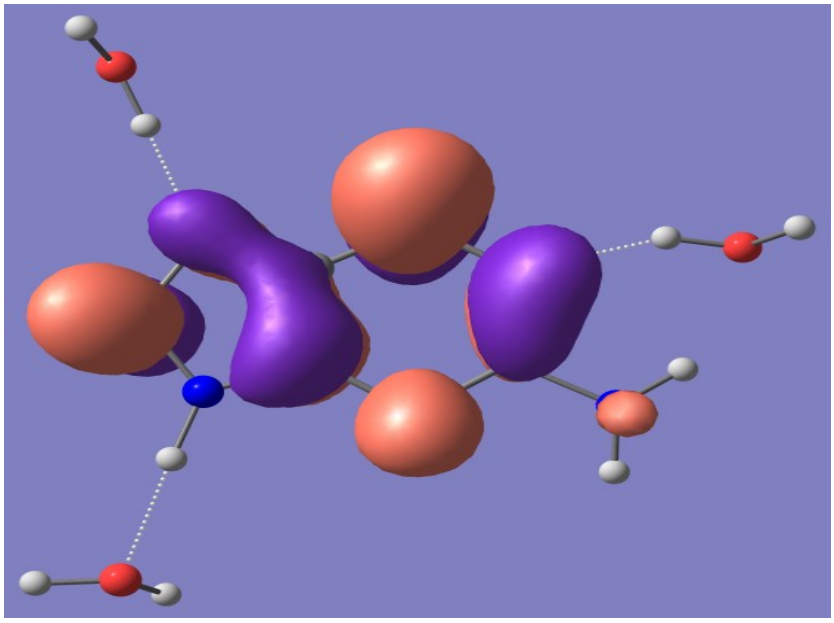

Second vertical transition
of 2-Ap N9H hydrogen
bonded to three water
molecules

n-π*

Occupied MO
(energy level 49),
n non-bonding MO

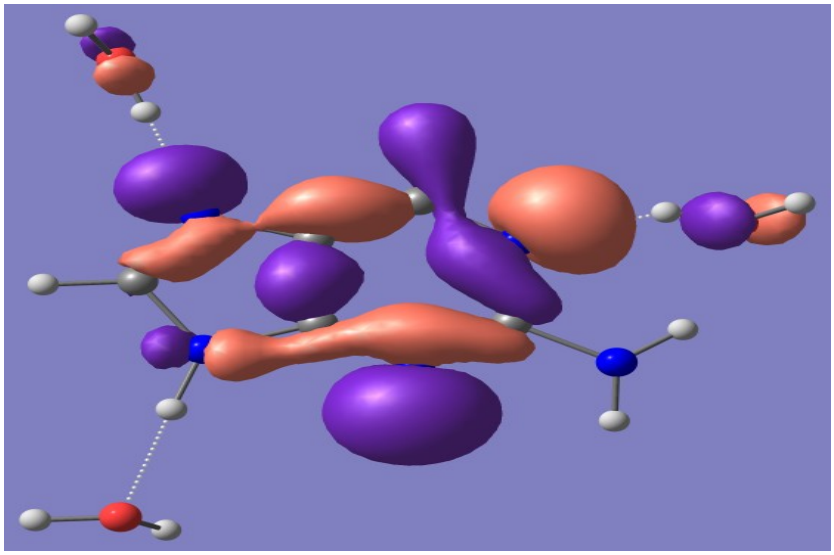

Figure 4.37 Diagram of molecular orbitals of 2-Ap A

Comparison of the predicted energies of the molecular orbitals involved in the first three vertical transitions of 2-Ap A non-hydrogen bonded and hydrogen bonded to three water molecules

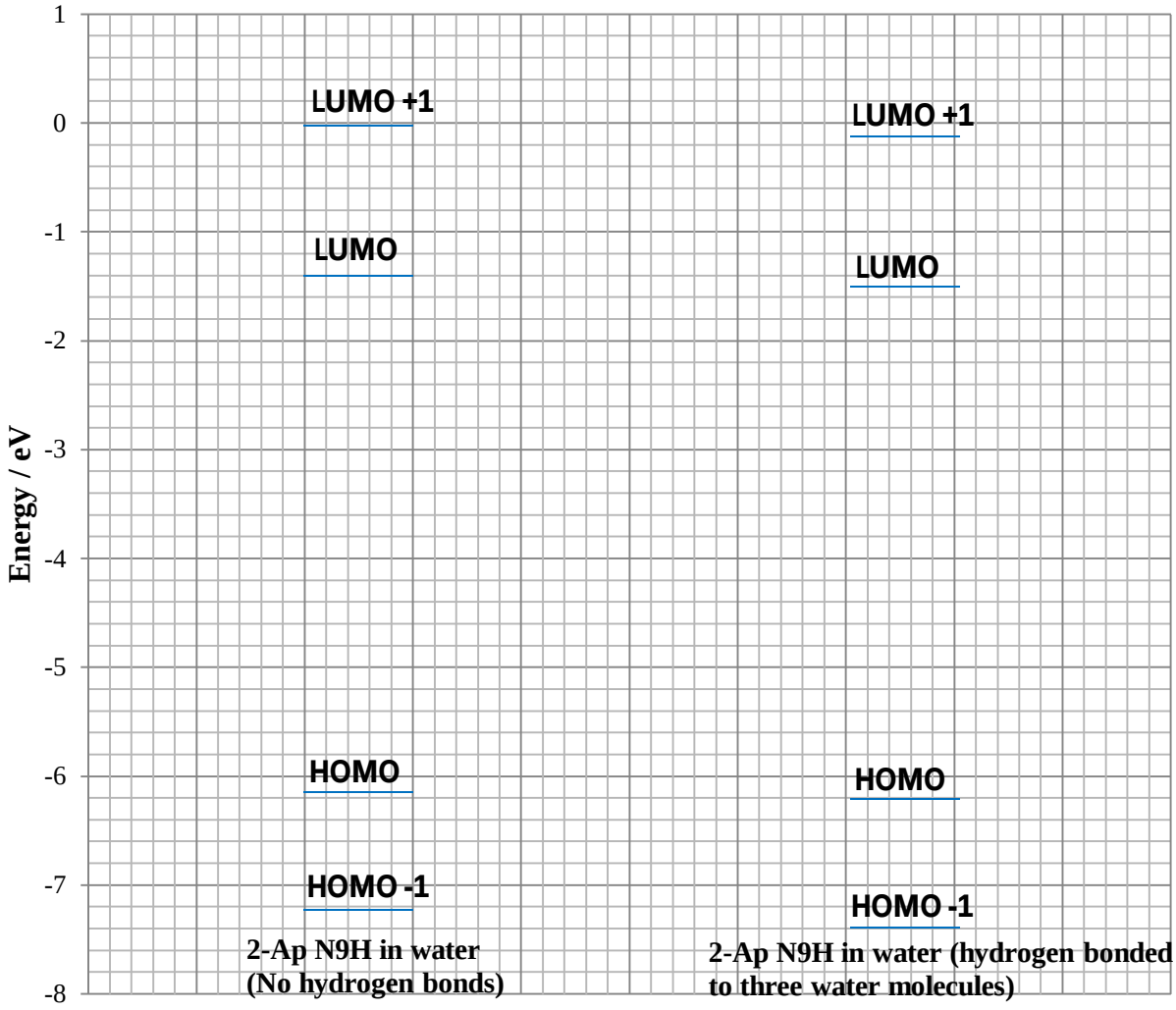

The Figure 4.38 shows the comparison between the experimental absorption bands of 2-Ap in water with the theoretically predicted maxima of 2-Ap A non-hydrogen and hydrogen bonded to three water molecules. The predicted wavelength of the first vertical transition is red-shifted with respect to the predicted wavelength of the first vertical transition obtained in absence of hydrogen bonds. The energy of the S_1 state is in a good agreement with the experimental absorption band. It should be noted that a slightly better agreement was found when one water molecule was hydrogen bonded to the amino group of 2-Ap A, see Figure 4.34.

Figure 4.38 2-Ap absorption spectrum and calculated 2-Ap$_{complex}$ 3H$_2$O transitions

Experimental absorption spectrum of 2-Ap in water and predicted vertical transition represented as red lines for 2-Ap A in water without considering hydrogen bonding formation and as blue lines for 2-Ap A in water including hydrogen bonding formation (3 water molecules). The oscillator strength indicating the probability of the transitions are also reported

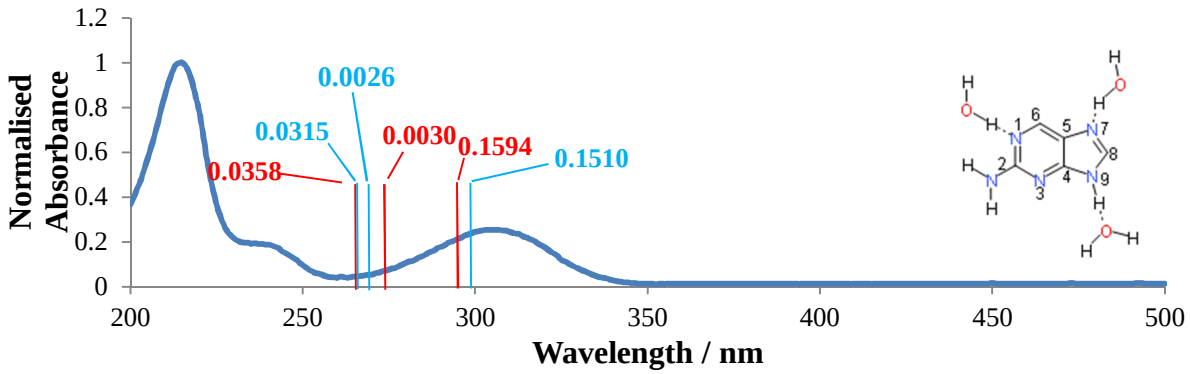

The Figure 4.39 provides a comparative summary between experimental and theoretical absorption (implicit and explicit solvent) of 2-Ap N9H tautomer in water.

Figure 4.39 Theoretical and experimental absorption of 2-Ap N9H tautomer

Summary and comparison between experimental and theoretical absorption, implicit and explicit solvent (1 and 3 water molecules) of 2-Ap N9H tautomer

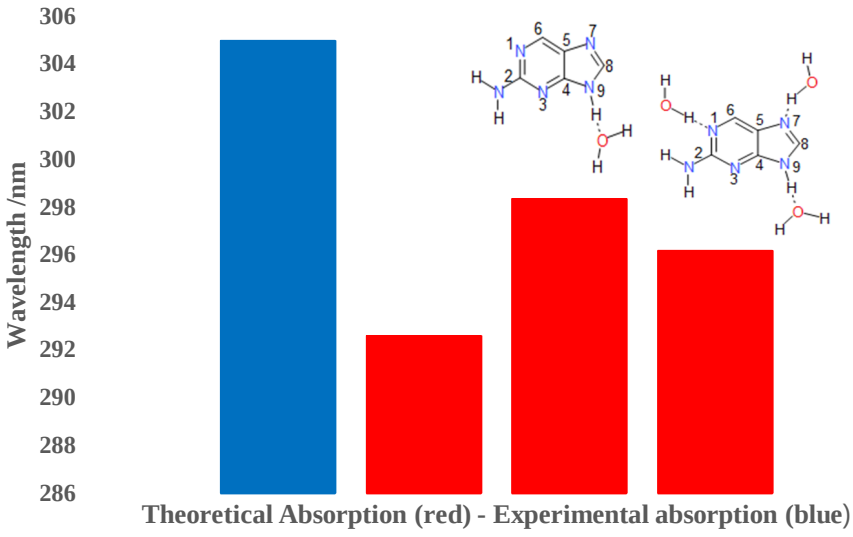

4.10.2 Pc A tautomer hydrogen bonded to water molecules

The energies of the optimized geometries of Pc A interacting with a water molecule with its nitrogen atoms within the heterocyclic structure and oxygen atom of the carbonyl group are shown in Table 4.17.

Table 4.17 Single point energies of Pc A interacting with one water molecule

This table displays the dipole moments (D) and single point energy calculations (a.u) of the optimized geometries of Pc A tautomer interacting with one water molecule given as $E_{complex}$. The difference between $E_{complexes}$ and (Pc A + water molecule single point energies) are also reported

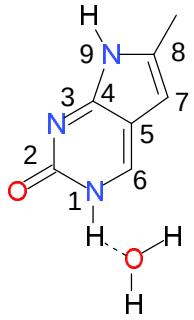	μ_g = 6.7560 D $E_{complex}$ = -586.7794 a.u $E_{complex}$ - (Pc + $1H_2O$) = - 0.0054 a.u	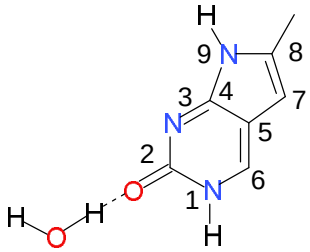	μ_g = 8.8137 D $E_{complex}$ = -586.7799 a.u $E_{complex}$ - (Pc + $1H_2O$) = - 0.0059 a.u
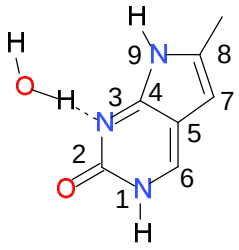	μ_g = 12.7263 D $E_{complex}$ = -586.7688 a.u $E_{complex}$ - (Pc + $1H_2O$) = 0.0052 a.u	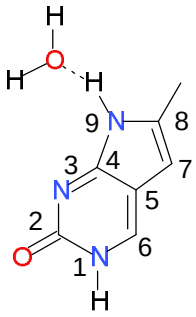	μ_g = 6.7280 D $E_{complex}$ = -586.7795 a.u $E_{complex}$ - (Pc + $1H_2O$) = - 0.0055

The Table 4.17 contains the dipole moments and single point energies given as Pc $A_{complexes}$ $3H_2O$. The difference in energy reported was calculated by considering the energy of Pc A as free base, - 510.3628 a.u taken from Table 4.2 and the theoretically predicted single point energy of one water molecule which is as previously already calculated to be - 76.4112 a.u. Then, Pc A energy + 1 water molecule energy = - 586.7740 a.u.

The assignments and the molecular orbitals involved in the first three singlet transitions of Pc A hydrogen bonded to one water molecule are reported as follows:

When the donor hydrogen atom linked with N1 was linked with a water molecule the first vertical transition was found to be a π-π* (HOMO of energy level 44 – LUMO of energy level 45). The second vertical transition is a π-Rydberg transition (HOMO of energy level 44 – unoccupied molecular orbital of energy level 46). The third vertical transition is of π-π* character (occupied molecular orbital of energy level 43 – LUMO of energy level 45).

The generated computational data obtained when the oxygen atom of the carbonyl group and the acceptor hydrogen atom N3 are hydrogen bonded to a water molecule revealed that the first vertical transition is a π-π* transition (HOMO of energy level 44 – LUMO of energy level 45). The second vertical transition is of π-π* character (occupied molecular orbital of energy level 43 – LUMO of energy level 45). The third vertical transition is an n-π* transition (occupied molecular orbital of energy level 42 – LUMO of energy level 45).

In the case of the hydrogen atom linked with the N9 atom when hydrogen bonded to a water molecule the first vertical transition is a π-π* transition (HOMO of energy level 44 – LUMO of energy level 45). The second vertical transition results to be a π-Rydberg transition (HOMO of energy level 44 – unoccupied molecular orbital of energy level 46). The third vertical transition is of π-π* character (occupied molecular orbital of energy level 43 – LUMO of energy level 45).

The Table 4.18 contains the theoretically predicted energies, assignments and oscillator strengths of the first three singlet and triplet states of Pc A hydrogen bonded to one water molecule.

Transitions of Rydberg character were predicted when one water molecule was linked with hydrogen bond donor groups HN9 and HN1. No Rydberg orbitals were predicted when the acceptor hydrogen bond atoms, the Oxygen atom of the carbonyl functional group and N3, participated in hydrogen bonding formation. The Figure 4.40 shows the comparison between the experimental absorption bands of Pc in water with the theoretically predicted maxima of Pc A non-hydrogen and hydrogen bonded to one water molecule.

Table 4.18 Vertical transitions of Pc A hydrogen bonded to one water molecule

First three singlet and triplet state energies and oscillator strengths of Pc A hydrogen bonded to one water molecule. The water molecule interacts with the heteroatoms and the carbonyl group of the probe

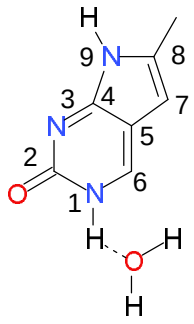	**S_1 (π-π^*)** **ΔE** 3.6866 eV 336.31 nm ***f*** 0.0902	**S_2 (π-R)** **ΔE** 4.6172 eV 268.53 nm ***f*** 0.0000	**S_3 (π-π^*)** **ΔE** 4.8762 eV 254.26 nm ***f*** 0.0089	**T_1 (π-π^*)** **ΔE** 2.4796 eV 500.01 nm ***f*** 0.0000	**T_2 (π-π^*)** **ΔE** 4.0912 eV 303.05 nm ***f*** 0.0000	**T_3 (π-π^*)** **ΔE** 4.3513 eV 284.94 nm ***f*** 0.0000
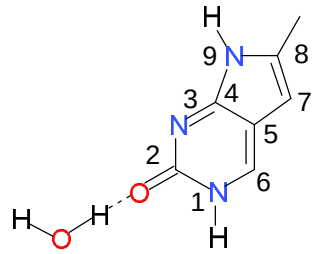	**S_1 (π-π^*)** **ΔE** 3.6980 eV 335.27 nm ***f*** 0.0815	**S_2 (π-π^*)** **ΔE** 4.6470 eV 266.80 nm ***f*** 0.0080	**S_3 (n-π^*)** **ΔE** 4.8686 eV 254.66 nm ***f*** 0.0014	**T_1 (π-π^*)** **ΔE** 2.4938 eV 497.16 nm ***f*** 0.0000	**T_2 (π-π^*)** **ΔE** 4.0884 eV 303.26 nm ***f*** 0.0000	**T_3 (π-π^*)** **ΔE** 4.3317 eV 286.23 nm ***f*** 0.0000
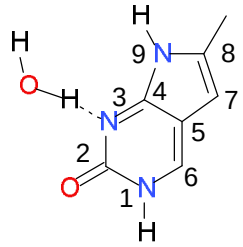	**S_1 (π-π^*)** **ΔE** 3.6920 eV 335.82 nm ***f*** 0.0808	**S_2 (π-π^*)** **ΔE** 4.6609 eV 266.01 nm ***f*** 0.0092	**S_3 (n-π^*)** **ΔE** 4.8877 eV 253.67 nm ***f*** 0.0010	**T_1 (π-π^*)** **ΔE** 2.4833 eV 499.27 nm ***f*** 0.0000	**T_2 (π-π^*)** **ΔE** 4.0986 eV 302.51 nm ***f*** 0.0000	**T_3 (π-π^*)** **ΔE** 4.3261 eV 286.60 nm ***f*** 0.0000
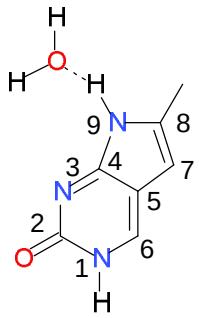	**S_1 (π-π^*)** **ΔE** 3.6517 eV 339.53 nm ***f*** 0.0818	**S_2 (π-R)** **ΔE** 4.6239 eV 268.14 nm ***f*** 0.0000	**S_3 (π-π^*)** **ΔE** 4.8703 eV 254.57 nm ***f*** 0.0100	**T_1 (π-π^*)** **ΔE** 2.4474 eV 506.60 nm ***f*** 0.0000	**T_2 (π-π^*)** **ΔE** 4.1051 eV 302.02 nm ***f*** 0.0000	**T_3 (π-π^*)** **ΔE** 4.3042 eV 288.05 nm ***f*** 0.0000

As shown in Figure 4.40, the maxima of the calculated S_1 state of Pc A when participating in hydrogen bonding formation with one water molecule at the following positions: hydrogen of the N1H group, the oxygen atom of the carbonyl group and the N3 atom are blue-shifted with respect to the maximum wavelength of the predicted S_1 of Pc A solvated only. These theoretically calculated maxima are in an even better agreement with the experimental absorption band, perfectly coinciding with the experimental maximum of the absorption spectrum of Pc in water. In the case of the hydrogen donor atom bonded to N9, the formation

of hydrogen bonding with a water molecule at that position within the molecule generated a calculated absorption maximum which is red-shifted compared to the solvated one and the experimental one.

Figure 4.40 Pc absorption spectrum and calculated $Pc_{complex}$ $1H_2O$ transitions

Experimental absorption spectrum of Pc in water and predicted vertical transition represented as red lines for Pc A in water without considering hydrogen bonding formation and as blue lines for Pc A in water including hydrogen bonding formation (1 water molecule). The oscillator strength indicating the probability of the transitions are also reported

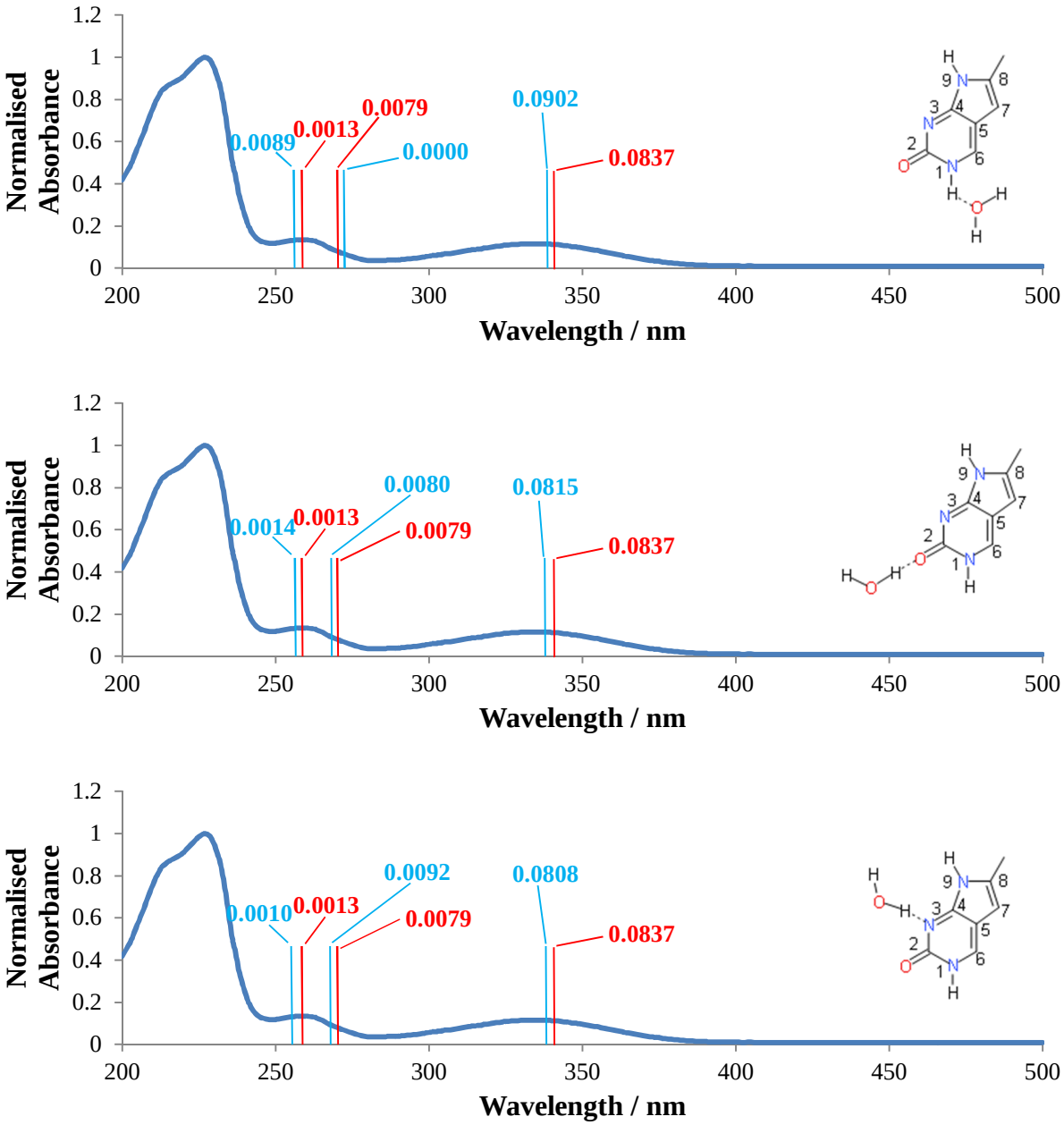

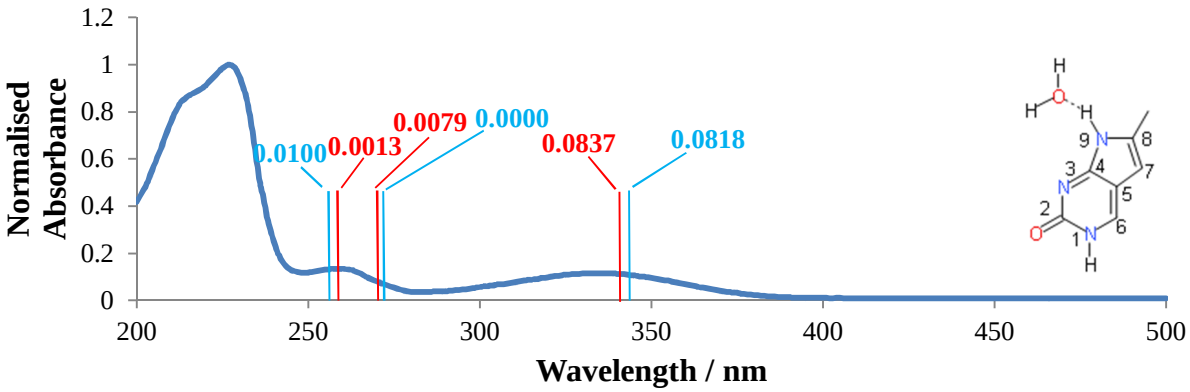

From the computational study of Pc N1H hydrogen bonded to water molecules, it appears that when the water molecules interacted with the hydrogen acceptor atoms of the molecule the maxima wavelengths of the first vertical transition are blue shifted with respect to the maxima wavelengths of the first vertical transition obtained when water molecules are linked with the hydrogen acceptor atoms of the molecule. Similarly to 2-Ap N9H (A), also Pc N1H (A) when hydrogen bonded resulted to be energetically more stable compared to the non-hydrogen bonded counterpart -510.362822 a.u, see Tables 4.2 and 4.17 for comparison. As in the case of 2-Ap A, Pc A was hydrogen bonded to three water molecules precisely at the following positions: the hydrogen atom linked to N1 and N9, and the oxygen atom of the carbonyl atom as displayed below in Figure 4.41

The Table 4.19 contains the single point energy of the optimized geometries of Pc A hydrogen bonded to three water molecules its dipole moment and the difference in energy between the Pc $A_{complex}3H_2O$ and the energy of the base plus the energy of three water molecules, Pc A + $3H_2O$ = - 739.5964 a.u.

The Pc $A_{complex}3H_2O$ is more stable in terms of energy than the Pc $A_{complexes}$ when only one water molecule was hydrogen bonded to different electronegative sites within the fluoroprobe, see Table 4.17. The Table 4.20 contains the computational data of the first three vertical transitions of Pc A bonded to three water molecules at the positions shown in Figure 4.41.

Figure 4.41 Pc A interacting with three water molecules

Optimized Pc A tautomer interacting with three water molecules (positions N9H, N1H and carbonyl group) visualised on Chemcraft

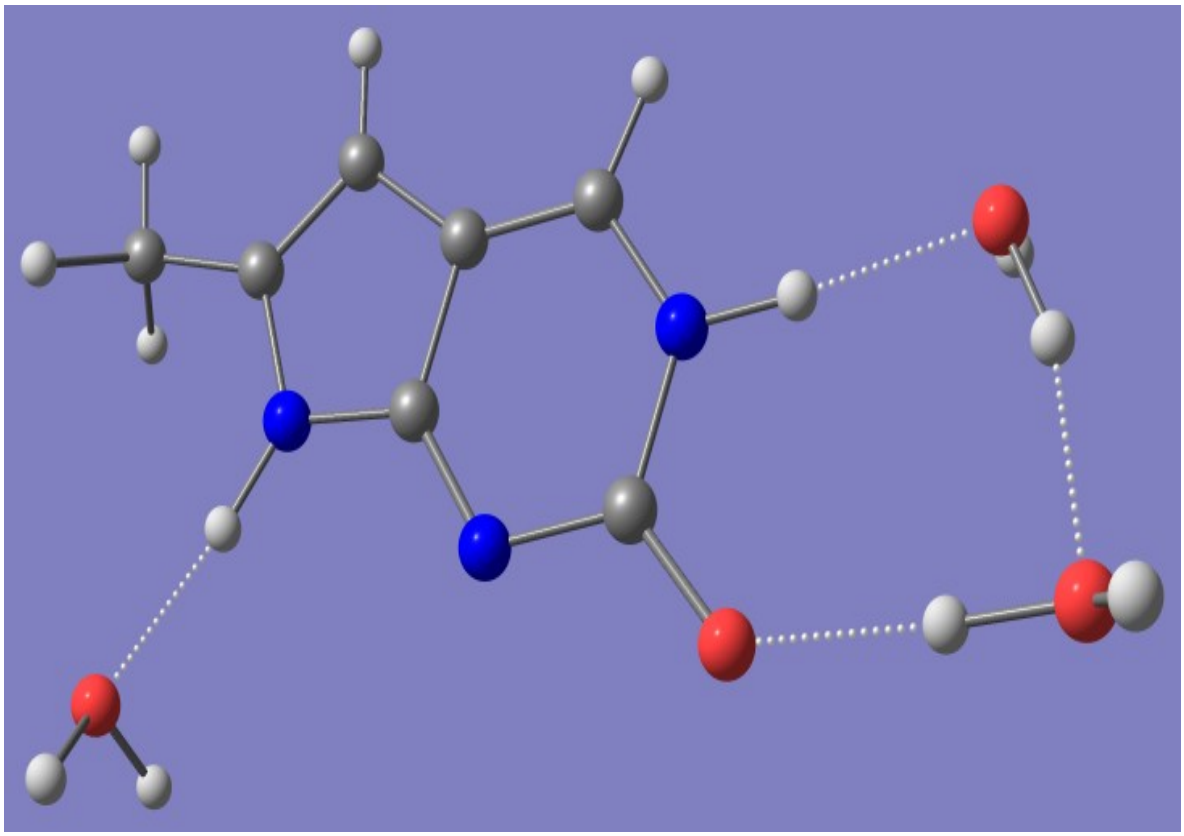

Table 4.19 Single point energies of Pc A interacting with three water molecules

This table displays the dipole moments (D) and single point energy calculations (a.u) of the optimized geometries of Pc A tautomer interacting with three water molecules given as $E_{complex}$. The difference between $E_{complex}$ and (Pc A + three water molecules single point energies) are also reported

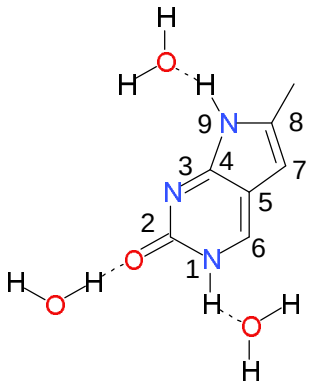	μ_g = 6.1839 D $E_{complex}$ = - 739.6197 a.u $E_{complex}$ - (Pc + $3H_2O$) = - 0.0233 a.u

Table 4.20 Vertical transitions of Pc A hydrogen bonded to three water molecules

First three singlet and triplet state energies and oscillator strengths of Pc A hydrogen bonded to three water molecules. The water molecules interact with the heteroatoms and the carbonyl group of the probe

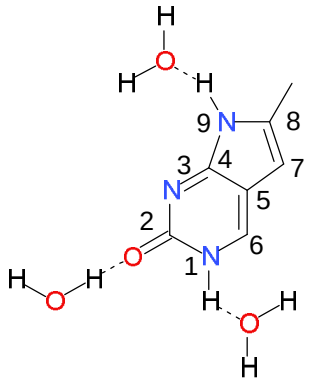

S_1 (π-π^*)	S_2 (π-π^*)	S_3 (π-R)	T_1 (π-π^*)	T_2 (π-π^*)	T_3 (π-π^*)
ΔE	**ΔE**	**ΔE**	**ΔE**	**ΔE**	**ΔE**
3.7033 eV	4.6418 eV	4.9333 eV	2.5071 eV	4.0951 eV	4.3109 eV
334.79 nm	267.10 nm	251.32 nm	494.54 nm	302.76 nm	287.61 nm
f	***f***	***f***	***f***	***f***	***f***
0.0830	0.0092	0.0000	0.0000	0.0000	0.0000

The first vertical transition is a π-π* transition (HOMO of energy level 54 – LUMO of energy level 55). The second vertical transition is a π-π* transition (HOMO of energy level 53 – LUMO of energy level 55). The third vertical transition is of Rydberg character, a π-R transition (HOMO of energy level 54 – unoccupied molecular orbital of energy level 56). The occupied molecular orbital of energy level 53 is mainly located on all the heteroatoms of the imidazole and pyridine rings. The LUMO of energy level 55 is prevalently located on the nitrogen atoms of the structure and also some electronic density was observed on the alkyl substituent of the imidazole ring whereas the Oxygen atom of the carbonyl group was completely stripped of its electronic density as shown in Figure 4.42. The manifestation of intramolecular charge transfer (ICT) between electron acceptor and donor groups from ground states to excited states of fluoroprobes has been extensively studied (Grabowski *et al.* 1979; Zietz and Retting; 2000). Another peculiar example of ICT is shown in Figure 4.18. As displayed in the figure the HOMO is mainly located on the Oxygen atom and the pyridine ring whereas the LUMO is located on both pyridine and imidazole rings and the alkyl substituent of the latter (the HOMO and LUMO of the third vertical transition of Pc A in water, an n-π* electronic transition, resemble the ones predicted in vacuum as displayed in Figure 4.18). As opposed to 2-Ap A no intermolecular charge transfer between water molecules and Pc A was predicted either with one or three water molecules considered.

Figure 4.42 Second vertical transition of Pc A bonded to three water molecules

A π-π* transition. Manifestation of Intramolecular charge transfer between acceptor/donor electron groups

Unoccupied MO
(energy level 55),
π* antibonding MO

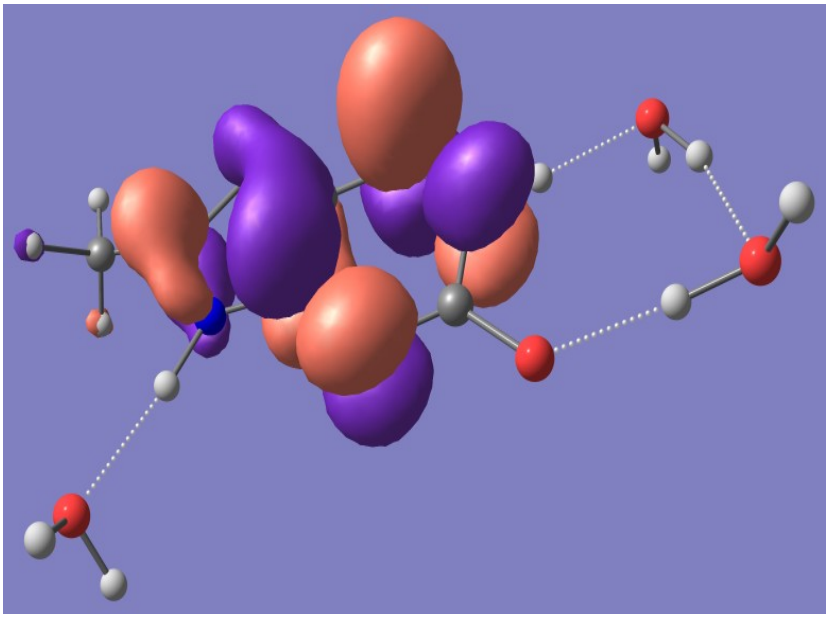

Second vertical transition
of Pc A hydrogen
bonded to three water
molecules

π-π*

Occupied MO
(energy level 53),
π bonding MO

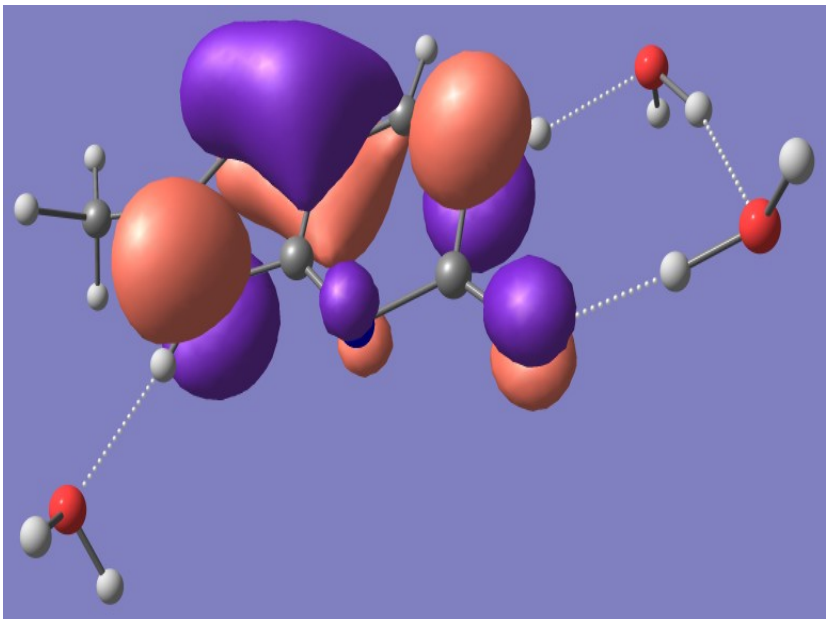

The energy diagram shown in Figure 4.43 illustrates the HOMOs and LUMOs of the molecule with and without the influence of hydrogen bonds with water molecules.

Figure 4.43 Diagram of HOMOs and LUMOs of Pc A

Comparison of the predicted energies of the molecular orbitals involved in the first three vertical transitions of Pc A non-hydrogen bonded and hydrogen bonded to three water molecules

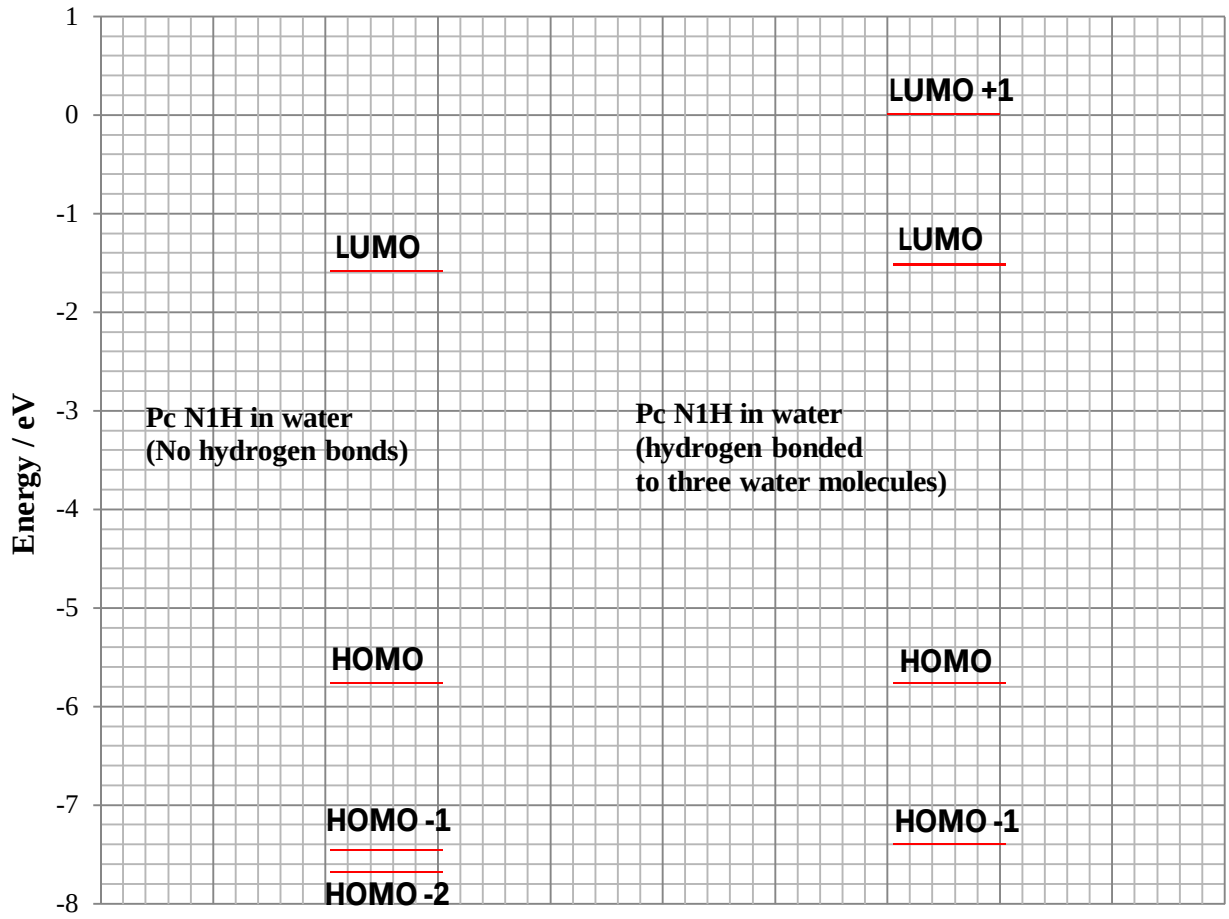

When Pc was linked with three water molecules two occupied molecular orbitals and two unoccupied molecular orbitals were predicted for the first three vertical transitions. Similarly to 2-Ap A, see Figure 4.37, the separation in energy between the HOMO and LUMO in absence and presence of hydrogen bonds appears to be almost equal. The Figure 4.44 shows the comparison between the experimental absorption bands of 2-Ap in water with the theoretically predicted maxima of 2-Ap A non-hydrogen and hydrogen bonded to three water molecules. As shown in Figure 4.44 the predicted maxima of the first three vertical transitions are blue-shifted compared to the predicted maxima in absence of hydrogen bonds.

Figure 4.44 Pc absorption spectrum and calculated $Pc_{complex}$ $3H_2O$ transitions

Experimental absorption spectrum of Pc in water and predicted vertical transition represented as red lines for Pc A in water without considering hydrogen bonding formation and as blue lines for Pc A in water including hydrogen bonding formation (3 water molecules). The oscillator strength indicating the probability of the transitions are also reported

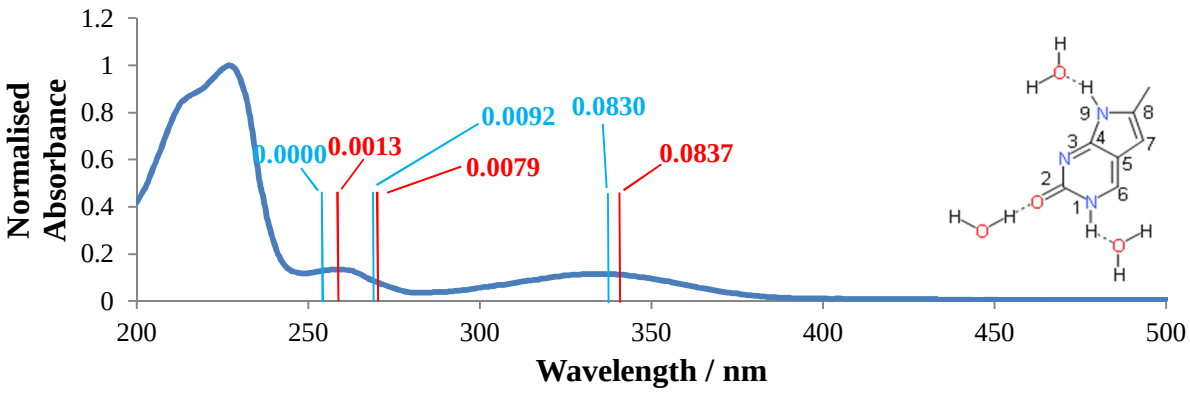

The energy of the S_1 state is in an excellent agreement with the experimental absorption band. The figure 4.45 illustrates a summary of the experimental and theoretical absorption (implicit and explicit solvent) of Pc A tautomer in water.

Figure 4.45 Theoretical and experimental absorption of Pc A tautomer

Summary and comparison between experimental and theoretical absorption, implicit and explicit solvent (1 and 3 water molecules) of Pc A tautomer

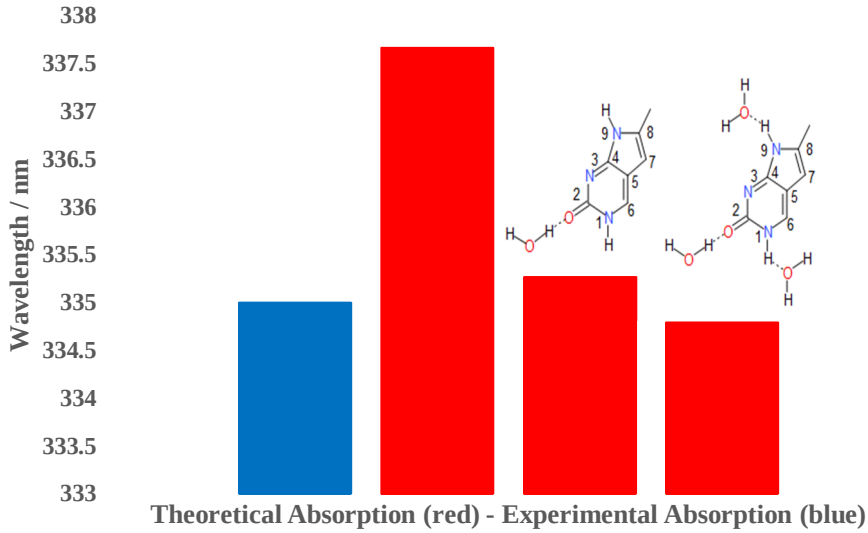

It should be noted that even though the functional B3LYP is a well-established method to describe biological systems at a very low computational cost other DFT methods tend to fare better at improving stabilization of molecules when non-covalent intermolecular interactions are involved. In fact, B3LYP tends to overestimate interaction energies of hydrogen bonded complexes because of dispersion interactions (Tsuzuki and Luthi, 2001; Zhao and Truhlar, 2004; Zhao and Truhlar, 2005). Thus, geometry stability of nucleic acids may be improved by using less popular DFT methods such as: P86 and PW91. P86 is the gradient corrections of Perdew along with its local correlation functional (Perdew and Zunger, 1981; Perdew, 1986). PW91 is the Perdew and Wang's 1991 gradient-corrected correlation functional (Perdew *et al.* 1996). These correlation functionals when combined with exchange functionals proved to give improved theoretical data which can be reasonably matched with experimental data obtained through crystallographic studies of the natural bases (Wjist *et al.* 2006).

4.11 Applying laws of photochemistry

The predicted singlet state energies of 2-Ap A as free base and linked with three water molecules are illustrated in Figure 4.46. The figure shows the remarkable influence of the hydrogen bonding formation on the energy gap existing between the two low-lying electronic states n-π* and π-π*. The separation of the two low-lying states of the molecule increases when the molecule is hydrogen bonded to water. The singlet states are not the only states to be affected by the influence of the hydrogen bonding formation but also the triplet states are affected. The Figure 4.47 shows the increase in energy of T_2 and T_3 triplet states of the hydrogen bonded 2-Ap A molecule. It should be noted that the character of these states is inverted. The T_2 triplet state is no longer an n-π* state but a π-π* state and the T_3 triplet state was found to be n-π* state and not a π-π* state. The comparison of the singlet and triplet states of 2-Ap A in water (the hydrogen bonded molecule) and chloroform (solvent with a very low dielectric constant see Table 3.2 and incapable of forming hydrogen bonds) as shown in Figure 4.48 may help to understand the higher rate of fluorescence of the molecule measured in protic (water has the highest dielectric constant and it is a hydrogen bond donor as well as a hydrogen bond acceptor solvent) solvents capable of forming hydrogen bonds with the fluorescent base.

Figure 4.46 Hydrogen and non- hydrogen bonded 2-Ap A singlet states

Difference in n-π* and π-π* energy gap between the non-hydrogen bonded and hydrogen bonded 2-Ap A tautomer

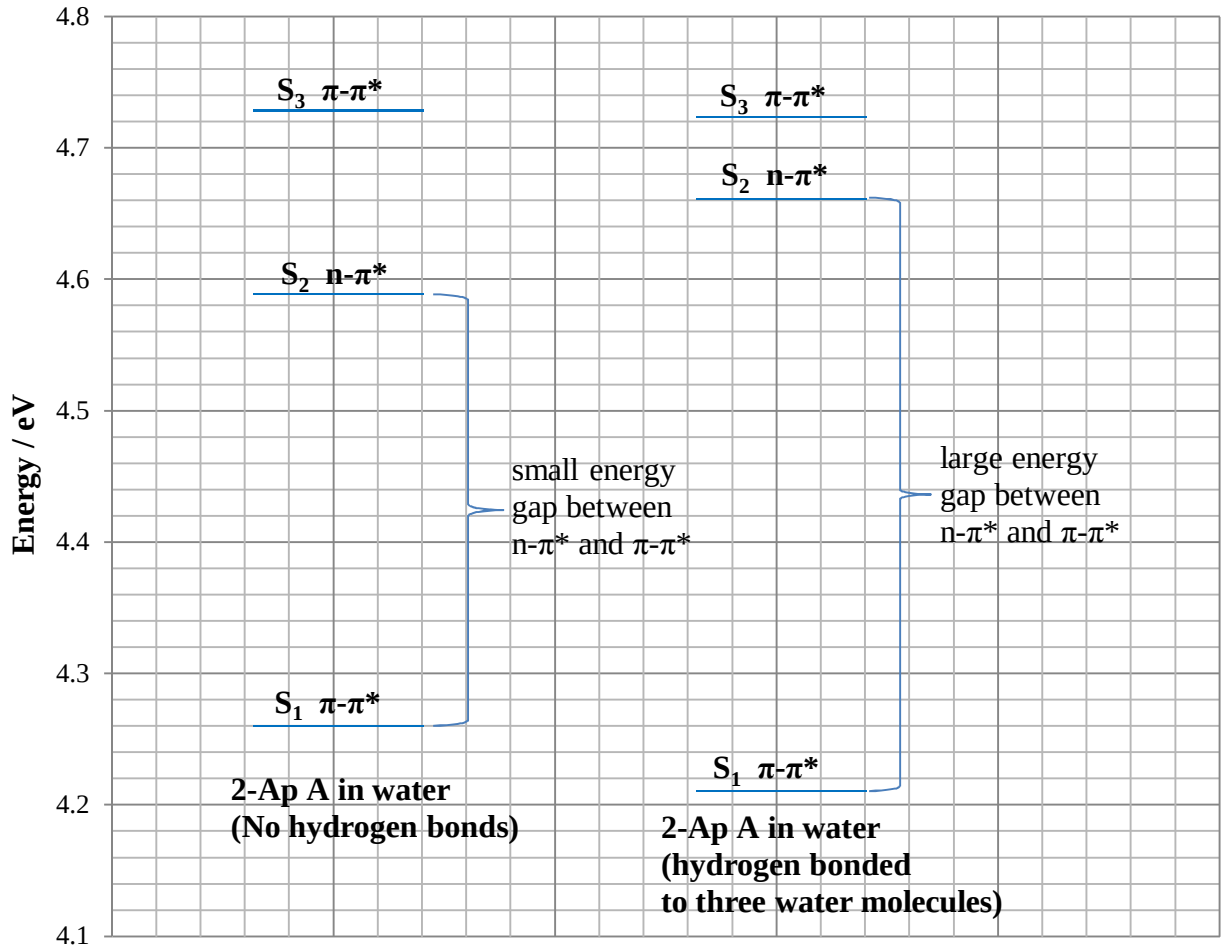

Transitions from singlet states to triplet sates are considered forbidden because they are transitions between two states of different spin multiplicity (change of spin, see Jablonski diagram in the general introduction) and therefore, the rate of ISC (intersystem crossing) k_{ISC} is small. The rate of ISC is governed by El-Sayed's selection rules (El-Sayed, 1968). According to his rules the rate of ISC from the lowest singlet state to the triplet manifold is large if the radiationless transition involves a change of orbital type (see Chapter 2 Section 2.3.4 for a detailed explanation about this rule), for example, a transition from $^1(\pi\text{-}\pi^*)$ to $^3(\text{n-}\pi^*)$.

Figure 4.47 Hydrogen and non-hydrogen bonded 2-Ap (A) singlet and triplet states

The first three singlet and triplet electronic states of hydrogen and non-hydrogen bonded 2-Ap A tautomer

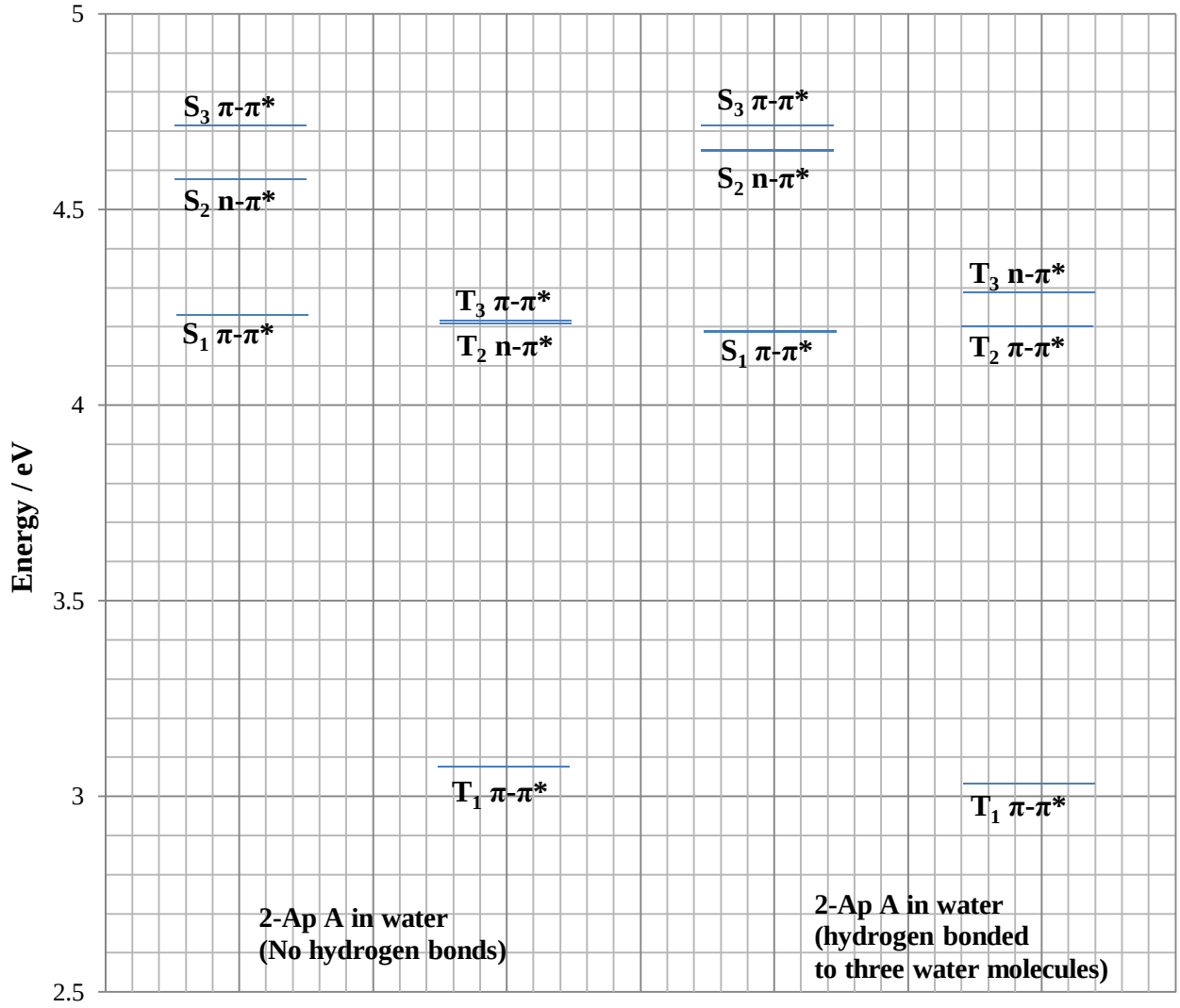

As shown in Figure 4.48 the intersystem crossing from a S_1 π-π* to a T_2 π-π* of 2-Ap in water is highly unlikely because it takes place between two states of the same orbital type. In addition to this the transition is not energetically favoured because the triplet state is higher in energy compared to the singlet state. In the case of 2-Ap in chloroform, ISC between a S_1 π-π* and a T_2 n-π* is less forbidden because of change of orbital type and energetically favoured, being T_2 n-π* lower in energy than S_1 π-π*. Thus, the decrease in fluorescence of 2-Ap in polar solvents of low dielectric constants may not only be due to vibronic coupling between the dark state n-π* and the bright state π-π* but also because of ISC competing with

fluorescence. This combination of vibronic coupling with a calculated large ISC is a theoretical prediction of decrease in rate of fluorescence of 2-Ap in non-polar solvents that would be consistent with the experimental studies. As shown in Table 3.1 the experimental quantum yields of 2-Ap in water and chloroform are 0.686 ± 0.016 and 0.129 ± 0.004 respectively.

Figure 4.48 Singlet and triplet states of 2-Ap A in water and chloroform

The radiative transitions (fluorescence) and non-radiative transitions (IC and ISC) in water and chloroform are displayed. For convenience the vibrational levels of the excited and ground states are not included also IC has been shown as a wavy arrows which are indicative of vibrational relaxation (see Chapter 2 for details)

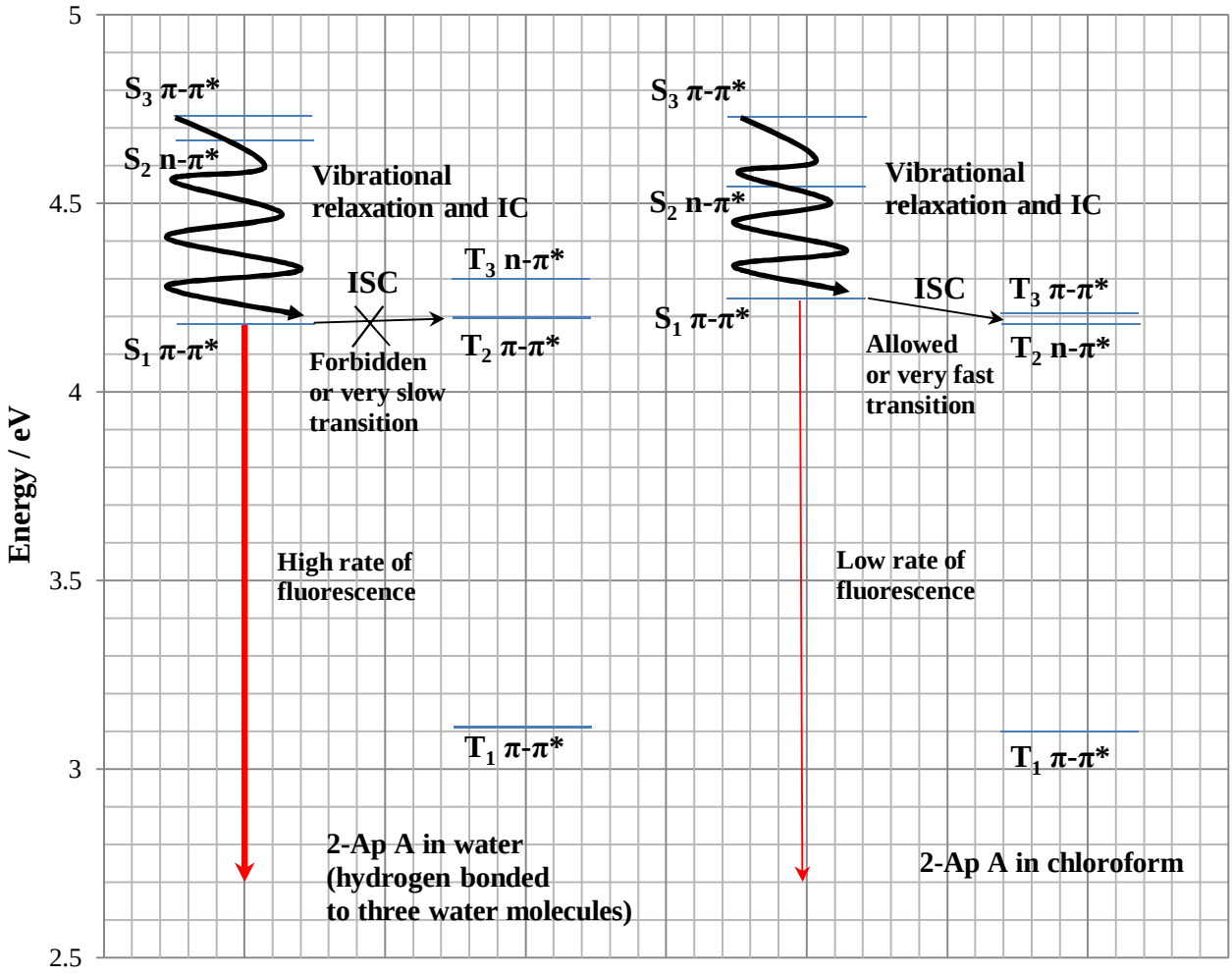

Figure 4.49 Hydrogen and non-hydrogen bonded Pc A singlet and triplet states

The first three singlet and triplet electronic states of non-hydrogen and hydrogen bonded Pc A tautomer

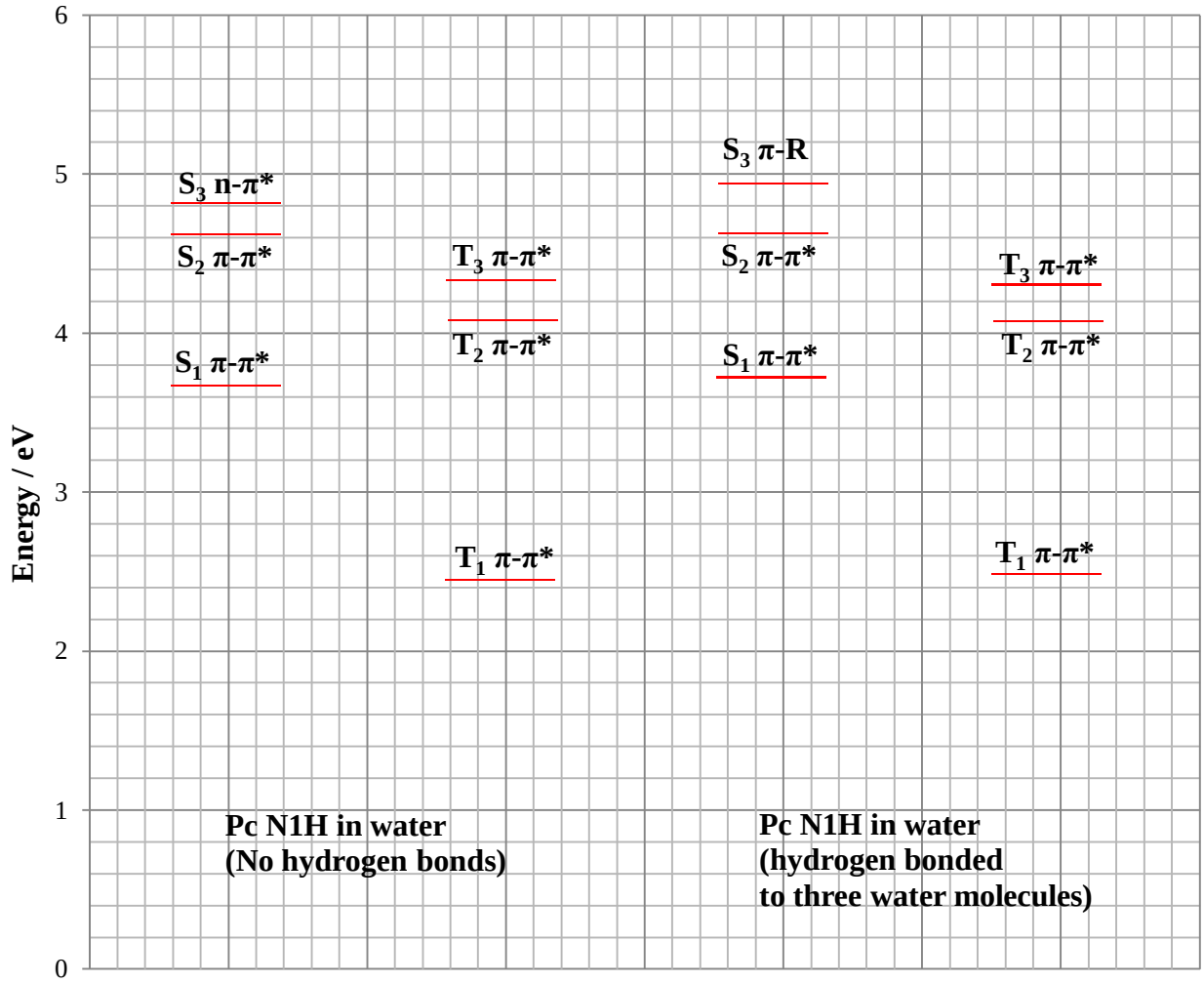

In the case of Pc, no particular difference between the non-hydrogen and hydrogen bonded base can be observed in terms of computed singlet and triplet electronic state energies, see Figure 4.49. The separation between S_2 and S_1 states of the base non-linked and linked with water molecules results is invariant, therefore, the formation of hydrogen bonds seems not to have any influence on the rate of vibronic coupling between the electronic states. All the predicted triplet states are of π-π* character as well as the first two singlet states. Therefore, fast ISC between them is very unlikely or slow to take place; not only because of the same nature of the calculated states, but also because the S_1 states are predicted to be much higher in energy than the T_1 states and lower in energy than the T_2 states. The higher rate of

fluorescence in alcohols, for example n-propanol, see Table 3.6, may be due to the different energy gap between S_1 and S_0. The computationally predicted HOMO (S_0) of the base in n-propanol is lower in energy than the one in water as shown in Figure 4.23. If the energy gap between S_1 and the ground state S_0 is large the rate for fluorescence emission is much bigger because fluorescence can effectively compete with IC (internal conversion) processes.

4.12 Summary and concluding remarks

Density functional theory studies on 2-aminopurine and pyrrolocytosine proved to be tedious and laborious task but in spite of that, the results obtained from this work appear to be in a reasonable agreement with the experimental data reported in Chapter 3. This section is meant to be a brief collection of the most salient points which have been treated in this chapter.

- The most energetically stable geometry of 2-Ap in both solution and vacuum was found to be the amino tautomer 2-Ap A.
- Unlike 2-Ap, Pc was found to have two energetically stable geometries, depending on the phase used. The keto form (Pc A) in solution and the enol form (Pc D) in vacuum.
- The first vertical transition of 2-Ap and Pc in both phases was found to be of π-π^* character (first singlet state).
- The theoretically predicted energies of the first vertical transitions of 2-Ap A in water and organic solvents is red-shifted with respect to the experimental absorption bands. Whereas the ones of Pc A are in an excellent agreement with the absorption bands.
- As in the case of the theoretical excitation energies the theoretical emission energies of 2-Ap A are red-shifted compared to the experimental emissions whereas the theoretical emission energies of Pc A match the maxima of the fluorescence emissions.
- The theoretical difference in dipole moment between the first excited state S_1 and the ground state of the bases is in disagreement with the experimental difference in dipole moment calculated *via* the Lippert model in Chapter 3.
- The optimized geometry of 2-Ap A in the ground state was predicted to be non-planar whereas the optimized geometry in the S_1 state was predicted as planar. Planarity may facilitate radiative processes over non-radiative processes.

- In absence of explicit water molecules the gap in energy between the bright state π-π* (S_1) and the dark state n-π* (S_2) of 2-Ap A is small whereas in presence of explicit solvent molecules the gap is large. A large gap helps fluorescence to compete against internal conversion (IC).
- The small fluorescence quantum yield of 2-Ap in non-polar solvents may be due to ISC which can efficiently compete with fluorescence emissions, according to the predicted singlet and triplet state energies of 2-Ap in chloroform. On the other hand, hydrogen bonding formation may be responsible for intense fluorescence (given the big quantum yield measured in polar solvents) because it does not facilitate ISC processes.

Optimization and frequency calculations of the bases in their first excited state using DFT at B3LYP/6-31G+ (d,p) level of accuracy required a reasonable amount of CPU time. Roughly it took 2000 CPU hours to achieve that on Gaussian 09 by using 4 to 8 processors (probably the best trade off, because increasing the number of processors speeds up the calculations but at an enormous CPU time cost which proved to be not worthwhile in the long run). The optimization of the bases were usually performed quite quickly, on average 4 up to 8 hours were required for the molecules to converge whereas frequency calculations required up to 5 days. Then, one may need between 10000 to 20000 CPU hours to obtain the theoretical fluorescence emissions of the bases interacting with explicit water molecules (estimated time by testing). But unfortunately, insufficient CPU time was available to complete all the calculations necessary in explicit solvent molecules. All the computational calculations on the bases were performed on the most energetically stable tautomer after optimization.

In the case of 2-Ap the N9H tautomer was predicted to be a local minima but the relative stability of the N7H tautomer is very close to the one of the N9H tautomer as shown in Table 4.1. The N7H tautomer of adenine and 2-Ap deserves particular attention. In fact, as described in the literature the N7H tautomer of 2-Ap (like the N9H) tautomer is predominantly found in water and highly fluorescent (Mishra *et al*. 2000; Neely *et al*. 2004; He *et al*. 2005) and the very weak fluorescence emission of adenine seems to come exclusively from the N7H tautomer of the natural base (Callis, 1983). Also, it should be reminded that the N9H tautomer does not exist in a Watson and Crick base-pairing

conformation because the sugar group (ribose or deoxyribose) removes the N9H heteroatom from the set of possible adenine and 2-Ap tautomers. Shukla and Leszczynski studied the ground and excited state geometries of nucleic acid bases (Shulka and Leszczynski, 2007). The bases were optimized by using at HF/6-311G (d,p) and CIS/6-311G (d,p) level and they reported a planar geometry of both bases in the ground state with exception of the amino ring which resulted to be pyramidal with respect to the purine ring. In the excited state the N9H tautomer geometry was predicted to be invariant from the one predicted in the ground state whereas the N7H tautomer was predicted to be non-planar. The non-planarity of the N7H tautomer was not only due to the amino group but also a fragment of the purine ring appeared as non-planar with respect to the entire purine ring. In the case of hydrated tautomers, when three water molecules were explicitly included, the N7H tautomer was considered to be planar (Shulka and Leszczynski, 2003). Then, it would be interesting to extend this work by also considering how the N7H tautomer geometry of 2-Ap may respond to hydration and predict its theoretical fluorescence emission.

Chapter 5: Experimental infrared study on pyrrolocytosine and cytosine

5.1 Introduction to infrared spectroscopy

In the previous chapter, computational density functional calculations revealed that the enol form of Pc is the most stable one in vacuum whereas the keto form was found to be the most energetically stable tautomer in solutions, see Figure 4.3 and Table 4.2. These findings are in agreement with past computational studies on cytosine which can formally exist as six tautomers as shown in Figure 5.1. Extensive experimental and computational studies showed that the natural base in solutions is essentially found as the keto tautomeric form although disagreement within the literature still exist on whether the main keto form is the aminooxo or the iminooxo one whereas all the quantum chemistry studies indicate that the hydroxyl tautomer is the dominant one (Watson and Crick, 1953; Lee *et al*. 1972; Kwiatkowski and Pullman, 1975; Dreyfus *et al*. 1976; Sembrano *et al*. 2000; Zhao *et al*. 2006; Shukla and Leszczynski, 2007; Wolken *et al*. 2007).

Figure 5.1 Tautomers of cytosine

The six tautomers of cytosine, as keto and hydroxyl amino/imino forms

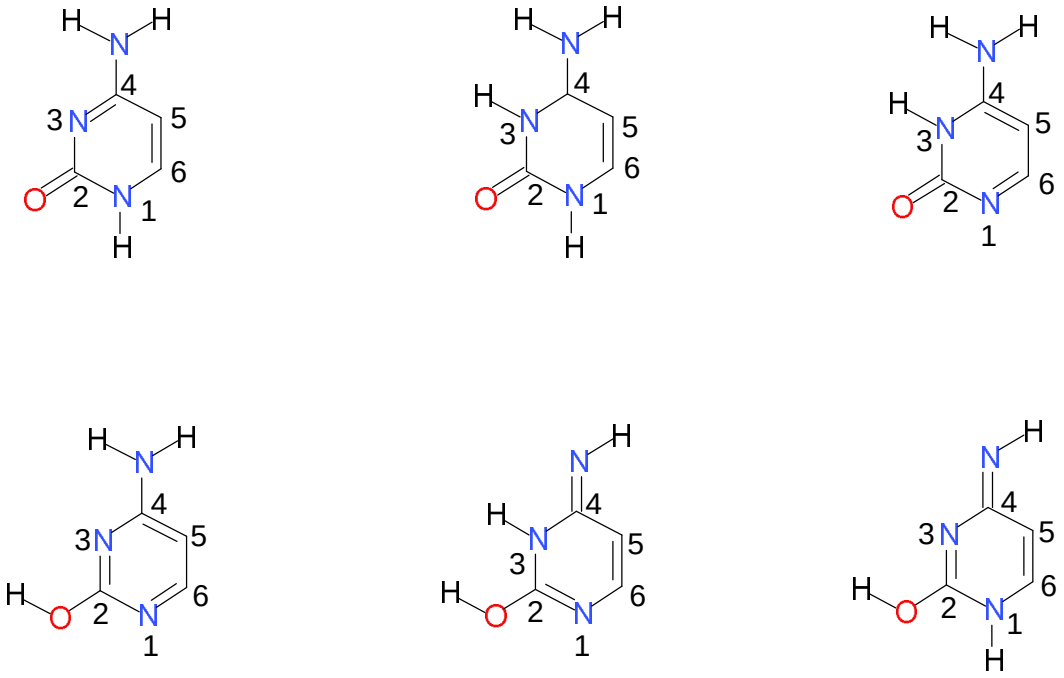

Currently, it seems that no experimental infrared studies on Pc can be found in the literature and therefore, this chapter is intended to present FTIR spectra of Pc along with cytosine (for comparison purposes) in different solvents in an attempt to elucidate the tautomeric nature of the modified nucleobase in solutions of different polarity, mainly focusing on the OH and C=O vibrational modes.

5.2 Theory of Infrared spectroscopy. A brief overview

As already described in Chapter 2 (see Section 2.2 equation 2.8), the distribution of energy possessed by a molecule can be defined as the sum of different energies. Infrared spectroscopy deals with vibrational energy. Every atom possesses three degrees of freedom, which correspond to motions along the three Cartesian coordinates x, y and z. A polyatomic molecule of n atoms has 3 n total degrees of freedom. Three degrees of freedom are required to describe translational motions and three degrees of freedom correspond to rotational motions (in the case of linear molecules the degrees of freedom are 2). Thus, the remaining 3n – 6 degrees of freedom are the fundamental vibrations for non-linear molecules or also called normal modes of vibration. The fundamental requirement for infrared activity is a change in dipole moment of the molecule upon absorption of light. It is important to note that the total number of observed absorptions does not represent the total number of fundamental absorptions because some fundamental vibrations may not be IR active. The main IR active modes are illustrated in Figure 5.2.

Figure 5.2 Vibrational modes

Main vibrational modes for a non-linear molecule (IR active)

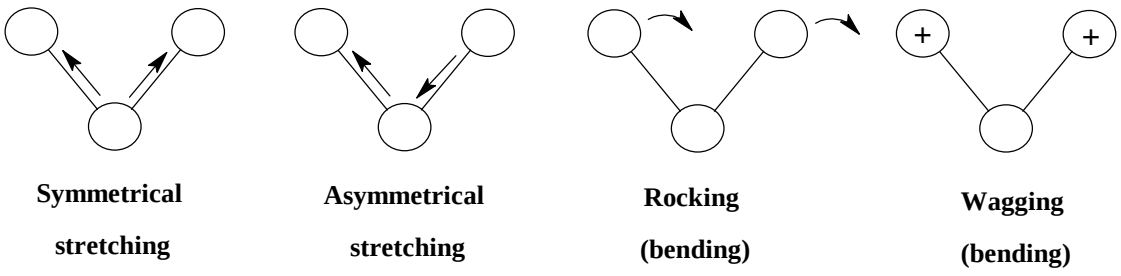

IR absorption bands are usually presented as percent transmittance against wavenumbers unit (cm^{-1}). This format provides the best dynamic range for both weak and intense bands. The IR region is divided into three regions, near infrared (13000-4000 cm^{-1}), mid infrared (4000-200 cm^{-1}) and far infrared (200-10 cm^{-1}). The mid region is the most used region because it is the most informative one for structural elucidation and compound identification. FTIR (Fourier Transform Infrared) instruments have almost completely replaced dispersive spectrometers because of the following distinctive advantages:

- Felgett adavantage. Better speed and sensitivity
- Jaquinot advantage. Increased optical throughput
- Connes advantage. Internal laser reference
- Simpler mechanical design, enormous decrease in stray light thanks to the interferometer which modulates all the frequencies and better and faster data station

5.3 Materials and methods

FTIR spectra were measured by using a Satellite FTIR Thermo Mattson spectrometer with the following setting: resolution 4.0, scanning velocity 6.25 and reverse velocity 25.0. A background spectrum (air + calcium plate) was performed at the beginning of each experimental session and upon request when needed (for example when default settings were changed). The plates used were calcium fluoride plates which can be safely used when measuring spectra of compounds dissolved in aqueous and alcoholic solvents, but they absorb below 820 cm^{-1}. The concentrations used of the samples studied, Pc and cytosine (Sigma, minimum 99 %) ranged from 1 to 2 mg/mL as suggested by Dreyfus and co-workers in their FTIR studies on cytosine and its derivatives (Dreyfus *et al*. 1979). Apparently, cytosine and pyrrolocytosine have poor solubility within this concentration range in solvents with low dielectric constant. It should be noted that the infrared spectra of C and Pc in different solvents shown in the next section, did not undergo solvent subtraction. This is because negative infrared bands were generated by applying solvent subtraction.

5.4 Results and discussion

This section shows the acquired FTIR spectra of the solvents used and the bases, cytosine and Pc, dissolved in these solvents along with the assignment of the main absorption frequencies, figure 5.3-5.14 (the spectra have been ordered according to the dielectric constant of the solvent used, going from the lowest to the highest dielectric constant, see Table 3.2 in Chapter 3). The interpretation of the spectra of cytosine and Pc in highly hygroscopic solvents, such as ethers and DMSO, proved to be problematic because these solvents tend to absorb water/moisture from the air, affecting the FTIR spectrum within the 3300 and 3600 cm^{-1} wavenumber range. The extent of this absorption mainly depends on the exposure duration of the solvents to air. The most remarkable case is the one of DMSO (dimethyl sulfoxide). When the FTIR spectrum of DMSO was measured, bands due to moisture absorption were clearly observed, but the magnitude of these bands increased enormously because of sample preparation, see Figure 5.12. Even though moisture can greatly affect part of the IR spectra, it does not mask, completely, the OH stretching of heterocyclic compounds, which occurs between 3100 and 3400 cm^{-1} but, it does eventually mask the NH vibrational stretching of the NH_2 functional group of cytosine, occurring within 3300-3500 cm^{-1}. The FTIR of cytosine and Pc in solvents having low dielectric constant (diethyl ether, chloroform and THF) show absorption bands between 1575 and 1640 cm^{-1} which may be indicative of C=O stretching. The bands of Pc appear to be red-shifted compared to cytosine. No distinctive and broad OH bands were observed. In the case of chloroform (which is an excellent solvent used in infrared absorption frequency interpretation because of its transparency within almost all the mid-infrared region), the NH stretching of the NH_2 group of cytosine was clearly observed because chloroform is not hygroscopic, see Figure 5.4. The FTIR spectra of cytosine and Pc in ethyl acetate were not reported because the solvent absorbs within the region in which carbonyl group absorbs, having a strong peak at circa 1750 cm^{-1}, see Figure 5.4. As in the case of the other solvents with low dielectric constant no particular band indicative of OH stretching of the bases was detected. Regarding the bases dissolved in alcohols: ethanol, isopropanol, n-propanol and methanol, they all generated absorption frequency bands between 1600 and 1650 cm^{-1} and therefore, labelled as C=O stretching, as shown in the Figures 5.7-5.10. Once again the bands of Pc are red-shifted compared to C, especially in the case of n-propanol whereas no red-shifting was found in methanol. Obviously, given the nature of the alcohols which possess a hydroxyl group then, discerning the OH stretching of the bases is virtually impossible.

Figure 5.3 FTIR spectra of Cytosine and Pyrrolocytosine in diethyl ether

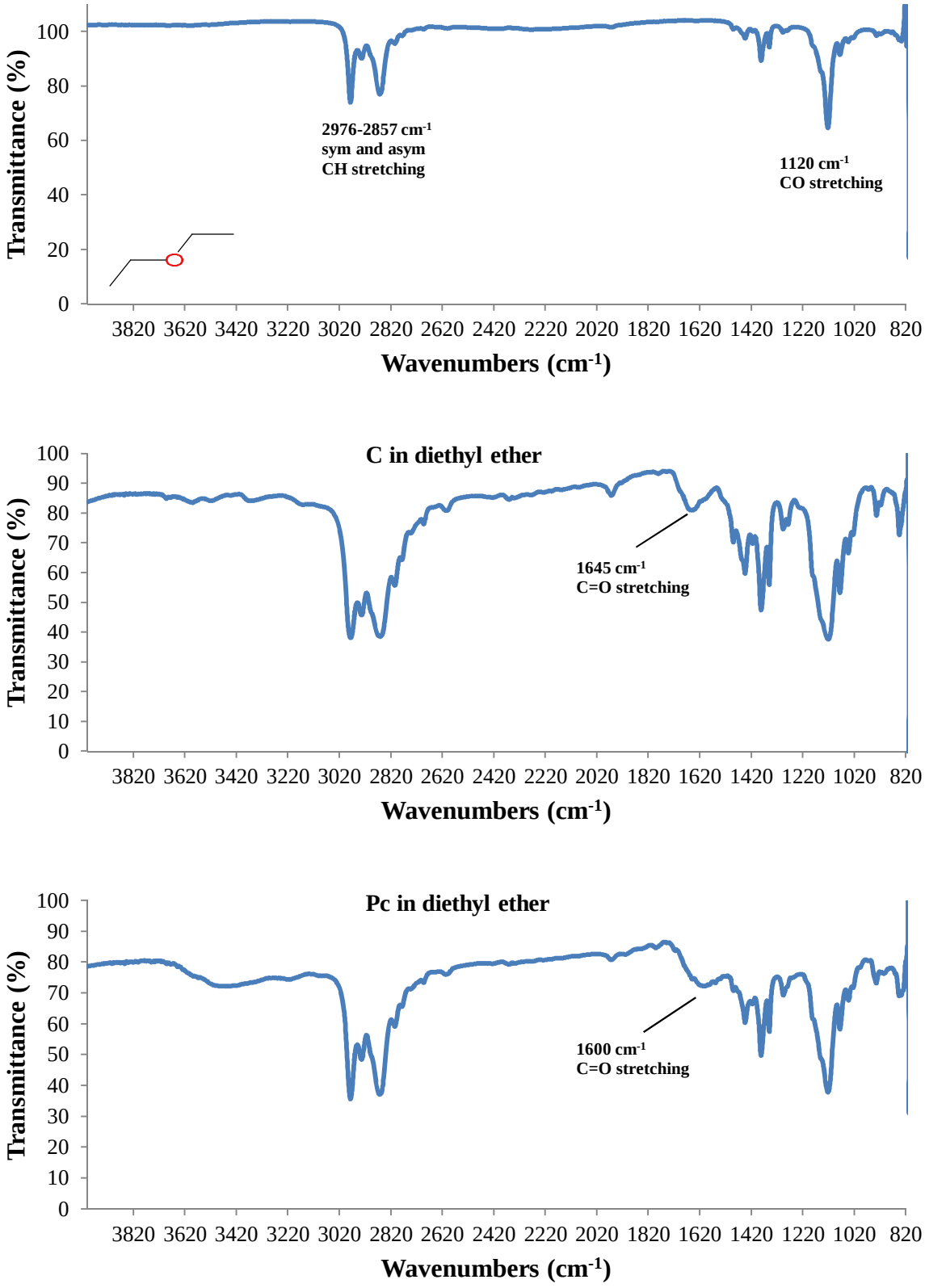

Figure 5.4 FTIR spectra of Cytosine and Pyrrolocytosine in chloroform

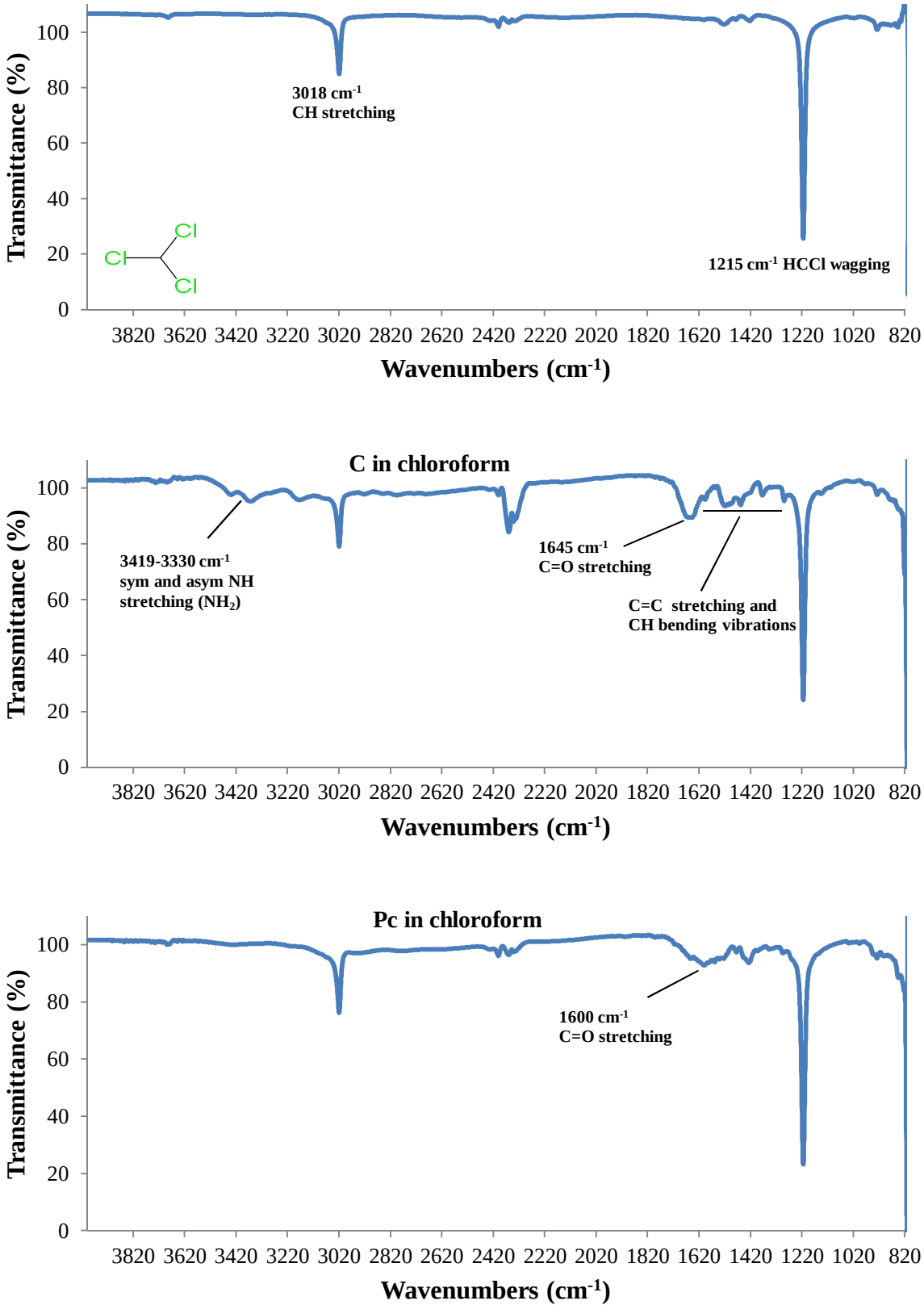

Figure 5.5 FTIR spectrum of ethyl acetate

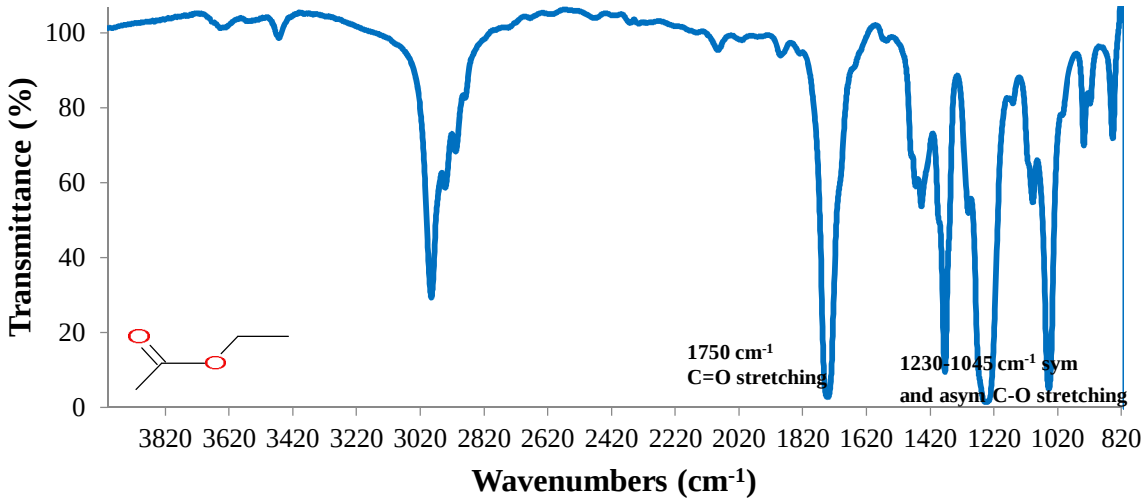

According to the infrared data of the bases in aprotic solvents having high dielectric constant, acetonitrile and DMSO, illustrated in Figures 5.11-5.12, were found to be as keto form with frequency bands going from 1628 to 1655 cm^{-1} with Pc slightly red-shifted with respect to cytosine in acetonitrile. Similarly to ethyl acetate, water absorbs within a region at which the carbonyl functional group absorbs. Precisely, a band of medium intensity was found at 1640 cm^{-1} and assigned as OH deformation vibration, see Figure 5.14. Also, water strongly absorbs within 2700 and 3700 cm^{-1} with a maximum intensity found at 3310 cm^{-1} and referred as OH stretching. Therefore, water is not a suitable candidate as a solvent to assign C=O and OH stretching of any solute dissolved in it. As a consequence of this, heavy water was used instead of water because heavy water has, as normal water, the same characteristic OH bands but they are red-shifted as shown in Figure 5.13. The interpretation of the infrared bands of the bases in heavy water is arguably difficult and controversial. First, heavy water is hygroscopic and thus, the OH stretching of the bases cannot be accurately and precisely assigned. Second many bands in the case of cytosine were found and splitting of these bands is clearly observable. This splitting may be due to many factors but generally because of the presence of more than one single tautomeric form, hydrogen bonding formation or caused by resonance precisely, Fermi resonance (when two fundamental IR bands of similar energy split in such a way that a band increases in intensity whereas the other decreases in intensity due to mixing of the two energy states). In the case of Pc only one single band of relatively intense absorption was found at 1440 cm^{-1}, and assigned as CH3 bending, a methyl group which is a peculiar group of Pc.

Figure 5.6 FTIR spectra of Cytosine and Pyrrolocytosine in THF

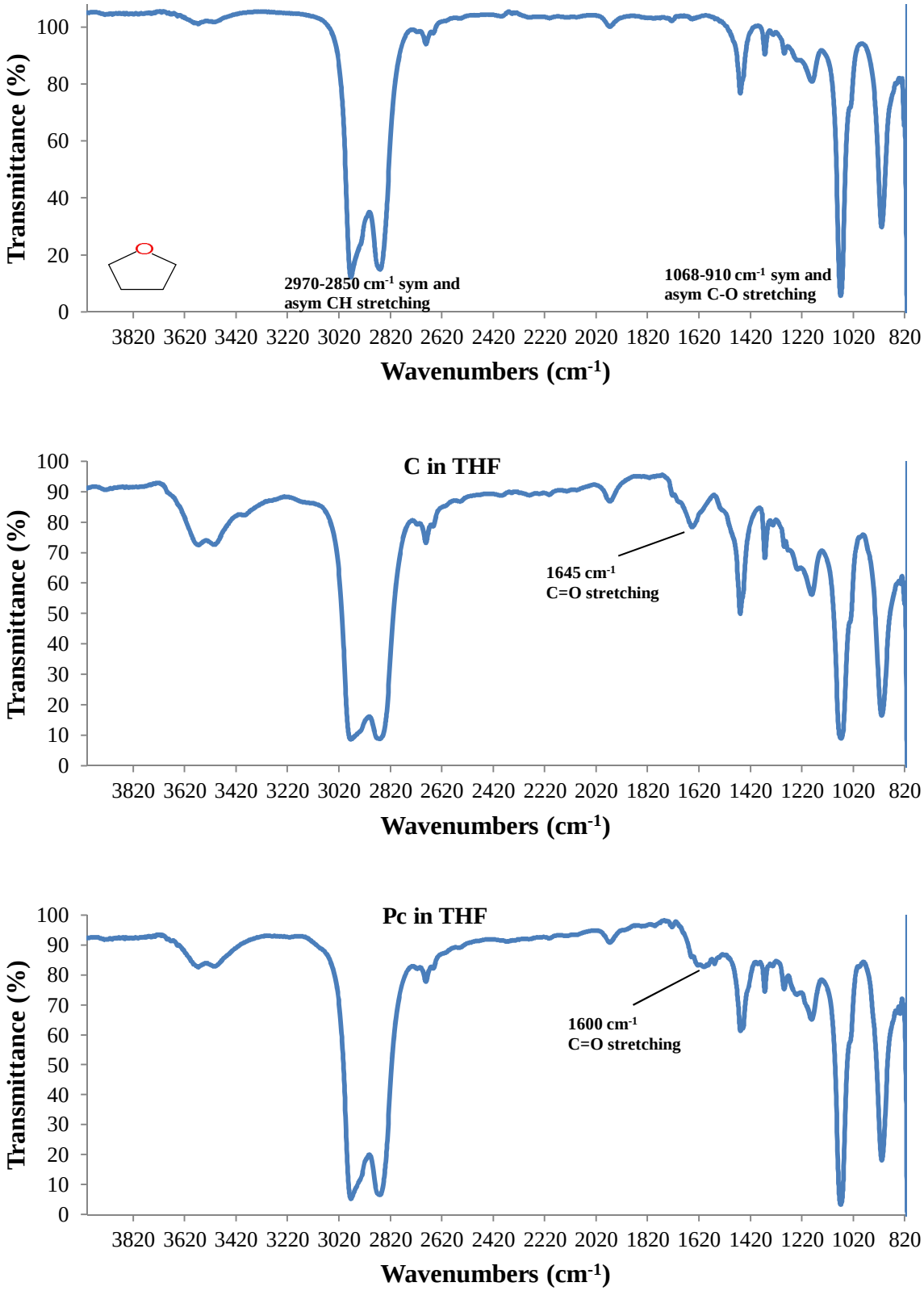

Figure 5.7 FTIR spectra of Cytosine and Pyrrolocytosine in ethanol

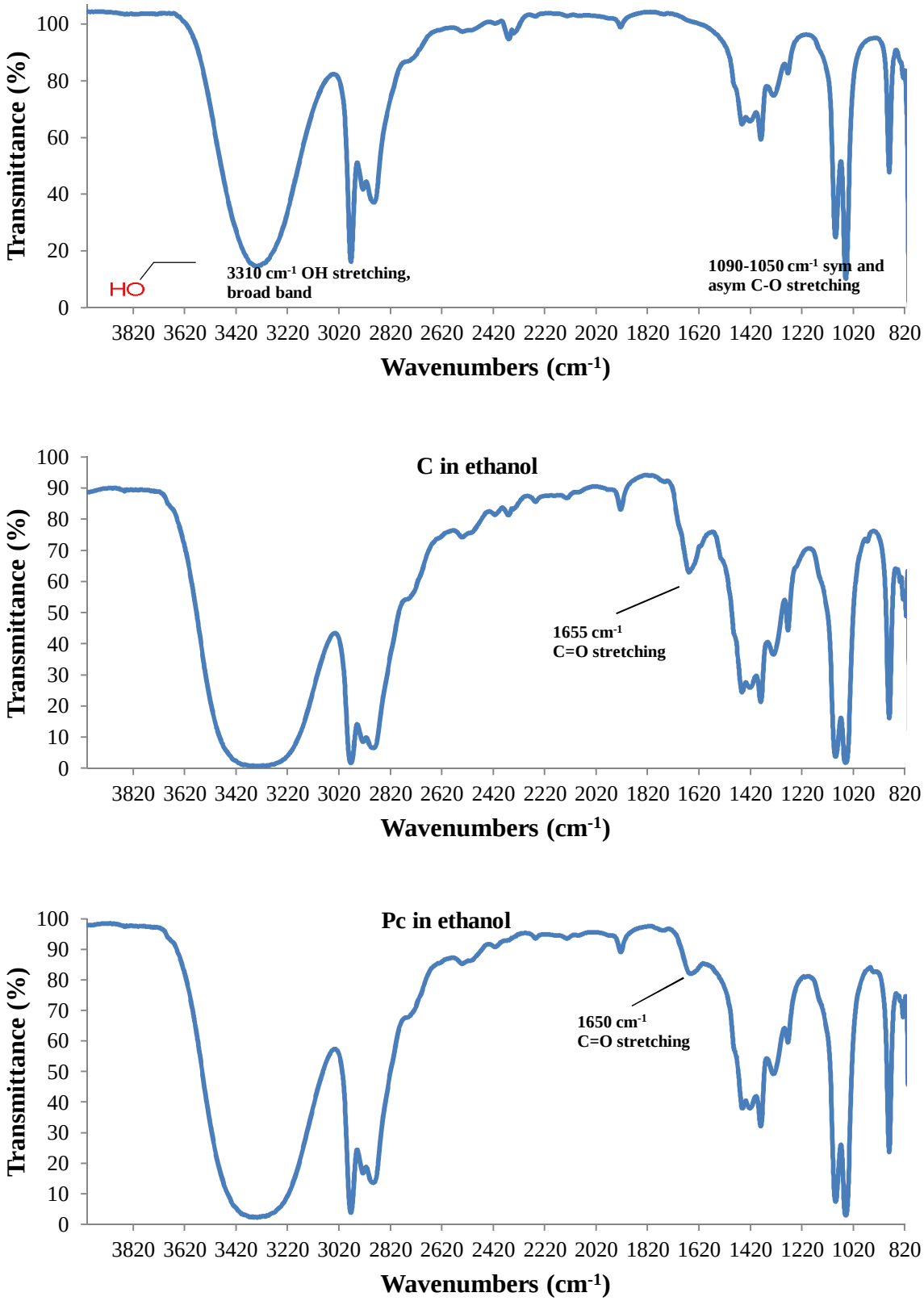

Figure 5.8 FTIR spectra of Cytosine and Pyrrolocytosine in isopropanol

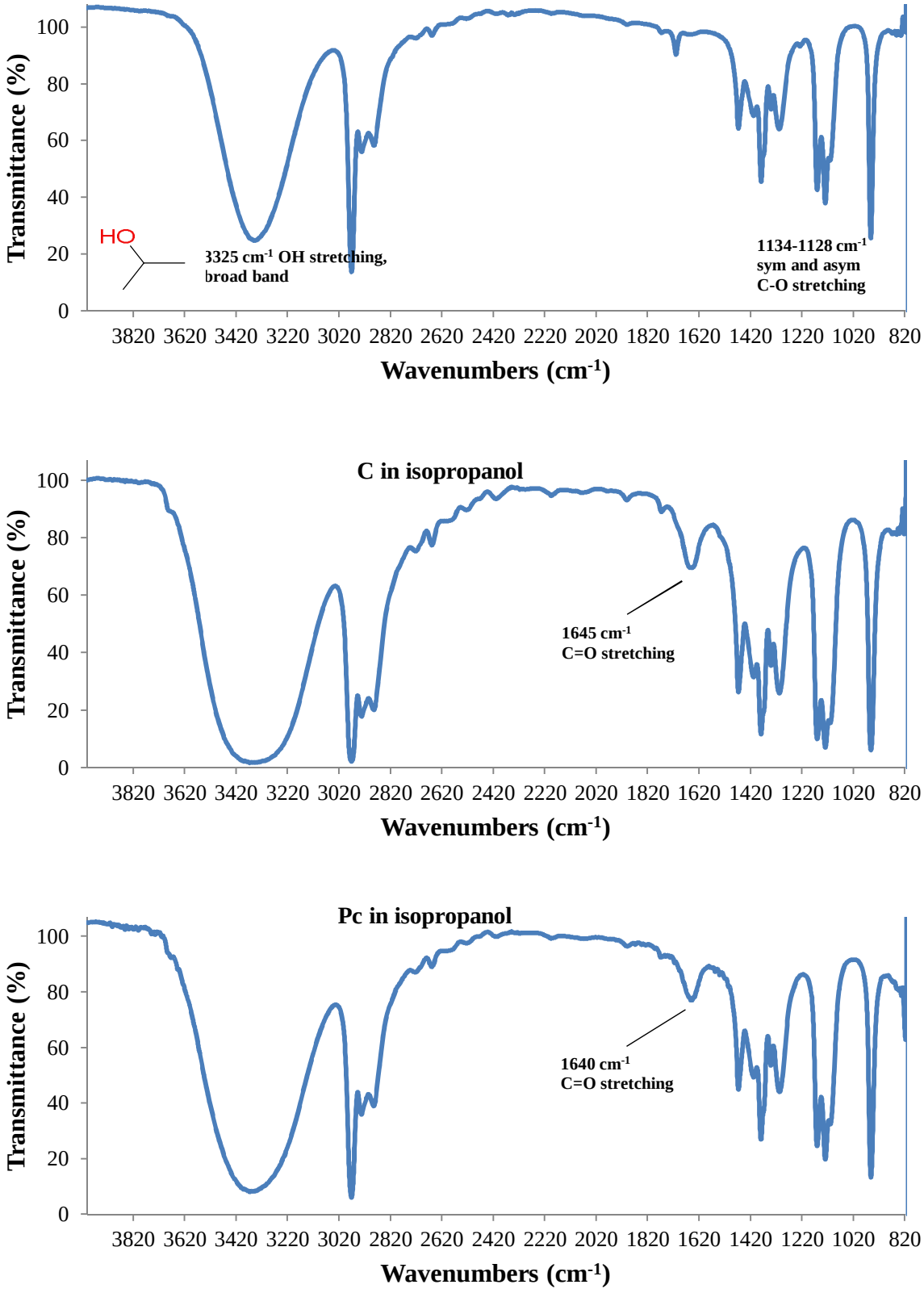

Figure 5.9 FTIR spectra of Cytosine and Pyrrolocytosine in n-propanol

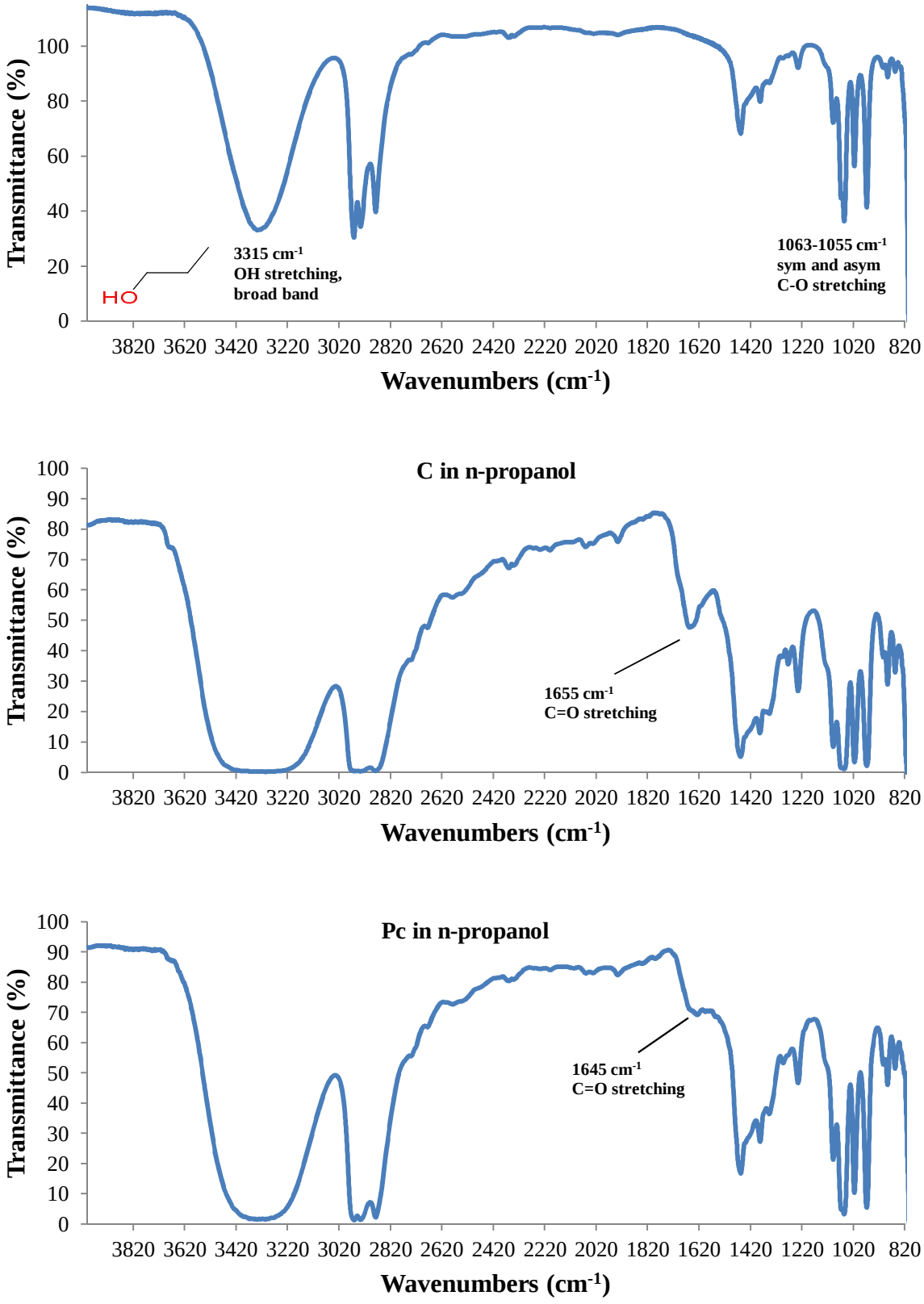

Figure 5.10 FTIR spectra of Cytosine and Pyrrolocytosine in methanol

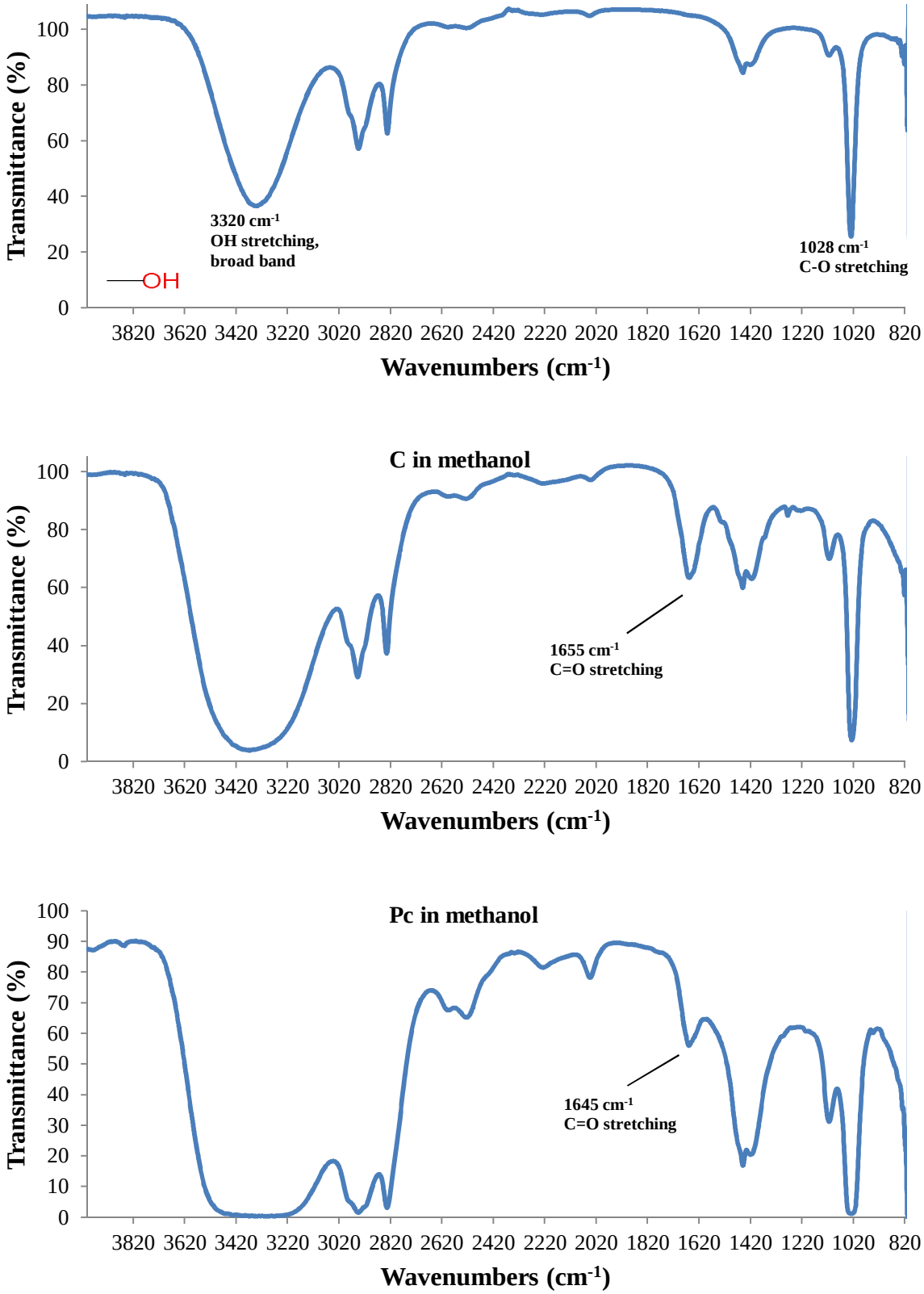

Figure 5.11 FTIR spectra of Cytosine and Pyrrolocytosine in acetonitrile

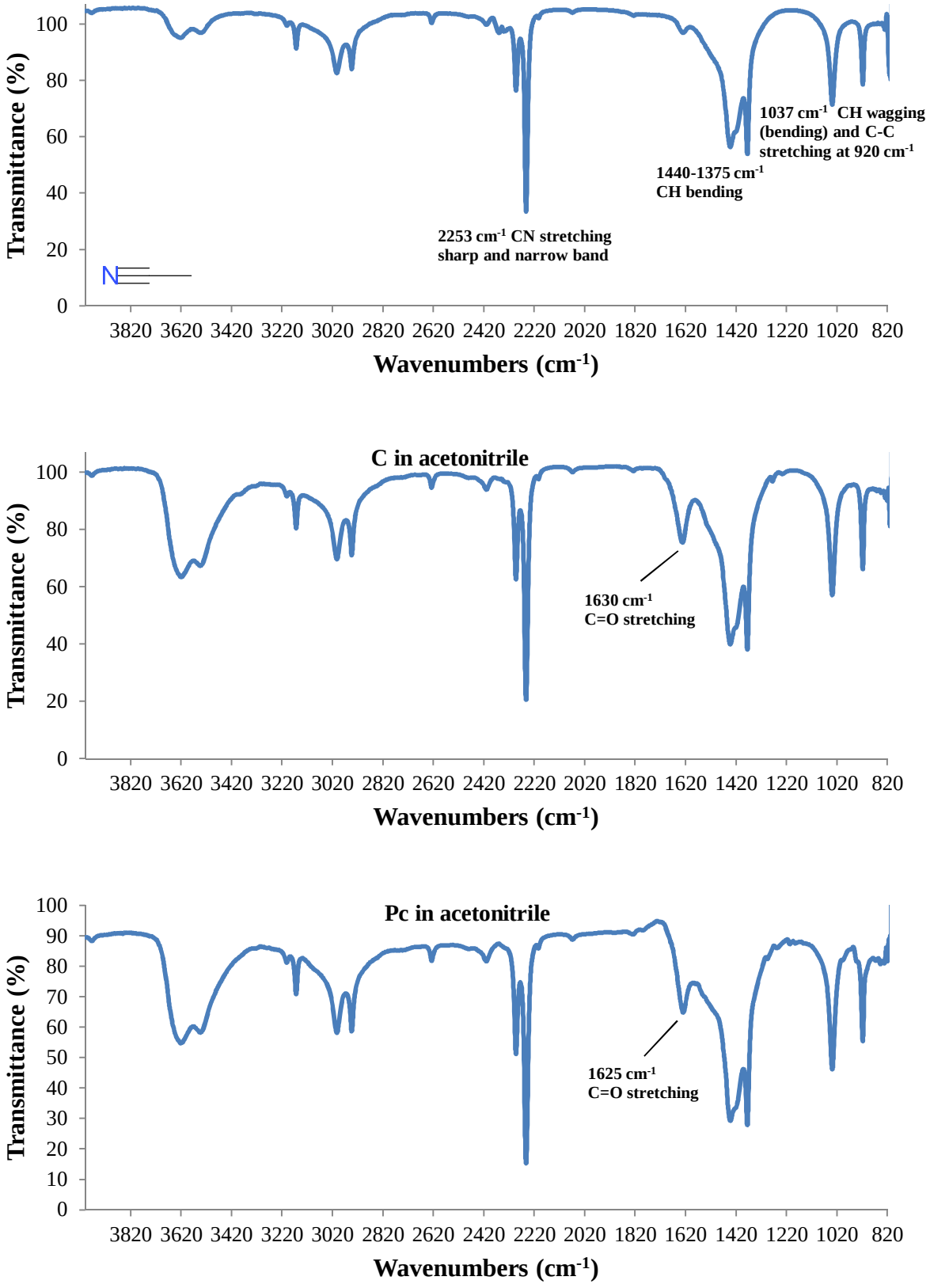

Figure 5.12 FTIR spectra of Cytosine and Pyrrolocytosine in DMSO

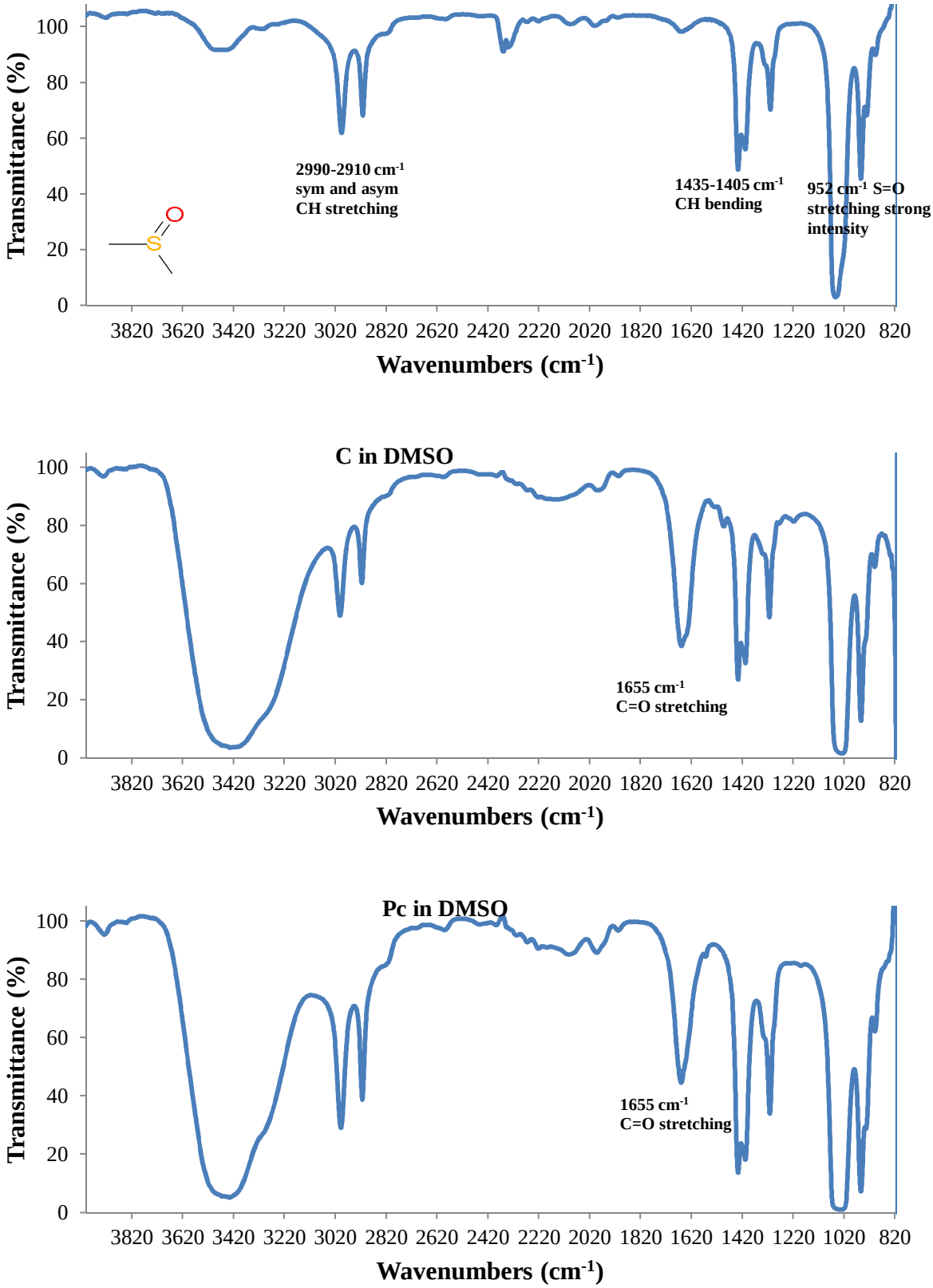

Figure 5.13 FTIR spectra of Cytosine and Pyrrolocytosine in heavy water

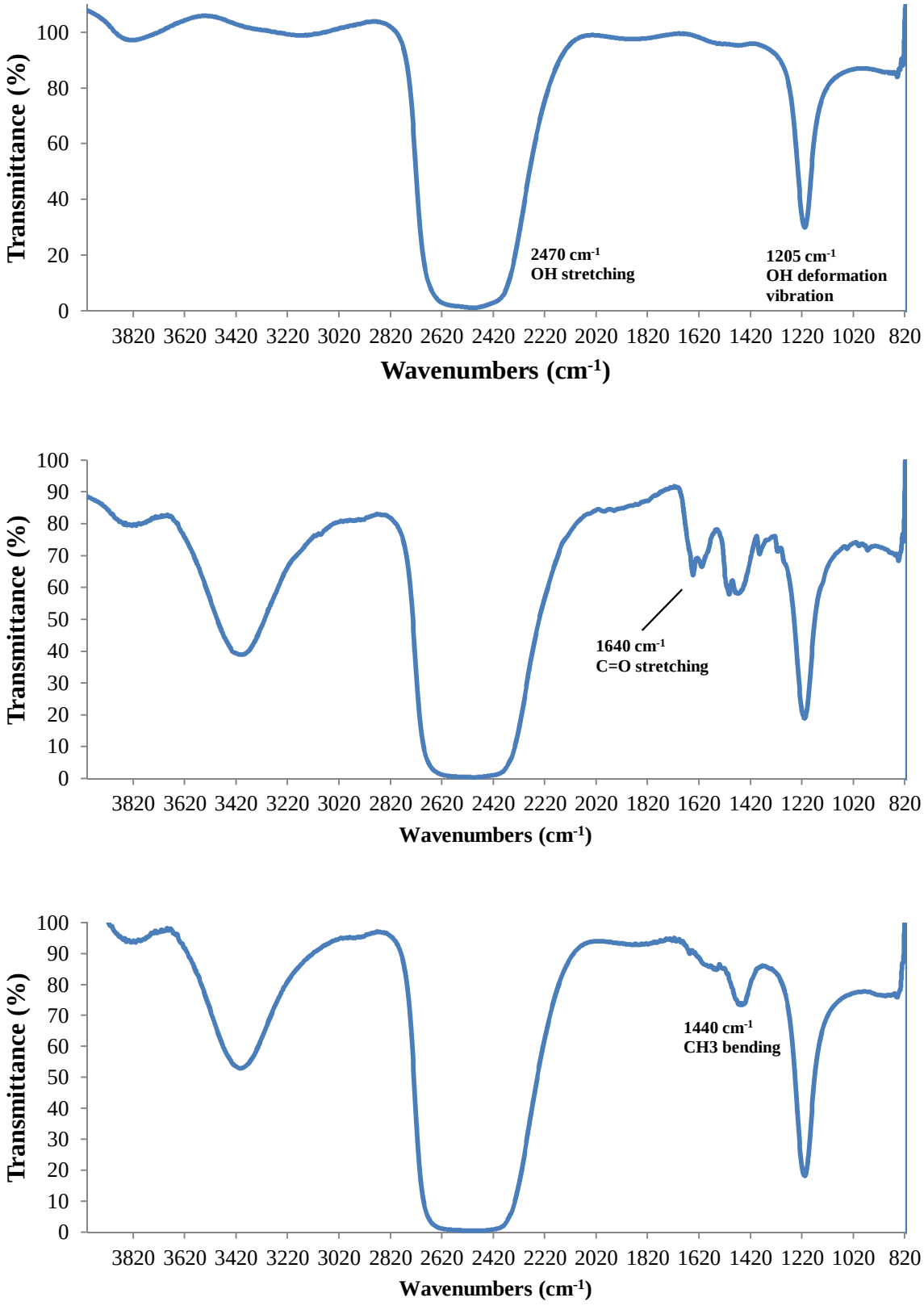

Figure 5.14 FTIR spectrum of water

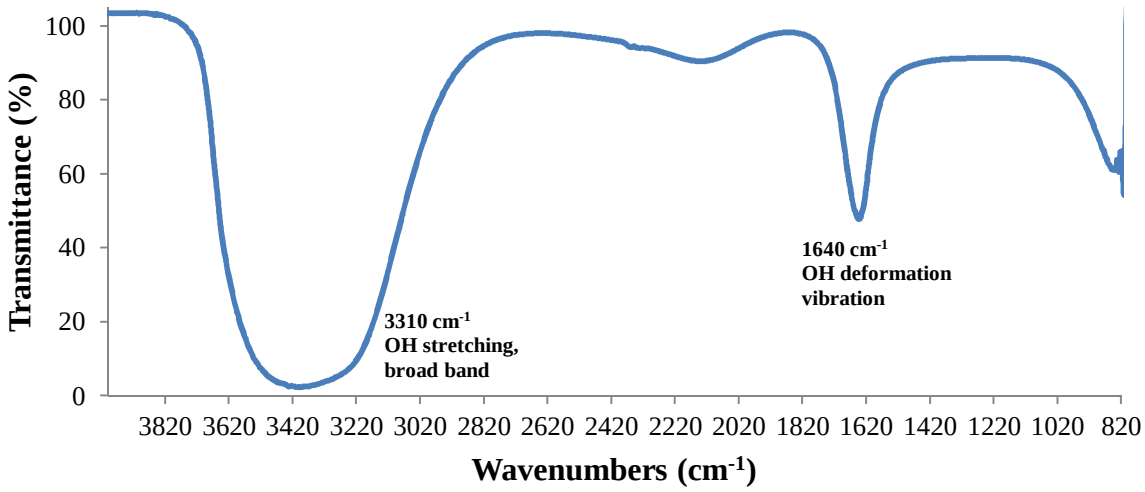

The Table 5.1 sums up the obtained infrared results in terms of the position of the likely C=O infrared stretching bands of cytosine and pyrrolocytosine in different solvents (where observation was possible). The table clearly shows that in the case of cytosine the infrared bands are usually blue-shifted with respect to the ones of pyrrolocytosine.

Table 5.1 C=O FTIR bands of cytosine and pyrrolocytosine in different solvents

Table showing the observed carbonyl stretching frequencies of cytosine and pyrrolocytosine in different solvents

Solvent	C=O stretching of Cytosine	C=O stretching of Pyrrolocytosine
Diethyl Ether	1650-1640 cm^{-1}	1605-1595 cm^{-1}
Chloroform	1650-1640 cm^{-1}	1605-1595 cm^{-1}
THF	1650-1640 cm^{-1}	1605-1595 cm^{-1}
Ethanol	1660-1650 cm^{-1}	1655-1645 cm^{-1}
Isopropanol	1650-1640 cm^{-1}	1645-1635 cm^{-1}
n-propanol	1660-1650 cm^{-1}	1650-1640 cm^{-1}
Methanol	1660-1650 cm^{-1}	1650-1640 cm^{-1}
Acetonitrile	1635-1625 cm^{-1}	1630-1620 cm^{-1}
DMSO	1660-1650 cm^{-1}	1660-1650 cm^{-1}
Heavy Water	1645-1635 cm^{-1}	Not clearly observed

5.5 Concluding remarks

Infrared analysis and interpretation of cytosine and pyrrolocytosine in solution proved to be difficult because of the low solubility of the bases in solvent of any polarity especially solvents having low polarity, and atmospheric water which partially obscures the infrared region in which the functional group OH absorbs. Nevertheless, the keto tautomer seems to be the most prevalent tautomer in both C and Pc but the presence of a minor percentage of enolic tautomers cannot be excluded. NMR spectroscopy may be used to assess the different proportion in enol and keto tautomerism of pyrrolocytosine in different solvents because the functional groups OH and C=O give characteristic and distinctive chemical shifts in a ^{13}C nuclear magnetic resonance spectrum. Elucidation of tautomer structures of Pc in gas phase may be achieved by using the combined techniques gas chromatography/mass spectrometry. Chemical compounds can exist as a mixture of two or more tautomers that may exhibit different chromatographic behaviours and the keto-enol equilibrium can be measured via electron ionization (electron-impact induced fragmentation of molecular ions). The advantage of gas phase over liquids is that intermolecular interactions and hydrogen bonding formations which are usually responsible for IR frequency shifting are excluded by transferring the tautomeric system into gas phase (Allegretti *et al*. 2007).

Chapter 6: Fluorescence of 2-aminopurine and pyrrolocytosine nucleotides

6.1 Introduction to 2-aminopurine and pyrrolocytosine oligonucleotides

The quantum yields of 2-aminopurine (2-Ap) and pyrrolocytosine (Pc) as free bases and incorporated into oligonucleotides in water and different phosphate buffers of neutral pH were measured to study and compare changes in fluorescence emission with respect to the local environment and therefore, probing the dynamics of the bases when base-stacked and base-paired. Thus, the fluorescence properties of 2-Ap and Pc can be used to identify mismatched base pairing (Lawrence *et al.* 1986; Reha-Krantz *et al*. 2011). Also, the spectroscopic properties (UV, fluorescence, CD and anisotropy spectroscopic properties) of these fluorophores can help discern the likely formation of secondary structures of G-rich oligonucleotides in salts (Mergny *et al*. 1998; Berova *et al*. 2000; Tinsley and Walter, 2004).

The bases incorporated into oligonucleotides were studied in sodium and potassium buffers not only to simulate biological environments but also to neutralize the negative charges of the sugar-phosphate backbone *via* the positive ions Na^+ and K^+. Salts are known to act as fluorescence quenchers by promoting the formation of non-fluorescent states (Vamosi *et al*. 1996). Monovalent and divalent salts have also the ability to trigger and stabilize the formation of secondary and tertiary structures (Draper, 2004; Woodson, 2005). As a consequence of these findings, Stern-Volmer plots were generated to assess whether the fluorescence of the fluoroprobes is quenched or not, and, if they are quenched, to predict the type of fluorescence quenching (dynamic quenching or static quenching) and the extent of it by obtaining the Stern-Volmer quenching constant, K_{SV}.

The possible formation of secondary structures, with special emphasis on G-quadruplex formation (Rachwal and Fox, 2007; Phan and Mergny, 2002; Mergny *et al.* 1998), were studied by acquiring UV-melting profiles (changes of absorbance as a function of temperature) at different buffer concentrations along with the acquisition of CD (Circular Dichroism) spectra to discern and confirm the nature of the likely secondary structures formed, thus the different polymorphism of the oligonucleotides studied in water and different buffers (Berova *et al*. 2000). Finally, the rotational behavior of the fluoroprobes as free bases, single-stranded and double-stranded oligonucleotides was estimated by using steady-state anisotropy; a technique which allows the measurement of the extent of polarized light of the emitting species in order to assess the size and shape of the fluorescent molecules (Lakowicz, 1999).

6.2 Materials and methods used

The following nucleic acid samples were used: GPcG, G_9PcG_9, C_9GC_9, G2ApG, G_92ApG_9, C_9TC_9 (purified by HPLC, delivered freeze-dried, Cambio Ltd Cambridge UK), Pc free base, Pc deoxyribose (Pc_{dr}), Pc ribose (Pc_r) (100 % purity by HPLC, Berry Associates Inc Dexter USA), 2-Ap free base (minimum 99.0 %, Sigma), 2-Ap_{dr} (Carbosynth Ltd) and quinine sulphate dihydrate (standard sample ≥ 99.0 % Fluka). The quantum yields of the samples were measured in buffer solutions at pH 7 precisely, 0.1 M sodium chloride and 0.049 M sodium phosphate (**buffer A**), 5 mM sodium phosphate (**buffer B**), 50 mM sodium phosphate (**buffer C**), 0.1 M sodium chloride (**buffer D**), 5 mM potassium phosphate (**buffer E**) 50 mM potassium phosphate (**buffer F**), 0.1 mM sodium phosphate (**buffer G**), 0.5 mM sodium phosphate (**buffer H**), 1 mM sodium phosphate (**buffer I**). The buffers were made from sodium and potassium phosphate monobasic (NaH_2PO_4 and KH_2PO_4 minimum 99.0 % Sigma), and dibasic (Na_2HPO_4 and K_2HPO_4 minimum 99.0 % Sigma), sodium chloride (NaCl minimum 99.5 % Sigma). Buffers were filtered prior to the use to eliminate impurities which may encourage the growth of bacteria especially in buffers ranging from pH 6 to 8. The DNA sample concentration used to measure the absorbance/fluorescence intensity was 0.1 mg/mL. The formation of the duplexes $G_9PcG_9 \circ C_9GC_9$ and $G_92ApG_9 \circ C_9GC_9$ was performed by using 1:1 ratios of single-stranded oligonucleotides in water and buffers into propylene micro centrifuge tubes fitted into propylene floats, floating on distilled water contained in a water circulating bath. The water was heated to 90º C. When the required temperature was reached the tubes containing the solutions remained in the heated water for circa 10 minutes, then, the solutions were slowly cooled down by keeping them floating in the water of the turned off circulating bath for 30 minutes, and then removed from the float and left at room temperature for circa 1 hour.

Melting curves were obtained by using the double-beam spectrometer Thermospectronic UV-1 for absorbance measurements, connected to a MultiTemp III refrigerated circulating bath, an instrument which cools water down to -10 °C and heats it up to 90 °C. The oligonucleotide samples studied were within concentration range of 2-0.5 x 10^{-5} M, at which the optical density detected at 260 is at least 0.2 or greater than it. Melting curves have been generated plotting at least 10-15 changes of absorbance as a function of temperature. The temperature was monitored from 10-15 °C up to 70-75 °C and the absorbance measured for each 2 to 5 °C increments of temperature within the temperature range. After each increment of temperature the solutions required at least 10-15 minutes to be thermally equilibrated and

they were properly stirred up prior to absorbance measurements. Absorbance readings at 405 nm have been recorded to detect possible artefacts such as: formation of release of air bubbles, temperature-dependent aggregation of the sample studied and improper positioning of the cuvettes (Mergny and Lacroix, 2003). No sudden changes in absorbance at 405 nm have been recorded for all the analysed samples; therefore, the occurrence of artefacts mentioned above can be excluded.

The CD spectra of $G_9$2ApG_9 in water and sodium phosphate buffers were obtained by using the Aviv Model 62DS/ 202 series instrument. Up to 7 scans were acquired and averaged for each sample and the following parameters were adopted: wavelength step 0.200 nm, averaging time 1.000 s, time constant 1000 ms and bandwidth 1.0 nm.

Anisotropy measurements were collected by using a Fluoromax3 fluorimeter connected to a circulating water bath to keep the temperature of the solutions at the desired temperatures (20, 40, 60 and 80°C). The fluorescence emission signals used in order to calculate the G factor and then anisotropy were: VV (vertically-vertically polarized light), VH (vertically-horizontally polarized light), HV (horizontally-vertically polarized light) and HH (horizontally-horizontally polarized light). The following parameters were adopted to collect the data obtained: excitation and emission monochromator slits = 5.000 nm, and integration time equal to 0.100000 s.

6.3 Pc and 2-Ap oligonucleotides. Results and discussion

This section shows the quantum yield measurements (as gradients obtained by plotting absorbance values against the integrated fluorescence areas) and the maxima excitation and emission wavelengths (λ_{ex}, λ_{em}) of Pc and 2-Ap as free bases and oligonucleotides in water and different buffer solutions. This section also displays graphs constructed as fluorescence emission changes as a function of buffer concentration and temperature.

6.3.1 Pc free base and Pc nucleosides

The quantum yields of Pc as free base in water and buffer A along with Pc nucleosides were measured in order to understand differences in Pc fluorescence as free base and attached to sugar groups, deoxyribose and ribose, see Figure 6.1.

Figure 6.1 Pc_{dr} and Pc_r

Pc base attached to deoxyribose (Pc_{dr}) and ribose (Pc_r) *via* the 1,1 N-glycosidic bond

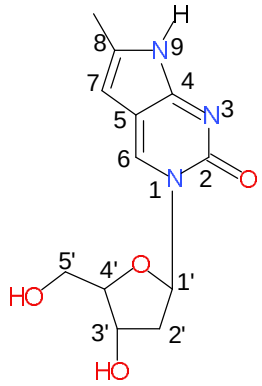

Pc deoxyribose, Pc_{dr}

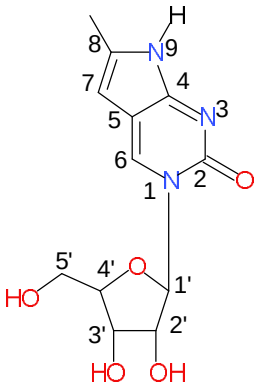

Pc ribose, Pc_r

The Table 6.1 shown below contains the quantum yield measurements of Pc as free base and nucleosides in water and buffer A. The quantum yield measurements of Pc in water and buffer A appear to be identical within linear standard regression error. The maxima excitation and emission wavelength are identical. The quantum yield plots are shown in Figure 6.2

Table 6.1 Spectroscopic data of Pc as free base and Pc nucleosides

Φ_F, λ_{ex}, λ_{em} of Pc and Pc nucleosides in water and buffer A (0.1 M sodium chloride and 0.049 M sodium phosphate)

Compound analysed	λ_{ex}	λ_{em}	$\Phi_F \pm 2\sigma$
Pc in water	335-337 nm	447-449 nm	0.044 ± 0.004
Pc in buffer A	335-337 nm	447-449 nm	0.045 ± 0.003
Pc deoxyribose in water	341-343 nm	453-455 nm	0.036 ± 0.004
Pc deoxyribose in buffer A	341-343 nm	453-455 nm	0.035 ± 0.002
Pc ribose in water	341-343 nm	455-457 nm	0.028 ± 0.004
Pc ribose in buffer A	341-343 nm	455-457 nm	0.030 ± 0.004

Figure 6.2 Quantum yield slopes of Pc in buffer A and water

Quantum yield plots of the free base Pc in water and buffer A (0.049 M sodium phosphate and 0.1 M sodium chloride)

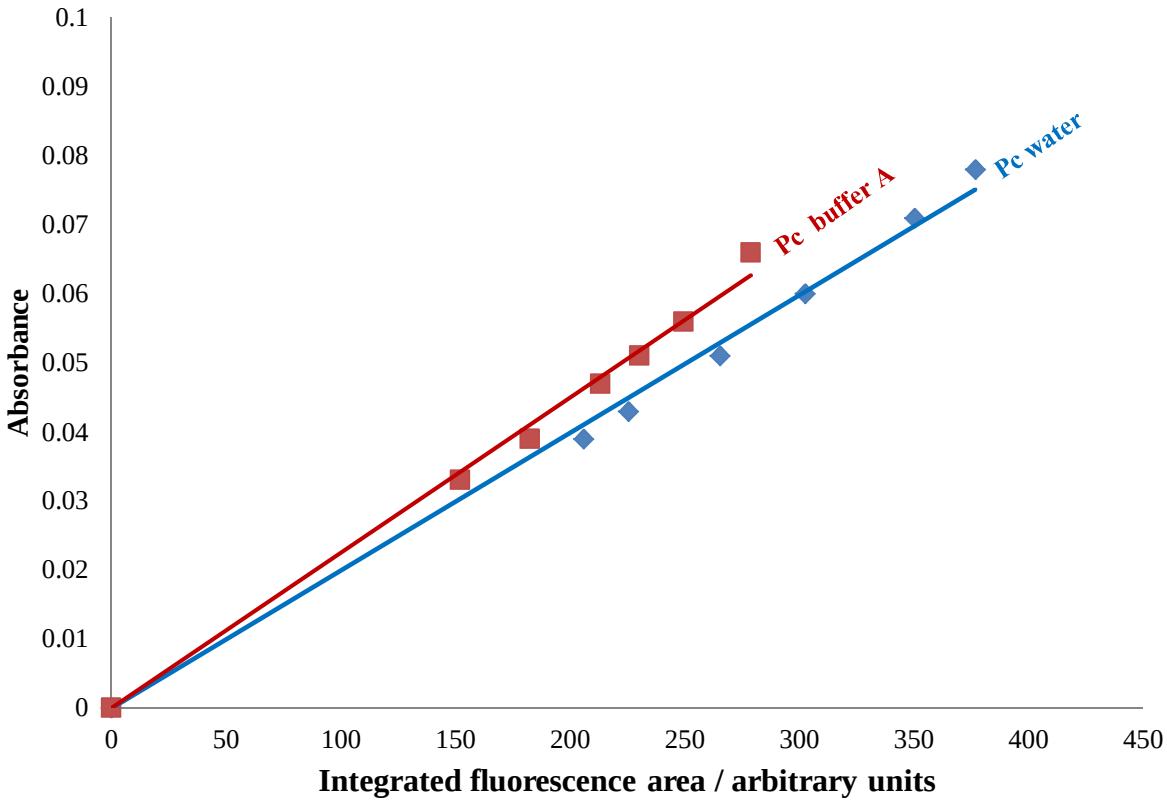

The addition of a deoxyribose or a ribose sugar group causes the fluorescent base excitation maxima to be shifted to longer wavelengths in both water and buffer A, also the emission wavelength is red-shifted compared to Pc. The measured fluorescence intensity of the nucleosides is lower than the one of Pc as free base, especially when ribose is attached to the fluorescent base. This depression in fluorescence intensity could be explained by the reduction of the energy gap between S_0 and S_1 states of Pc. Because of the proximity in energy between S_1 and S_0 states IC can effectively compete against fluorescence resulting in loss of energy *via* vibrational relaxation to the ground state, and as a consequence of that, fewer Pc molecules fluorescing (see the energy gap law in Chapter 2, see Section 2.3.5). The Figure 6.3 illustrates the quantum yield slopes of the nucleosides in water and buffer A.

Figure 6.3 Quantum yield slopes of Pc nucleosides

Quantum yield plots of Pc nucleosides, Pc_{dr} and Pc_r, in water and buffer A (0.049 M sodium phosphate and 0.1 M sodium chloride)

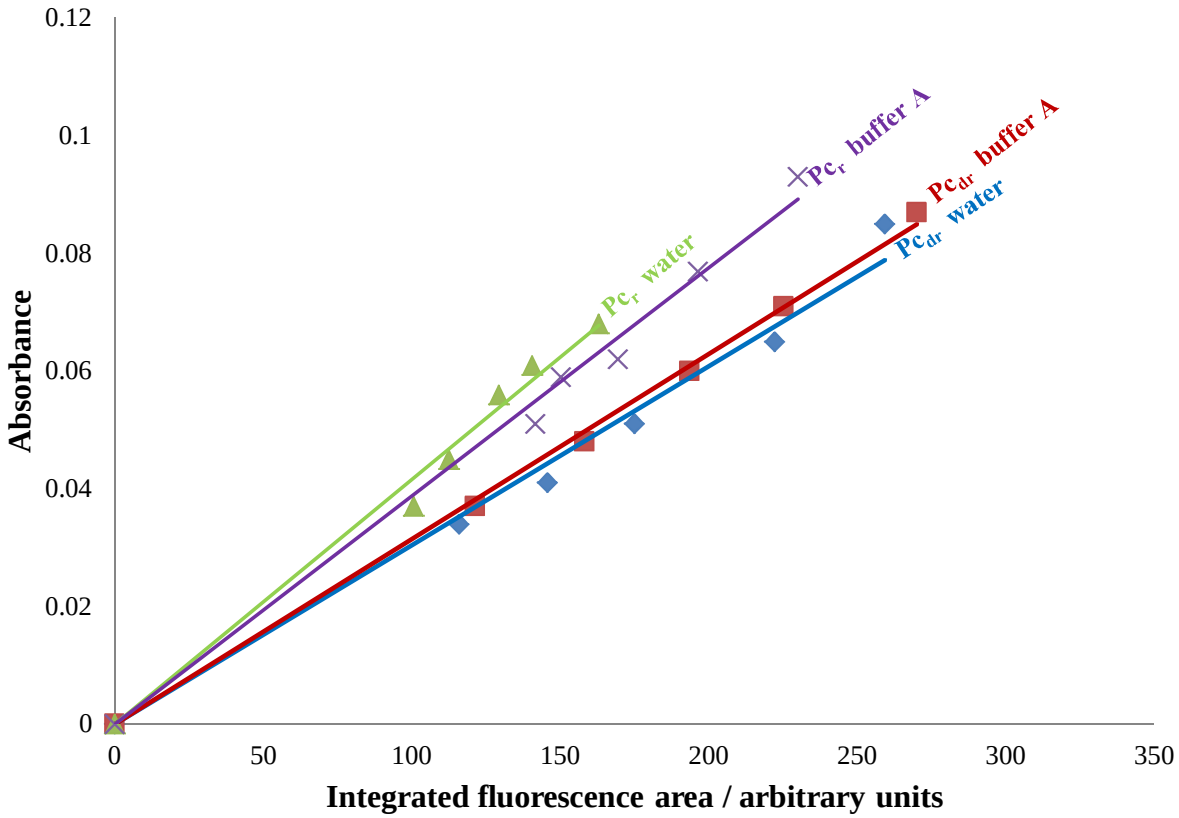

6.3.2 G-rich oligonucleotides containing Pc

The quantum yield measurements of oligonucleotides containing Pc base-paired with guanine bases were measured. Also, the changes in fluorescence of the probe when hydrogen bonded to its complementary base guanine (G) were reported. The Figure 6.4 and 6.5 show the trinucleotide GPcG as a 3D structure and hydrogen bonding formation between Pc and G, and G and C, when the single-stranded oligonucleotide G_9PcG_9 is bound to its complementary single-stranded oligonucleotide C_9GC_9 to form a duplex.

Figure 6.4 GPcG trinucleotide

This chemical structure was drawn by using the 2D software Symyx Draw 3.2 and converted into a 3D structure by using Chemsketch version 12 to emphasize the stacking between Pc and guanine bases

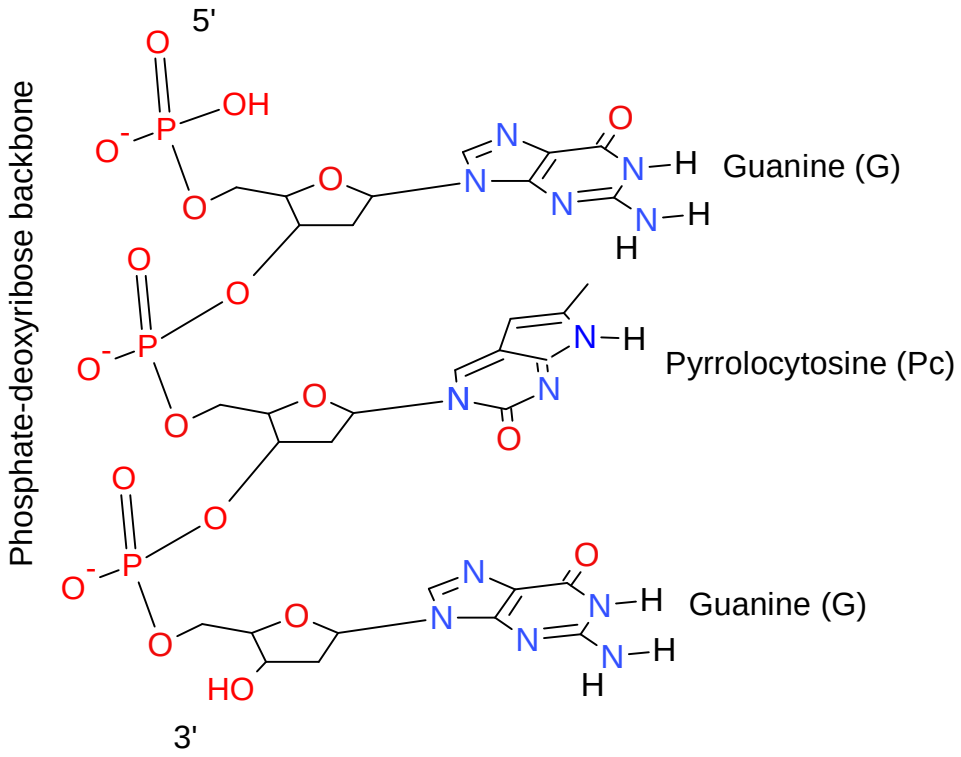

Figure 6.5 G◦Pc and G◦C hydrogen bonded complementary bases

Hydrogen bonding formation taking place between G◦Pc and G◦C bases

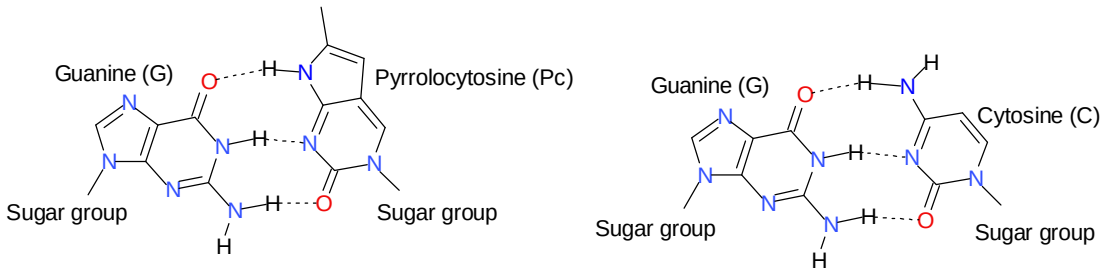

The Table 6.2 contains the quantum yield of trinucleotides, single-stranded and double-stranded oligonucleotides in water and buffer A.

Table 6.2 Spectroscopic data of G-rich oligonucleotides containing Pc

Φ_F, λ_{ex}, λ_{em} of G-rich oligonucleotides containing Pc in water and buffer A (0.1 M sodium chloride and 0.049 M sodium phosphate)

Compound analysed	λ_{ex}	λ_{em}	$\Phi_F \pm 2\sigma$
GPcG in water	347-349 nm	449-451 nm	0.040 ± 0.002
GPcG in buffer A	347-349 nm	449-451 nm	0.038 ± 0.003
G_9PcG$_9$ in water	347-349 nm	447-449 nm	0.036 ± 0.003
G_9PcG$_9$ in buffer A	347-349 nm	447-449 nm	0.043 ± 0.003
G_9PcG$_9$∘C$_9$GC$_9$ in water	351-353 nm	447-449 nm	0.023 ± 0.004
G_9PcG$_9$∘C$_9$GC$_9$ in buffer A	351-353 nm	447-449 nm	0.039 ± 0.002

The fluorescence of Pc as a trinucleotide, flanked by two guanine bases, was found to be reduced compared to the free base, see Figures 6.2 and 6.6 for comparison. The reduction in fluorescence emission was also accompanied by longer wavelength excitation and emission maxima. This difference in fluorescence emission between the free base and as a trinucleotide is in agreement with the literature (Hardman *et al.* 2008), Φ_F = 0.038 ± 0.002 and 0.036 ± 0.002 of Pc and GPcG respectively in 50 mM sodium phosphate buffer at pH 7. They also found out that the quantum yield of GPcG is larger than the one of the dinucleotide GPc, Φ_F = 0.021 ± 0.001. They attributed this reduction in fluorescence to the exposure of the base to solvent which would act as a dynamic quencher, stating that the fluorescence of GPcG is less affected because the guanines may somehow shield the fluorescent base from the solvent. This assumption is very questionable because the free base Pc seems to be only slightly affected by sodium phosphate as shown in the Stern-Volmer plot of Figure 6.9. The measured Stern-Volmer quenching constant of Pc in sodium phosphate is so small that the effect of the solvent on the fluorescence of Pc can be considered as negligible in the working sodium phosphate buffer concentrations. Then, the smaller fluorescence quantum yield of Pc as a trinucleotide may be due to the addition of the sugar group or electron transfer from guanine bases to Pc because guanine has the lowest ionization potential among all the nucleobases and therefore, it would behave as an electron donor, as in the case of 2-Ap (Kelley and Barton, 1999; Wan *et al.* 2000; Jean and Hall, 2001; Larsen *et al.* 2004).

Figure 6.6 Quantum yield slopes of GPcG in water and buffer A

Quantum yield slopes of GPcG in water and buffer A (0.049 M sodium phosphate and 0.1 M sodium chloride)

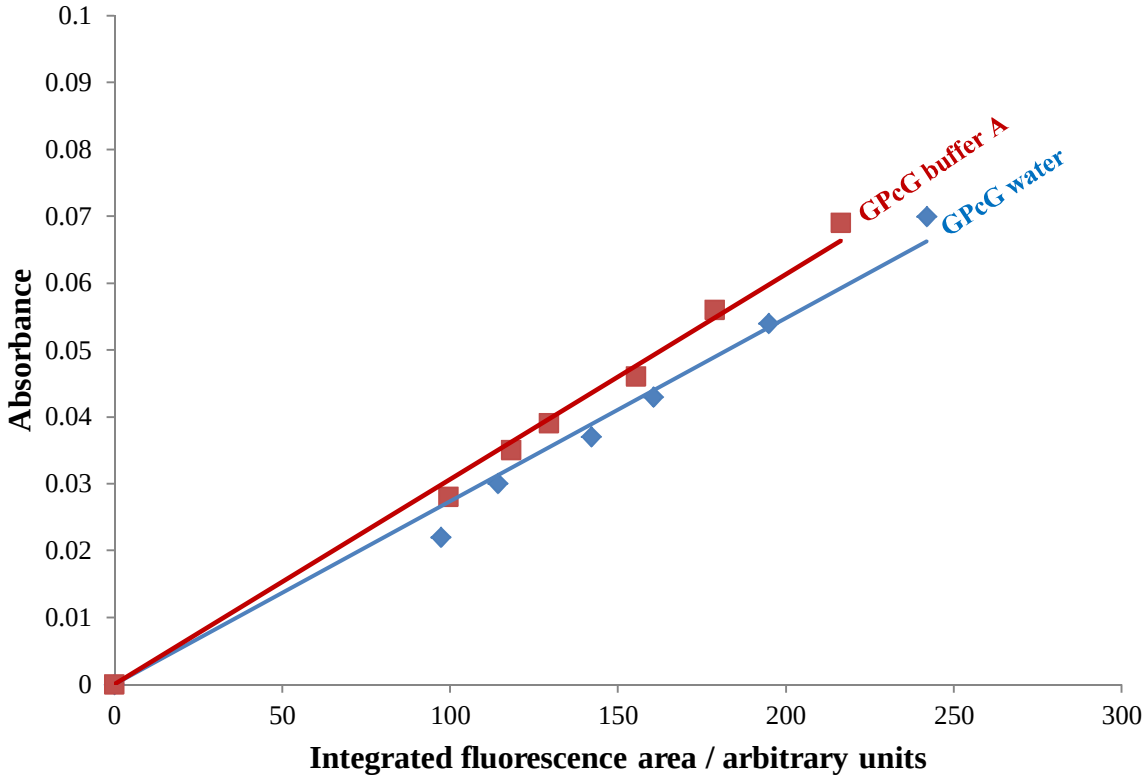

The situation becomes more complicated when the quantum yield of Pc incorporated into longer oligonucleotides is measured, see Figure 6.7 showing the slopes of the single and double-stranded oligonucleotides in water and buffer A. The quantum yield measurement of G_9PcG_9 ($\Phi_F = 0.036 \pm 0.003$) is slightly smaller than the quantum yield of GPcG ($\Phi_F = 0.040 \pm 0.002$) when measured in water, see Table 6.2. This would confirm the electron transfer theory explained before and that the decrease in fluorescence mainly depends on the guanine bases flanking the probe, regardless of the length of the oligonucleotide. The quantum yield of the duplex was found to be smaller than the single-stranded oligonucleotide, $\Phi_F = 0.036 \pm 0.003$ and 0.023 ± 0.004. This further reduction in fluorescence emission is likely to be caused by hydrogen bonding formation in a helical environment (Hardman and Thompson, 2006; Hardman *et al.* 2008). The most unexpected results came from the quantum yield measurements of G_9PcG_9 and $G_9PcG_9{\circ}C_9GC_9$ in buffers, $\Phi_F = 0.043 \pm 0.003$ and 0.039 ± 0.002 respectively. The increase in fluorescence of these G-rich oligonucleotides containing

Pc compared to their counterparts in water may be caused by formation of secondary structure in the presence of salts.

Figure 6.7 Quantum yield slopes of G_9PcG_9 and $G_9PcG_9{\circ}C_9GC_9$ in water and buffer A

Quantum yield slopes of G_9PcG_9 and $G_9PcG_9{\circ}C_9GC_9$ in water and buffer A (0.049 M sodium phosphate and 0.1 M sodium chloride)

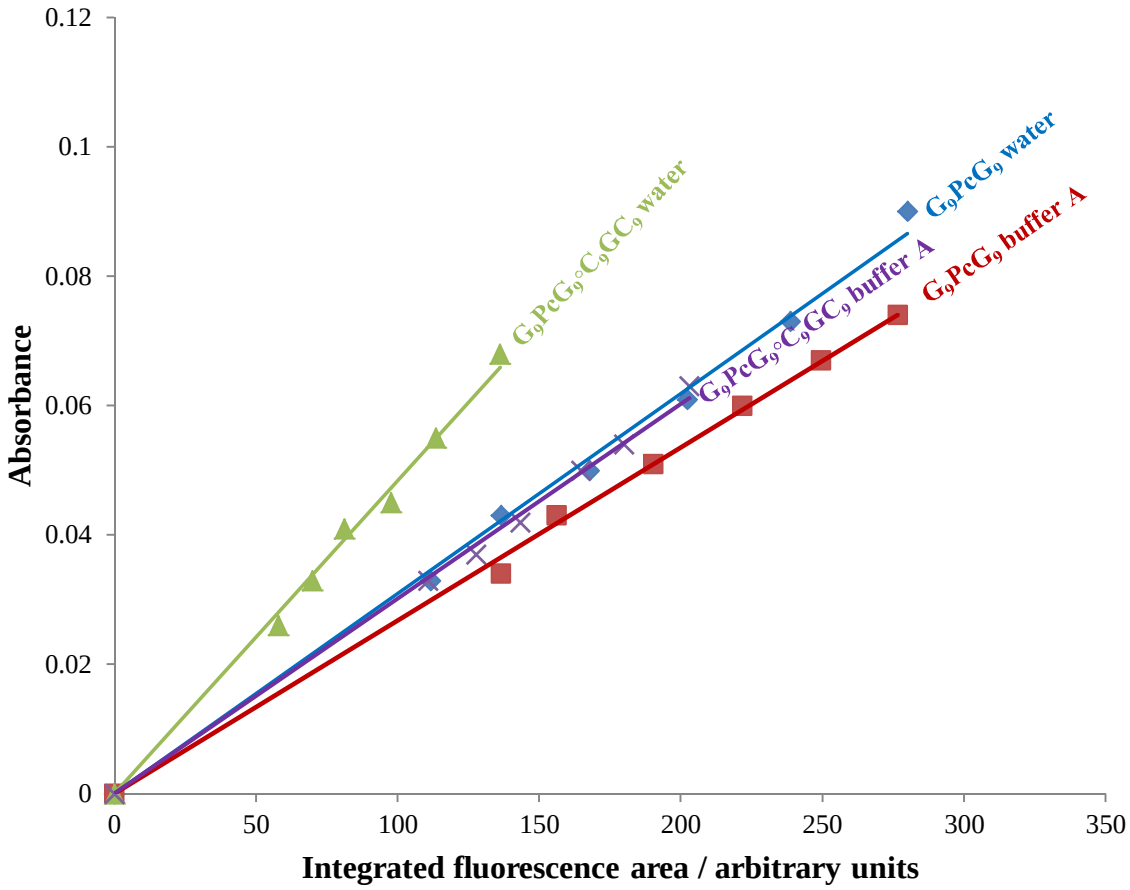

In fact, G-quadruplex secondary structures are known to be formed in oligonucleotides with guanine repeats in the presence of the stabilizing ion Na^+ (Gellert *et al.* 1962), see Figure 6.20. Tinsley and Walter recorded a large decrease in fluorescence of RNA oligonucleotides in buffer solutions containing NaCl. Precisely, they observed a decrease in fluorescence up to 40 % in contrast to the free base Pc and double-stranded oligonucleotide whose their fluorescence remained invariant (Tinsley and Walter, 2006). They suggested that the drastic quenching of fluorescence intensity of the single-stranded oligonucleotide compared to the duplex may be understood as a result of an enhanced base-stacking or secondary structure formation in the presence of counter-ions from buffer solutions (Zuker, 2003). Regarding the

maxima excitation, the maximum excitation wavelength in nm becomes longer from the free base to nucleosides and oligonucleotides as follows: Pc (335-337 nm) < Pc nucleosides (341-343 nm) < GPcG and G_9PcG_9 (347-349 nm) < $G_9PcG_9{\circ}C_9GC_9$ (351-353 nm). The maxima emissions are generally the same for Pc as free base and oligonucleotides whereas in the case of the nucleosides they are of longer wavelength, see Table 5.1 and 5.2.

6.3.3 2-Ap free base and 2-Ap$_{dr}$

The Table 6.3 shown below, contains the quantum yield measurements of 2-Ap in water, buffer A, B, C and D.

Table 6.3 Spectroscopic data of 2-Ap free base

Φ_F, λ_{ex}, λ_{em} of 2-Ap free base in water and buffer solutions: 0.1 M sodium chloride and 0.049 M sodium phosphate (buffer A), 5 mM sodium phosphate (buffer B), 50 mM sodium phosphate (buffer C) and 0.1 M sodium chloride (buffer D)

Compound analysed	λ_{ex}	λ_{em}	$\Phi_F \pm 2\sigma$
2-Ap in water	304-306 nm	370-372 nm	0.686 ± 0.016
2-Ap in buffer A	304-306 nm	370-372 nm	0.442 ± 0.008
2-Ap in buffer B	304-306 nm	370-372 nm	0.660 ± 0.016
2-Ap in buffer C	304-306 nm	370-372 nm	0.434 ± 0.010
2-Ap in buffer D	304-306 nm	370-372 nm	0.670 ± 0.014

The quantum yield of 2-Ap in water was found to be 0.686 ± 0.016 see Table 6.3, this quantum yield measurement is in agreement with the quantum yield measurement in the literature (Holmen *et al*. 1997). As shown in Table 6.3 the quantum yield measurements decrease as the concentration of sodium phosphate increases, 2-Ap in buffer C = 0.434 ± 0.010 and 2-Ap in buffer A = 0.442 ± 0.008. According to Ward and his collegues salts such as NaCl, KCl and $MgCl_2$ can quench the fluorescence of 2-Ap by 15 % (Ward *et al*. 1969) but, the quantum yield measurement of 2-Ap in sodium chloride reported herein is practically the one measured in water; therefore, the decrease in fluorescence is to be attributed to the presence of phosphate ions which may behave as fluorescence quanchers. For example, phosphate ions can affect the fluorescence emission of thryptophan derivatives (Alev-

Behmoras, 1979). The Figure 6.8 illustrates the quantum yield plots of 2-Ap in water and different buffers.

Figure 6.8 Quantum yield plots of 2-Ap

Quantum yield plots of 2-Ap free base in water, 0.1 M sodium chloride and 0.049 M sodium phosphate (buffer A), 5 mM sodium phosphate (buffer B), 50 mM sodium phosphate (buffer C) and 0.1 M sodium chloride (buffer D)

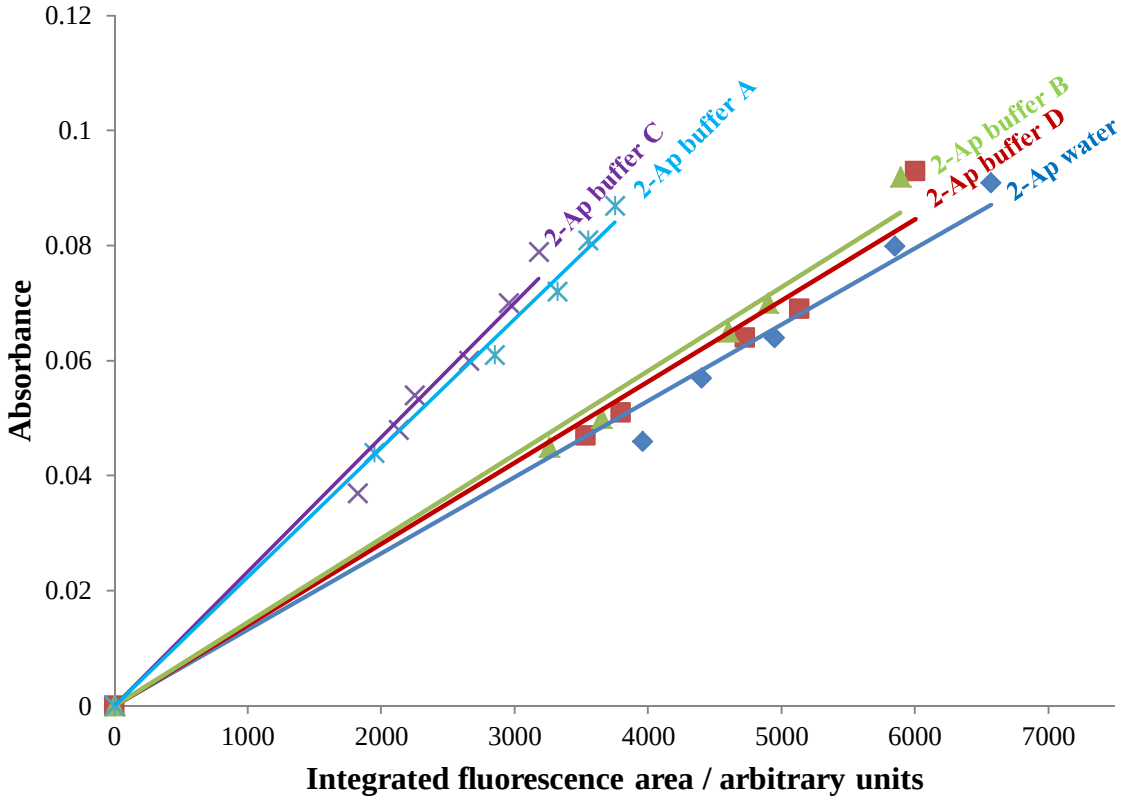

The rate of deactivation of the excited fluorophores depends on the nature of the quencher and therefore, the excited probes are deactivated depending on the quenching rate constant of the quencher, K_Q. If it is assumed that the quenching is dynamic then the kinetics of this intermolecular process follows the Stern-Volmer relationship, given as equations 6.1 and 6.2 see Chapter 2 Section 2.3.6.

$$\frac{I_F}{I_F} = 1 + k_Q \tau [Q] \quad (6.1)$$

or,

$$\frac{I_F}{{}^{Q}I_F} = 1 + K_{SV}[Q] \quad (6.2)$$

where I_F is the fluorescence emission of the probe in the absence of the quencher whereas ${}^{Q}I_F$ is the fluorescence of the base in presence of the quencher. The term τ is the fluorescence lifetime of the probe in absence of the quencher. The product of the term $K_Q \tau$ is the Stern-Volmer quenching constant K_{SV}. The Stern-Volmer quenching constant is found from the slope of the linear function obtained by plotting I_F / ${}^{Q}I_F$ against the concentration of the quencher [Q]. Figure 6.9, shows the Stern-Volmer plots of 2-Ap and Pc in sodium phosphate solutions at 20 ºC.

Figure 6.9 Stern-Volmer plots of 2-Ap and Pc in sodium phosphate at 20 ºC

Stern-Volmer plots were generated by plotting I_F / ${}^{Q}I_F$ measurements against the molar sodium phosphate concentration. The Stern-Volmer quenching constants (K_{SV}) of 2-Ap and Pc are 15.061 and 0.5285 respectively

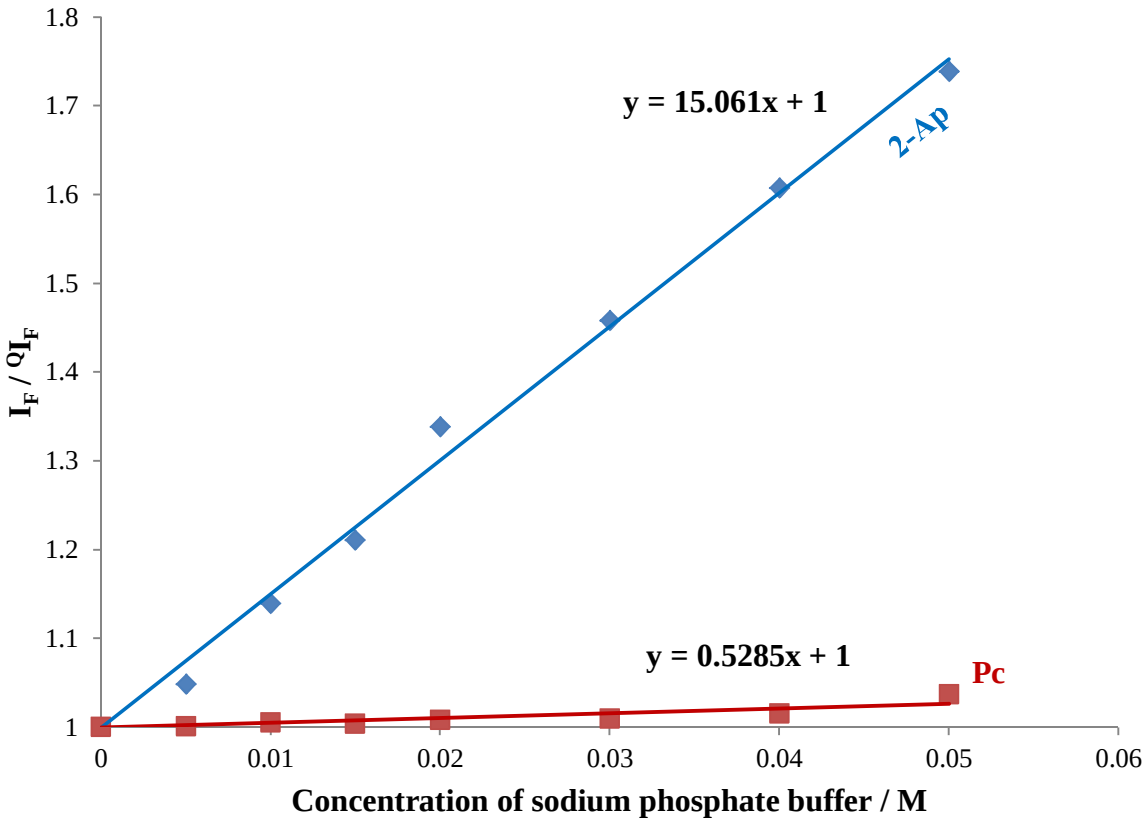

The two generated Stern-Volmer plots point out the striking difference in decrease in fluorescence of 2-Ap as opposed to Pc as the concentration of sodium phosphate increases. In the case of Pc, the effect of sodium phosphate as a quencher is almost negligible. The linear relationship alone, found as the ratio of the fluorescence emissions increase as a function of quencher concentration, cannot attest whether the quenching is dynamic or static in the case of 2-Ap at 20 ºC. Figure 6.10 shows another Volmer plot this time generated at 60 ºC and compared to one previously generated at 20 ºC. The greater slope of the plot obtained at 60 ºC may be indicative of dynamic quenching over static quenching because as explained in Chapter 2 Section 2.3.6 Figure 2.19, an increase in slope would result from an increase in diffusion rates. Furthermore, no particular shifts or changes (which are consistent with static quenching) in the absorption spectra of the probe in presence or absence of sodium phosphate were observed, such shifts occur when distinct ground state fluorophore-quencher complexes are excited (Fraiji *et al.* 1992, Lakowics, 1999).

Figure 6.10 Stern-Volmer plots of 2-Ap in sodium phosphate at 20 and 60 ºC

Comparing Stern-Volmer plots of 2-Ap in sodium phosphate at 20 at 60 ºC. The slope at 60 ºC was found to be much bigger (30.956) than the one measured at 20 ºC (15.061).

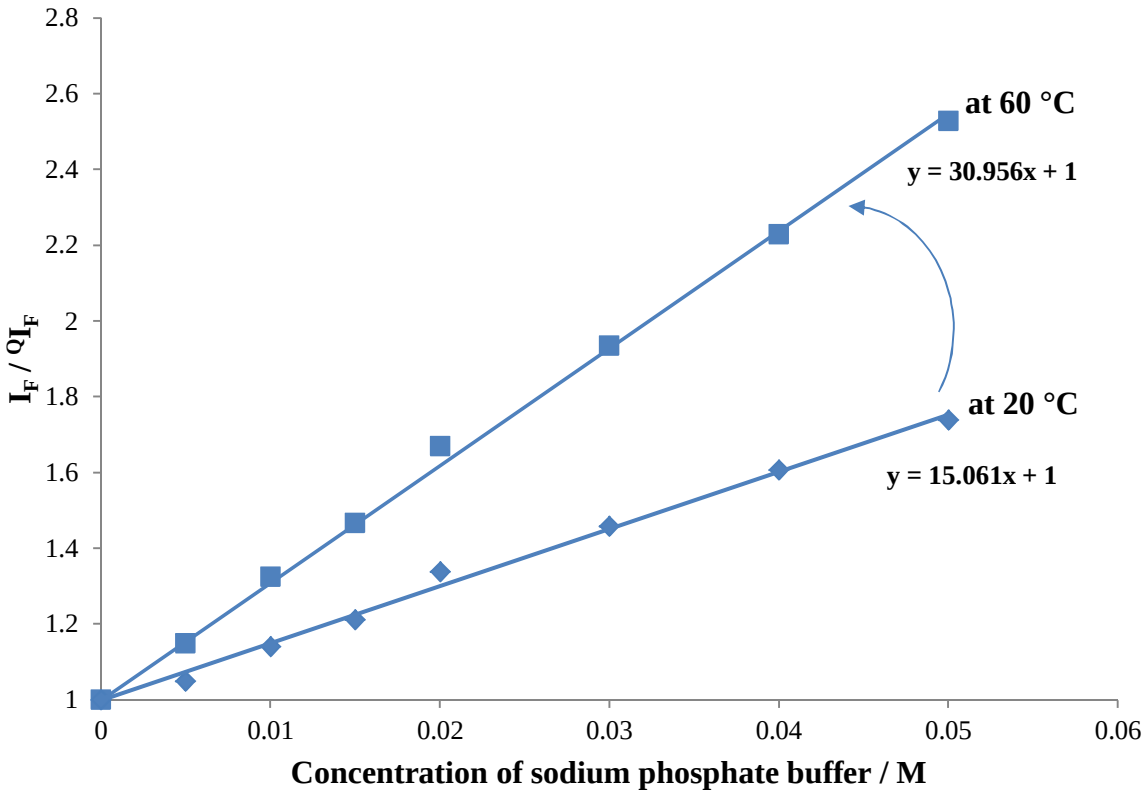

Even though all the experimental findings point towards dynamic quenching processes as the main intermolecular deactivation process, the only unambiguous evidence for that (dynamic quenching) can only be attained by measuring the emission lifetimes (Valeur, 2002), see Chapter 2, Figure 2.20. The changes in fluorescence emissions of 2-Ap in water and sodium phosphate as a function of temperature (from 25°C to 80°C) were accurately monitored and compared, see Figure 6.11. The decrease in fluorescence as the temperature increases in both water and sodium phosphate is due to non-radiative processes (IC and ISC) related to thermal agitation processes such as: collisions with solvent molecules and intramolecular vibration and rotation motions of the probe (Valeur, 2002) which are more efficient at higher temperatures and thus, competing with fluorescence.

Figure 6.11 Temperature dependence of 2-Ap fluorescence in sodium phosphate

Temperature dependence measurements of 2-Ap in 50 mM sodium phosphate and water. Even in absence of a quenching agent the emission fluorescence is depressed because of thermal agitation. Fluorescence normalized to 1 at 25°C.

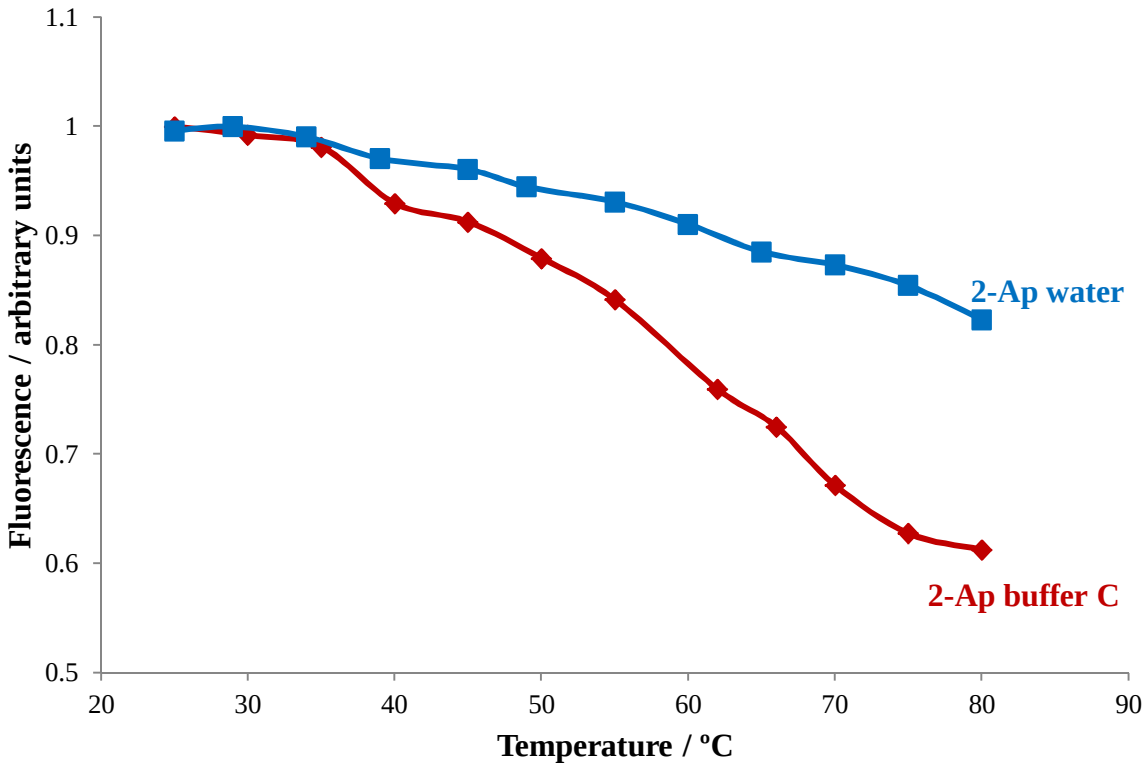

But as clearly displayed, the temperature dependence measurement of 2-Ap fluorescence in sodium phosphate is much more sensitive than the one in water because sodium phosphate ions act as quenching agents. The Figure 6.12 displays the quantum yield slopes of 2-Ap_{dr} in water and buffer and the Table 6.4 contains the spectroscopic data. The fluorescence quantum yield of the nucleoside in water is remarkably bigger than the one of the free base only, Φ_F = 0.773 ± 0.010 and 0.686 ± 0.011. Like in the case 2-Ap, the quantum yield of 2-Ap_{dr} is dramatically reduced in buffer A almost certainly because of dynamic quenching due to phosphate ions. The maximum emission wavelength of 2-Ap_{dr} was found to be marginally blue-shifted compared to 2-Ap.

Figure 6.12 Quantum yield plots of 2-Ap_{dr}

Quantum yield plots of 2-Ap_{dr} (2-Ap deoxyribose) in water and 0.1 M sodium chloride and 0.049 M sodium phosphate (buffer A)

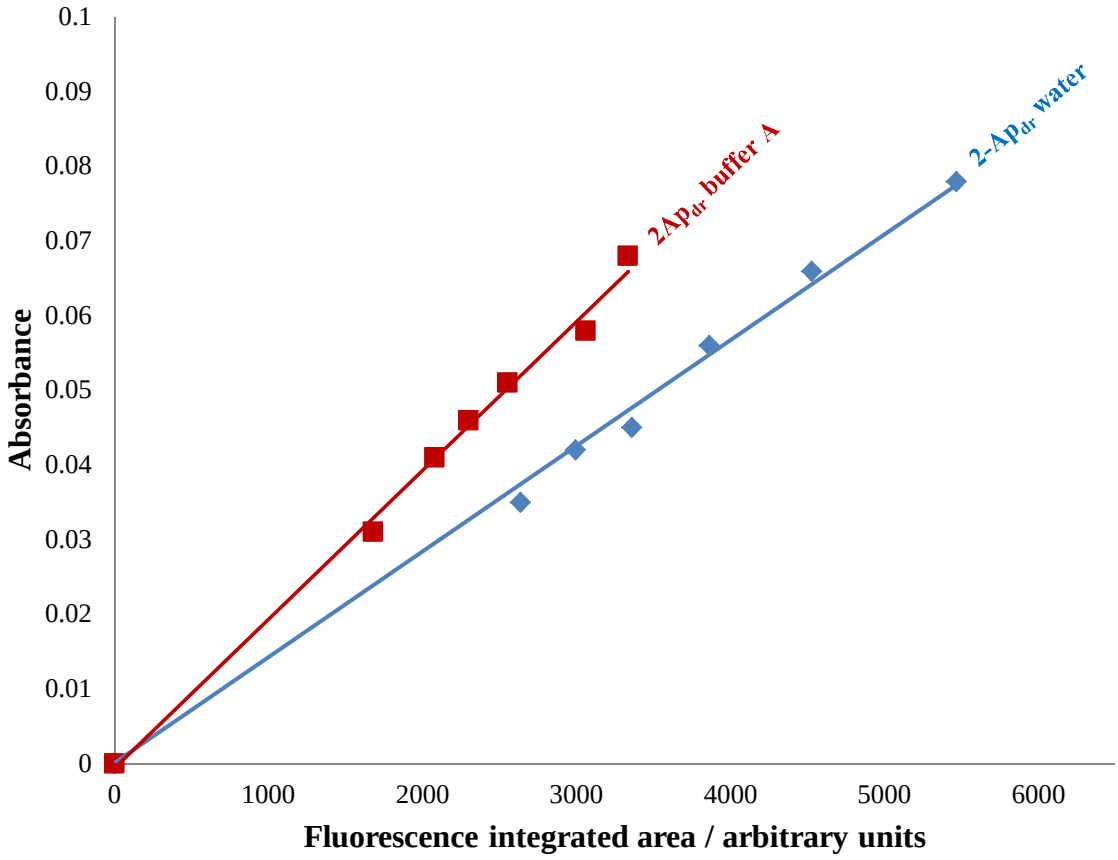

Table 6.4 Spectroscopic data of 2-Ap$_{dr}$

Φ_F, λ_{ex}, λ_{em} of 2-Ap$_{dr}$ (2-Ap deoxyribose) in water and buffer A (0.1 M sodium chloride and 0.049 M sodium phosphate)

Compound analysed	λ_{ex}	λ_{em}	$\Phi_F \pm 2\sigma$
2-Ap$_{dr}$ in water	304-306 nm	368-370 nm	0.773 ± 0.010
2-Ap$_{dr}$ in buffer A	304-306 nm	368-370 nm	0.599 ± 0.011

In order to confirm that phosphate ions can also behave as quenching agents on the fluorescence of 2-Ap nucleosides a 2-Ap$_{dr}$ Stern-Volmer plot was generated, see Figure 6.13. As shown later, phosphate ions can also reduce the fluorescence of the oligonucleotide even though the K_{SV} results to be smaller than the one measured for the free base only.

Figure 6.13 Stern-Volmer plot of 2-Ap$_{dr}$ in sodium phosphate

Stern-Volmer plot of 2-Ap$_{dr}$ in sodium phosphate generated by plotting I_F / $^{Q}I_F$ measurements against the molar sodium phosphate concentration. The Stern-Volmer quenching constant (K_{SV}) resulted to be 12.509

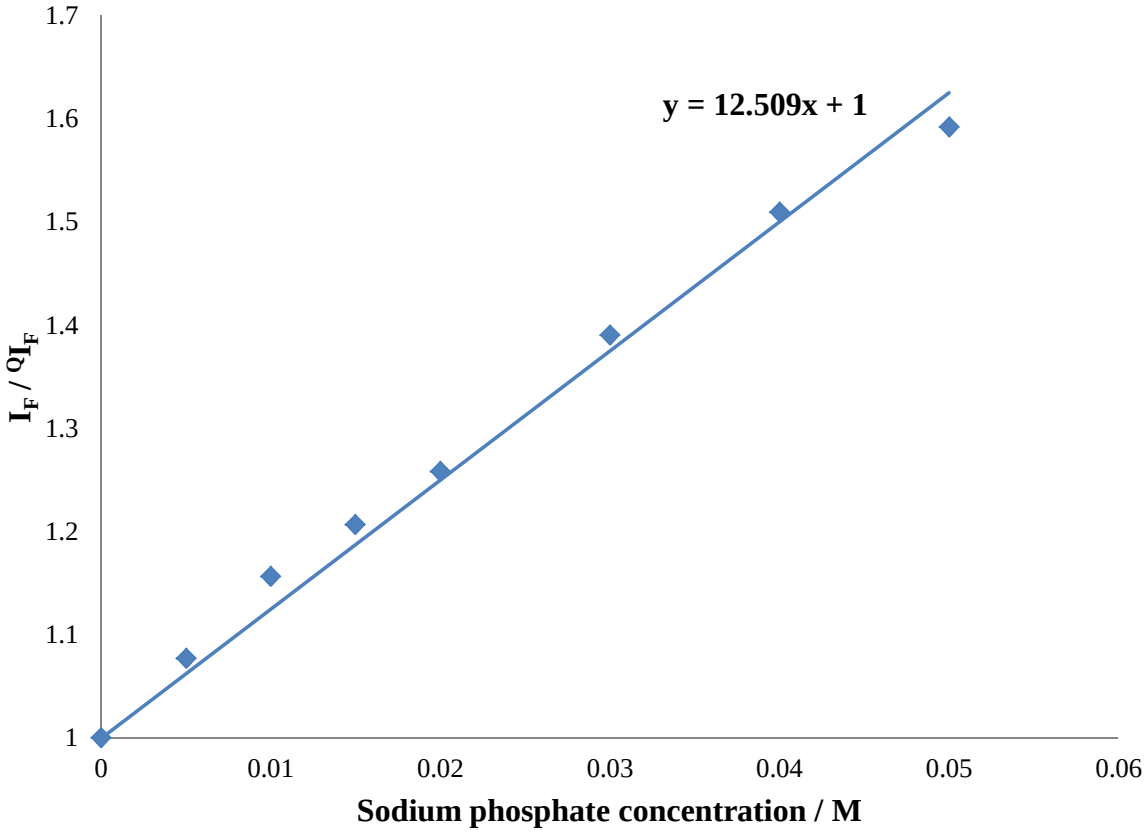

Evans *et al* (Evans *et al*. 1992) on a study of 2-Ap fluorescence, reported a slight increase in emission energy of the nucleosides, a blue shift of 1-2 nm compared to the emission energy of 2-Ap as free base in water. This slight blue shift is an agreement with the data included in Table 6.4. Also, they stated that 2-Ap attached to both deoxyribose or ribose caused a little change in fluorescence emission (± 15%) compared to the free base. Unfortunately, no accurate quantum yield measurements of 2-Ap and 2-Ap$_{dr}$ were reported in this article for comparison with the ones obtained herein.

6.3.4 G-rich oligonucleotides containing 2-Ap

The spectroscopic measurements of G-rich oligonucleotides containing 2-Ap as single and double-stranded oligonucleotides were reported in Table 6.5. Depictions of a G2ApG trinucleotides and hydrogen bonding formation taking place between 2-Ap and thymine (T) can be seen in Figures 6.14 and 6.15.

Figure 6.14 G2ApG trinucleotide

This chemical structure was drawn by using the 2D software Symyx Draw 3.2 and converted into a 3D structure by using Chemsketch version 12 to emphasize the stacking between 2-Ap and guanine bases

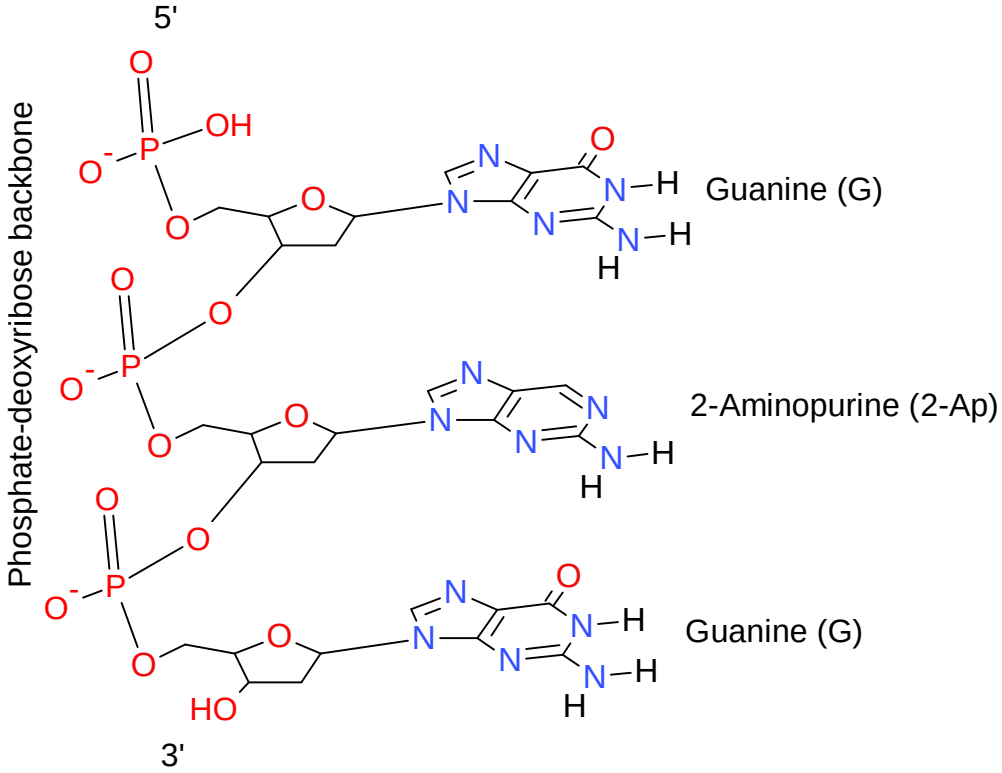

Figure 6.15 2-Ap◦T hydrogen bonded complementary bases

Hydrogen bonding formation taking place between 2-Ap and thymine (T) bases

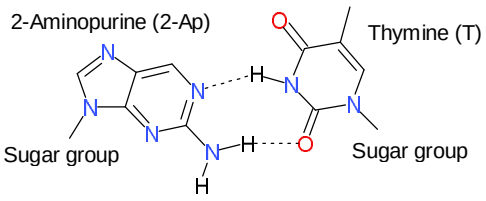

Table 6.5 Spectroscopic data of G-rich oligonucleotides containing 2-Ap

Φ_F, λ_{ex}, λ_{em} of G-rich oligonucleotides containing 2-Ap in water, buffer B (5 mM sodium phosphate), buffer C (50 mM sodium phosphate), buffer E (5 mM potassium phosphate) and buffer F (50 mM potassium phosphate)

Compound analysed	λ_{ex}	λ_{em}	$\Phi_F \pm 2\sigma$
G2ApG in water	304-306 nm	367-369 nm	0.138 ± 0.004
G2ApG in Buffer C	304-306 nm	367-369 nm	0.076 ± 0.002
$G_9$2ApG_9 in water	304-306 nm	368-370 nm	0.053 ± 0.005
$G_9$2ApG_9 in Buffer B	304-306 nm	368-370 nm	0.097 ± 0.004
$G_9$2ApG_9 in Buffer C	304-306 nm	368-370 nm	0.094 ± 0.006
$G_9$2ApG_9 in Buffer E	306-308 nm	368-370 nm	0.180 ± 0.006
$G_9$2ApG_9 in Buffer F	306-308 nm	368-370 nm	0.183 ± 0.005
$G_9$2ApG_9◦C9TC9 in water	311-313 nm	370-372 nm	0.044 ± 0.004
$G_9$2ApG_9◦C9TC9 in buffer C	309-311 nm	368-370 nm	0.058 ± 0.005

The quantum yield measurements of the trinucleotides containing 2-Ap contained in the Table 6.5 above show the difference in fluorescence in water and sodium phosphate. As in the case of the free base, the base incorporated into a trinucleotide may also be susceptible to dynamic quenching due to phosphate ions as shown in Figure 6.16 along with the quantum yield plots of G2ApG in water and buffer C are illustrated in Figure 6.17.

Figure 6.16 Stern-Volmer plot of G2ApG in sodium phosphate

Stern-Volmer plot of G2ApG in sodium phosphate generated by plotting I_F / $^{Q}I_F$ measurements against the molar sodium phosphate concentration. The Stern-Volmer quenching constant (K_{SV}) was calculated to be 8.181

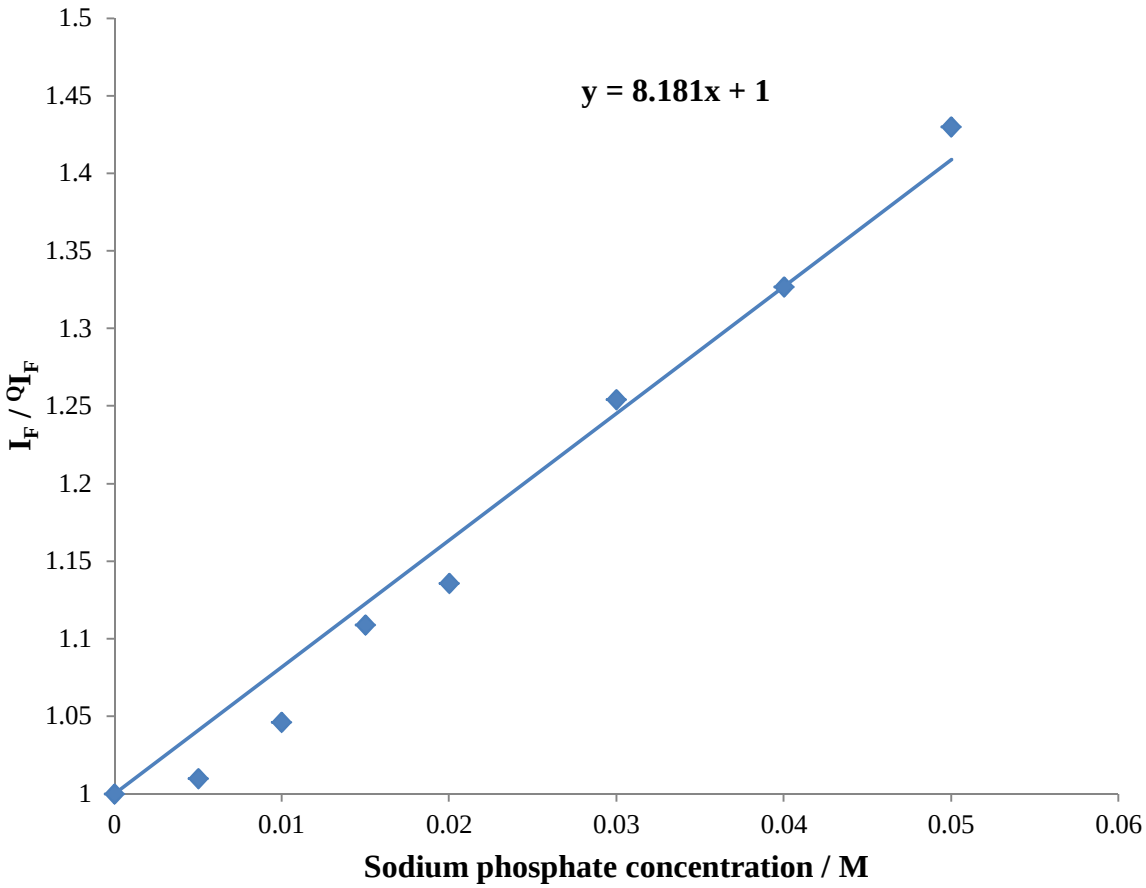

The drastic decrease in fluorescence of the fluoroprobe 2-Ap, up to 100 fold reduction in fluorescence intensity when incorporated into an oligonucleotide is still a controversial topic in the current literature (Reynisson and Steenken, 2004; Wan *et al*. 2005; Ward *et al*. 1969). It seems that the degree of quenching depends on the nature of the neighboring bases

(Nordlund *et al*. 1989; Guest *et al*. 1991; Hochstrasser *et al*. 1994; Kelley and Barton, 1999; Larsen *et al*. 2001; Fiebing *et al*. 2002). In the instance of 2-Ap flanked by guanine bases the stronger decrease in fluorescence compared to the other bases may be attributed to electron transfer (Nordlund *et al*. 1993; Kelley and Barton, 1999; Wan *et al*. 2000; Xu and Nordlund, 2000; Kawai *et al*. 2001; Fiebing *et al*. 2002; O'Neill *et al*. 2003) even though no charge-separated product state was observed (Larsen *et al*. 2004; O'Neill *et al*. 2004). The quenching of 2-Ap when flanked with guanine bases may also be caused by transition to a dark state rather than by electron transfer (Somsen *et al*. 2005). Stacking and collisional quenching of neigbouring bases are also important attributable factors to decrease of fluorescence, whereas in contrast 2-Ap seems to be insensitive to bases pairing, thus hydrogen bonding formation between the bases (Ward *et al*. 1969; Rachofsky *et al*. 2001).

Figure 6.17 Quantum yield slopes of G2ApG in water and buffer C

Quantum yield slopes of G2ApG in water and buffer C (50 mM sodium phosphate)

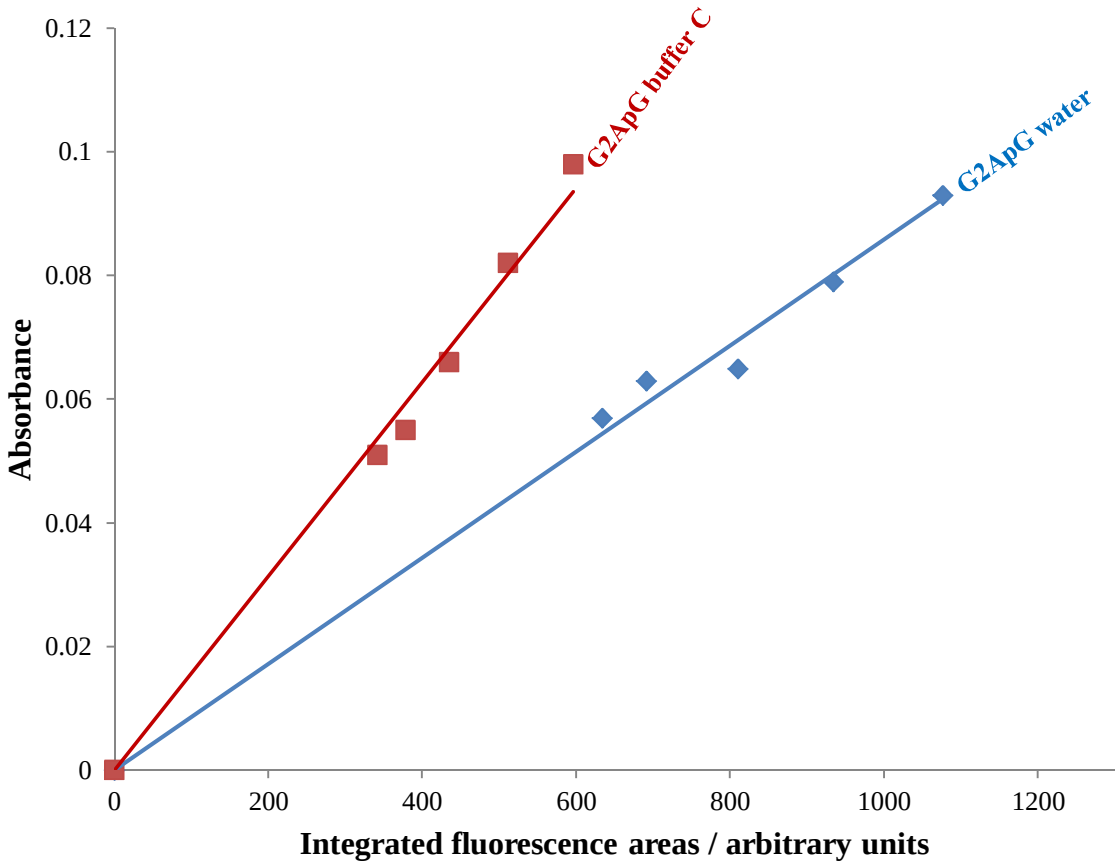

The quantum yield of the oligonucleotide $G_9$2ApG_9 in water was found to be smaller (Φ_F = 0.053 ± 0.005) than the trinucleotide containing the fluoroprobe (Φ_F = 0.138 ± 0.004) as seen in Table 6.5, and the quantum yield plots of the G-rich oligonucleotides containing 2-Ap are shown in Figure 6.18.

Figure 6.18 Quantum yield slopes of $G_9$2ApG_9 and $G_9$2ApG_9∘C_9TC_9

Quantum yield slopes of single-stranded oligonucleotides in water, buffer C (50 mM sodium phosphate) and buffer F (50 mM potassium phosphate). Quantum yield slopes of double-stranded oligonucleotides in water and buffer C

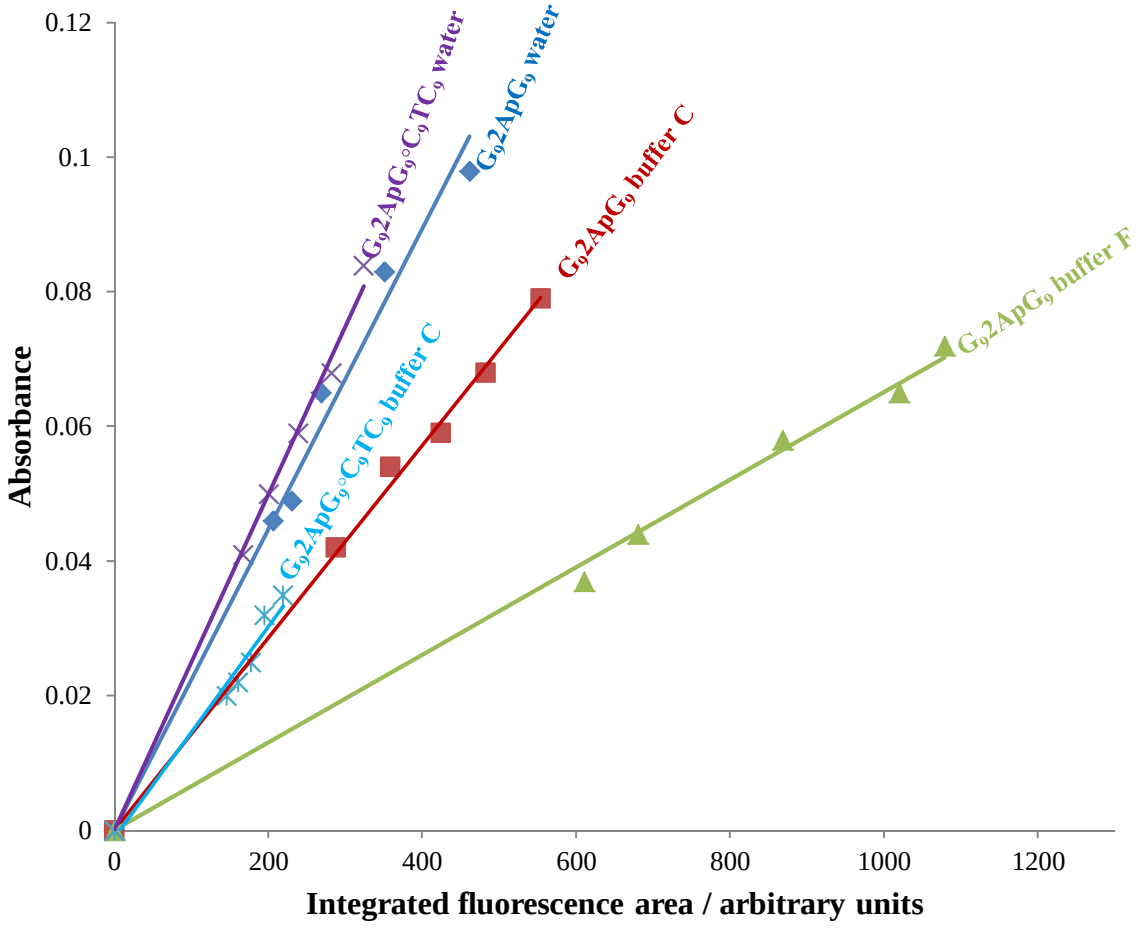

This reduction in fluorescence may be due to a more rigid stacking between the guanine bases flanking 2-Ap which may bring about a change in conformational geometry of the probe favouring radiationless pathways or less collisional quenching between bases. A further decrease in fluorescence was measured when $G_9$2ApG_9 is hydrogen bonded to its complementary strand C_9TC_9 (Φ_F = 0.044 ± 0.004). As described in the literature, base

-pairing appears not to play a big role in affecting the fluorescence of 2-Ap, thus the reduction in fluorescence observed may be a consequence of a "more" hydrophobic environment in which the probe resides. Since, the fluorescence of 2-Ap is extremely high in water, (probably because of the high dielectric constant of the solvent coupled with hydrogen bonding formation with the surrounding molecules, see Chapter 3 and 4) therefore, an environment which can shield 2-Ap from water exposure would drastically render 2-Ap less fluorescent. As in the case of Pc, see Table 6.2, the quantum yield measurements of the single and double-stranded oligonucleotides in buffers is bigger than their counterparts in water, probably because of secondary structure formation. Sodium phosphate seems not to act as quencher, in fact the quantum yields of the single-stranded oligonucleotide in buffer B and C are virtually identical (Φ_F = 0.097 ± 0.004 and 0.094 ± 0.006). As displayed in Figure 6.19 higher concentrations of sodium phosphate buffers do not cause higher fluorescence intensities of the oligonucleotide.

Figure 6.19 $G_9$2ApG_9 fluorescence as a function of sodium phosphate concentration

Normalised fluorescence emission of $G_9$2ApG_9 as a function of sodium phosphate concentration. As shown in the generated graph the maximum fluorescence emission (or plateau measurement) was found to be between 5 and 10 mM sodium phosphate concentration at which an increase in fluorescence by circa 100% was recorded

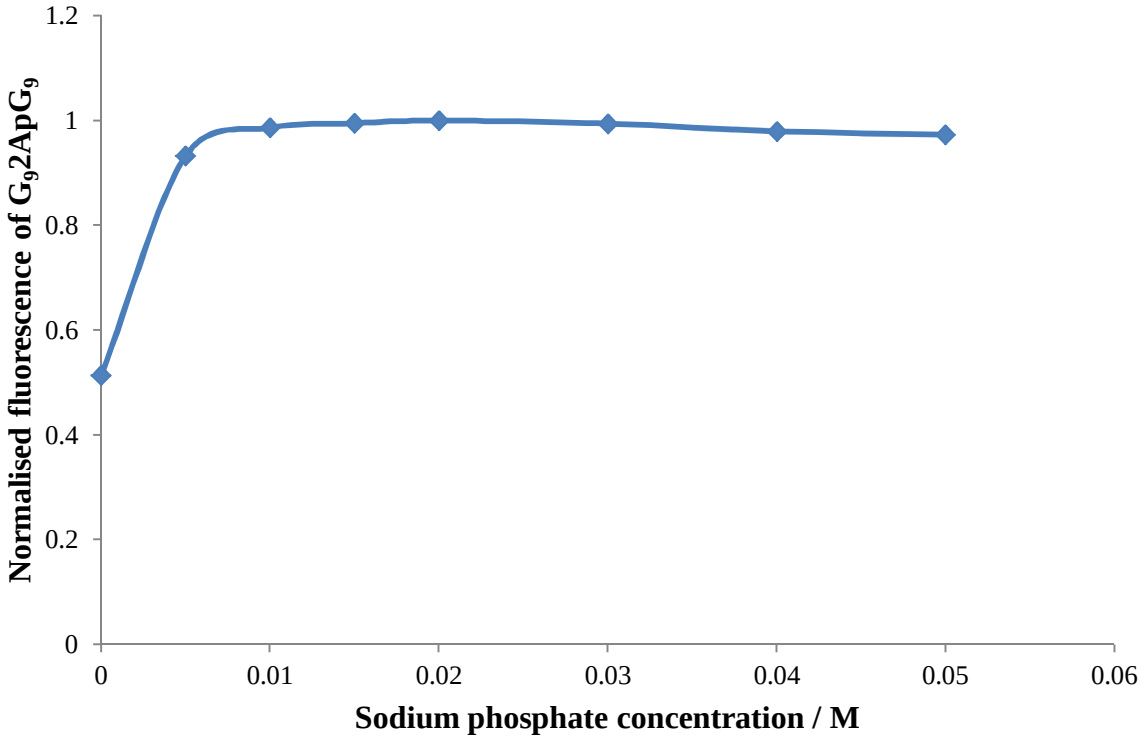

It is very important to note that when potassium phosphate buffers were used, buffer E and F, the measured quantum yields roughly doubled (Φ_F = 180 ± 0.006 and 183 ± 0.005) compared to the ones obtained by using sodium phosphate buffers. Once again, as in the case of sodium phosphate, 5 mM of buffer concentration is sufficient to cause a large increase in fluorescence emission. This may signify that just a small amount of salts in solutions may bring about a conformational change within the oligonucleotide. Potassium and sodium ions are both stabilizing metal ions coordinating G-quadruplex structures.

6.4 Introduction to secondary structure study

If 2-Ap fluorescence is quenched in the presence of sodium phosphate, then why is the quantum yield measurement of $G_9$2ApG_9 in sodium phosphate is bigger than the quantum yield measurement of $G_9$2ApG_9 in water? The answer to this question may be found in the polymorphic properties of oligonucleotides. The oligonucleotides have different secondary structures in different solvent conditions such as temperature, ionic strength and pH (Berova *et al*. 2000). G-rich oligonucleotides are known to form G-quadruplex secondary structures in the presence of a stabilizing metal ion such as K^+ and Na^+ as shown in Figure 6.20.

Figure 6.20 G-quadruplex structure (planar view)

A planar G-quadruplex structure sharing the stabilizing metal ion Na^+ within the center of the molecule

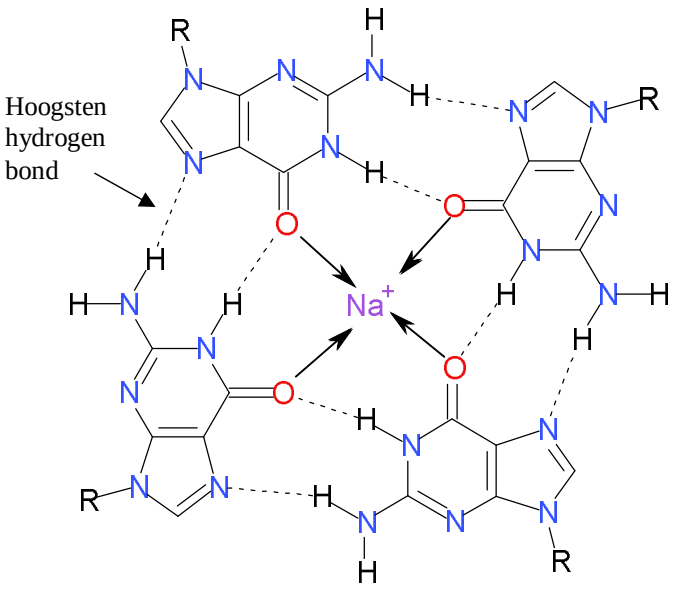

UV spectroscopy, fluorescence spectroscopy and circular dichrosim (CD) were used to ascertain the presence of G-quadruplex structures in sodium phosphate buffer solutions.

6.4.1 Introduction to UV-melting curves. Results and discussion

The transition between an ordered structure of a nucleic acid and a disordered, or denatured, structure is commonly monitored *via* UV melting curves. Melting curves are obtained by measuring the change in absorbance at a particular wavelength as a function of temperature. As the temperature increases the ordered regions of stacked base pairs are disrupted. This disruption results in an increase in absorbance. This increase in absorbance is known as hyperchromicity. The extent of hyperchromicity is proportional to the degree of unstacking among the nuclear bases. The reverse is hypochromicity which is a measure of the degree of stacking and pairing between the bases. Figure 6.21 shows a simple denaturation of a double-stranded oligonucleotide.

Figure 6.21 Melting of a duplex

A double-stranded oligonucleotide denatured *via* melting

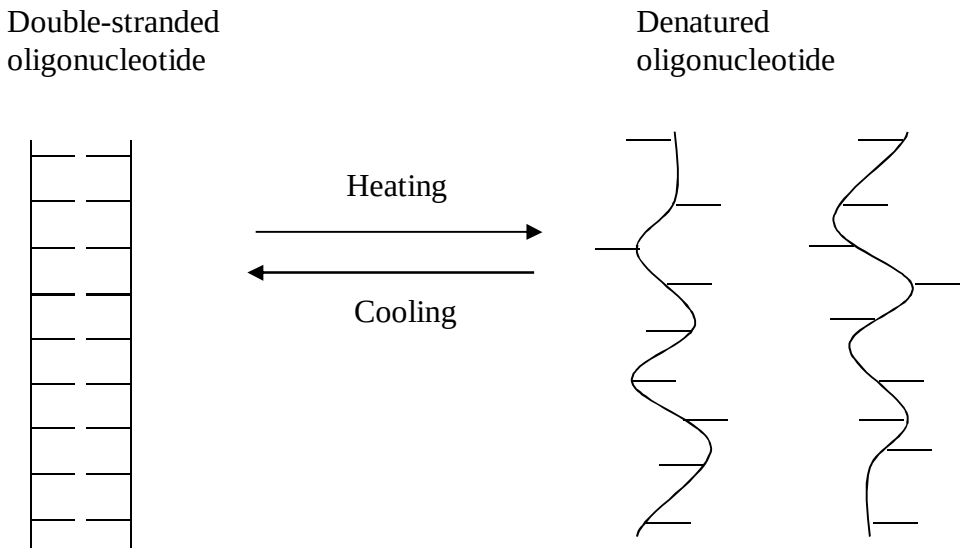

Melting curves are generated to investigate the stability of different DNA secondary structures and thus their polymorphic properties. Different DNA secondary structures have specific UV-melting profiles according to their structural features and therefore, a melting curve can be used for recognizing DNA G-quadruplex secondary structures from other DNA secondary structures (Puglisi and Tinoco, 1989; Santa Lucia, 2000; Benight *et al.* 2001;

Rachwal and Fox, 2007). According to the literature, by recording changes in absorbance at 260 nm an increase in absorbance of 25-30% as a function of temperature from 20 to 90 °C is expected for a G-quadruplex of 22 base pairs in different buffers (mainly NaCl and KCl) at pH 4.5-7.2 (of these 22 base pairs 12 of them are guanine bases) (Phan and Mergny, 2002). Figure 6.22 shows the UV-melting curves at 260 nm of $G_9$2ApG_9 in water and buffer solutions.

Figure 6.22 UV-melting curve of $G_9$2ApG_9 (sodium phosphate) recorded at 260 nm

UV-melting curves at 260 nm of $G_9$2ApG_9 in water, buffer G (0.1 mM sodium phosphate), buffer H (0.5 mM sodium phosphate), buffer I (1 mM sodium phosphate) and buffer B (5 mM sodium phosphate). The absorbance measurements are normalised to 1 at 70 °C

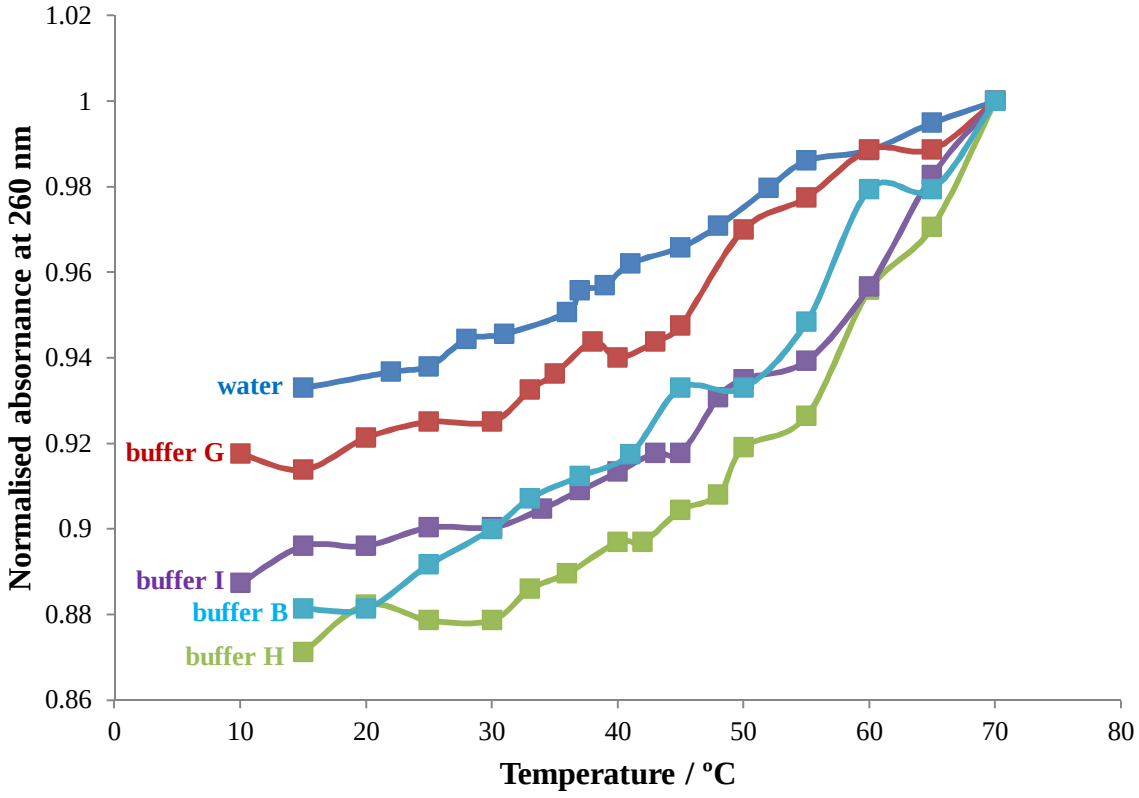

The melting curves obtained show a small hyperchromicity (absorbance increasing as a function of increasing temperature) for the oligonucleotide in all the solutions. The melting curve of $G_9$2ApG_9 in water is slightly flatter compared to the other curves which better resemble G-rich oligonucleotide melting curve profiles with a larger increase in absorbance within the 35-65 °C temperature range. For example G_9ApG_9 in buffer H gave the larger increase in absorbance (around 15% from 15 to 70 °C) compared to the other solutions. The parameter T_m of the curves (which is the maximum of the first derivative) could not be

precisely found because many maxima were observed. Although a small degree of hyperchromicity was recorded (the degree of hyperchromicity is small but it could be bigger if the oligonucleotides were melted at higher temperatures) all the curves are similar. No distinguishable polymorphic differences in $G_9$2ApG_9 were observed by changing the concentration of phosphate ions in solution. Formation of G-quadruplexes can be confirmed by using another wavelength besides the conventional wavelength of 260 nm which is also used for other secondary structures such as duplexes, triplexes and *i*-motifs (Phan and Mergny, 2002). If G-quadruplex structures are present in solution, a large decrease (up to 80% for a G-quadruplex of 21 base pairs of which 12 are guanine bases) in absorbance (hypochromicity) at 295 nm on melting is a good evidence of G-quadruplexes (Mergny *et al.* 1998). The melting profile curves of $G_9$2ApG_9 with absorbance measurements collected at 295 nm instead of 260 nm can be seen in Figure 6.23.

Figure 6.23 UV-melting curve of $G_9$2ApG_9 (sodium phosphate) recorded at 295 nm

UV-melting curves at 295 nm of $G_9$2ApG_9 in water, buffer G (0.1 mM sodium phosphate), buffer H (0.5 mM sodium phosphate), buffer I (1 mM sodium phosphate) and buffer B (5 mM sodium phosphate). The absorbance measurements are normalised to 1 at 70 °C

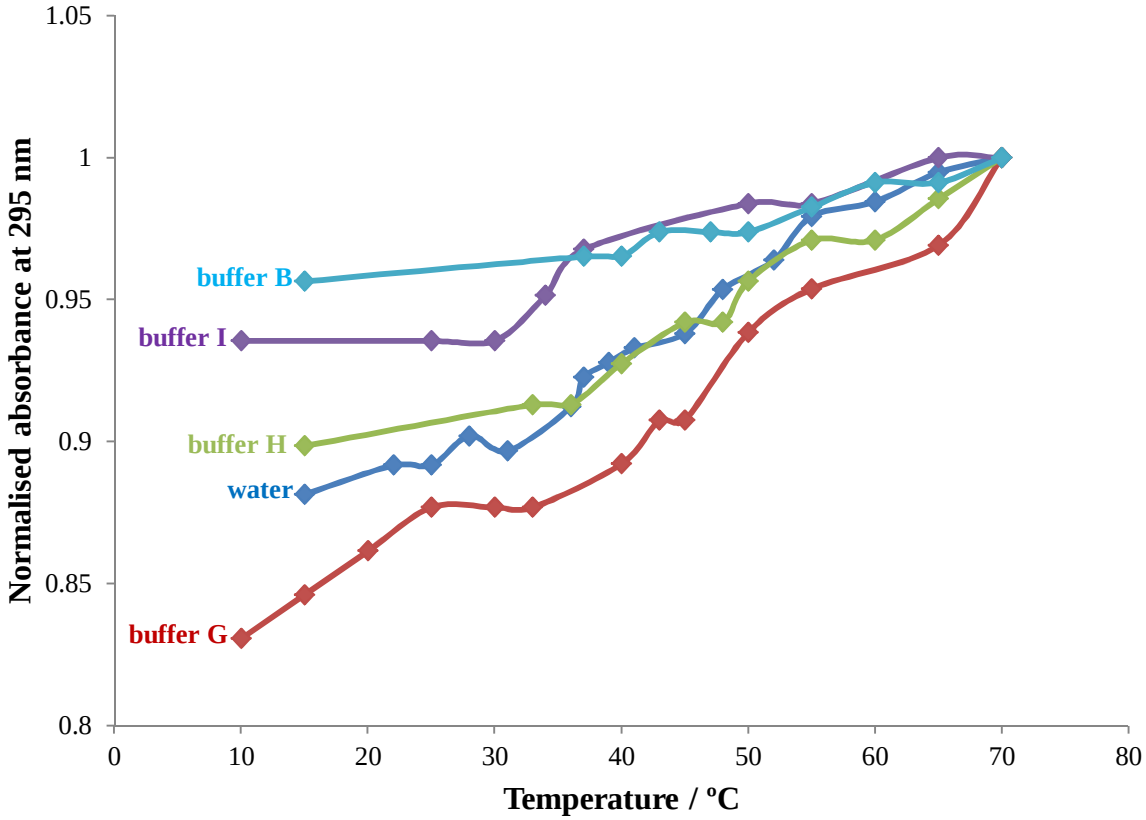

Like the melting curves of the oligonucleotide in sodium phosphate, no particular decrease in absorbance at 295 was observed when potassium phosphate was used and once again no precise T_m was reported because no distinguishable flat functions and inflection points which are typical of melting curves were observed. The Figures 6.24 and 6.25 depict the melting curves of $G_9 2ApG_9$ in 5 mM and 50 mM potassium phosphate. The two melting curves have a very similar melting pattern and in both the absorbance increases at 260 and 295 nm.

Figure 6.24 UV-melting curve of $G_9 2ApG_9$ (potassium phosphate) recorded at 260 nm

UV-melting curves at 260 nm of $G_9 2ApG_9$ in buffer E (5 mM potassium phosphate) and buffer F (50 mM potassium phosphate. The absorbance measurements are normalised to 1 at 75 °C

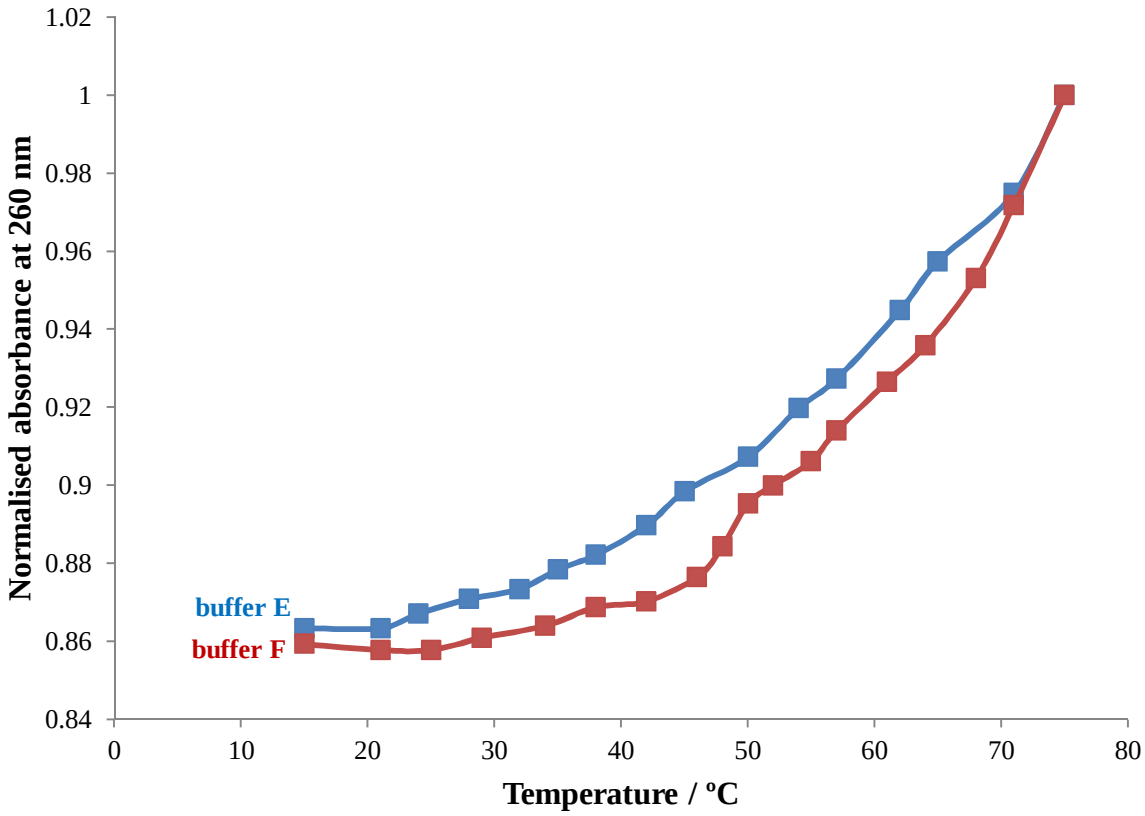

As in the case of 2-Ap incorporated into a G-rich oligonucleotide melting curves of G_9PcG_9 were generated. Figure 6.26 shows the melting curve of G_9PcG_9 in buffer A (0.049 M sodium phosphate and 0.1 M sodium chloride).

Figure 6.25 UV-melting curve of $G_9$2ApG_9 (potassium phosphate) recorded at 295 nm

UV-melting curves at 295 nm of $G_9$2ApG_9 in buffer E (5 mM potassium phosphate) and buffer F (50 mM potassium phosphate. The absorbance measurements are normalised to 1 at 75 °C

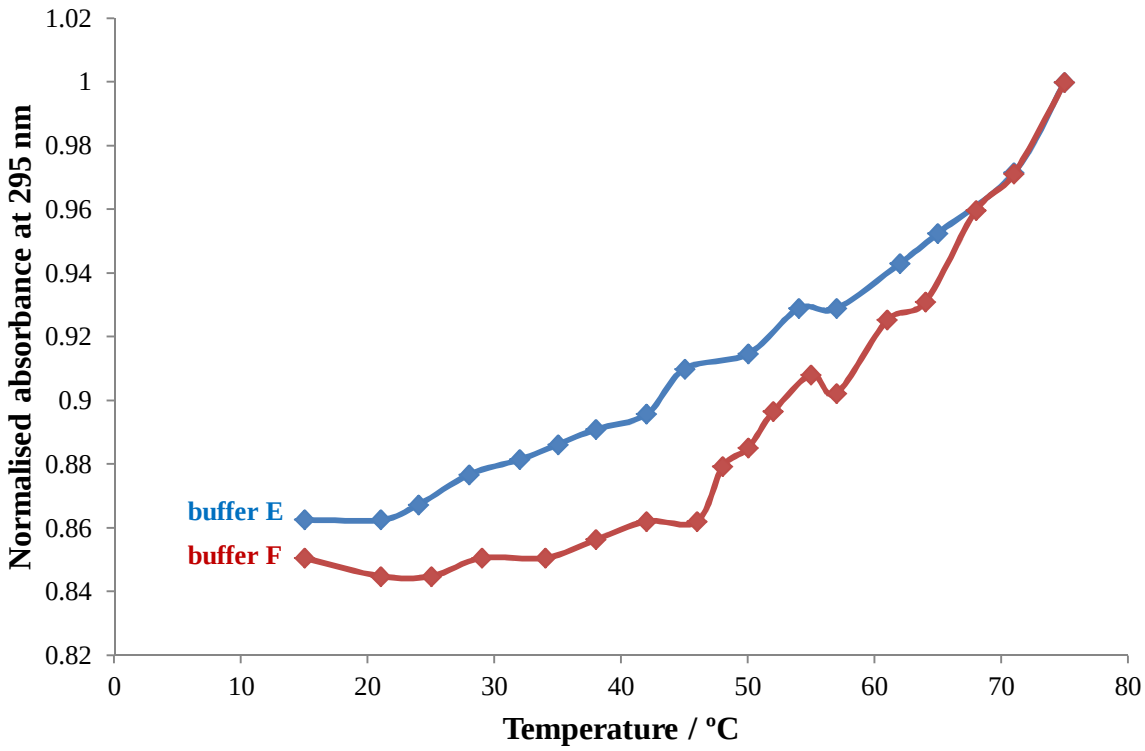

The melting curves of G_9PcG_9 in buffer A recorded at 260 and 295 nm are similar to each other. Then, from the data collected for both $G_9$2ApG_9 and G_9PcG_9 one would assume that the formation of secondary structures such as G-quadruplexes, triplexes and *i*-motifs may be very unlikely. The single-stranded oligonucleotides could still fold into helices, the canonical A, B and Z-DNA, but the geometry of the stacking between the bases may change depending on the buffer used and pH. For example, the Z conformations are more stable than the B conformations at very high salt concentrations, and therefore, the exposure of the bases to solvent is strongly dependent of the assumed conformation (Voet *et al.* 2005). Or non-canonical conformations of DNA structures may exist in buffer solutions. In fact, although DNA does not exhibit the structural complexity of proteins because of its limited repertoire of secondary structures and no comparable tertiary or quaternary structures, DNA can come in many forms (Rich, 1993).

Figure 6.26 UV-melting curve of G_9PcG_9 in buffer A

UV-melting curve at 260 and 295 nm of G_9PcG_9 in buffer A (0.049 M sodium phosphate and 0.1 M sodium chloride). The absorbance measurements are normalised to 1 at 75 °C

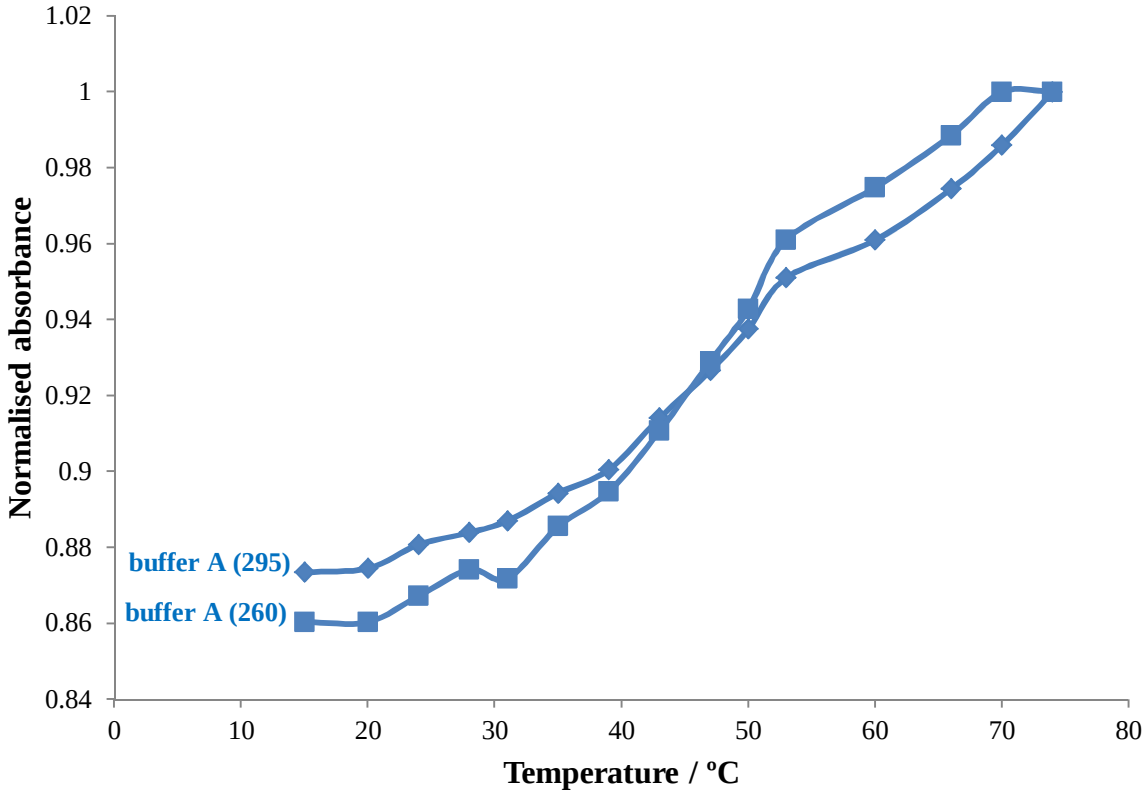

If from one hand the melting curves of the single-stranded oligonucleotides did not show any decrease in absorbance at 295 nm, indicating no formation of G-quadruplexes and *i*-motifs, on the other hand the melting of duplexes showed some peculiar and striking changes in absorbance at 295 nm as shown in Figure 6.27 and 6.28. In both double-stranded oligonucleotides $G_92ApG_9{\circ}C_9TC_9$ and $G_9PcG_9{\circ}C_9GC_9$ hypochromicity at 295 nm was observed in both water (a small one) and buffers (a large one). According to the literature melting curves of duplexes show a much larger increase in absorbance at 260 nm compared to single-stranded oligonucleotides (Phan and Mergny, 2002; Mergny *et al*. 1998). This larger increase in hyperchromicity at 260 nm of the duplexes compared to the single-stranded oligonucleotides was observed for the oligonucleotides containing 2-Ap, but not for the ones containing Pc.

Figure 6.27 UV-melting curve of $G_9$2ApG_9◦C_9TC_9

UV-melting curves at 260 and 295 nm of $G_9$2ApG_9◦C_9TC_9 in water and buffer C (50 mM sodium phosphate)

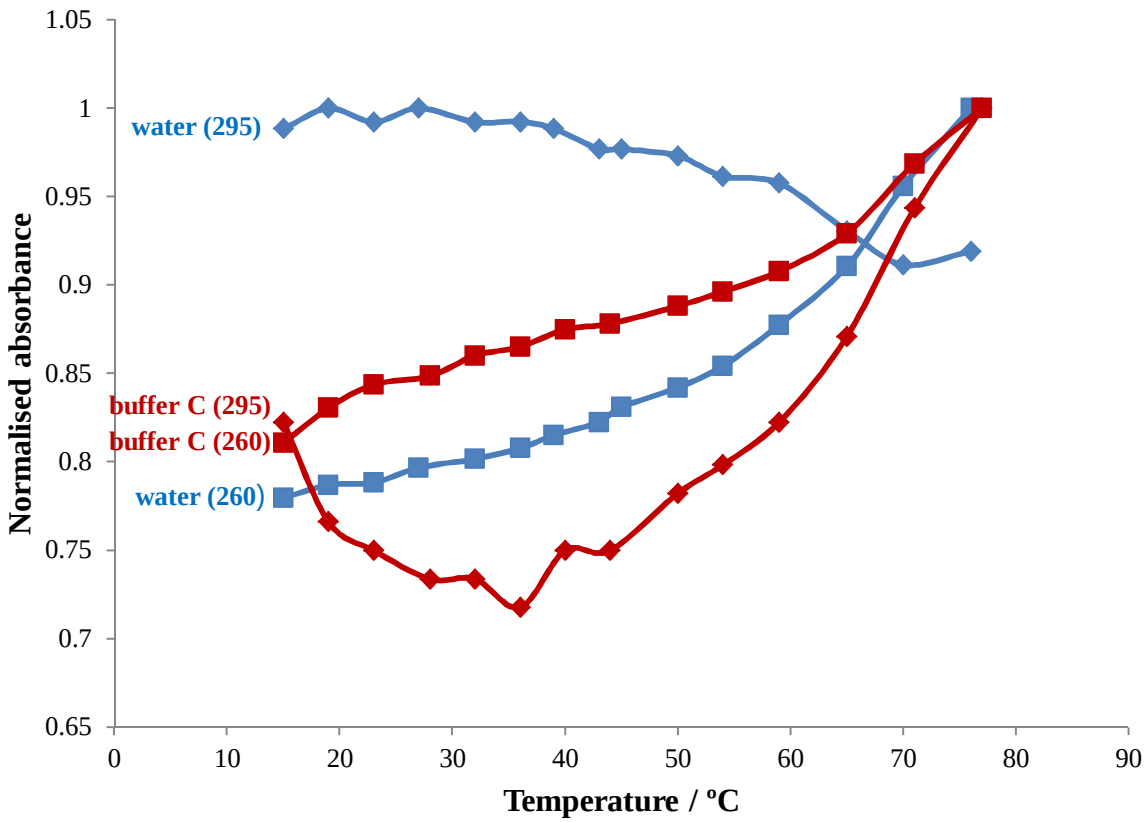

The decrease in absorbance at 295 nm may be attributed to presence of *i*-DNA structures, precisely a four stranded nucleic acid (also called H motif). A structure based on C◦G G◦C base pairs forming a four stranded arrangement with bases not participating in bases-pairing as loops (Gehring *et al*. 1993; Leroy *et al*. 1993). An example of how G_9PcG_9 with its complementary strand C_9GC_9 may participate in the formation of a four stranded oligonucleotide is depicted in Figure 6.29. If a large decrease in absorbance at 295 nm may attest the formation of secondary structures from G and C-rich oligonucleotides then, melting a double-stranded oligonucleotide without cytosine should not reveal any decrease in absorbance at 295 nm. The Figure 6.30 shows the melting curves of A_9PcA_9◦T_9GT_9 in sodium chloride and no decrease in absorbance at 295 nm was measured. This finding is a supportive evidence for formation of *i*-motif DNA when C and G-rich oligonucleotides interact together in buffer solutions and probably even in water.

Figure 6.28 UV-melting curve of $G_9PcG_9{\circ}C_9GC_9$

UV-melting curves at 260 and 295 nm of $G_9PcG_9{\circ}C_9GC_9$ in water, buffers A (0.049 M sodium phosphate and 0.1 sodium chloride) and buffer D (0.1 M sodium chloride)

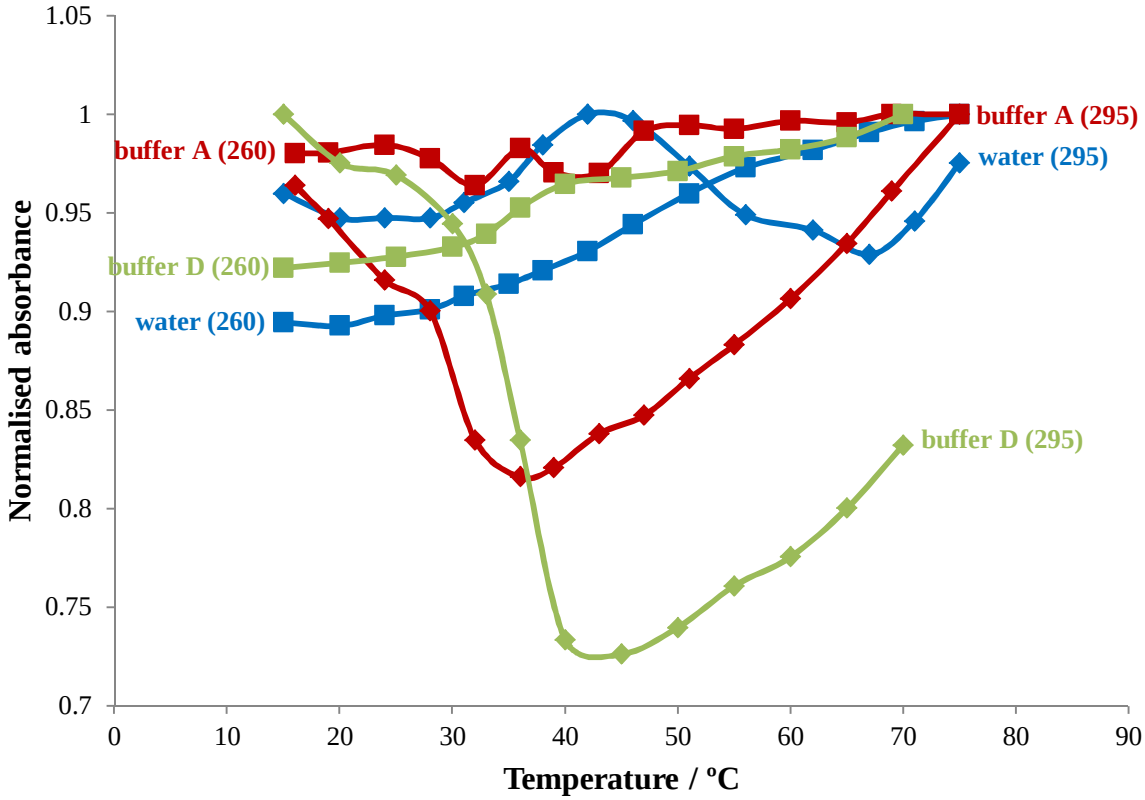

Figure 6.29 Four stranded nucleic acid (G_9PcG_9 and C_9GC_9)

A hypothetical four stranded structure in which C bases are based-paired to G bases

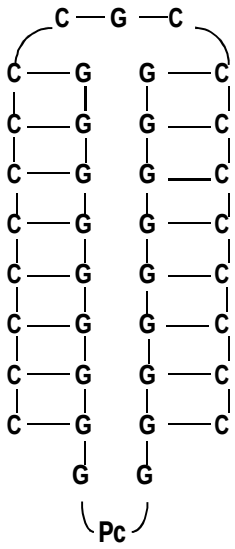

Figure 6.30 UV-melting curve of $A_9PcA_9 \circ T_9GT_9$

UV-melting curve at 260 and 295 nm of A_9PcA_9 T_9GT_9 in buffer D (0.1 M sodium chloride)

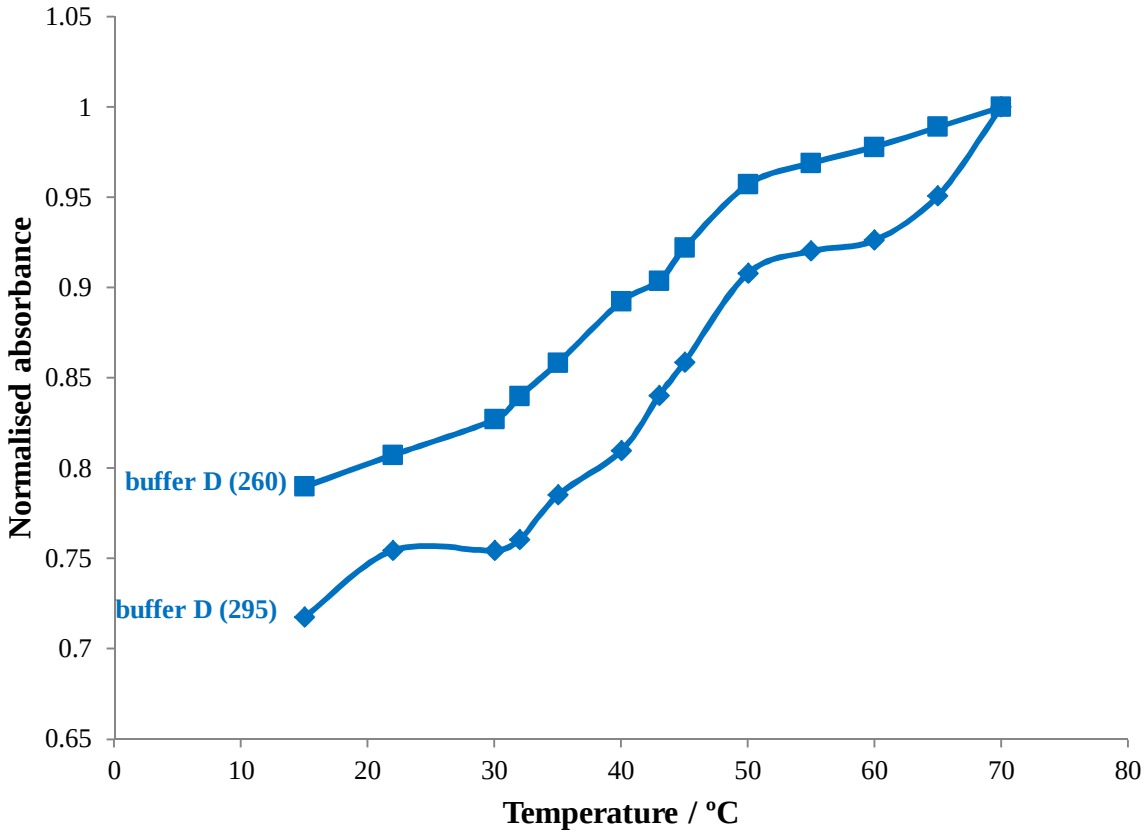

6.5 Fluorescence melting curve

In principle, the higher sensitivity of fluorescence can be exploited, instead of absorbance, to obtain melting profiles of DNA samples. Fluorescence emission of G_92ApG_9 in water and buffer C (50 mM sodium phosphate) were monitored as a function of temperature and normalised. Previous experiments showed that the fluorescence of the probe incorporated into a G-rich oligonucleotide is not reduced because of collisions with phosphate ions acting as dynamic quenchers but on the contrary the fluorescence of G_92ApG_9 is increased in buffers see Table 6.5 and Figure 6.19. Thus, the purpose of this experiment is to observe drastic changes in fluorescence of the oligonucleotide in buffer as the temperature increases relatively to the fluorescence measured in water. The fluorescence melting curves, see Figure 6.31, clearly show a greater decrease in fluorescence intensity emission in sodium phosphate than in water.

Figure 6.31 Fluorescence melting curve of $G_9$2ApG_9

Fluorescence melting curves of $G_9$2ApG_9 in water and buffer C (50 mM sodium phosphate). Fluorescence normalised to 1 at 80 °C

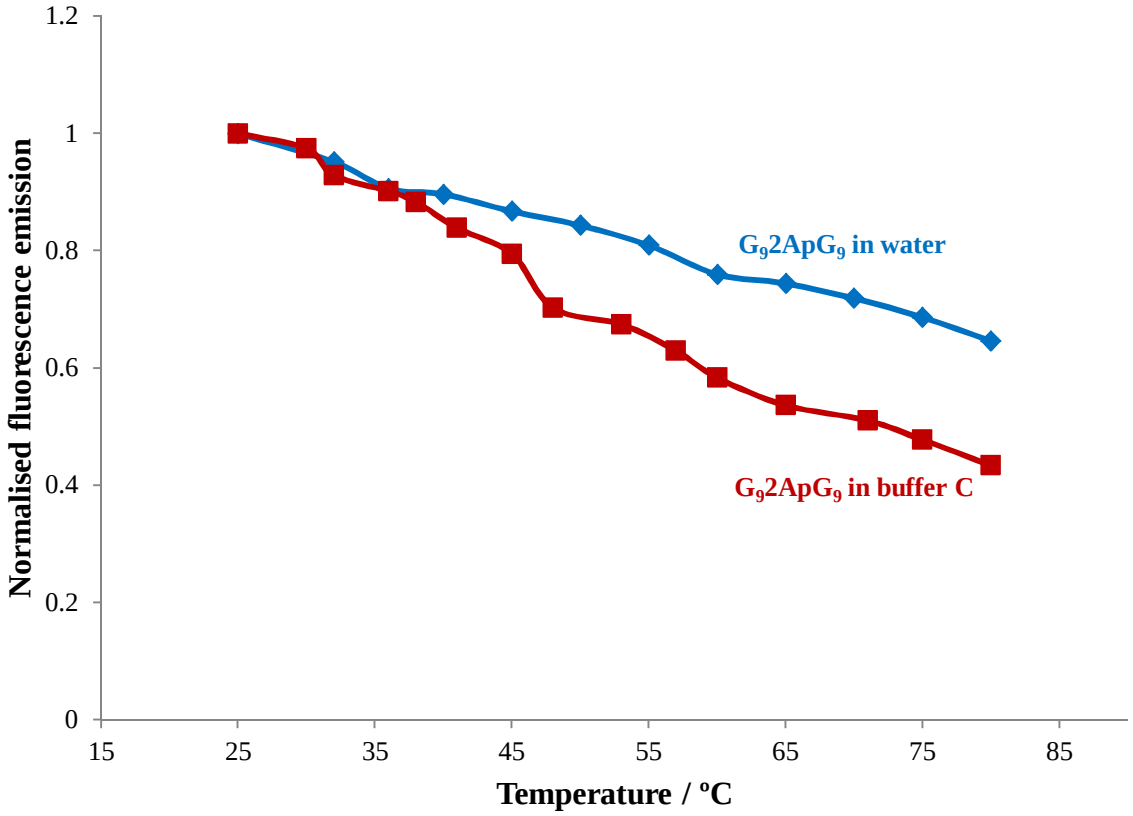

The discrepancy in fluorescence emission intensity between the two $G_9$2ApG_9 samples is visible after 40 °C as shown in the figure. This change in fluorescence may be interpreted in two different ways. The first assumption is the following: the two oligonucleotides have different structures in water and sodium phosphate, because of formation of secondary structures in buffers (even though UV-melting profiles did not show any particular difference between them), and at higher temperatures the unfolding of this secondary structure would expose 2-Ap to sodium phosphate and therefore, to collisional events with the quencher. Whereas the second assumption is the following: the structure of the oligonucleotides in water and sodium phosphate are identical but in the case of the buffer, the sodium phosphate ions would accommodate themselves into the oligonucleotides grooves, affecting the stacking of the bases at low temperature, and behave as dynamic quenchers at higher temperatures when they are no longer fitted into the oligonucleotide grooves. Then, in other words, the buffers may act as a fluorescence booster at room temperature by affecting the stacking and shielding the probe of the oligonucleotide, favouring fluorescence, and act as a fluorescence

quencher at higher temperatures when the 2-Ap is no longer shielded within the oligonucleotides.

6.6 Introduction to Circular Dichroism (CD)

CD is a spectroscopy technique which can be employed to gain information on DNA secondary structures. Unlike UV-visible absorption spectroscopy which can be used to collect absorption bands of the natural DNA bases, no CD signal can be collected from the natural bases themselves. The natural bases have a plane of symmetry and because of their symmetry they are not intrinsically optically active. A molecule can generate CD signals if it is optically active only. The sugars, deoxyribose and ribose, attached to the nucleobases are asymmetric inducing a circular dichroism in the absorption bands. In the case of oligonucleotides, the stacking of the bases coupled to formation of hydrogen bonding between bases (double-stranded oligonucleotides) render the whole molecule a super asymmetric molecule whose CD signals depend on the base-base interactions within the molecule itself. Thus, the CD spectra can be extremely sensitive to nucleic acid secondary structures (Berova *et al*. 2000).

6.6.1 Results and discussion

The available CD reference spectra of nucleic acids are specifically used for CD studies on telomeric DNA sequences. The closest DNA sequence to $G_9$2ApG_9 found is that of a G polynucleotide, precisely a deoxyribose G_{12}. The CD spectrum of G_{12} taken from the literature (Balagurumoorthy *et al.* 1992) is presented above in Figure 6.32 with its characteristic CD features edited into the spectrum. The CD signals of G_{12} were measured in sodium phosphate buffer and the positive and negative peaks along with the cross-over points (see Figure 6.32) obtained are characteristic features of a parallel quadruplex G polynucleotide (Balagurumoorthy *et al.* 1992).

These CD features of G_{12} are the following:

Positive peaks: **261-262 nm**

Negative peaks: **241-242 nm**

Cross-over points: **222-223 nm** and **247-248 nm**

Figure 6.32 CD spectrum of G_{12}

CD spectrum of deoxyribose G_{12} in sodium phosphate displayed as –– – – —. Pertinent features are highlighted (taken from Balagurumoorthy *et al.*, 1992)

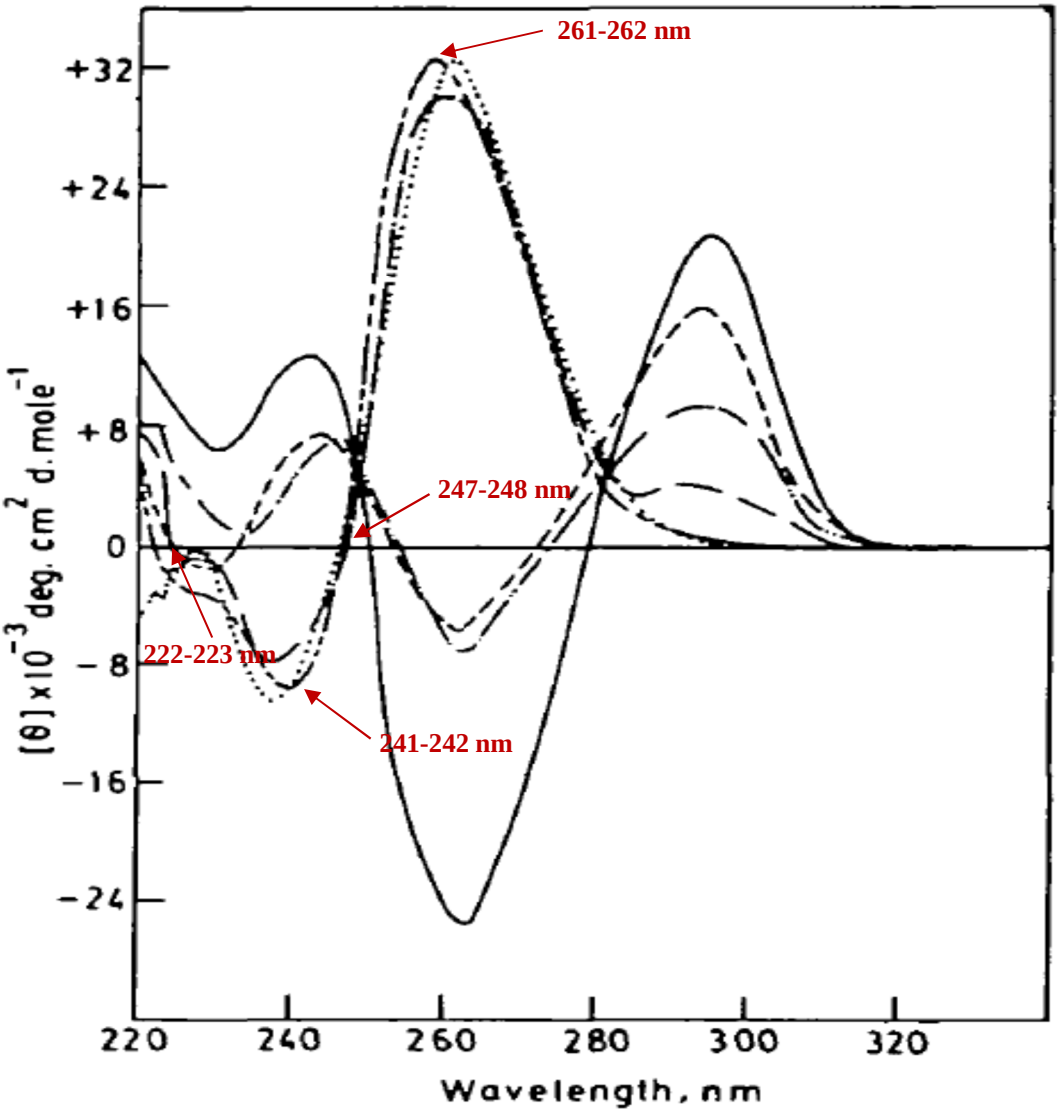

The CD spectra of $G_9$2ApG_9 in water and sodium phosphate buffers, buffer B and C, are shown in Figure 6.33. No significant difference is found between the CD spectra therefore, no polymorphic changes were observed when the concentration of sodium ions was increased. Thus, any spectrum can be used to be compared to the reference spectra of G_{12}.

Figure 6.33 CD spectra of $G_9$2ApG_9

The CD spectra of $G_9$2ApG_9 in water ——, buffer B (5 mM sodium phosphate) – – – and buffer C (50 mM sodium phosphate) ——, pertinent features are highlighted

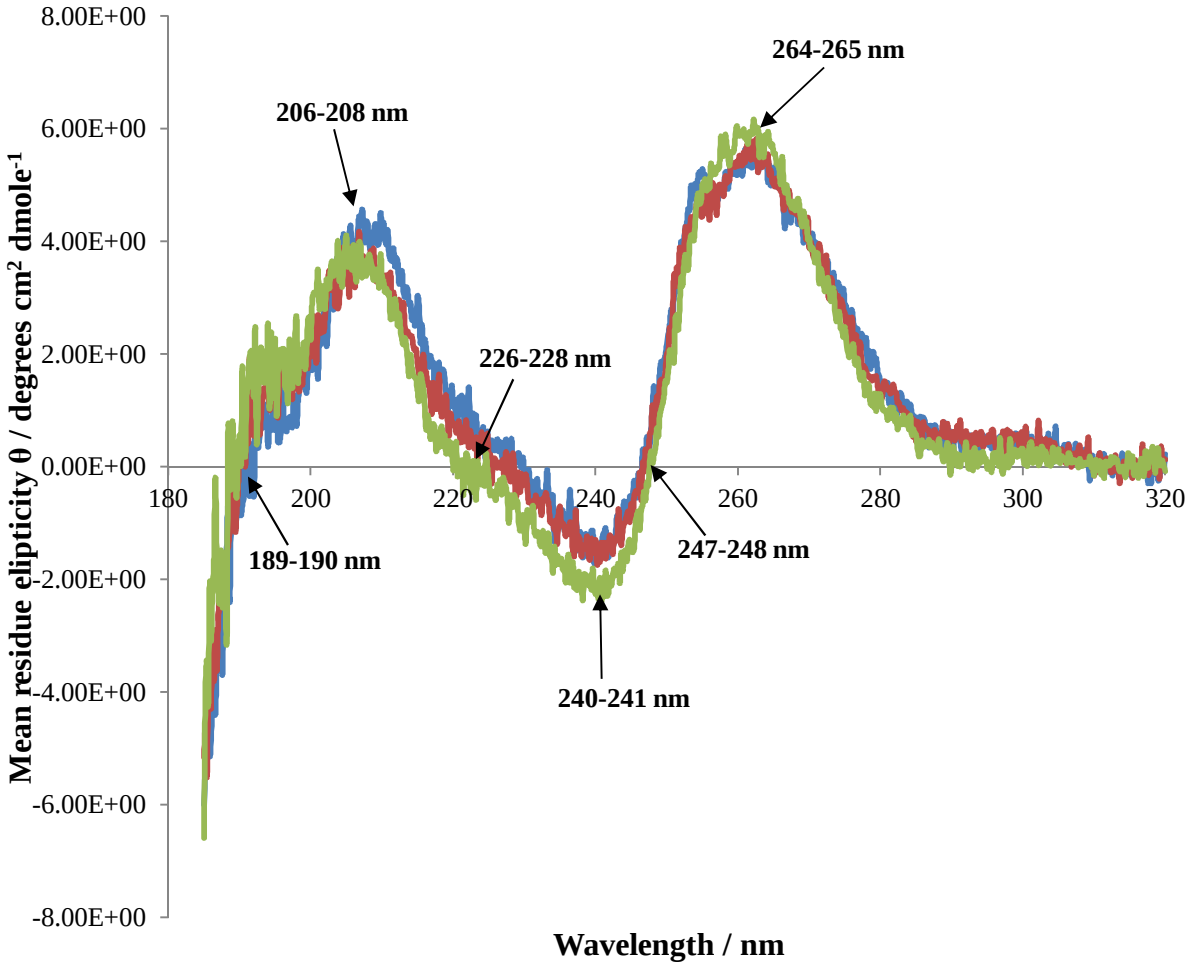

The CD features of $G_9$2ApG_9 are the following:

Positive peaks: **206-208 nm** and **264-265 nm**

Negative peaks: **240-241 nm**

Cross-over points: **189-190 nm**, **226-228 nm** and **247-248 nm**

The maxima wavelengths of the peaks and the cross-over points of the CD spectra of $G_9$2ApG_9 are closely similar to the ones of the CD spectrum found in the literature G_{12}, except for the positive peak at 206-208 nm and the cross-over points at 189-190 nm which cannot be compared with the literature spectrum because of the shorter scale adopted of the published CD spectrum. It is very important to notice that even if this positive peak was not included in the literature spectrum, it is expected to be around 7-8 (mean residue elipticity θ / degrees cm^2 $dmole^{-1}$) by considering the trend of the spectrum. Then, this measurement would be circa 4 times smaller than the other positive peak of the CD spectrum of G_{12} occurring at 260-261 nm, which is around 32. Whereas, in the case of $G_9$2ApG_9 the height of the positive peak at 264-265 nm is slightly bigger, circa 6, than the positive peak at 206-208 nm, which was found to be approximately 4 in height. Then, from a relative point of view the CD features of $G_9$2ApG_9 would not match the ones of G_{12} and therefore, conclusive answers cannot be given. Also, the fact that the CD spectrum of $G_9$2ApG_9 in water is practically identical to the CD spectra in buffer solutions makes the interpretation of the CD data complicated, because formation of G-quadruplex (in this case a parallel G-quadruplex, assuming the data obtained match the ones of the literature) in water should not be expected.

6.7 Introduction to steady-state anisotropy

Anisotropy is a physical chemistry term that means having properties that differ according to the direction of measurement. When polarized light is used to irradiate a sample, the emission from it is also polarized. The magnitude of polarized light is described in terms of anisotropy. This can be explained by the fact that fluorophores possess transition moments for absorption and emission of light which lie along specific directions within the fluorophores themselves. Fluorophores absorb polarized light (in a homogeneous solution the ground-state fluoroprobes are randomly orientated) with electronic vectors aligned or parallel to their transition momenta. When small fluorophores in solution of low viscosity are analysed, their emission is typically depolarized or partially depolarized. This, because the rate of rotational diffusion during the lifetime of the ground excited state fluorophores is much faster than the rate of emission. Therefore as a consequence of high rotational diffusion, anisotropy (r) measurements become close to 0. Anisotropy measurements can provide information on the size and shape of macromolecules or the rigidity of molecular environments. The extent of depolarization is calculated by determining the intensity of light emitted parallel, $I_{\parallel}$ (S_V), and perpendicular, $I_{\perp}$ (S_H), with respect to the excitation light.

6.7.1 Measuring anisotropy

Anisotropy measurements were collected using an L-format method because the fluorimeter used has one emission channel only. The Figure 6.34 shows an L-format or single-channel method.

Figure 6.34 L-format or single-channel method

A Schematic diagram of an L-format or single-channel method to collect fluorescence anisotropy. The polarizers illustrated are placed in such a way that vertically (V) and horizontally (H) polarized light can be measured

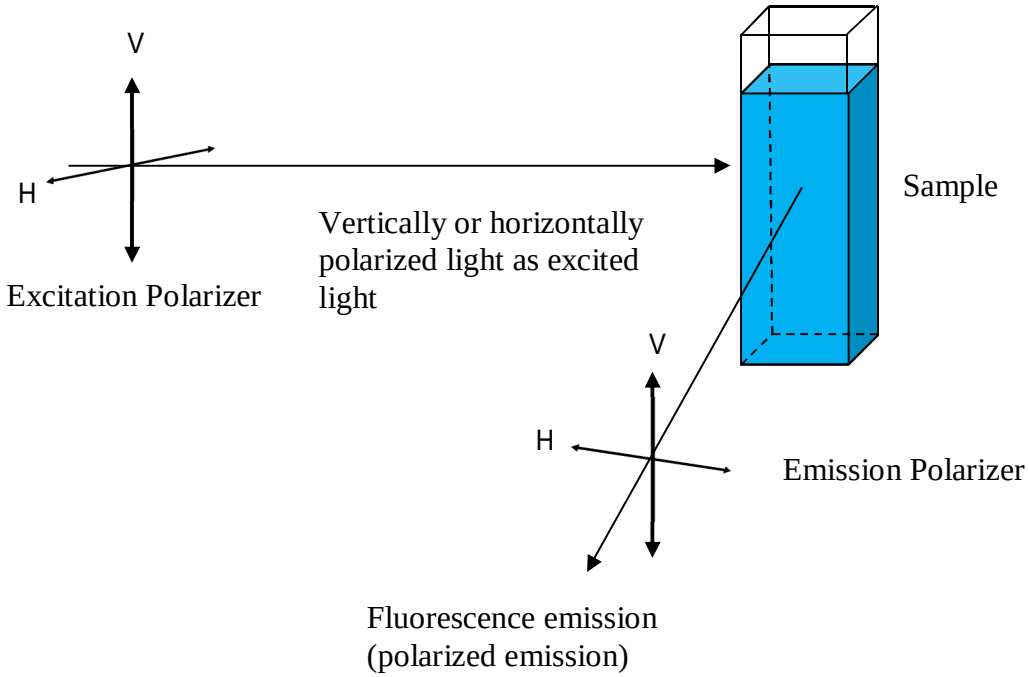

For example, the sample is excited with vertically polarized light I_V, the emission intensity is collected as vertically polarized light and horizontally polarized light respectively, I_V and I_H. Therefore, the following emission intensities I_{VV} and I_{VH} are measured. Knowing this, the anisotropy (r) is defined by the following formula:

$$r = \frac{I_{vv} - GI_{vh}}{I_{vv} + 2GI_{vh}} \quad (6.3)$$

G is a correction factor that accounts for the different sensitivities of the vertically and horizontally polarized components and therefore, it corrects for efficiency differences within instrument optics. The G factor is measured through the following ratio:

$$G = \frac{I_{hv}}{I_{hh}} \quad (6.4)$$

6.7.2 Discussion and results

According to Tinsley and Walter (Tinsley and Walter, 2004) steady-state anisotropy can allow to monitor the incorporation of the small fluoroprobe Pc into a large oligonucleotide (they studied an oligonucleotide of 22 bases. Pc is centrally located within the oligonucleotide) because the probe would become increasingly immobile from a free base, to a single and double-stranded oligonucleotide, presumably due to a combination of more local stacking interactions and slower rotational diffusion of the larger oligonucleotides. They measured the following anisotropies in buffer solutions (at 25 ºC) at the following excitation wavelengths:

0.06 for the free base Pc (353 nm)

0.13 for the Pc single-stranded oligonucleotide (352 nm)

0.20 for the Pc double stranded oligonucleotide (351 nm)

(It should be noted that the maximum excitation they used for the free base is not in agreement with the one reported herein, which was observed between 335 and 337 nm, see Table 6.1). They observed an increase in anisotropy by circa three times from the free base to the duplex. The Table 6.6 shows anisotropy measurements of Pc, GPcG, G_9PcG_9 and $G_9PcG_9{\circ}C_9GC_9$ in water and buffer A as a function of temperature.

Table 6.6 Anisotropy measurements of Pc as free base and oligonucleotides

Anisotropy measurements of Pc, GPcG, G_9PcG_9 and $G_9PcG_9{\circ}C_9GC_9$ in water and buffer A collected at 20, 40, 60 and 80 °C. The maxima excitation wavelengths used to excite the molecules can be found in table 5.1 and 5.2)

Compound analysed	Anisotropy measurements (r) at different temperatures			
	20 ˚C	40 ˚C	60 ˚C	80 ˚C
Pc water	**0.0054**	**0.0049**	**0.0039**	**0.0037**
Pc buffer A	**0.0075**	**0.0074**	**0.0069**	**0.0041**
GPcG water	**0.0524**	**0.0298**	**0.0274**	**0.0242**
GPcG buffer A	**0.0711**	**0.0588**	**0.0559**	**0.0496**
G_9PcG_9 water	**0.1975**	**0.1580**	**0.1352**	**0.1050**
G_9PcG_9 buffer A	**0.2189**	**0.1695**	**0.1370**	**0.1010**
$G_9PcG_9{\circ}C_9GC_9$ water	**0.2239**	**0.1614**	**0.1041**	**0.0894**
$G_9PcG_9{\circ}C_9GC_9$ buffer A	**0.2506**	**0.1936**	**0.1463**	**0.1185**

The anisotropy measurements contained in the Table 6.6 are all within the theoretically acceptable anisotropy values (anisotropy measurements should always be within 0.40 and -0.20. Any anisotropy measurement outside this range of values must be considered as an unacceptable measurement usually due to unwanted light or scattered light) (Lakowicz, 1999). By no means should the measurements in Table 6.6 be considered as absolute anisotropy measurements of Pc because anisotropy is very sensitive to temperature, (as shown in the table anisotropy decreases as the temperature of the solution increases, because the probe would rotate/move much faster and therefore, the emitted light becomes increasingly depolarized), the solvent used (the anisotropy collected in buffer A is visibly bigger than the one collected in water) and up to a certain extent to the excitation wavelength used, thus these data herein serve to compare changes in anisotropy as the structure of the molecules containing the probe becomes bigger. The measurements obtained are relatively different compared to the ones obtained by Tinsley and Walter. First of all, the anisotropy of the free base Pc is relatively very small compared to the anisotropy of the duplex (or any another possible secondary structure), 40 or even 50 times smaller in both water and buffer. The anisotropy of the trinucleotides is about 4-5 times smaller than the duplexes. A slight increase in anisotropy was observed between the presumably sluggish duplexes and the faster single-stranded oligonucleotides, but this difference is not as big as the one recorded by Tinsley and Walter. Overall, the buffer causes the probe to rotate/move slower than in water. This may be due to an increase in rigidness of the probe exposed to buffer solvents or simply the environment in which the probe is exposed becomes more viscous. Similar results were found for 2-Ap. The anisotropy measurements of 2-Ap as free base and incorporated into oligonucleotides are summarized in the Table 6.7. Once again, all the anisotropy measurements obtained are bigger in buffer than in water and even a smaller increase in anisotropy was measured between the duplexes and the single-stranded oligonucleotides. To conclude, anisotropy is an efficient technique at differentiating small molecules from large molecules, but it seems to fail at differentiating molecules which are relatively closer in size. This conclusion was not dictated by the small difference observed between the double and single-stranded oligonucleotides (because they may fold into unpredictable conformations, not just the canonical DNA structures but even other secondary structures such as G-quadruplexes or *i*-motifs for example a four stranded structure may be formed), but by the small difference in anisotropy between the trinucleotides and the free bases.

Table 6.7 Anisotropy measurements of 2-Ap as free base and oligonucleotides

Anisotropy measurements of 2-Ap, G2ApG, $G_9$2ApG_9 and $G_9$2ApG_9◦C_9GC_9 in water and buffer C collected at 20, 40, 60 and 80 ºC. The maxima excitation wavelengths used to excite the molecules can be found in tables 5.3 and 5.5

Compound analysed	Anisotropy measurements (r) at different temperatures			
	20 ˚C	40 ˚C	60 ˚C	80 ˚C
2-Ap water	**0.0032**	**0.0028**	**0.0026**	**0.0024**
2-Ap buffer A	**0.0099**	**0.0088**	**0.0078**	**0.0062**
G2ApG water	**0.0087**	**0.0071**	**0.0069**	**0.0069**
G2ApG buffer A	**0.0161**	**0.0147**	**0.0135**	**0.0131**
$G_9$2ApG_9 water	**0.1764**	**0.1437**	**0.1119**	**0.0766**
$G_9$2ApG_9 buffer A	**0.1982**	**0.1533**	**0.1241**	**0.1075**
$G_9$2ApG_9◦C_9GC_9 water	**0.1871**	**0.1524**	**0.1186**	**0.0812**
$G_9$2ApG_9◦C_9GC_9 buffer A	**0.2062**	**0.1616**	**0.1342**	**0.1204**

6.8 Summary and concluding remarks

The fluorescence emission of Pc and 2-Ap as free bases and incorporated into oligonucleotides in water and different buffers can dramatically differ due to many different factors. This section briefly summarized the findings reported in this chapter:

- Pc fluorescence intensity is depressed when the probe is attached to both deoxyribose and ribose sugar groups whereas the fluorescence of 2-Ap_{dr} appears to be enhanced compared to free base.
- The fluorescence emission of 2-Ap free base and 2-Ap_{dr} is strongly quenched by phosphate ions, almost certainly because of dynamic quenching. The fluorescence of Pc seems to be almost unaffected by phosphate ions.
- Pc fluorescence is slightly reduced when incorporated into a trinucleotide (GPcG) whereas incorporation of 2-Ap into the same trinucleotide (G2ApG) causes a very large decrease in fluorescence compared to free probe even in water.
- When both 2-Ap and Pc are incorporated into G-rich single-stranded oligonucleotides their fluorescence is more intense in buffers than in water. The same trend was observed for the double-stranded oligonucleotides.
- The maxima excitation wavelengths of Pc is blue-shifted compared to the excitation maxima of Pc when incorporated into oligonucleotides or even when only attached to sugar groups. In the case of 2-Ap the measured maxima excitation wavelengths was the same except for the duplexes, which require longer wavelengths.
- The UV-melting curves of $G_9$2ApG_9 and G_9PcG_9 in both water and buffers did not show any decrease in absorbance at 295 nm, peculiar to G-quadruplexes. On the contrary a large hypochromicity at 295 nm was recorded for the melting of the duplexes which may be indicative of four stranded structures.
- The CD spectra of $G_9$2ApG_9 in buffers and water appear to be the same, indicating no particular polymorphic change in the oligonucleotide structure from water to buffer solutions.
- Steady-state anisotropy measurements of free bases and oligonucleotides are higher in buffers than in water. This finding is consistent with a smaller decrease in depolarized light of the probes in buffers, probably attributable to a more viscous environment, which would render the probes more rigid and therefore more sluggish.

As reported by Ward and coworkers (Ward *et al.* 1969) 2-Ap becomes non-fluorescent in acidic environments. Therefore, measuring the fluorescence of 2-Ap as free base and incorporated into oligonucleotides as a function of pH, may provide suggestive information on how the probe may shield itself from the solvent when incorporated into oligonucleotides.

Fluorescence lifetimes of 2-Ap as free base and oligonucleotides in buffer solutions should be collected to confirm that the base undergoes dynamic quenching in presence of quenching agents such as phosphate ions. Also, since it was found out that phosphate ions act as 2-Ap fluorescence quenchers, most likely due to dynamic quenching (although only sodium phosphate buffers at pH 7 were tested) then, it would be interesting to know whether K_{SV} remains constant as a function of pH or not. Time-resolved measurements can reveal structural information on the oligonucleotides studied that are usually obscured in steady-state measurements. It was showed through measured fluorescence decay data that 2-Ap incorporated into a DNA helix may be resolved into four distinct species (Nordlund *et al*. 1989; Guest *et al*. 1991). The biggest populations of the resolved species represent well-stacked base pair conformations whereas smaller populations are indicative of unstacked and partially stacked 2-Ap bases. Since time-resolved measurements not only can resolve different base stacked species, but also allows the determination of changes in the relative populations. Thus, time-resolved measurements may be used to elucidate the formation of secondary structures besides duplexes such as *i*-motifs. NMR is a powerful spectroscopic technique that has been used widely used to investigate the structure of nucleic acids. ^{1}H NMR is used for the study of oligonucleotides in aqueous buffers with water suppression in conjunction with ^{31}P NMR to study the nucleic acid phosphodiester backbone properties. If from one hand NMR is very efficient at investigating the nucleic acid structures at the local level, therefore, powerful at discerning duplexes, triplexes, quadruplexes, hairpin loops and other secondary structures (Phan *et al*. 2001; Phan *et al*. 2002), on the other hand, NMR is less efficient at giving information on global properties, for example the existing structural differences between DNA A and B helixes or DNA duplex bending (Wijmenga and van Buuren, 1998). Then, NMR would prove to be a perfect technique to be used in conjunction with the melting profiles obtained to attest the formation of *i*-motifs, specifically triplexes or four stranded oligonucleotides. The only main downside of NMR is its low sensitivity thus, NMR samples must be highly concentrated. DNA structures can also be determined by crystallization and X-ray diffraction. In the present, a large number of oligonucleotides are being crystallized. When a crystal is irradiated with X-ray light a diffraction pattern is generated from which, with the combination of mathematical calculations, a three dimensional picture is obtained. But as in the case of NMR, highly concentrated solutions of oligonucleotides are necessary to provide a thermodynamic driving force required for crystal formation. In most cases the resolution of the structure of the oligonucleotides may appear poor because it does not extend beyond 2 Å (0.2 nm), but it sufficient to point out the

structural features of the heterocyclic bases and sugar-phosphate backbone (Egli, 2004). Intercalates such as ethidium bromide and its derivatives can be used to discriminate single-stranded oligonucleotides from duplexes, G-quadruplexes and other secondary structures. Ethidium bromide is a reagent which can intercalate DNA. Precisely, it intercalates double-stranded oligonucelotides and other secondary structures by inserting itself between the stacked bases. Ethidium bromide is a fluorescent molecule and it emits in the visible range 500-700 nm, and the intensity is variable depending on the secondary structure encountered (for example Ethidium bromide intercalating duplexes emits strongly compared to G-quadruplexes). A fluorescence emission region which greatly differs from the one of 2-Ap and Pc (320-500 nm), therefore the fluorescence of ethidium bromide and derivatives can be selectively collected (Koeppel *et al*. 2001; Reha *et al*. 2003). Then, these chemicals may help understand why G_9PcG_9 and G_92ApG_9 have different fluorescence intensities in water and buffers.

Chapter 7 General conclusions and future work

Watson and Crick in their seminal paper published in 1953 highlighted the importance of pyrimidine and purine bases to occur in their most canonical or plausible tautomeric forms (the amino and keto forms) in order to form a correct matching between bases *via* hydrogen bonding formation (Watson and Crick, 1953). However, a decade later rare tautomeric forms were hypothesized which may occur *via* proton exchange (Löwdin, 1963). Precisely, proton exchange may promote the formation of enol and imino tautomers which can cause mismatched-base pairing which may trigger mutations during DNA replication (Topal and Fresco 1976; Harris *et al*. 2003; Rothwell and Waksman, 2005; Wang *et al*. 2011). The modified nucleobases 2-aminopurine (2-Ap) and pyrrolocytosine (Pc) are fluorescent probes which replace adenine and cytosine respectively without disrupting the chemical environment in which natural nucleobases exist (Millar, 1996; Jameson and Eccleston, 1997; Rist and Marino, 2002). Thus, the fluorescence properties of these bases which act as potent base substitution mutagen, can be used to recognise mismatched base pairing (Lawrence *et al*. 1986; Reha-Krantz *et al*. 2011).

Solvation studies of 2-aminopurine (2-Ap) and pyrrolocytosine (Pc) have shown that the nature of solvents, in particular their polarity and ability to form hydrogen bonds with the solute molecules, can have a profound impact on the emission fluorescence of the base. Generally, polarity appears to increase fluorescence emission with the exception of Pc in water which has a very low quantum yield with respect to the quantum yield measurements obtained in other solvents. Also, the larger Stokes shift of both bases in water indicates that hydrogen bonding formation plays a characteristic role as a function of spectroscopic displacements as reported in Chapter 3. The polarity of the solvent and its ability to form hydrogen bonds can affect the tautomeric equilibrium mainly due to the different hydrogen bond patterns the solvent molecules can undergo with the natural bases. In fact, X-ray studies on oligonucleotides which carry mismatched-base pairs, suggest that water may have a stabilizing effect on the mismatched-base pairs by promoting the formation of favourable interactions with hydrophilic regions of the nucleobases (Kennard, 1985).

DFT studies presented in Chapter 4 revealed that the most stable tautomers of 2-Ap in polar and non-polar solvent is an amino tautomer (N9H amino tautomer) whereas in the case of Pc the most stable geometry was found to be a keto tautomer (N1H N9H keto tautomer) in solution and an enol tautomer (N1H N9H enol tautomer) in vacuum. The Figure 7.1 shows

the standard and anomalous pairings of the natural bases and the proposed standard and anomalous pairings of the fluorescent bases.

Figure 7.1 Standard and anomalous base pairings

This figure illustrates the formation of hydrogen bonds between complementary bases in their canonical forms (standard pairings) and the formation of hydrogen bonds involving rare tautomers, specifically imino and enol ones (anomalous pairings)

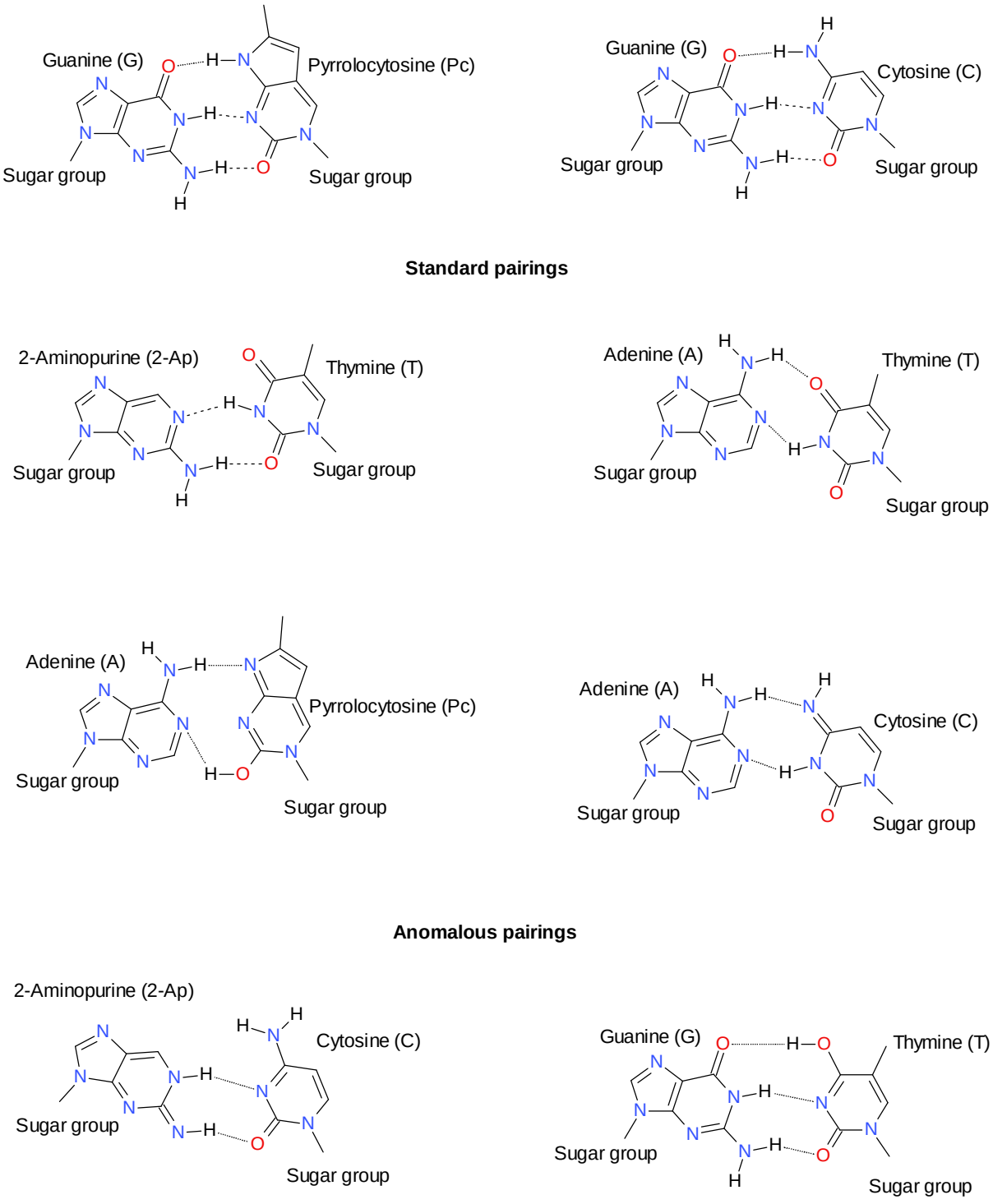

The predicted singlet and triplet vertical transition energies have revealed that in the case of 2-Ap fluorescence quenching in solvents having low dielectric constant may not only be attributable to their low polarity or incapability to form hydrogen bonds with solute molecules, but also due to a combination of vibronic coupling and efficient intersystem crossing (ISC). Also, DFT predicted a planar amino group geometry of 2-Ap N9H amino tautomer in its excited state (S_1) with respect to the purine ring whereas the amino group was found to be pyramidal when the fluorescent probe is in its ground state (S_0). The planarity of the amino group of the molecule in its first excited state may facilitate radiative processes in particular fluorescence over non-radiative processes such as intersystem crossing (ISC) and internal conversion (IC).

Although computational methods can be used to predict the most stable tautomer of 2-Ap and Pc, more than one tautomer can be present in solution and different tautomers may have different proportions and lifetimes (Neely *et al*. 2004). Therefore, it is essential to understand the different emitting properties of the possible tautomeric forms of the bases if they were to be used as base substitution mutagen in order to recognise mismatched-base pairs. The existence and proportion of tautomeric forms of 2-Ap and Pc can be assessed by various spectroscopic techniques beyond infrared spectroscopy (a technique which failed to differentiate tautomeric species because of the hygroscopic nature of the solvents used as mentioned in Chapter 5). For instance, in the case of Pc, its enol and keto tautomeric forms can be discerned by proton NMR. In fact, the very rapid hydroxyl proton exchange of the hydroxyl group with adding the deuterium of water (heavy water) to the sample in chloroform D can be exploited to assign hydroxyl proton resonance signals as described in the shown chemical equation:

$$\mathbf{R\text{-}O\text{-}H + D_2O \rightleftharpoons R\text{-}O\text{-}D + D\text{-}O\text{-}H} \quad \mathbf{(7.1)}$$

Thus, by removing the hydroxyl proton its resonance signal disappears in the proton NMR spectrum. Also the sensitivity of the hydroxyl proton resonance signal can be used to hydrogen bonding formation (Lin and Frey, 2000; Antonov, 2013)

Elucidation of tautomer structures of Pc in gas phase may be achieved by using the combined techniques gas chromatography/mass spectrometry. Mass spectrometry has shown to be a

useful technique for the study of tautomerism of organic molecules because the electron ionization process seems not to affect the tautomeric equilibria. In fact, it has been demonstrated that the exchange of enolizable hydrogen atoms for deuterium atoms occurs in the inlet system of a mass spectrometer; thus, the keto-enol equilibrium is established in the inlet system (Karliner *et al*. 1965). Besides this, the tautomeric system in the gas phase is not affected by external factors such as solvent effect and intermolecular interactions (hydrogen bonds). In other words, the system becomes unimolecular (Terent'ev and Kalandarishvili, 1996). The estimation of the keto-enol equilibra by gas chromatography and mass spectrometry was found to be in line with results obtained through semiempirical calculations, specifically the Austin Model 1 (AM1) (Allegretti *et al*. 2007).

Although many factors such as the nature of the solvent and hydrogen bonding formation may contribute to changes in fluorescence emission of 2-Ap it was found that the fluorescence of this particular base is extremely sensitive in some buffers as opposed to others. Buffer made of phosphates, for example sodium phosphate, can drastically reduce the fluorescence emission of the fluorophore, almost certainly due to dynamic quenching or collisional quenching described and explained in both Chapter 2 and 6 of this thesis.

Time-resolved fluorescence lifetime measurements are usually obtained by Time-Correlated Single-Photon Counting (TCSPC). This is a very sensitive method to measure fluorescence lifetimes because the molecules are excited by pico/femtosecond lasers (the lifetime of 2-Ap in water was found to be in the range of 11-12 ns) (Holmen *et al*. 1997; Neely *et al*. 2004). The excitation and subsequent emission process is repeated many times (usually up to 10,000 counts in the peak channel). The plotting of the data generates a histogram which describes the number of events (the count of the individual photons) against time. If the fluorescence lifetime of the bases is much longer than the excitation pulse then the logarithm of the emission intensity is plotted against time and the lifetime is measured as the slope of the resulting linear fit. On the other hand, if the fluorescence lifetime of the bases is shorter than the excitation pulse the emission lifetime is measured through the least squares iterative reconvolution method (Lampert *et al*. 1983; Gratton *et al*. 1984; Hungerford and Birch, 1996).

The data reported in Chapter 6 show that the quantum yield measurements of both bases when incorporated into oligonucleotides in water and buffers solutions were found to be smaller than the ones previously measured of free bases, but the decrease in fluorescence is

more pronounced in water. The difference in fluorescence depression of 2-Ap and Pc G-rich oligonucleotides in water and buffer solutions may be due to secondary structure formations in presence of stabilizing metal ions which can coordinate structures such as G-quadruplexes, but UV-melting curves and CD did not reveal any particular polymorphic change in the single-stranded oligonucleotides (structural change) when measurements were collected in both water and buffers. In contrast, the UV-melting curves of the bases incorporated into G-rich duplexes revealed a large hypochromicity at 295 nm (decrease in absorbance as a function of temperature) which may be indicative of four-stranded structures.

Although X-ray crystallography is one of the most accurate method for structure determination, a very laborious preparation of the crystals of Pc and 2-Ap incorporated into oligonucleotide is necessary to form suitable and small crystals (0.1-0.5 mm) (Egli, 2004), X-ray crystallography offers the possibility of obtaining structural information on higher DNA secondary structures. For instance, human telomeric G-quadruplexes were revealed through X-ray crystallography snapshots in at least nine different conformations (Parkinson *et al*. 2002; Dai *et al*. 2007; Lim *et al*. 2009; Heddi and Phan, 2011). Thus, the structures of possible G-quadruplexes or four-stranded oligonucleotides (as mentioned in Chapter 6) may be revealed using the fluorescence properties of 2-Ap and Pc for comparative studies such as detection of conformational and discrimination of these structures. Assessing the conformational changes of higher secondary structures of DNA may represent a key to many biological processes such as: chromosome replication (Schaffitzel *et al*. 2001; Paeschke *et al*. 2005), cellular senescence (Collado *et al*. 2007; Ruzankina *et al*. 2008) and molecular recognition (Shafer and Smirnov, 2000).

References

Abe, H., Abe, N., Shibata, A., Ito, K., Tanaka, Y., Ito, M., Saneyoshi, H., Shuto, S. & Ito, Y., (2012). **Structure Formation and Catalytic Activity of DNA Dissolved in Organic Solvents.** Angewandte Chemie International Edition 51, 6475-6479.

Alev-Behmoras, T., Toulme, J. J and Helene, C., (1979). **Effect of Phosphate Ions on the Fluorescence of Tryptophan Derivatives.** Biochimie 61, 957-960.

Allegretti, P. E., Schiavoni, M. M., Castro, E. A and Furlong, J. J., (2007). **Tautomeric Equilibria Studies by Mass Spectrometry.** World Journal of Chemistry 2, 25-62.

Andersson, K., Malmqvist, P. A and Roos, B. O., (1992). **Second-Order Perturbation-Theory with a Complete Active Space Self-Consistent Field Reference Function.** The Journal of Physical Chemistry 96, 1218-1226.

Anslyn. E. V and Dougherty. D. A., (2006). **Modern Physical Organic Chemistry.** University Science Books Sausalito, California.

Antonov, L., (2013). **Tautomerism. Methods and Theories.** John Wiley-VCH

Balagurumoorthy, P., Brahmachari, S. K., Mohanty, D, Bansal M and Sasisekharan, V., (1992). **Hairpin and Parallel Quartet Structure for Telomeric Sequences.** Nucleic Acids Research 20, 4061-4067.

Becke, A. D., (1988). **Density-Functional Exchange-Energy Approximation with Correct Asymptotic Behaviour.** Physics Review A 38, 3098-3100.

Becke, A. D., (1993). **Density-Functional Thermochemistry. III. The Role of the Exact Exchange.** The Journal of Physical Chemistry 98, 5648-5652.

Benight, A. S., Pancoska, P., Owczarzy, R., Vallone, P. M., Nesetril, J., Riccelli, P.V., (2001). **Calculating Sequence-Dependent Melting Stability of Duplex DNA Oligomers and Multiplex Sequence Analysis by Graphs.** Methods in Enzymology 340, 165-192.

Berova, N., Nakanishi, K and Woody R.W., (2000). **Circular Dichroism, Principles and Applications.** Wiley Second Edition Chapter 24-25.

Berry, D. A., Jung, K. Y., Wise, D. S., Saracel, A. D., Pearson, W. H., Mackie, H., Radolph, J. B and Somers, R. L., (2004). **Pyrrolo-dC and Pyrrolo-C: Fluorescent Analogs of Cytidine and 2'-Deoxycytidine for the Study of Oligonucleotides.** Tetrahedron Letters 45, 2457-2461.

Bevington, P. R., (1992). **Data Reduction and Error Analysis for the Physical Sciences.** McGraw-Hill Second Edition, London.

Black G., Chase J., Chatterton J., Daily J., Elsethagen T., Feller D., Gracio D., Jones D., Keller T., Lansing C., Matsumoto S., Palmer B., Peterson M., Schuchardt K., Stephan E., Sun L., Swanson K., Taylor H., Thomas G., Vorpagel, E., Windus T., Winters C., (2009). **Extensible Computational Chemistry Environment (ECCE), A Problem Solving Environment for Computational Chemistry. Software Version 6.0.** Developed and distributed by Pacific Northwest National Laboratory, P.O. Box 999, Richland, Washington 99352, USA.

Blancafort, J., (2006). **Excited-State Potential Energy Surface for the Photophysics of Adenine.** Journal of the American Chemical Society 128, 210-219.

Bondi, A., (1964). **Van der Waals Volume of Radii.** The Journal of Physical Chemistry A 68, 441-451.

Brand, L., Seliksar, C. J and Turner, D. C., (1971). **The Effects of Chemical Environment on Fluorescent Probes.** In Probes of Structure and Function of Macromolecules and Membranes, 17-39.

Broo, A., (1998). **A Theoretical Investigation of the Physical Reason for the Very Different Luminescence Properties of the Two Isomers Adenine and 2-Aminopurine.** The Journal of Physical Chemistry A 102, 526-531.

Callis, P. R., (1983). **Electronic States and Luminescence of Nucleic Acid Systems.** Annual Review of Physical Chemistry 34, 329-357.

Canuel, C., Mons, M., Piuzzi, F., Tardivel, B., Dimicoli, I and Elhanine, M., (2005). **Excited Sates Dynamics of DNA and RNA Bases: Characterization of a Stepwise Deactivation Pathway in the Gas Phase.** The Journal of Chemical Physics 122, 74316-74321.

Chachisvlis, M and Zewail, A. H., (1999). **Femtosecond Dynamics of Pyridine in the Condensed Phase: Valence Isomerization by Conical Intersections.** The Journal of Physical Chemistry A 103, 7408-7418.

Chen, H and Lin, S., (2006). **Theoretical Study on the Excitation Energies of Six Tautomers of Guanine: Evidence for the Assignment of the Rare Tautomers.** The Journal of Physical Chemistry A 110, 12360-12362.

Cherkasov, A. S., (1960). **Influence of the Solvent on the Fluorescence Spectra of Acetylanthracenes.** Akad Nauk SSSR Bulletin of Physical Sciences, 597-601.

Cockett, M and Doggett, G., (2012). **Maths for Chemists.** Royal Society of Chemistry Publishing Tutorial Chemistry Texts Second Edition.

Collado, M., Blasco, M. A and Serrano, M., (2007). **Cellular Senescence in Cancer and Aging.** Cell 130, 223-233.

Colthrup, N. B., Daly, L. H and Wiberley, S. E., (1990). **Introduction to Infrared and Raman Spectroscopy.** Academic Press, San Diego, CA 1-73.

Condon, E., (1926). **A Theory of Intensity Distribution in Band Systems.** Physical Review 28, 1182-1201.

Cramer, C. J., (2002). **Essentials of Computational Chemistry.** John Wiley & Sons.

Crespo-Hernandez, C., Cohen, B., Hare, P and Kohler, B., (2004). **Ultrafast Excited-State Dynamics in Nucleic Acids.** Chemical Reviews 104, 1977-2019.

Cui S., Yu J., Kühner F., Schulten K and Gaub H. E., (2007). **Double-Stranded DNA Dissociates into Single Strands when Dragged into a Poor Solvent.** Journal of the American Chemical Society 129, 14710-14716.

Dai, J., Punchihewa, C., Ambrus, A., Chen, D., Jones, R. A and Yang, D., (2007). **Structure of the Intramolecular Human Telomeric G-quadruplex in Potassium Solution: a Novel Adenine Triple Formation.** Nucleic Acids Research 35, 2440-2450.

Dhani, S., De Mello, A., Rumbles, G., Bishop, S., Phillips, D and Beeby, A., (1995). **Phthalocyanine Fluorescence at High Concentration: Dimers or Reabsorption Effect?** Photochemistry and Photobiology 61, 341-346.

Domke, W. E., Yarkony, R. D and Köppel, H., (2004). **Conical Intersections. Electronic Structure Dynamics and Spectroscopy.** Advances Series in Physical Chemistry 15. World Scientific Singapore.

Dong, F and Miller, R. E., (2002). **Vibrational Transition Moment Angles in Isolated Biomolecules: A Structural Tool.** Science 298, 1227-1230.

Downton, M. T and Wang, F., (2005). **Differentiation of Adenine Non-Planarity in Valence Molecular Orbitals.** Molecular Simulation 32, 667-673.

Draper, D. E., (2004). **A Guide to Ions and RNA Structure**. RNA 10, 335-343.

Dreyfus, M., Bensaude, O., Dodin, G and Dubois, J. E., (1976). **Tautomerism in Cytosine and 3-Methylcytosine. A Thermodynamic and Kinetic Study.** Journal of the American Chemical Society 98, 6338-6349.

Dunning, T. H., (2000). **A Road Map for the Calculation of Molecular Binding Energies.** The Journal of Physical Chemistry A 104, 9062-9080.

Egli, M., (2004). **Nucleic Acid Crystallography: Current Progress.** Current Opinions in Chemical Biology 8, 580-591.

El-Sayed, M. A., (1968). **The Triplet State: Its Radiative and Non-Radiative Properties.** Accounts of Chemical Research 1, 8-16.

Englman, R and Jortner, J., (1970). **The Energy Gap Law for Radiationless Transitions in Large Molecules.** Molecular Physics 18, 145-164.

Evans, K., Xu, D., Kim, Y and Nordlund, T. N., (1992). **2-Aminopurine Optical Spectra: Solvent, Pentose Ring and DNA Helix Melting Dependence.** Journal of Fluorescence 2, 209-216.

Feyereisen, M. W., Feller, D and Dixon, D. A., (1996). **Hydrogen Bond Energy of the Water Dimer.** The Journal of Physical Chemistry 100, 2993-2997.

Fiebing, T., Wan, C and Zewail, A. H., (2002). **Femtosecond Charge Transfer Dynamics of a Modified DNA Base: 2-Aminopurine in Complexes with Nucleotides.** Physical Chemistry Chemical Physics 3, 781-788.

Flükiger, P., Lüthi, H. P., Portmann, S and Weber, J., (2000). **Molekel 4.0**. Swiss Center for Scientific Computing, Manno Switzerland.

Foreman, J. B., Head-Gordon, M., Pople, J. A and Frisch, M. J., (1992). **Toward a Systematic Molecular Orbital Theory for Excited States.** The Journal of Physical Chemistry 96, 135-149.

Foresman, J. B and Frisch, A., (1996). **Exploring Chemistry with Electronic Structure Methods.** Gaussian, inc second edition.

Fraiji, L. K., Hayes, D. M and Warner, T. C., (1992). **Static and Dynamic Fluorescence Quenching Experiments for the Physical Chemistry Laboratory.** Journal of Chemical Education 69, 424-428.

Franck, J., (1926). **Elementary Processes of Photochemical Reactions.** Transactions of the Faraday Society 21, 536-542.

Frisch, M. J., Trucks, G. W., Schlegel, H. B., Scuseria, G. E., Robb, M. A., Cheeseman, J. R., Montgomery, J. A., Jr., Vreven, T., Kudin, K. N., Burant, J. C., Millam, J. M., Iyengar, S. S., Tomasi, J. J., Barone, V., Mennucci, B., Cossi, M., Scalmani, G., Rega, N., Petersson, G. A., Nakatsuji, H., Hada, M., Ehara, M., Toyota, K., Fukuda, R., Hasegawa, J., Ishida, M., Nakajima, T., Honda, Y., Kitao, O., Nakai, H., Klene, M., Li, X., Knox, J. E., Hratchian, H. P., Cross, J. B., Adamo, C., Jaramillo, J., Gomperts, R., Stratmann, R. E., Yazyev, O., Austin, A. J., Cammi, R., Pomelli, C., Ochterski, J. W., Ayala, P. Y., Morokuma, K., Voth, G. A., Salvador, P., Dannenberg, J. J., Zakrzewski, V. G., Dapprich, S., Daniels, A. D., Strain, M. C., Farkas, O., Malick, D. K., Rabuck, A. D., Raghavachari, K., Foresman, J. B., Ortiz, J. V., Cui, Q., Baboul, A. G., Clifford, S., Cioslowski, J., Stefanov, B. B., Liu, G., Liashenko, A., Piskorz, P., Komaromi, I., Martin, R. L., Fox, D. J., Keith, T., Al-Laham, M. A., Peng, C. Y., Nanayakkara, A., Challacombe, M., Gill, P. M. W., Johnson, B., Chen, W., Wong, M. W., Gonzalez, C and Pople, J. A., (2003). **Gaussian 03, Revision B.04. Gaussian 09, Revision A.01.** Gaussian, Inc., Pittsburgh, PA.

Frisch, A., Frisch, M. J and Trucks, G. W., (2003). **Gaussian 03: User's Reference.** Gaussian, inc manual version 7.0.

Gagliardi, L. B., Castells, C. B., Rafols, C., Roses, M and Bosch, E., (2007). **Static Dielectric Constants of Acetonitrile/Water Mixtures at Different Temperatures and Debye-Huckel A and a_0B Parameters for Activity Coefficients.** Journal of Chemical Engineering Data 52, 1103-1107.

Gehiring, K., Leroy, J. L and Guéron, M., (1993). **A Tetrameric Structure with Protonated Cytosine.Cytosine Base Pairs.** Nature 363, 561-565.

Gellert, M., Lipsett, M. N and Davies, D. R., (1962). **Helix Formation by Guanylic Acid.** Proceedings of the National Academy of Sciences of the United States of America 48, 2013-2018.

Grabowski, Z. R., Rotkiewicz, K and Siemiarczuk, A., (1979). **Dual Fluorescence of Donor-Acceptor Molecules and the Twisted Intramolecular Charge Transfer (TICT) States.** Journal of Luminescence 18, 420-424.

Grabowski, Z. R., Rotkiewicz, K., Siemiarczuk A., Cowley, D. J and Baumann W., (1979). **Twisted Intramolecular Charge Transfer States (TICT). A New Class of Excited States with a Full Charge Separation.** Nouveau Journal de Chimie 3, 443-454.

Gratton, E., Jameson, D. M and Hall, R. D., (1984). **Multifrequency Phase and Modulation Fluorometry.** Annual Review of Biophysics and Bioengineering 13, 105-124.

Guest, C. R., Hochstrasser, R. A., Sowers, L. C and Millar, D. P., (1991). **Dynamics of Mismatched Base Pairs in DNA.** Biochemistry 30, 3271-3279.

Gustavsson, T., Sharonov, A., Onidas, D., Markovitsi, D., (2002). **Adenine, Deoxyadenosine and Deoxyadenosine 5'-Monophosphate Studied by Femtosecond Fluorescence Up-Conversion Spectroscopy.** Chemical Physics Letters 356, 49-54.

Han, K and Guang, J., (2011). **Hydrogen Bonding and Transfer in the Excited State.** Wiley.

Hardman, S. J. O., Thompson, K. C., (2006). **Influence of Base Stacking and Hydrogen Bonding on the Fluorescence of 2-Aminopurine and Pyrrolocytosine in Nucleic Acids.** Biochemistry 49, 9145-9155.

Hardman, S. J. O., Thompson, K. C and Botchway, S. W., (2008). **Evidence for a Nonbase Stacking Effect for the Enviroment-Sensitive Fluorescent Base Pyrrolocytosine-Comparison with 2-Aminopurine**. Phochemistry and Photobiology 84, 1473-1479.

Hare, P. M., Crespo-Hernandez, C. E and Kohler, B., (2007). **Internal Conversion to the Electronic Ground State Occurs *via* Two Distinct Pathways for Pyrimidine Bases in Aqueous Solution.** Proceedings of the National Academy of Sciences of the United States of America 104, 435-440.

Harris, V. H., Smith, C. L., Cummins, J. W., Hamilton., A. L., Adams, H., Dickman, M., Hornby, D. P and Williams, D. M., (2003). **The Effect of Tautomeric Constant on the Specificity of Nucleotide Incorporation during DNA Replication: Support for the Rare Tautomer Hypothesis of Substitution Mutagenesis.** Journal of Molecular Biology 365, 1389-1401.

He, R., Duan, X and Li,Y., (2005). **Theoretical Investigation of Spectral Properties and Tautomerization Mechanism of 2-Aminopurine.** Physical Chemistry Chemical Physics 8, 587-591.

Heddi, B and Phan, A. T., (2011). **Structure of Human Telomeric DNA in Crowded Solution.** Journal of the American Chemical Society 133, 9824-9833.

Hobza, P and Sponer, J., (1999). **Structure, Energetics, and Dynamics of the Nucleic Acid Base Pairs: Nonempirical *ab initio* Calculations.** Chemical Reviews 99, 3247-3276.

Hochstrasser, R. A., Carver, T. E., Sowers, L. C and Millar, D. P., (1994). **Melting of a DNA Helix Terminus within the Active Site of a DNA Polymerase.** Biochemistry 33, 11971-11979.

Hogendorf, W. F. J., Verhagen, C. P, Malta, E., Goosen, N., Overkleeft, H. S, Filippov, D. V and Van der Marel, G. A., (2009). **The Synthesis of a Menthol Derivative of 2-Aminopurine as a Fluorescent DNA Lesion.** Tetrahedron 65, 10430-10435.

Holmen, A., Norden, B and Albinsson, B., (1997). **Electronic Trasition Moments of 2-Aminopurine.** Journal of the American Chemical Society 119, 3114-3121.

Hollas, J. M., (1996). **Modern Spectroscopy.** 3rd Edition, John Wiley & Sons, New York.

Hungerford, G and Birch, D. J. S., (1996). **Single-photon Timing Detectors for Fluorescence Lifetime Spectroscopy.** Measurement Science and Technology 7, 121-135.

Jameson, D. M and Eccleston, J. F., (1997). **Fluorescent Nucleotide Analogs: Synthesis and Application.** Methods in Enzymology 278, 363-390.

Jansen, H. B and Ros, P., (1969). **Non-Empirical Molecular Orbital Calculations on the Protonation of Carbon Monoxide.** Chemical Physics Letters 3, 140-143.

Jean, J. M and Hall, K. B., (2001). **2-Aminopurine Fluorescence Quenching and Lifetimes: Role of Base Stacking.** Proceedings of the National Academy of Sciences of the United States of America 98, 37-41.

Kamlet, M. J., Abboud, J. L and Taft, R. W., (1977). **The Solvatochromic Comparison Method. 6. The π^* Scale of Solvent Polarities.** Journal of the American Chemical Society 99, 6027-6038

Karliner, J., Budzikiewicz, H and Djerassi, C., (1965). **Fragmentation and Hydrogen Transfer Reactions of β-Hydrindanones. Synthesis of Deuterated β-Hydrindanones.** Journal of the American Chemical Society 87, 580-591.

Kawai, M., Lee, M.J., Evans, K. O and Nordlund, T. M., (2001). **Temperature and Base Sequence Dependence of 2-Aminopurine Fluorescence Bands in Single and Double-Stranded Oligonucleotides.** Journal of Fluorescence 11, 23-32.

Klán, P and Wirz, J., (2009). **Photochemistry of Organic Compounds. From Concepts to Practice.** Wiley.

Kelley, S. O and Barton J. K., (1999). **Electron Transfer between Bases in Double Helical DNA.** Science 283, 375-381.

Kennard, O., (1985). **Structural Studies of DNA Fragments: the G.T Wobble Base Pair in A, B and Z DNA; the G.A Base Pair in B-DNA.** Journal of Biomolecular Structure and Dynamics 3, 205-226.

Klessinger, M and Michl, J., (1995). **Excited States and Photochemistry of Organic Molecules.** VCH, New York.

Koeppel, F., Riou, J. F., Laoui, A., Mailliet, P., Arimondo, P. B., Labit, D., Petitgenet, O., Helene, C and Mergny, J. L., (2001). **Ethidium Derivatives Bind to G-Quartets, Inhibit Telomerase and Act as Fluorescent Probes for Quadruplexes.** Nucleic Acids Research 29, 1087-1096.

Köppler, H., Domcke, W and Cederbaum, L. S., (1984). **Multimode Molecular Dynamics Beyond the Born-Oppenheimer Approximation.** Advanced in Chemical Physics 57, 59-246.

Kwiatkowski, J. S and Pullman, B., (1975). **Tautomerism and Electronic Structure of Biological Pyrimidines.** Advances in Heterocyclic Chemistry 18, 199-335

Lakowicz, J. R., (1999). **Principles of Fluorescence Spectroscopy.** Kluwer Academic Second Edition.

Lakowicz, J. R., (2006). **Principles of Fluorescence Spectroscopy.** Springer Third Edition.

Lampert, R. A., Chewter L. A and Phillips, D., (1983). **Standards for Nanosecond Fluorescence Decay Time Measurement.** Analytical Chemistry 55, 68-73.

Larsen, O. F. A., van Stokkum, I. H. M., Gobets, B., van Grondelle, R and van Amerongen, H., (2001). **Probing the Structure and Dynamics of a DNA Hairpin by Ultrafast Quenching and Fluorescence Depolarization.** Biophysical Journal 81, 1115-1126.

Larsen, O. F. A., van Stokkum, I. H. M., de Weerd, F. L., Vengris, M A., Aravindakumar, C. T., van Grondelle, R., Geacintov, N. E and van Amerongen, H., (2004). **Ultrafast Transient-Absorption and Steady-State Fuorescence Measurements on 2-Aminopurine Substituted Dinucleotides and 2-Aminopurine Substituted DNA Duplexes.** Physical Chemistry Chemical Physics 6, 154-160.

Lawrence, C., Sowers, G., Fazakerleyt, Eritjat, R., Kaplan, B. E and Goodman, M. F., (1986). **Base Pairing and Mutagenesis: Observation of a Protonated Base Pair between 2-Aminopurine and Cytosine in an Oligonucleotide by Proton NMR.** Proceedings of the National Academy of Science of the United States 83, 5434-5438.

Lee, G. C. Y., Prestegard, J. H and Chan, S. I., (1972). **Tautomerism of Nucleic Acid Bases. I Cytosine.** Journal of the American Chemical Society 94, 951-959.

Lee, C., Yang, W and Parr, R. G., (1988). **Development of the Colle-Salvetti Correlation-Energy Formula into a Functional of the Electron Density.** Physics Rewiew B 37, 785-789.

Leroy, J. L., Gehiring, K., Kettani, A and Guéron, M., (1993). **Acid Multimers of Oligodeoxycytidine Strands: Stoichiometry, Base Pair Characterization and Proton Exchange Properties.** Biochemistry 32, 6019-6031.

Leszczynski, J., (1992). **Are the Amino Groups in the Nucleic Acid Bases Coplanar with the Molecular Rings? *Ab initio* HF/6-31G* and MP2/6-31G* Studies.** International Journal of Quantum Chemistry 44, 43-55.

Leszczynski, J., (2000). **Isolated, Solvated and Complexed Nucleic Acid Bases: Structures and Properties.** Advances in Molecular Structure Research 6, 209-265. JAI Press.

Lide, D., (2000). **Handbook of Physics and Chemistry.** 81st Edition. CRC Press, Boca Raton, FL.

Lim, E. C., (1977). **In Excited Sates.** Ed Lim, E, Academic New York

Lim, E. C., (1986). **Proximity Effect in Molecular Photophysics: Dynamical Consequences of Pseudo-Jahn-Teller Interaction.** The Journal of Physical Chemistry 90, 6770-6777.

Lim, K. W., Amrane, S., Bouaziz, S., Xu, W., Mu, Y., Patel, D. J., Luu, K. N and Phan, A. T., (2009). **Structure of the Human Telomere in K+ Solution: a Stable Basket-type G-quadruplex with only Two G-tetrad Layers.** Journal of the American Chemical Society 131, 4301-4309.

Lin, J and Frey, P. A., (2000). **Strong Hydrogen Bonds in Aqueous and Aqueous-Acetone Solutions of Dicarboxylic Acids: Activation Energies for Exchange and Deuterium Fractionation Factors.** Journal of the American Chemical Society 122, 11258-11259.

Lippert, Von E., (1957). **Spektroskopische Bistimmung des Dipolmoments Aromatischer Veribindungen im Ersten Angeregten Singulettzustand.** Z Electrochem, 61, 962-975.

Löwdin, P. O., (1963). **Proton Tunneling in DNA and its Biological Implications.** Reviews of Modern Physics 35, 724-732.

Matanga, N., Kaifu, Y and Koizumu., M., (1956). **Solvent Effects upon Fluorescence Spectra and the Dipole Moments of Excited Molecules.** Bulletin of the Chemical Society of Japan 29, 465-470.

Matei, I., Ionescu, S and Hillebrand, M., (2010). **Solute-Solvent Hydrogen Bond Formation in the Excited-State. Experimental and Theoretical Evidence.** Department of Physical Chemistry, Faculty of Chemistry, University of Bucarest. Bd. Regina Elisabeta 4-12, Bucharest, Romania.

Mehra, R., (2003). **Application of Refractive Index Mixing Rule in Binary Systems of Hexadecane and Heptadecane with N-Alkanols at Different Temperatures.** Proceedings of the Indian Academy of Science 115, 147-154.

Melhuish, W. H., (1961). **Quantum Efficiencies of Fluorescence of Organic Substances: Effect of Solvent and Concentration of the Fluorescent Solute.** Journal of Physical Chemistry 65, 229-235.

Mergny, J. L., Phan, A. T and Lacroix, L., (1998). **Following G-Quartet Formation by UV-Spectroscopy.** Federation of European Biochemical Societies Letters 435, 74-78.

Mergny, J. L., and Lacroix, L., (2003). **Analysis of Thermal Melting Curves.** Oligonucleotides 13, 515-537.

Millar, D. P., (1996). **Fluorescence Studies of DNA and RNA Structure and Dynamics.** Current Opinion in Structural Biology 6, 322-326.

Mishra, S. K, Shukla, M. K and Mishra, P. C., (2000). **Electronic Spectra of Adenine and 2-Aminopurine: an *ab initio* Study of Energy Level Diagrams of Different Tautomers in Gas Phase and Aqueous Solution.** Journal of Spectrochimica Acta A Molecular and Bimolecular Spectroscopy 56, 1355-1384.

Mishra, S. K and Mishra, P. C., (2001). **An *ab initio* Study of Electronic Structure and Spectra of 8-Bromoguanine: a Comparative Study with Guanine.** Spectrochimica Acta A, Molecular and Biomolecular Spectroscopy 57, 2433-2450.

Neely, R. K., Magennis, S. W., Dryden, D. T. F., and Jones, A. C., (2004). **Evidence of Tautomerism in 2-Aminopurine from Fluorescence Lifetime Measurements.** The Journal of Physical Chemistry B 108, 17606-17610.

Neely, R., Magennis, Parsons, S and Jones, A., (2007). **Photophysics and X-Ray Structure of Crystalline 2-Aminopurine.** Chemphyschem: A European Journal of Chemical Physics and Physical Chemistry 8, 1095-1102.

Noguera, M., Blancafort, L., Sodupe, M and Bertran, J., (2006). **Canonical Watson-Crick Base Pair Interactions in π-π^* Type Triplet States.** Molecular Physics: An International Journal at the Interface between Chemistry and Physics 104, 925-931.

Nordlund, T. M., Andersson, S., Nilson, L and Rigler, R., (1989). **Structure and Dynamics of a Fluorescent DNA Oligomer Containing the EcoRI Recognition Sequence: Fluorescence, Molecular Dynamics and NMR Studies.** Biochemistry 28, 9095-9103.

Nordlund, T. M., Xu, D and Evans, K. O., (1993). **Excitation Energy Transfer in DNA: Duplex Melting and Transfer from Normal Bases to 2-Aminopurine.** Biochemistry 32, 12090-12095.

Olivucci, M., (2005). **Computational Photochemistry.** Elsevier Amsterdam.

O'Neill, M. A., Becker, H. C., Wan, C., Barton, J. H and Zewail, A. H., (2003). **Ultrafast Dynamics in DNA-Mediated Electron Transfer: Base Gating and the Role of Temperature.** Angewandte Chemie International Edition 42, 5896-5900.

O'Neill, M. A., Dohno, C and Barton, J. K., (2004). **Direct Chemical Evidence for Charge Transfer between Photoexcited 2-Aminopurine and Guanine in Duplex DNA.** Journal of the American Chemical Society 126, 1316-1317.

Ooshika, Y., (1954). **Absorption spectra of dyes in solution.** Journal of Physical Society of Japan 9, 954-602.

Paeschke, K., Simonsson, T., Postberg, J., Rhodes, D and Lipps, H. J., (2005). **Telomere end-binding Proteins Control the Formation of G-quadruplex DNA Structures in Vivo.** Nature Structural and Molecular Biology 12, 847-854.

Parker, C., (1968). **Photoluminescence of Solutions. With Applications to Photochemistry and Analytical Chemistry.** Publisher by Elsevier Pub co, first edition.

Parkinson, G. N., Lee, M. P and Neidle, S., (2002). **Crystal Structure of Parallel Quadruplexes from Human Telomeric DNA.** Nature 417, 876-880.

Pecourt, J-M. L., Peon, J and Kohler, B., (2000). **Ultrafast Internal Conversion of Electronically Excited RNA and DNA Nucleosides in Water.** Journal of the American Chemical Society 122, 9348-9349.

Peon, J and Zewail, A. H., (2001). **DNA/RNA Nucleotides and Nucleosides: Direct Measurement of Excited-State Lifetimes by Femtosecond Fluorescence Up-Conversion.** Chemical Physics Letters 348, 255-262.

Perdew, J. P and Zunger, A., (1981). **Self-interaction correction to density-functional approximations for many-electron systems.** Physical Review B, 23 5048-5079.

Perdew, J. P., (1986). **Density-functional approximation for the correlation energy of the inhomogeneous electron gas.** Physical Review B, 33, 8822-8824.

Perdew, J. P., Burke, K and Wang, Y., (1996). **Generalized gradient approximation for the exchange-correlation hole of a many-electron system.** Physical Review B, 54 16533-16539.

Perun, S., Sobolewski, A. L and Domcke, W., (2005). ***Ab initio* Studies on the Radiationless Decay Mechanisms of the Lowest Excited States of 9H Adenine.** Journal of the American Chemical Society 127, 6257-6265.

Perun, S., Sobolewski, A. L and Domcke, W., (2006). ***Ab initio* Studies on the Photophysics of 2-Aminopurine.** Molecular Physics 104, 1113-1121.

Perun, S., Sobolewski, A. L and Domcke, W., (2006). **Role of Electron-Driven Proton-Transfer Processes in the Excited-State Deactivation of the Adenine-Thymine Base Pair.** The Journal of Physical Chemistry A 110, 9031-9038.

Phan, A. T., Guéron, M and Leroy, J. L., (2001). **Investigations of Unusual DNA Motifs.** Methods in Enzymology 338, 341-371.

Phan, A. T and Mergny, J. L., (2002). **Human telomeric DNA: G-quadruplex, i-motif and Watson-Crick Double Helix.** Nucleic Acids Research 30, 4618-4625.

Puglisi, J. D and Tinoco I., (1989). **Absorbance Melting Curves of RNA.** Methods in Enzymology 180, 304-325.

Rachofsky, E. L., Ross, A. J. B., Krauss, M and Osman, R., (2001). **CASSCF Investigation of Electronic Excited States of 2-Aminopurine.** The Journal of Physical Chemistry A 105, 190-197.

Rachofsky, E., Osman, R and Ross J., (2001). **Probing Structure and Dynamics of DNA with 2-Aminopurine: Effects of Local Environment on Fluorescence.** Biochemistry 40, 946-956.

Rachwal, P. A and Fox, K. R., (2007). **Quadruplex Melting.** Methods 43, 291-301.

Reichardt, C., (1990). **Solvents and Solvent Effects in Organic Chemistry.** VCH second edition.

Reha, D., Kabelác, M., Ryjácek, F., Sponer, J., Sponer, J. E., Elstner, M., Suhai, S and Hobza, P., (2003). **Intercalators. 1. Nature of Stacking Interactions between Intercalators (Ethidium, Daunomycin, Ellipticine, and 4', 6-diaminide-2-phenylindole) and DNA Base Pairs. *Ab initio* Quantum Chemical, Density Functional Theory, and Empirical Potential Study.** Journal of the American Chemical Society 124, 3366-3376.

Reha-Krantz, L. J., Hariharan, C., Subuddhi, U., Xia, S., Zhao, C., Beckman, J., Christian, T and Konigsberg, W., (2011). **Structure of the 2-Aminopurine-Cytosine Base Pair Formed in the Polymerase Active Site of the RB69 Y567A-DNA Polymerase.** Biochemistry 50, 10136-10149.

Reynisson, J and Steenken, S., (2004). **One Electron Reduction of 2-Aminopurine in the Aqueous Phase. A DFT and Pulse Radiolysis Study.** Physical Chemistry Chemical Physics 7, 659-665.

Rhys Williams, A. T and Winfield, S. A., (1983). **Relative Fluorescence Quantum Yields Using a Computer-controlled Luminescence Spectrometer.** Analyst 108, 1067-1071.

Rich, A., (1993). **DNA Comes in Many Forms.** Gene 135, 99-109.

Rist, M. J and Marino, J. P., (2000). **Association of an RNA Kissing Complex Analysed Using 2-Aminopurine Fluorescence.** Nucleic Acids Research 29, 2401-2408.

Rist, M. J and Marino, J. P., (2002). **Fluorescent Nucleotide Base Analogs as Probes of Nucleic Acid Structure, Dynamics and Interactions.** Current Organic Chemistry 6, 775-793.

Robb, M. A., Olivucci, M and Bernardi, F., (1998). **Encyclopaedia of Computational Chemistry.** Wiley, Chichester.

Rotkiewicz, K., Grellman, K. H and Grabwoski, Z. R., (1973). **Reinterpretation of the Anomalous Fluorescence of p-n, N-Dimethylamino-benzonitrile.** Chemical Physics Letters 19, 315-318.

Rothwell, P. J and Waksman, G., (2005). **Structure and Mechanism of DNA Polymerases.** Advances in Protein Chemistry 71, 401-440.

Ruzankina, Y., Asare, A and Brown, E. J., (2008). **Replicative Stress, Stem Cells and Aging.** Mechanisms of Ageing and Development 129,460-466.

Sahu, P. K., Mishra, R. K and Lee, S., (2005). **A Density Functional Theory Study for the Hydrogen-Bonded Nucleic Acid Base Pair: Cytosine Dimer.** The Journal of Physical Chemistry A, 2887-2893.

Salter, L. M and Chaban, G. M., (2002). **Theoretical Study of Gas Phase Tautomerization Reactions for the Ground and First Excited Electronic States of Adenine.** The Journal of Physical Chemistry A 106, 4251-4256.

Sandorfy, C., (1999). **The Role of Rydberg States in Spectroscopy and Photochemistry.** Kluwer Academic Publisher, Dordrecht. The Netherlands.

Santa Lucia, J., (2000). **Spectrometry and Fluorimetry.** M.G Gore Ed, Oxford University Press, 329-356.

Santosh, C and Mishra, P. C., (1991). **Electronic Spectra of 2-Aminopurine and 2,6-Diaminopurine: Phototautomerism and Fluorescence Reabsorption.** Spectrochimica Acta part A Molecular and Biomolecular Spectroscopy 47, 1685-1693.

Schaffitzel, C., Berger, I., Postberg, J., Hanes, J., Lipps, H. J and Pluckthun, A., (2001). **In Vitro Generated Antibodies Specific for Telomeric Guanine-Quadruplex DNA React with *Stylonychia Lemnae* Macronuclei.** Proceedings of the National Academy of Sciences of the United States of America 98, 8572-8577.

Seefeld, K. A., Plutzer, C., Lowenich, D., Haber, T., Linder, R., Kleinermanns, K., Tatchen, J and Marian, C. M., (2005). **Tautomers and Electronic States of Jet-Cooled 2-Aminopurine Investigated by double Resonance Spectroscopy and Theory.** Physical Chemistry Chemical Physics 7, 3021-3026.

Sembrano, J. R., de Souza, A. R., Queralt, J. J and Andres, J., (2000). **A Theoretical Study on Cytosine Tautomers in Aqueous Media by Using Continuum Models.** Chemical Physics Letters 317, 437-443.

Serrano-Andrés, L., Merchán, M and Borin, A. C., (2006). **Adenine and 2-Aminopurine: Paradigms of Modern Theoretical Photochemistry.** Proceedings of National Academy of Sciences of the United States of America 103, 8691-8696.

Serrano-Andrés, L., Merchán, M and Borin, A. C., (2006). **A Three-State Model for the Photophysics of Adenine.** Chemistry. A European Journal 12, 6559-6571.

Shafer, R. H and Smirnov I., (2000). **Biological Aspects of DNA/RNA Quadruplexes.** Biopolymers 56, 209-227.

Shulka, M. K and Leszczynski, J., (2003). **In Computational Chemistry: Reviews of Current Trends.** Leszczynski, J 8, 249. World Scientific, Singapore.

Shulka, M. K and Leszczynski, J., (2004). **TDDFT Investigation on Nucleic Acid Bases: Comparison with Experiments and Standard Approach.** Journal of Computational Chemistry 25, 768-778.

Shulka, M. K and Leszczynski, J., (2005). **Time-Dependent Density Functional Theory (TD-DFT) Study of the Excited State Proton Transfer in Hypoxanthine.** International Journal of Quantum Chemistry 105, 387-395.

Shulka, M. K and Leszczynski, J., (2006). **A Theoretical Study of Hydration of 4-Thiouracil in the Electronic Singlet Excited State.** Journal of Molecular Structure: THEOCHEM 771, 149-155.

Shulka, M. K., Leszczynski, J., Sponer, J and Lankas, F., (2006). **In Computational Studies of RNA and DNA.** Challenges and Advances in Computational Chemistry and Physics 2, 433.

Shulka, M. K and Leszczynski, J., (2007). **Electronic Spectra, Excited State Structures and Interactions of Nucleic Acid Bases and Base Assemblies: A Review.** Journal of Biomolecular Structure and Dynamics 25, 93-118.

Smagowicz, J and Wierzchowski, K. L., (1974). **Lowest Excited State of 2-Aminopurine.** Journal of Luminescence 8, 210-232.

Socrates, G., (1994). **Infrared Characterisistics Group Frequencies.** John Wiley & Sons, New York.

Somsen, O. J. G., van Hoek, A and van Amerongen, H., (2005). **Fluorescence Quenching of 2-Aminopurine in Dinucleotides.** Chemical Physics Letters 402, 61-65.

Sponer, J., Leszczynski, J and Hobza, P., (2002) **Electronic Properties, Hydrogen Bonding, Stacking and Cation-Binding of DNA and RNA Bases.** Biopolymers 61, 3-36.

Stokes, G. G., (1852). **On the Change of Refrangibility of Light.** Philosophical Transactions of the Royal Society of London 142, 463-562.
Suppan, P., (1994). **Chemistry and Light.** Royal Society of Chemistry.

Suppan, P and Ghoneim N., (1997). **Solvatochroism.** The Royal Society of Chemistry.

Tamaki T., (1980). **Polar Fluorescent State of 1 and 2-Acetylantharacene. The Perturbation of Protic Solvents.** Bulletin of the Chemical Society of Japan, 577-582.

Tamaki T., (1982). **The Photoassociation of 1- and 2-Acetylanthracene with Methanol.** Bulletin of the Chemical Society of Japan, 1761-1767.

Terent'ev, P. B and Kalandarishvili, A. G. **Application of Mass Spectrometry for the Analysis of Organic Tautomeric Compounds.** Mass Spectrometry Reviews 15, 339-363.

Thompson, K. C and Miyake, N., (2005). **Properties of a New Fluorescent Cytosine Analogue, Pyrrolocytosine.** The Journal of Physical Chemistry B 109, 6012-6019.

Tinsley, R. A and Walter, N. G., (2006). **Pyrrolo-C as a Fluorescent Probe for Monitoring RNA Secondary Structure Formation.** A Publication of RNA Society 12, 522-529.

Tleugabulova, D and Reha-Krantz, L. J., (2007). **Probing DNA Polymerase-DNA Interactions: Examining the Template Strand in Exonuclease Complexes Using 2-Aminopurine Fluorescence and Acrylamide Quenching.** Biochemistry 46, 6559-6569.

Topal, M. D and Fresco J. R (1976) **Complementary Base Pairing and the Origin of Substitution Mutations.** Nature 263, 285-289.

Turro, N. J., Ramamurthy, V and Scaiano, J. C., (2009). **Principles of Molecular Photochemistry. An Introduction.** University science books.

Tsuzuki, S and Luthi, H. P., (2001). **Interaction Energies of van der Waals and Hydrogen Bonded Systems Calculated Using Density Functional Theory: Assessing the PW91 Model.** The Journal of Chemical Physics 114, 3949-3957.

Valdes, H., Klusak, V., Pitonak, M., Exner, O., Stary, I., Hobza, P and Rulisek, L., (2008). **Evaluation of the Intramolecular Basis Set Superposition Error in the Calculations of Larger Molecules: [n]Helicenes and Phe-Gly-Phe Tripeptide.** Journal of Computational Chemistry 29, 861-870.

Valeur, B., (2002). **Molecular Fluorescence: Principles and Applications.** Wiley-vch.

Vamosi, G., Gohlke, C and Clegg, R. M., (1996). **Fluorescence Characteristics of 5-Carboxytetramethylrodamine Linked Covalently to the 5' end of Oligonucleotides: Multiple Conformers of Single-Stranded Dye-DNA Complexes.** Biophysical Journal 71, 972-994.

Velapoldi, R and Mielenz, K., (1980). **A Fluorescence Standard Reference Material: Quinine Sulphate Dihydrate.** National Borough of Standards Special Publication 139, 260-264.

Voet, D., Voet, J. G and Pratt, C. W., (2005). **Fundamentals of Biochemistry. Life at Molecular Level.** Wiley and Sons Second Edition.

Wan, C., Fiebig, T., Schiemann, O., Barton, J. K and Zewail, A. H., (2000). **Femtosecond Direct Observation of Charge Transfer between Bases in DNA.** Proceedings of the National Academy of Science of the United Sates 97, 14052-14055.

Wan, C., Xia, T., Becker, H and Zewail, A. H., (2005). **Ultrafast Unequilibrated Charge Transfer: A New Channel in the Quenching of Fluorescent Biological Probes.** Chemical Physics Letters 412, 158-163.

Wang, W., Hellinga, H. W and Beese, L. S., (2011). **Structural Evidence for the Rare Tautomer Hypothesis of Spontaneous Mutagenesis.** Proceedings of the Natural Academy of Science of the United States of America 108, 17644-17648.

Ward, D. C., Reich, E and Stryer. L., (1969). **Fluorescence Studies of Nucleotides and Polynucleotides. I. Formycin, 2-Aminopurine Riboside, 2-6- Diaminopurine Riboside, and the Derivatives.** The Journal of Biological Chemistry 224, 1228-1237.

Wardle, B., (2010). **Principles and Applications of Photochemistry.** Wiley.

Wassam, W and Lim, E. C., (1978). **Proximity Effect in Radiationless Transitions.** The Journal of Chemical Physics 68, 433-454.

Watson, J. D and Crick F. H. C., (1953). **Molecular Structure of Nucleic Acids. A Structure for Deoxyrobise Nucleic Acids.** Nature 171, 737-738.

Wayne, R. P., (1988). **Principles and Applications of Photochemistry.** Oxford Science Publications.

Wijmenga, S. S and van Buuren, B. N. M., (1998). **The Use of NMR Methods for Conformational Studies of Nucleic Acids.** Progress in Nuclear Magnetic Resonance Spectroscopy 32, 287-387.

Wijst, T., Guerra, C. F., Swart, M and Bickelhaupt, M. F., (2006). **Performance of Various Density Functionals for the Hydrogen Bonds in DNA Base Pairs.** Chemical Physics Letters 426, 415-421.

Wolken, J. K., Yao, C., Turecek, F., Polce, M. J and Wesdemiotis, C., (2007). **Cytosine Neutral Molecules and Cation-Redicals in the Gas Phase Structures, Energetics, Ion Chemistry and Neutralization-Reionization Mass Spectroscopy.** International Journal of Mass Spectrometry 267, 30-42.

Woodson, S. A., (2005). **Metal Ions and RNA Folding: A Highly Charged Topic with a Dynamic Future.** Current Opinion in Chemical Biology 9, 104-109.

Xu, D and Nordlund, T. M., (2000). **Sequence Dependence of Energy Transfer in DNA Oligonucleotides.** Biophysical Journal 78, 1042-1058.

Yarkony, D. R., (1995). **Modern Electronic Structure Theory.** World Scientific Singapore.

Zhao, Y and Truhlar, G. D., (2004). **Hybrid Meta Density Functional Theory Methods for Thermochemistry, Thermochemical Kinetics, and Noncovalent Interactions: The MPW1B95 and MPWB1K Models and Comparative Assessments for Hydrogen Bonding and van der Waals Interactions.** The Journal of Physical Chemistry A 108, 6908-6918.

Zhao, Y and Truhlar, D. G., (2005). **Benchmark Databases for Nonbonded Interactions and their Use to Test Density Functional Theory.** Journal of Chemical Theory and Computation 1, 415-432.

Zhao, Z., Zhang, Q., Gao, C and Zhuo, Y., (2006). **Motion of the Hydrogen Bond Proton in Cytosine and the Transition between its Normal and Imino States.** Physics Letters A 359, 10-13.

Zhurko, G. A., (2006). **Chemcraft 1.6**, http:/www.chemcraftprog.com

Zietz, B and Retting, W., (2000). **Do Twisting and Pyramidalization Contribute to the Reaction Coordinate of Charge-Transfer Formation in DMABN and Derivatives?** Chemical Physics Letters 317, 187-196.

Zuker, M., (2003). **Mfold Web Server for Nucleic Acid Folding and Hybridization Prediction.** Nucleic Acids Research 31, 3406-3415.